UK-RAS NETWORK
ROBOTICS & AUTONOMOUS SYSTEMS

UK-RAS19 CONFERENCE: *'Embedded Intelligence: Enabling & Supporting RAS Technologies'*

PROCEEDINGS

UK-RAS19 CONFERENCE PROCEEDINGS: 24th January 2019

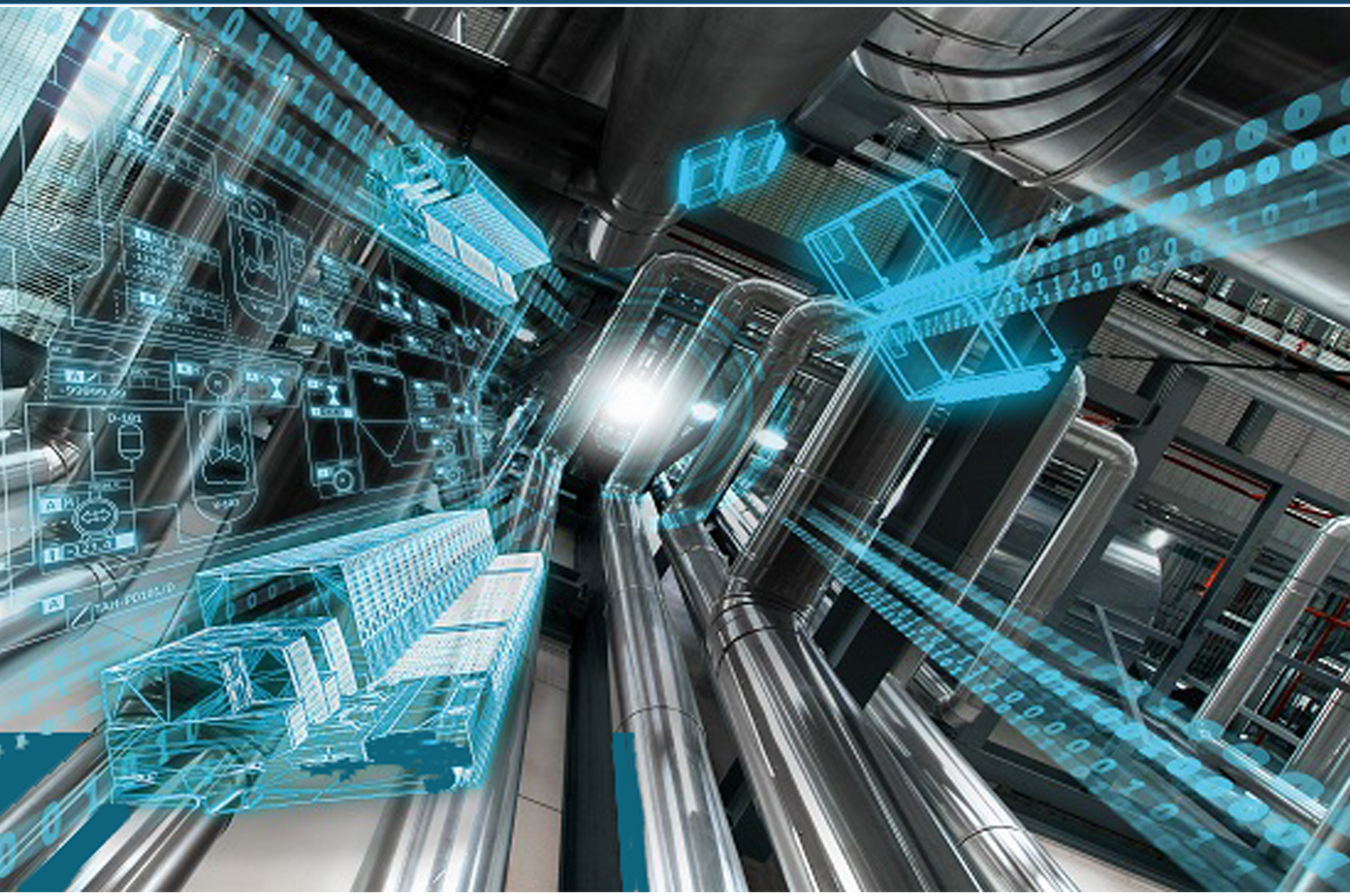

CDT-EI EPSRC CENTRE for Doctoral Training in Embedded Intelligence

EPSRC
Engineering and Physical Sciences Research Council

Table of Contents

Research Papers

A Deep Adaptive Framework for Robust Myoelectric Hand Movement Prediction
C. P. Robinson, B. Li, Q. Meng, and M. T. G. Pain — ***1***

Evaluation of U- shaped weld prep identification and tracking
D. De Becker, J. Dobrzanski, J. Hodgson, M. Goh, P. Kinnell, and L. Justham — ***4***

A Bioinspired Approach for Mental Emotional State Perception towards Social Awareness in Robotics
J. J. Bird, D. R. Faria, L. J. Manso, and A. Ekárt — ***8***

MoDSeM: Modular Framework for Distributed Semantic Mapping
G. S. Martins, J. F. Ferreira, D. Portugal, and M. S. Couceiro — ***12***

Controlling a Bipedal Robot with Pattern Generators Trained with Reinforcement Learning
C. Kouppas, Q. Meng, M. King, and D. Majoe — ***16***

Development of a Debris Clearance Vehicle for Limited Access Environments
C. West, W. Cheah, V. Rajasekaran, A. West, F. Arvin, S. Watson, M. Giuliani, R. Stolkin, and B. Lennox — ***20***

Model based 3D point cloud segmentation for automated selective broccoli harvesting
H. A. Montes, G. Cielniak, and T. Duckett — ***24***

Enabling functional resilience in autonomous multi-arm and multi-vehicle cooperative tasks
A. K. Behera — ***28***

In process monitoring and control of automated TIG welding processes
J. Dobrzanski, D. De Becker, and L. Justham — ***32***

Dynamic, Anytime Task and Path Planning for Mobile Robots
C. Wong, E. Yang, X.-T. Yan, and D. Gu — ***36***

An Information Theoretic Approach to Path Planning for Frontier Exploration
C. Rhodes, C. Liu, and W.-H. Chen — ***40***

Underwater Scene Segmentation by Deep Neural Network
Y. Zhou, J. Wang, B. Li, Q. Meng, E. Rocco, and A. Saiani — ***44***

Poster Papers

Exploiting System Capacity with a Distributed Routing Strategy for UAVs
W. Bonnell ***48***

Towards Symbiotic Human-Robot Collaboration: Human Movement Intention Recognition with an EEG
A. Buerkle, N. Lohse, and P. Ferreira ***52***

Development of a Multi-robotic System for Exploration of Biomass Power Plants
S. An, F. Arvin, S. Watson, and B. Lennox ***56***

Transfer Learning in Assistive Robotics: From Human to Robot Domain
D. A. Adama, A. Lotfi, R. Ranson, and P. Trindade ***60***

Towards a Dataset of Activities for Action Recognition in Open Fields
A. Gabriel, N. Bellotto, and P. Baxter ***64***

Semantic enhanced navigation among movable obstacles in the home environment
N. Sun, E. Yang, J. Corney, Y. Chen, and Z. Ma ***68***

A Mixed Reality Approach to Robotic Inspection of Remote Environments
E. Welburn , T. Wright , C. Marsh, S. Lim, A. Gupta, W. Crowther, and S. Watson ***72***

Multi-Cameras based Decision Making at Mini-Roundabouts for Autonomous Vehicles
W. Wang, Q. A. Nguyen, P. W. Hing Chung, and Q. Meng ***75***

Acoustic side-scan on enclosed underwater environment
P. Yibin, and P. N. Green ***79***

Establishing Continuous Communication through Dynamic Team Behaviour Switching
T. Zhivkov, E. Schneider, and E. I. Sklar ***83***

Trajectory Creation Towards Fast Skill Deployment in Plug-and-Produce Assembly Systems: A Gaussian-Mixture Model Approach
M. Zimmer, A. Al-Yacoub, P. Ferreira, and N. Lohse ***87***

Movement and Gesture Recognition Using Deep Learning Technology
B. Xie , B. Li, and A. Harland ***91***

Visual Features as Frames of Reference in Task-Parametrised Learning from Demonstration
S. El Zaatari, and W. Li ***94***

Can underwater environment simulation contribute to vision tasks for autonomous systems?
J. Wang, Y. Zhou, B. Li, Q. Meng, E. Rocco, and A. Saiani ***98***

Development of a Simulated Production Environment for Plug-And-Produce Architecture Testing
W. Eaton **100**

A Novel Wireless Measurement While drilling System for Geotechnical and Geophysical Applications
M. Khater, and W. Al-Nuaimy **104**

Integration of Calibration and Forcing Methods for Predicting Timely Crop States by Using AquaCrop-OS Model
T. Zhang, J. Su, C. Liu, and W.-H. Chen **108**

Locust Recognition and Detection via Aggregate Channel Features
D. Yi, J. Su, and W.-H. Chen **112**

An Embedded System for Real-Time 3D Human Detection
H. Cai, L. Jiang, J. Wang, M. Saada, and Q. Meng **116**

Walking Motion Real-time Detection Based on Walking Stick Equipped with MPU and Raspberry Pi
J. Wang, M. Saada, H. Cai, and Q. Meng **118**

Subclass Discriminant Analysis based Myoelectric Hand Motion Recognition
D. Zhou, Y. Fang, Z. Ju, and H. Liu **121**

The Intelligent Control Strategy and Verification for Precise Water-fertilizer Irrigation System
Y. Zhang, Z. Wei, L. Zhang, and W. Jia **125**

A Framework for Anomaly Detection in Activities of Daily Living using an Assistive Robot
S. W. Yahaya, A. Lotfi, and M. Mahmud **131**

A Deep Adaptive Framework for Robust Myoelectric Hand Movement Prediction

Carl Peter Robinson, Baihua Li, Qinggang Meng, and Matthew T.G. Pain

***Abstract*— This work explored the requirements of accurately and reliably predicting user intention using a deep learning methodology when performing fine-grained movements of the human hand. The focus was on combining a feature engineering process with the effective capability of deep learning to further identify salient characteristics from a biological input signal. 3 time domain features (root mean square, waveform length, and slope sign changes) were extracted from the surface electromyography (sEMG) signal of 17 hand and wrist movements performed by 40 subjects. The feature data was mapped to 6 sensor bend resistance readings from a CyberGlove II system, representing the associated hand kinematic data. These sensors were located at specific joints of interest on the human hand (the thumb's metacarpophalangeal joint, the proximal interphalangeal joint of each finger, and the radiocarpal joint of the wrist). All datasets were taken from database 2 of the NinaPro online database repository. A 3-layer long short-term memory model with dropout was developed to predict the 6 glove sensor readings using a corresponding sEMG feature vector as input. Initial results from trials using test data from the 40 subjects produce an average mean squared error of 0.176. This indicates a viable pathway to follow for this prediction method of hand movement data, although further work is needed to optimize the model and to analyze the data with a more detailed set of metrics.**

I. Introduction

The potential of the electromyography (EMG) signal generated by human muscles when performing activity has been explored in the myoelectric control of prosthetic devices for many decades, particularly in upper limb mechanisms. Major advancements in commercial hardware have led to instruments capable of intricate mechanical actions. Control strategies, however, have been less successful in their evolution, now seen as a bottleneck to providing effective means of daily life activity for amputees. Use of pattern recognition has garnered significant successes in laboratory conditions [1] and gradual translation to viable end product (www.coaptengineering.com). Much of this has been based on the classification methodology, which is still sequential in nature, only offering one hand function at a time and thus contradictory to the requirement for more fluid, natural movement in myoelectric prosthetics [2]. A more promising approach is the employment of a simultaneous and proportional methodology. Here, the objective is to control multiple degrees of freedom (DOFs) using regression, to estimate a continuous output value for each DOF. This establishes a mapping between EMG input and control output, proving more suitable for intuitive control. Deep learning has found many applications when applied to biological data [3]. In general, when applied to the problem of hand gesture recognition, convolutional neural networks (CNN), long short term memory (LSTM), or combinations of the two are employed [4], [5], [6]. These follow the classification methodology however, with [7] providing the only evidence so far of using regression for continuous prediction of hand kinematic data. They use an autoencoder (AE) to map two kinematic signals via nonlinear regression, for controlling two DOFs. This work uses a 3-layer LSTM model to map sEMG data for 17 human hand and wrist movements, taken from 40 subjects. A preprocessing stage where initial sets of features are extracted from the sEMG data, is used to provide LSTM model input. This is then mapped to 6 glove sensor readings representing the corresponding hand kinematic data.

II. Method

A. Preprocessing

Data from 40 intact subjects were downloaded from the NinaPro project website (http://ninapro.hevs.ch), specifically Exercise B's 17 hand and wrist movements from Database 2. The data was initially acquired using 12 Delsys Trigno wireless electrodes (Delsys, Inc, www.delsys.com). Eight electrodes were attached around the right forearm, at a fixed distance from the radio-humeral joint, two were fixed to the main activity spots of the anterior and posterior of the forearm, and two more placed on the biceps brachii and triceps brachii. All movements were repeated 6 times consecutively, each lasting approximately 5 seconds, plus a 3-second rest period where the subject returned their hand to a rest posture with data acquired at a 2 KHz sampling rate [8]. A CyberGlove II (www.cyberglovesystems.com) equipped with 22 sensors located around the joint positions of the fingers and wrist, was used to acquire hand kinematics. The glove uses resistive bend-sensing technology providing an 8-bit value (0 to 255) proportional to the bend angle for each sensor. Six sensors were chosen, representing metacarpophalangeal (MCP) and proximal interphalangeal (PIP) joints of interest around the thumb and fingers of the right hand, and additionally the wrist joint (Table I). This enabled sufficient data capture for all hand movements. An in-house MATLAB program separated movement repetitions into a matrix of time-ordered sEMG voltage data from the electrodes. Each movement's data was split such that repetitions 1, 3, 4, and 6 were allocated to a

C. P. Robinson, B. Li, and Q. Meng are with the Computer Science department, Loughborough University, Loughborough, LE11 3TU, UK. Corresponding author: C.P. Robinson; e-mail: c.p.robinson@ lboro.ac.uk).

M. T .G. Pain is with the Sport, Exercise, and Health Sciences department, Loughborough University, Loughborough, LE11 3TU, UK

training set and repetitions 2 and 5 to a test set. Data were normalized to have zero mean and unit standard deviation [8].

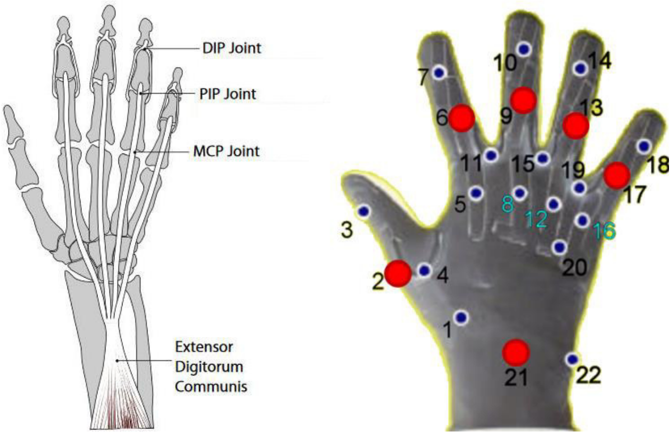

Figure 1. Joints of the finger and CyberGlove sensor locations. Red circles indicate the selected sensors, used for target kinematic data prediction.. Figure created by adapting detail from [9] and [10].

CYBERGLOVE SENSORS OF INTEREST FOR EXPERIMENT

Sensor	Location
2	MCP joint of the thumb
6	PIP joint of the index finger
9	PIP joint of the middle finger
13	PIP joint of the ring finger
17	PIP joint of the pinky finger
21	Radiocarpal joint of the wrist

A 256 ms sliding window was employed, as per our previous work, to segment the data. The increment was set at 25 ms to ensure a densely packed array of windows. Three time domain (TD) features were chosen based on performance in our previous research [11]. The first two are part of the prevalent Hudgins set [12] while the third feature is also commonly used in sEMG research:

- Waveform Length (WL) – a simple rolling calculation of the summation of the absolute difference between a signal sample x_k and its previous sample x_{k-1} (equating to Δx_k), for all samples N in one window:

$$WL = \sum_{k-1}^{N} |\Delta x_k| \tag{1}$$

- Slope Sign Changes (SSC) – a scalar count in terms of number of times the sEMG signal slope changes between positive and negative values, based on a threshold. Three consecutive window samples are used to check if sample x_k is greater or less than its neighbours (x_{k-1} and x_{k+1}):

$$\begin{gathered} x_k > x_{k-1} \text{ and } x_k > x_{k+1}, \text{ or} \\ x_k < x_{k-1} \text{ and } x_k < x_{k+1}, \text{ and} \end{gathered} \tag{2}$$

$$|x_k - x_{k-1}\ x_{k+1}| \geq 0.01\text{V or } |x_k - x_{k-1}\ x_{k-1}| \geq 0.01\text{V}$$

- Root Mean Square (RMS) – an indicator of average signal value, cancelling out the negative values by squaring them to obtain a mean value:

$$RMS = \sqrt{\frac{1}{N}\sum_{k=1}^{N} x_k^2} \tag{3}$$

Together, these features can provide useful information about sEMG signal waveform complexity and frequency, and muscle contraction intensity. They were extracted from each window, for all 12 electrodes, creating a feature vector v_t of 36 scalar features for one time window *t*. Corresponding glove sensor data was windowed using the same procedure and a mean signal feature extracted per window for each sensor. These 6 scalar values were appended to the existing feature vector v_t. For each hand movement, this process yielded a time-ordered feature matrix $F_{T,E,G}$ consisting of a set of v_t feature vectors:

$$\boldsymbol{F_{T,E,G}} = \begin{pmatrix} f_{t,i}^{e} & \cdots & f_{t,i}^{G} \\ \vdots & \ddots & \vdots \\ f_{T,i}^{e} & \cdots & f_{T,i}^{G} \end{pmatrix} \tag{4}$$

where *e* is a single sEMG electrode up to a maximum of *E* electrodes, *i* represents an extracted feature, *G* is the total number of glove sensors, and *T* the total number of time windows in one hand movement.

B. LSTM Model

An LSTM network is a type of recurrent neural network (RNN) existing as a series of states through time, suitable for analyzing data of a temporal nature, such as the sEMG signal. It utilizes a memory cell consisting of 3 logic gates and a persistent memory state, providing more control than a regular RNN as to the data flow through the network state per time step [13]. Research into LSTM usage in biosignal fields shows stacking several LSTM layers offers improved model performance [14], capturing more detailed temporal information. Initial trials and related work [15] prompted a design of 3 layers (Fig. 2). The 36 sEMG TD features were used as input to the model, which produced predicted kinematic output in the form of 6 glove sensor values, representative of the corresponding joint movements. The model was configured to evaluate 4 time steps of feature data when making a prediction and each LSTM layer was configured to have 200 hidden nodes, based on a prior optimization investigation that used a subset of subject data. After each layer, a dropout layer was added, implementing an arbitrary dropout rate of 30% in order to generalize the model and reduce the chance of overfitting. A dense, fully-connected layer using a tanh activation function completed the model, making the actual prediction of the 6 glove sensor outputs.

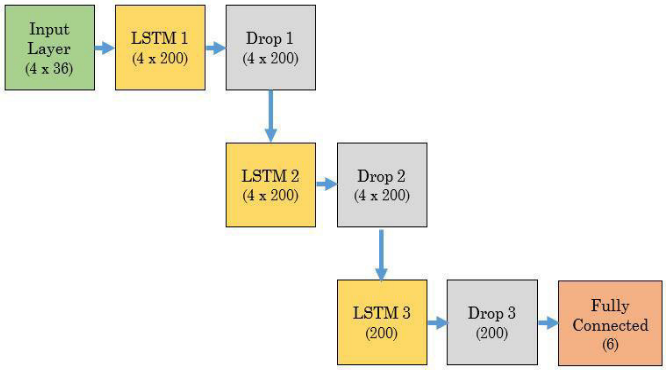

Figure 2. LSTM model structure.

The network was trained using the stochastic gradient descent optimization algorithm, learning rate of 0.3 with momentum of 0.9 applied to the gradient descent operation. Training took place over 40 epochs using a batch size of 600. All hyperparameters were tuned by conducting an optimization process using a 3-fold cross validation grid search.

III. Results

The mean squared error (MSE) was used as a model performance estimate. Individual subject's test data were evaluated with the trained LSTM model, predicting the 6 DOFs for each hand movement. An average MSE of 0.176 was achieved over 40 subjects and plots indicate reasonable DOF prediction over the 17 hand and wrist movements (Fig. 3).

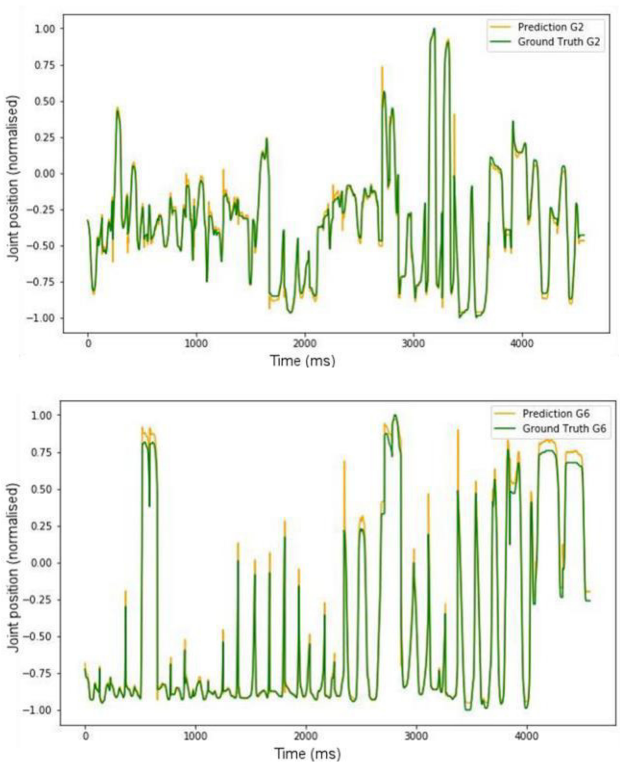

Figure 3. Predicted kinematic data (yellow) against ground truth glove sensor data (green) of thumb MCP joint (top) and index finger PIP joint (bottom) for 17 hand and wrist movements from test dataset of subject 1.

A more detailed analysis is required of this preliminary work, to provide a clearer indication of model performance. Use of additional performance metrics, including Pearson's correlation coefficient, would be applicable. Comparison against a benchmark from other research using a regression technique or simultaneous and proportional control of multiple DOFs is also required.

IV. Conclusion

The experiment performed here shows it is feasible to use an LSTM neural network to perform prediction of wrist and finger movements with a good degree of accuracy. Combining the deep model with a feature engineering phase has proved advantageous. Investigating the replacement of this phase with a CNN for automated feature extraction is a pertinent next step. There is also still room for improvement with further work needed to optimize the LSTM model structure and hyperparameters, include additional performance measurements and more detailed analysis, and compare results with related research.

References

[1] Nazmi, N. et al., "A Review of Classification Techniques of EMG Signals during Isotonic and Isometric Contractions," *Sensors*, 16(8), p.1304, 2016.

[2] Amsuess, S. et al., "Context-Dependent Upper Limb Prosthesis Control for Natural and Robust Use," *IEEE Trans Neural Syst Rehabil Eng.*, 24(7), pp.744–753, 2016.

[3] Mahmud, M. et al., "Applications of Deep Learning and Reinforcement Learning to Biological Data," *IEEE Trans Neural Netw Learn Syst*, 29(6), pp.2063–2079, 2018.

[4] Atzori, M., Cognolato, M. & Müller, H., "Deep learning with convolutional neural networks applied to electromyography data: A resource for the classification of movements for prosthetic hands," *Frontiers in Neurorobotics*, 10(Sep), pp.1–10, 2016.

[5] Xia, P., Hu, J. & Peng, Y., "EMG-Based Estimation of Limb Movement Using Deep Learning With Recurrent Convolutional Neural Networks," *Artificial Organs*, 42(5), pp.E67–E77, 2017.

[6] Wang, W. et al., "Sensor Fusion for Myoelectric Control Based on Deep Learning With Recurrent Convolutional Neural Networks." *Artificial Organs*, p.11, 2018.

[7] Vujaklija, I. et al., "Online mapping of EMG signals into kinematics by autoencoding," *Journal of Neuro Engineering and Rehabilitation*, 15(1), p.21, 2018.

[8] Atzori, M. et al. "Electromyography data for noninvasive naturally controlled robotic hand prostheses," *Scientific data* (2014), 1:140053, 2014.

[9] Elkoura, G. & Singh, K.,. "Handrix: animating the human hand," in *Proc. of ACM SIGGRAPH 2003 Symposium on Computer Animation*. pp. 110–120, 2003.

[10] Castellini, C., Passig, G. & Zarka, E., "Using ultrasound images of the forearm to predict finger positions." *IEEE Trans Neural Syst Rehabil Eng*, 20(6), pp.788–797, 2012.

[11] Robinson, C. et al. "Pattern classification of hand movements using time domain features of electromyography," in *Proc. 4th Int. Conf. on Movement Computing,* London, pp.1–6, 2017.

[12] Hudgins, B., Parker, P., & Scott, R.N., "A New Strategy for Multifunction Myoelectric Control," *IEEE Trans Biomed Eng, 40(1), pp.82–94, 1993.*

[13] Hochreiter, S. & Schmidhuber, J., "Long Short-Term Memory," *Neural Computation*, 9(8), pp.1735–1780, 1997.

[14] Deng, H., Zhang, L. & Shu, X., "Feature memory-based deep recurrent neural network for language modeling," *Applied Soft Computing Journal*, 68, pp.432–446, 2018.

[15] Tan, J.H. et al., "Application of stacked convolutional and long short-term memory network for accurate identification of CAD ECG signals," *Computers in Biology and Medicine*, 94(Dec 2017), pp.19–26, 2018.

Evaluation of U- shaped weld prep identification and tracking.

D De Becker, J Dobrzanski, J Hodgson, M Goh, P Kinnell, L Justham

***Abstract*—An autonomous welding system must be able to identify and extract the relevant features of the weld seam to generate an accurate weld path. Furthermore, the system must be able to adapt the weld torch position in real time during the weld. This has led to a two-stage approach, with the first stage identifying the weld path from a roughly scanned weld seam and the second stage adjusting the weld torch position in real time. In order to track weld seams, it has become popular to utilize a laser line scanner due to its versatility in measuring a wide range of materials and the non-contact nature.**

Three methods were explored in extracting the shoulders of a U-shaped weld prep. This included a clustering method utilizing a density based spatial clustering approach, a line of best fit approach and an image processing approach utilizing Hough line transforms. Both the clustering and line of best fit approach use a spline fit to find the bottom of the weld prep. While the image processing approach uses a circular Hough transform to find the same position. Further testing, with real world data, showed that the clustering approach struggled when the weld prep was not perpendicular to the scanning axis. This issue was not observed in either the line of best fit method or the image processing method, however the image processing method often found multiple lines on the same shoulder of the weld prep. This led to more testing being carried out with the line of best fit method which tended to be the most robust method. The main drawback of this method was the higher computational requirement. However, during the real-time seam track testing it was found that the robot position could be updated at 30Hz without the use of buffers.

I. Introduction

When two parts are joined by a weld, the interfacing area is known as the weld seam. In order to create a more homogeneous joint a weld prep is normally used. This is achieved by the machining both interfacing faces. When the two faces are joined the machined faces typically conform to patterns derived from either a U or V shape as these are easy to machine and conform to the British standards [1]. An image taken from the British standard showing various weld preps can be seen in Figure 2.

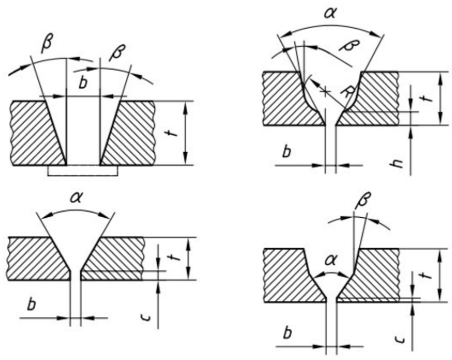

Figure 2. Weld prep examples taken from British standards BS EN ISO 9692-1:2013(E) [1].

The weld seam is a crucial component in obtaining good quality welds leading to weld seam tracking becoming more prevalent in the automation of welding processes. This can be seen in the increased interest in a large number of sectors including the automotive, ship building and nuclear repair industries [2] [3]. This is most likely due to the increased use of complex geometries, harsh working environment for welders as well as the increased need for better quality control [4][5]. With this greater need in weld seam tracking, many researchers have tended towards the use of laser line scanners due to their decrease in cost over the years as well as their ability to work with a wide variety of materials [4]. As stated by Pires et al. the trend for seam tracking techniques has been to move from a two pass approach obtaining the geometry and then following the tracked seam in the second pass to tracking the seam in real time while obtaining information about the weld seam [6].

II. Methodology

The purpose of this work is to identify a U-shaped weld prep using a laser line scanner with the intention of generating a robot weld path from the extracted features. This allowed for any errors in the machining or the work piece fitting process to be accounted for and the robot path to be adjust to these errors [7]. Once the scan path has been generated the robot

D De Becker is with the Intelligent Automation Centre at Loughborough University, LE11 3QZ, UK (email: d.de-becker@lboro.ac.uk).
J Dobrzanski is with the Intelligent Automation Centre at Loughborough University, LE11 3QZ, UK (email: J.Dobrzanski@lboro.ac.uk).
J Hodgson is with the Intelligent Automation Centre at Loughborough University, LE11 3QZ, UK (email: J.R.Hodgson@lboro.ac.uk).
M Goh is with the Intelligent Automation Centre at Loughborough University, LE11 3QZ, UK (email: Y.Goh@lboro.ac.uk).
P Kinnell is with the Intelligent Automation Centre at Loughborough University, LE11 3QZ, UK (email: P.Kinnell@lboro.ac.uk).
L Justham M Goh is with the Intelligent Automation Centre at Loughborough University, LE11 3QZ, UK (email: L.Justham@lboro.ac.uk).

could use the same seam tracking algorithm to weld the bespoke seam and adjust the path in real-time as the part warps and distorts due to the welding process. The equipment used during this evaluation included a Micro Epsilon 2900-100/BL laser line scanner, a KUKA KR16-2 controlled by a KRC-2 controller utilizing both KR-XML and Robot Sensor Interface (RSI). An image of the laser scanner calibration routine designed for this experiment can be seen in Figure 3.

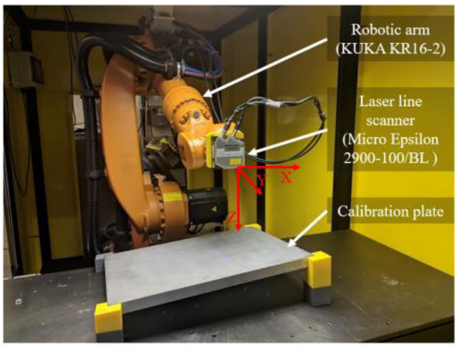

Figure 3. Setup used for generating the laser scan data.

During the testing the Laser scanners co-ordinate system was used. A depiction of this co-ordinate system can be seen in Figure 4. When the robot moves linearly over a weld prep, such as the image shown in Figure 5A, the laser scanner was able to capture the profile of the weld prep which can be seen in Figure 5B, this figure along with the other figures in this report use the laser scanners reference frame as described in Figure 4.

Figure 4. Image showing the laser scanner co-ordinate system.

The full profile of the weld seam was initially scanned with feature extraction used to generate a robot weld path. Once the weld path was generated the same feature extraction algorithm could be used to adjust the robot position in real time as the component warps and distorts under the welding conditions. Therefore, the feature extraction must be able to work in a deterministic and timely manner.

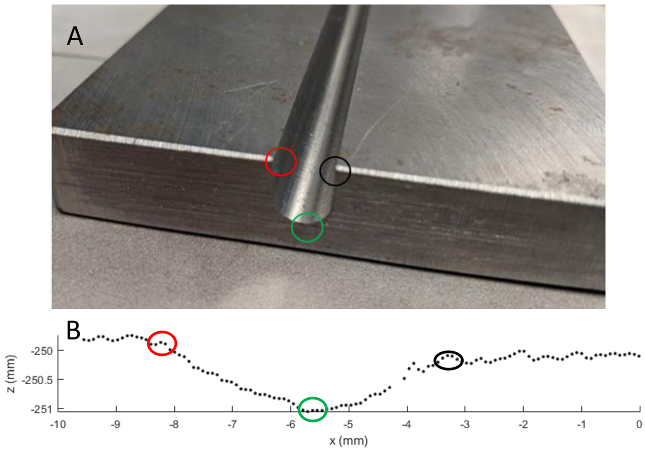

Figure 5. Example of a U-shaped weld prep (A) and a graph showing the laser scanner data of a U-shaped weld prep.

III. WELD PREP IDENTIFICATION

To identify the weld prep, raw data was taken from the laser scanner, an example of which can be seen in Figure 5B. The key features that needed to be extracted can be seen in Figure 6. These include the left shoulder labelled as A which is in red, the bottom of the U which is labelled B and C found in green and purple respectively, and finally the right shoulder D which can be seen in black. If the weld prep doesn't have a gap, then position B and C are coincident.

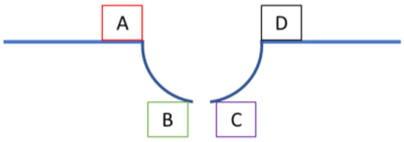

Figure 6. Diagram of a labelled U-shaped weld prep.

These features are paramount for a successful weld to be created as it stops the filler wire either touching down or contacting the wall of the weld seam. As well as identifying where to deposit the filler wire.

It was identified that finding feature A and D, as described in Figure 6, was the most prevalent as this would generate the region of interest to find feature B and C. In order to extract these features, three methods were explored:

- a clustering method
- a line of best fit method
- an image processing approach

Once the edges of the shoulders were identified for both the clustering and line of best fit approach, the data points between the two shoulders were extracted and a spline was fitted between them, an example of this can be seen in Figure 7. The data point closest to the bottom of the spline was assumed to be the bottom of the weld prep and thus position C or D in Figure 6 could be found. If there was data missing at the bottom of the weld prep it would be assumed that there was a gap between the two mating faces. Therefore, instead of C and D being coincident they would be identified as two separate points at either edge of the gap as described in Figure 6.

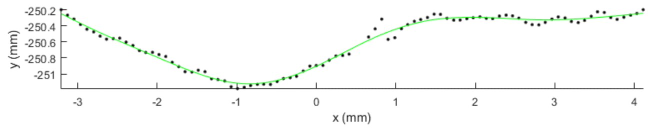

Figure 7. Identifying bottom of the U weld prep using a spline fit.

A. *Clustering approach*

The first approach used a simple clustering algorithm to find the shoulders. This method utilizes a Density-based spatial clustering [8] to group points based on their Z values, the group with the largest number of data points would be identified as the shoulders with the edge of the shoulders being identified as largest gap between neighboring points in the data. Alternatively, the edge of the shoulders could be found by clustering the shoulder values based on X values, as this would create two distinct groups for the left and right shoulders as shown in Figure 8.

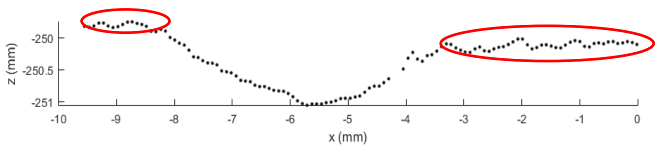

Figure 8. Approach 1(Clustering) showing the single cluster making up the two shoulders of the U weld prep.

The main drawback of this method was its susceptible nature to noise, particularly when gaps occurred in the data or if the data was not levelled. An example of the data not being levelled can be seen in Figure 9, this leads to the shoulders being misidentified, as the largest group no longer occurs at the shoulders.

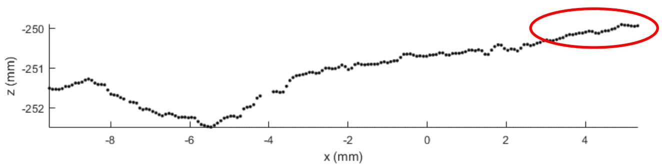

Figure 9. Misidentification of shoulders due to an off-axis scan.

B. *Line of best fit approach*

The second approach uses a line of best fit to identify the two shoulders as shown in Figure 10. The line of best fit was generated for both the left shoulder and right shoulder independently as shown by the red and blue lines respectively. The line of best fit was created by taking the first 1.5mm of the shoulders. This was approximately a third of the full shoulder length, thus having a good compromise between representing the shoulder accurately, while maintaining the capability of handling off center scans, such as the scan shown in Figure 9. Once the line of best fit was generated an upper and lower limit could be set for the edges of the shoulders. Once the points deviate outside the lower limit, this was identified as the edge of the shoulder. The lines of best fit also allowed for more information to be categorized such as the height and angle difference between the two shoulders. This could be used in an adaptive welding process to change the relevant robot or welding torch orientation in real-time.

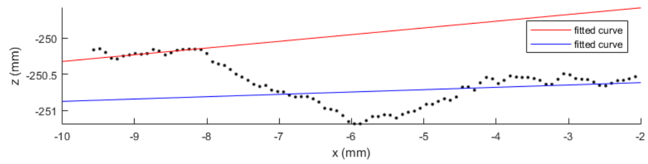

Figure 10. Approach 2 (Line of best fit) to find the shoulders of the weld prep.

This implementation can also be used to level the data, thus dismissing the problems identified in the clustering method. However, it does require some initial conditions; this includes the maximum gap size at the bottom of the weld prep, the minimum shoulder length to generate the lines of best fit, as well as the minimum and maximum size of the prep itself. These values make the overall finding of the two shoulders much more robust compared to the clustering process. This method can also be used to identify other types of weld preps including V preps and U/V hybrid preps as it only requires a straight shoulder leading into the weld prep.

C. *Image processing approach*

The third and final approach uses an image processing method known as Hough line transform [9] to find the shoulders of the weld seam. Unlike the other approaches it uses a circular Hough transform to find the bottom of the U prep as shown in Figure 11. The Hough transform uses a binary image of the laser scan data to identify the prominent lines within the image. This is based on information given by the user, including the minimum length of the line as well as the minimum distance between two-line segments. A processed image with lines and circles identified can be seen in Figure 11.

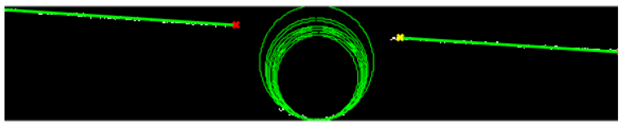

Figure 11. Approach 3 (Hough Transform) to find the shoulders and the bottom of the weld prep.

The main drawback of this method is in the conversion between an image which is measured in pixels and the data given by the laser scanner which is in mm. This conversion must be equal to the resolution of the laser scanner camera. If the image was set to a smaller resolution, then detail of the scan would be lost, while if the image was larger than the resolution of the laser scanner then the extra pixels would be redundant and increase the computing power required. This would lead to a very large image size which may be impossible to process on conventional hardware in real time. In testing it became apparent that 10μm resolution was the limit before the file size became too large to compute quickly, however this was finer than the resolution of the laser scanner used. Further testing also showed, that dependent on the input parameters selected, often multiple lines would be detected on the same shoulder, as shown in Figure 12. This would lead to further decisions needing to be made, most likely based on a maximum and minimum U prep size to decide which line was correct. The final drawback is that, due to the nature of the circular Hough transform, the image processing method can only be used on rounded weld preps, such as the U weld prep described in this paper.

Figure 12. Errors in the Hough line approach with multiple lines identified when only a single shoulder is present.

IV. EVALUATION AND CONCLUSION

Although the clustering approach is simple to implement, due to its inability of handling off axis scans, it is difficult to use in a real-time seam tracking application. Although, further work could be done on leveling the data before the clustering is completed. In contrast to this, the image processing approach using Hough transforms, allows for off axis measurements as well as being considerably quicker than the other methods. However, when testing on real world data it became apparent that this approach was very susceptible to the user inputs with multiple Hough lines generated when there is only a single line present. Due to the similar amount of user input required, it was decided to take the line of best fit approach further as this is the only approach that would be suitable for other weld prep shapes including V and hybrid U/V preps. This would increase the versatility of the system over the clustering approach or the image processing approach. However, it should be noted that this method does require higher amounts of computational power over the image processing approach.

As stated, the line of best fit approach was taken forward and implemented into the real-time robot control system. This system used the bottom of the U prep to track where the weld torch should be in real time. Initially a full scan of a seam was completed and a path generated the results of which can be seen in Figure 13, with the same colour convention used as in Figure 6. The figure shows a successful extraction of features with a smooth spline following both shoulders and the bottom of the prep without being distorted by the large amount of the reflection. Once the path was generated the U prep was moved a few mm from this generated path to simulate the seam moving under welding conditions. The robot scanned the weld prep at a constant frequency while moving at a constant speed of 5mm/s. The system was able to find all four features well as identifying the center of the weld prep, the robot was then told to adjust its position to move the center of the weld prep into the center of the laser scanners field of view. It was observed that the robot adjusted its position at 30Hz with a maximum offset of 0.5mm from the current position. This testing showed the successful implementation of a closed loop seam tracking algorithm which could be used in a real time welding application.

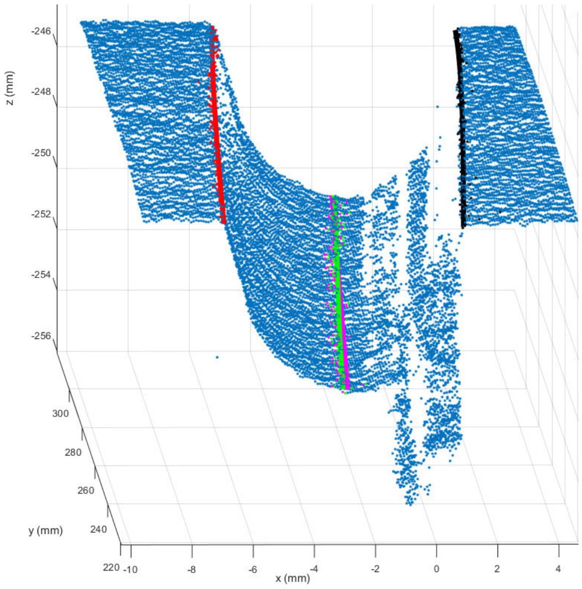

Figure 13. Image of feature extraction using the line of best fit method.

To further develop this seam tracking system, further work should test the versatility of the system by testing various weld prep shapes, as well as focusing on further refining the algorithm to remove outliers and including some more advanced adaptive welding techniques based on the orientation of the shoulders. Finally, some further testing could be done on the performance of this system during a real-world welding application.

ACKNOWLEDGMENT

The authors would like to thank the Intelligent Automation Centre at Loughborough University for the use of equipment and lab space to conduct this research.

REFERENCES

[1] British Standard, "BSI Standards Publication Welding and allied processes — Types of joint preparation shielded metal arc welding , gas welding ," BS EN ISO 9692-1:2013(E), 2013.

[2] J. N. Pires, A. Loureiro, T. Godinho, P. Ferreira, B. Fernando, and J. Morgado, "Welding robots," *IEEE Robot. Autom. Mag.*, vol. 10, no. 2, 2003.

[3] M. Wilson, "The role of seam tracking in robotic welding and bonding," *Ind. Rob.*, vol. 29, no. 2, 2002.

[4] A. Rout, B. B. V. L. Deepak, and B. B. Biswal, "Advances in weld seam tracking techniques for robotic welding: A review," *Robot. Comput. Integr. Manuf.*, vol. 56, 2019.

[5] Y. Zou, L. Jinchao, X. Chen, and R. Lan, "Learning Siamese networks for laser vision seam tracking," *J. Opt. Soc. Am.*, vol. 35, no. 11, 2018.

[6] J. N. Pires, A. Loureiro, and G. Bolmsjö, *Welding robots : technology, system issues and applications*. Springer, 2006.

[7] S. B. Chen, "Research evolution on intelligentized technologies for arc welding process," *J. Manuf. Process.*, vol. 16, no. 1, 2014.

[8] M. Ester, K. Hans-Peter, S. Jorg, and X. Xiaowei, "Density-Based Clustering Algorithms for Discovering Clusters in Large Spatial Databses with Noise," in *Association for the Advancement of Artificial Intelligence*, 1996, no. 96.

[9] P. V. Hough and A. A. Mich, "Method and means for recognizing complex patterns," US Patent 3069654, 1962.

A Bioinspired Approach for Mental Emotional State Perception towards Social Awareness in Robotics

Jordan J. Bird, Diego R. Faria, Luis J. Manso, and Anikó Ekárt

{birdj1, d.faria, l.manso, a.ekart}@aston.ac.uk

Abstract— **This preliminary study explores a new approach to EEG data classification by using the concept of evolutionary algorithms to perform attribute selection, as well as optimise a neural network for data classification in mental communication for robotics. EEG brainwave data is recorded from a preliminary set of subjects via the TP9, AF7, AF8, and TP10 electrodes used by the EEG headband, and 2550 statistical temporal features are extracted as dimensions of data. Nature inspired evolutionary algorithms select attributes before an evolutionary algorithm optimizes a neural network topology. A Long Short-Term Neural Network is also trained to perform deep learning on the data. Promising results show that the evolutionary optimised neural net scores 96.11% accuracy and the LSTM achieves 96.86%. The evolutionary neural network, although lacking in 0.75 accuracy points, has a training time far more optimal than the LSTM, at less than 25% of the required resource usage.**

I. Introduction

While deep learning is often applied to solve extremely complex problems, the procedure is often criticized for being expensive in computational resources and processing time requirements; due to the growing need for machine learning in both industrial and scientific applications of robotics, optimization is at the forefront of importance for their viability. Natural optimization, such as that observed in Darwinian evolution, are now becoming a viable option for solving real-world problems.

In Human-Robot Interaction (HRI), an increase in resource availability allows for the development of more degrees of interaction with a human, as well as the accuracy of classifying those discrete interactions, for example, in using complex techniques to classify a user's thought patterns as a point of input in social interaction with machines. Specifically, to classify a subject's emotional state requires a large amount of data to be processed in order to train a model which can then match minute patterns and rules to those states. Since the EEG signals are complex, non-linear, and non-stationary, temporal time-window and statistical extraction techniques must be employed in order to mathematically describe a wave pattern.

This paper presents a preliminary study in which an evolutionary simulation from a previous study derives, through a *survival of the fittest*, a fully connected neural network topology which can classify a dataset of an EEG brainwaves to emotional state. The accuracy closely matches that of modern deep learning techniques but is trained in under a quarter of the computational resources required.

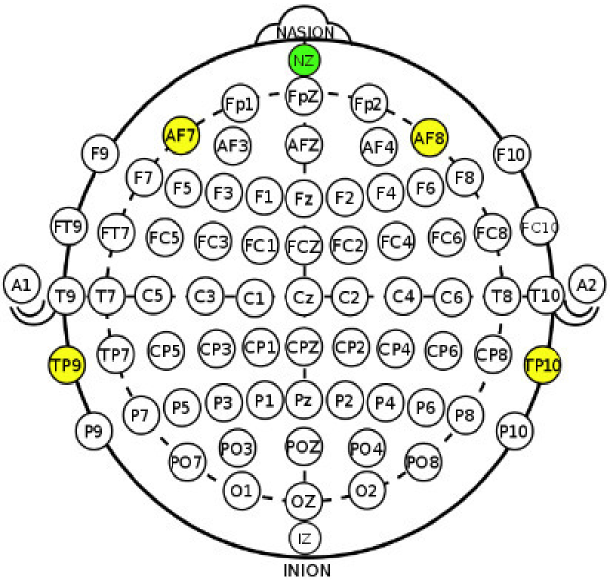

Fig 1. EEG sensors TP9, AF7, AF8 and TP10 of the MUSE headband.

II. Background

Electroencephalography, or EEG, is the measurement and recording of electrical activity produced by the brain [1]. Electrodes are placed on certain points around the cranium, which read minute electrophysiological currents produced by the brain due to nervous oscillation [2]. Raw electrical data is measured in Microvolts (uV), which over time produce wave patterns when gathered sequentially.

The MUSE is a commercially available EEG headband featuring four electrodes for recording brainwave activity, as seen in Fig 1. Placement positions correlate to the international standard EEG placement system [3].

Neuroscientific studies show that chemical composition influences nervous oscillation, which in turn generate

*All authors are with the School of Engineering and Applied Science,
Aston University. Birmingham, UK.

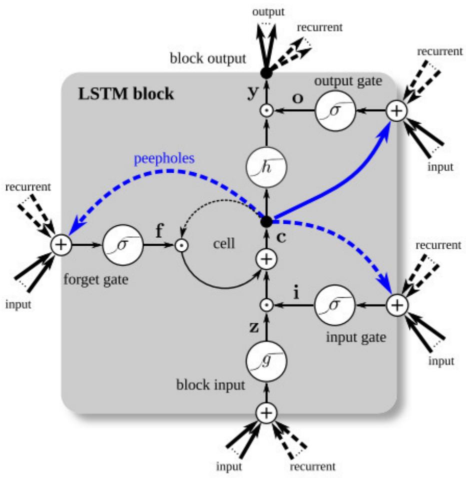

Fig 2. An illustrated LSTM unit [14]

electrical brainwave activity [13]. Emotions are a direct result of varying chemical compositions within the brain, and thus a side-effect of feeling emotion is to generate electrical brain activity, which can then be reverse engineered and classified and their source emotion(s).

In terms of emotional classification through different levels of user enjoyment, researchers successfully measured two distinct states of varying enjoyment of a task via binary classification techniques [4]. Muse headbands are also often used in neuroscience research projects due to their low cost, accessibility, and effectiveness in terms of classification and accuracy. In a related experiment, binary classification of two physical tasks achieved 95% accuracy using Bayesian probability methods [5].

A previous study used ensemble classification techniques to classify a user's emotional state, providing the dataset for this experiment [6], the best model was a Random Forest classifier with a classification accuracy of 97.89%. A related study also used classical machine learning techniques to classify whether someone was concentrative or relaxed [7] with success following the same method of statistical extraction.

Long-Short-Term-Memory (LSTM) is a technique in which multiple recurrent neural networks (RNN) predict an output based on their input and their current state. An illustration of the individual LSTM units can be observed in Figure 2, the operations that each unit will compute are given as follows.

Firstly, a logical forget will decide which information to discard and delete: W_f represents the learning-weighting matrix, h represents the output vector of the unit at provided timestep $t\text{-}1$, x_t being the current input vector, and finally b_f is a bias vector applied to the process.

$$f_t = \sigma\left(W_f \, . [h_{t-1}, x_t] + b_f\right) \tag{1}$$

The cell then stores certain information, i represents input data, with C_t being the vector of the new values generated by the process.

$$i_t = \sigma(W_i \, . [h_{t-1}, x_t] + b_i) \tag{2}$$

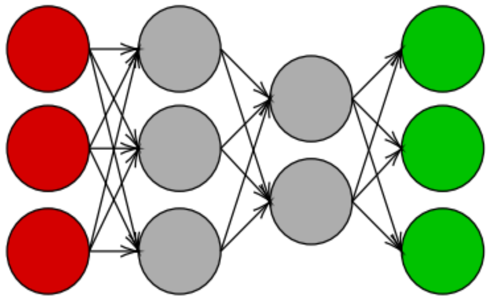

Fig 3. A Fully Connected Neural Network for classification of Three Inputs to Three Classes, with Two Hidden Layers of 3 and 2 Neurons

$$\tilde{C}_t = \tanh(W_c . [h_{t-1}, x_t] + b_c). \tag{3}$$

The cell is then updated using (1-3) in a convolutional operation:

$$\mathrm{C}_t = \mathrm{f}_t * \mathrm{C}_{t-1} + \mathrm{i}_t * \tilde{C}_t \tag{4}$$

An output is consequently generated where O_t represents the cell's output gate. The internal (hidden) state of the cell is subsequently updated:

$$\mathrm{o}_t = \sigma(\mathrm{W}_o [h_{t-1}, x_t] + b_o). \tag{5}$$

$$h_t = o_t * \tanh(C_t). \tag{6}$$

Fully Connected Artificial Neural Networks (ANN) also approximate and classify, though do not compute temporal states as with LSTM. An example of ANN architecture can be seen in Figure 3, where three inputs are computed to one of three output classes, via two hidden layers of 3 and 2 neurons respectively.

Learning is performed through backpropagation [8]. This is a case of automatic differentiation in which errors in classification or regression (when comparing outputs of a network to ground truths) are passed backwards from the final layer, to derive a gradient which is then used to calculate neuron weights within the network, dictating their activation. It must be noted that the network topology itself is static, and thus, is not optimized. Weighting refinement is carried out via the following process:

1. Generate a network; input nodes are equal to the number of data attributes, outputs are equal to the number of classes (or 1 for regression problems). Hidden layers, if any, are defined by human input.
2. Initialise the node weights randomly by a specified distribution algorithm (e.g. XAVIER).
3. Compute the gradients.
4. Backpropagate the errors through the network to update neuron weights.

Errors are calculated via various methods, e.g. distance from the ground truth where real numbers are concerned. For classification, entropy is calculated:

$$E(S) = -\sum_{i=1}^{c} P_i \text{ x } log_2(P_i) \, . \tag{7}$$

Comparison is thus the difference between two entropies, giving information gain or information loss when one model is compared to another. This is the value of the Kullback-Leibler (KL) divergence when a univariate probability distribution of a given attribute is compared to another [10]. Information gain is thus given as:

$$InfoGain(T, a) = H(T) - H(T|a). \quad (8)$$

Evolutionary algorithms search a problem space via a method inspired by natural evolution [11]. A population of solutions have a fitness metric and compete against one another for survival. This causes a race condition to occur when an environment can support fewer solutions than exist, the *survival of the fittest*, causing weaker solutions to be killed off and allowing the stronger to survive. This, over time, causes the population to increase in strength [12].

The evolutionary search in its simplest form follows this general process:

1. Population at generation 0 are initialized via a chosen distribution, e.g. Random.
2. The simulation begins until a defined termination:
    a. Select parent(s) for use in generating offspring.
    b. Evaluate the generated offspring's fitness.
    c. Kill off the weakest members based on the number of solutions that the environment can support.
3. Produce the strongest solution found after the simulation is terminated.

Previous work found success in evolutionary optimisation algorithms being applied to the selection of network topology in a single-objective approach to achieve the highest classification accuracy, and thus best applied to datasets in which class distribution is close to equal [9]. The problem space of deep neural networks grows exponentially with each added layer, and thus, an exhaustive search is an unrealistic option in terms of even the most state-of-the-art computer hardware. For this reason, heuristic search techniques are employed to efficiently explore the problem space.

III. METHOD

Data is acquired from a previous experiment [6]. Data is gathered from two subjects, male and female aged 20-22. The EEG data was recorded from a MUSE EEG headband where each subject viewed six films clips all with an obvious emotional valence. The emotional experiences caused by the clips formed a database of raw electrical readings which then had temporal statistics extracted. Statistical features extraction derived by [7] was adopted in this work.

As stated in [7], a time window of length 1s was introduced, overlapping every 0.5 seconds (e.g. *w1 0-1*, *w2 0.5-1.5*). Time windows are described by their extracted mathematical statistical features. Of the 2550 features generated for each object of data, an evolutionary search of 10 solution population members was performed for 10 generations to calculate the best set of features, since the dimensionality of the data was far too complex.

Two alternative models are explored and then trained with the generated dataset. Firstly, an LSTM topology is manually explored and tuned, as the models are far too computationally expensive to search with a metaheuristic approach. Secondly, the evolutionary algorithm will search the problem space of MLP neural networks, with a limitation of three maximum hidden layers a 100-neuron upper bound for each. A population of 10 are simulated for 10 generations, with roulette selection being used for breeding partners. The simulation is run three times with identical parameters for scientific validity. Both models are trained on 10-fold cross validation of the dataset, and finally compared in terms of classification accuracy and resources required to train. Both types of network are given 50 epochs to train, with a batch size of 50 for prediction. All random numbers were generated by the Java Virtual Machine (JVM) with a seed of 0.

Both models were trained on a Graphical Processing Unit (GPU) due to its high efficiency when compared to a Central Processing Unit (CPU). The GPU used was an Nvidia GTX1060 with 6GB of Graphical Memory and 1280 CUDA cores for computation. Displaying the OS (Windows 10) was the only other graphical process executing during the experiment.

IV. RESULTS

Evolutionary attribute selection performed on the dataset for 10 generations with a population of 10 found 500 attributes suitable for use in classification, and thus data dimensionality was reduced from 2550 to 500 for the dataset to be used in the experiments.

Manual tuning of the LSTM found that a single hidden layer of units consistently outperformed deeper networks. 25 units on the layer were found to be the most optimal, with a classification accuracy of 96.86%, as seen in Table I.

Three genetic simulations were executed as observed in Table II, the most optimal network was found to be a single hidden layer of 15 neurons, producing a classification accuracy of 96.11%.

Finally, the two best networks are compared in Table III, where, although slightly more accurate (+0.75), the LSTM took far longer to train (+48.45s).

V. CONCLUSION

To conclude, this experiment suggested two models for classifying a subject's mental emotional state based on the mathematical descriptions of recorded brainwave activity:

- An LSTM that achieved 96.86% and required 65.11s of resources to train
- An MLP with genetically optimised topology which achieved 96.11% and required 16.66s to train.

TABLE I. MANUAL TUNING RESULTS FOR LSTM TOPOLOGY FOR EMOTIONAL STATE CLASSIFICATION

LSTM Units	Classification Accuracy (%)
25	**96.86**
50	96.66
75	96.48
100	95.73
125	95.87

TABLE II. THE BEST SOLUTIONS OF MLP TOPOLOGY AT THE FINAL GENERATION OF THREE INDIVIDUAL EVOLUTIONARY SIMULATIONS

MLP Topology	Classification Accuracy (%)
1 hidden layer, 6 neurons	95.68
1 hidden layer, 15 neurons	**96.11**
2 hidden layers, (9, 5) neurons	94.37

TABLE III. COMPARISON OF TWO FINAL SOLUTIONS

Classifier	Classification Accuracy (%)	Training Time (s)
LSTM (Manual)	**96.86**	65.11
MLP (Genetic)	96.11	**16.66**

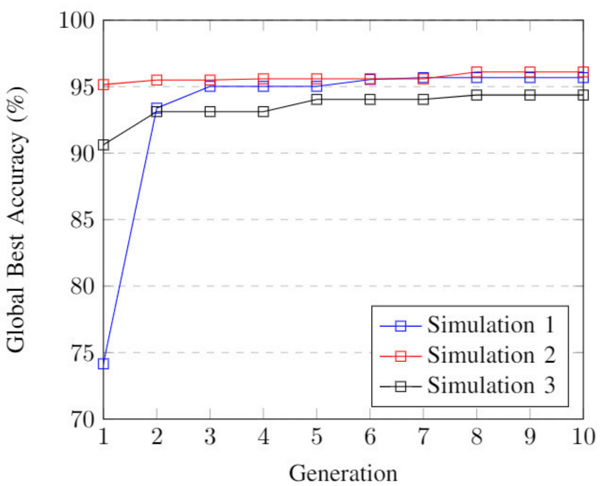

Fig 4. Three evolutionary simulations run on the dataset

Although the LSTM is slightly more accurate at prediction, the optmised MLP managed to classify with close accuracy in around one quarter of the required resources to train. Future work should concern applying the two experiments to larger datasets as well as problems of different dimensions, comparing the difference in classification ability and resource usage, and finally analysing the patterns observed between problem spaces. With enough computational resources available, the genetic search should be applied to the LSTM topology for a true comparison. Additionally, a multi-objective approach should be explored, not only concerning accuracy, but also efficiency in terms of resource usage. With an accurate model to classify Mental Emotional States, the next step is to endow a robot to socially interact to humans (i.e. by selecting proper (inter)actions) based on their feelings in order to provide some assistance (e.g. health care contexts: monitoring elderly mental health; assisting clinical sessions with children, etc.).

REFERENCES

[1] E. Niedermeyer and F. L. da Silva, "Electroencephalography: basic principles, clinical applications, and related fields". Lippincott Williams& Wilkins, 2005
[2] A. Coenen, E. Fine, and O. Zayachkivska, "Adolf beck: A forgotten pioneer in electroencephalography", Journal of the History of the Neurosciences, vol. 23, no. 3, pp. 276–286, 2014.
[3] H. H. Jasper, "The ten-twenty electrode system of the international federation", Electroencephalogr. Clin. Neurophysiol., vol. 10, pp. 370–375, 1958.
[4] M. Abujelala, C. Abellanoza, A. Sharma, and F. Makedon, "Brain-ee: Brain enjoyment evaluation using commercial eeg headband," in Proceedings of the 9th ACM international conference on pervasive technologies related to assistive environments, p. 33, ACM, 2016.
[5] E. Krigolson, C. C. Williams, A. Norton, C. D. Hassall, and F. L.Colino, "Choosing muse: Validation of a low-cost, portable eeg system for erp research", Frontiers in neuroscience, vol. 11, pp. 109, 2017
[6] J. J. Bird, A. Ekart, C. D. Buckingham, and D. R. Faria, "Mental emotional sentiment classification with an eeg-based brain-machine interface," in International Conference on Digital Image and Signal Processing (DISP'19), Springer, 2019.
[7] J. J. Bird, L. J. Manso, E. P. Ribiero, A. Ekart, and D. R. Faria, "A study on mental state classification using eeg-based brain-machine interface", in 9th International Conference on Intelligent Systems, IEEE, 2018.
[8] Y. Bengio, I. J. Goodfellow, and A. Courville, "Deep learning" Nature, vol. 521, no. 7553, pp. 436–444, 2015.
[9] J. J. Bird, A. Ekart, and D. R. Faria, "Evolutionary optimisation of fully connected artificial neural network topology," Computing Conference, 2019.
[10] S. Kullback and R. A. Leibler, "On information and sufficiency", Theannals of mathematical statistics, vol. 22, no. 1, pp. 79–86, 1951.
[11] P. A. Vikhar, "Evolutionary algorithms: A critical review and its future prospects", in Global Trends in Signal Processing, Information Computing and Communication (ICGTSPICC), 2016 International Conference on, pp. 261–265, IEEE, 2016.
[12] C. Darwin, "On the origin of species", 1859. Routledge, 2004.
[13] J. Gruzelier, "A theory of alpha/theta neurofeedback, creative performance enhancement, long distance functional connectivity and psychological integration", Cognitive processing, vol. 10, no. 1, pp. 101–109, 2009.
[14] K. Greff, R. K. Srivastava, J. Koutník, B. R. Steunebrink, and J. Schmidhuber, "Lstm: A search space odyssey,"IEEE transactions on neuralnetworks and learning systems, vol. 28, no. 10, pp. 2222–2232, 2017

MoDSeM: Modular Framework for Distributed Semantic Mapping*

Gonçalo S. Martins, João Filipe Ferreira, David Portugal and Micael S. Couceiro

Abstract— **This paper presents MoDSeM, a novel software framework for spatial perception supporting teams of robots. MoDSeM aims to provide a semantic mapping approach able to represent all spatial information perceived in autonomous missions involving teams of field robots, and to formalize the development of perception software, promoting the development of reusable modules that can fit varied team constitutions. Preliminary experiments took place in simulation, using a 100x100x100m simulated map to demonstrate our work-in-progress prototype's ability to receive, store and retrieve spatial information. Results show the appropriateness of ROS and OpenVDB as back-ends for supporting the prototype, achieving promising performance in all aspects of the task and supporting future developments.**

I. Introduction

The **Mo**dular Framework for **D**istributed **Se**mantic **M**apping (MoDSeM) aims to provide a semantic mapping approach able to represent all spatial information perceived in autonomous missions involving teams of field robots, such as those operating in precision forestry missions, aggregating the knowledge of all agents into a unified, cohesive representation. It also aims to formalize and normalize the development of new perception software, promoting the implementation of modular and reusable software that can be easily swapped according to the sensory abilities of each individual platform. This text presents an overview of MoDSeM and of some preliminary experiments using a work-in-progress implementation that evaluate the main design choices in a simulated forestry environment.

This article is structured as follows: the remainder of this section focuses on highlighting the paper's contributions, Section II presents the MoDSeM architecture, Section III presents our preliminary experiments and results, which are discussed in Section IV. Lastly, Section V presents our conclusions and future work.

Contribution and Related Work

MoDSeM's originality and contribution to the field lies in its focus on improving the technology readiness level (TRL) [1] of cooperative perception techniques, and on enabling them to operate in a coordinated, flexible and seamless manner. In fact, while works in perception are abundant, including probabilistic approaches [2] and works on several sub-problems of field robotics, including tree detection [3], crop/weed discrimination [4] or detection of plant disease [5]; very few of these techniques are available as easily-reusable software packages. These software packages, which include for instance mapping and localization techniques [6][1],[7][2], among others, constitute the most accessible way of testing perception techniques in the field, in conditions as close to real operation as possible. However, these packages represent only a small subset of the substantial body of work in perception, and are traditionally quite behind the state of the art. MoDSeM aims to tackle this issue by providing the means to integrate the output of these techniques, to make them usable by heterogeneous teams of robots, and by providing guidelines and formalisms for the development and integration of Perception Modules.

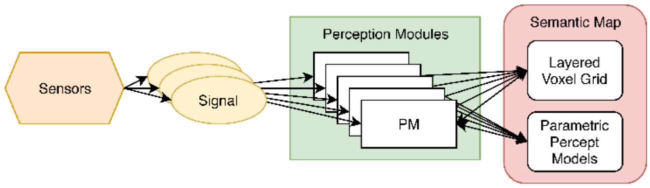

Figure 14: An overview of MoDSeM. Sensors produce signals, which are passed to independent perception modules. Percepts obtained by these modules are aggregated in a Semantic Map, containing layers for different kinds of information.

Software frameworks for robots have been developed for generic robots, such as ROS [8], YARP [9] or GenoM3 [10], and also specifically for agriculture and forestry robots [11]. These frameworks focus on improving software portability, and introduce some standards[3] on the basic common features and assumptions of the various modules. However, these frameworks do not tackle the particular issues of perception systems, such as achieving a common representation of the world with varying sensor input, or the storage and retrieval of this information, both current and in the past. Past efforts also do not define a development methodology to produce

*This work was supported by the Seguranças robóTicos coOPerativos (STOP, ref. CENTRO-01-0247-FEDER-017562), the Safety, Exploration and Maintenance of Forests with Ecological Robotics (SEMFIRE, ref. CENTRO-01-0247-FEDER-03269) and the Centre of Operations for Rethinking Engineering (CORE, ref. CENTRO-01-0247-FEDER-037082) research projects co-funded by the "Agência Nacional de Inovação" within the Portugal2020 programme.
Gonçalo S. Martins and Micael S. Couceiro are with Ingeniarius, Rua Coronel Veiga Simão, Edifício B CTCV, 3025-307 Coimbra, Portugal, (e-mail:{gondsm, micael}@ingeniarius.pt).
João Filipe Ferreira and David Portugal are with the Institute of Systems and Robotics, University of Coimbra, 3030-290 Coimbra, Portugal (e-mail: {jfilipe, davidbsp}@isr.uc.pt).
João Filipe Ferreira is also with Nottingham Trent University, Computational Neuroscience and Cognitive Robotics Laboratory, School of Science and Technology, Nottingham, United Kingdom (e-mail: joao.ferreira@ntu.ac.uk).

[1] https://github.com/OctoMap/octomap
[2] https://github.com/introlab/rtabmap
[3] *E.g.* ROS's REP 103: http://www.ros.org/reps/rep-0103.html

portable perception software, one of the main long-term goals

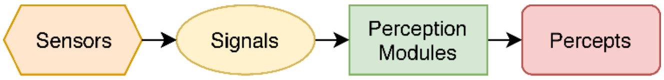

Figure 2: Traditional perception techniques implement a linear flow from sensors to percepts; signals are processed and percepts are output.

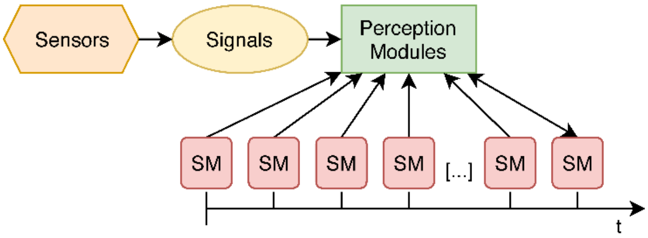

Figure 3: MoDSeM's non-linear perception pipeline: Perception Modules (PMs) are allowed to access previous versions of the Semantic Map (SM).

of MoDSeM. To the best of our knowledge, MoDSeM is the first attempt at such a system and methodology applied directly to the problem of perception.

II. MoDSeM

A. Overview

The framework is split into three main blocks (Fig. 1): the **Sensors**, which provide raw signals; the **Perception Modules** (PMs) which take these signals and produce percepts; the **Semantic Map** (SM), containing a unified view of the state of the workspace/world which can be used by any agent in the team to make decisions or to coordinate with others.

Each PM is expected to be decoupled from other modules, depending only on the available sensors and on the SM itself, ensuring that they become interchangeable, plug-and-play elements of the system, able to be swapped at will, depending on the computational power and available sensors on each robot. This allows for the employment of PMs in different systems without the need to re-design the global representation.

The semantic map works as a global output of the system, split into two components: the Layered Voxel Grid (LVG) and the Parametric Percept Models (PPM). Each layer of the LVG is itself a voxel grid containing information on a specific aspect of the world, such as occupancy or task-relevance (e.g. the presence of certain kinds of vegetation). The combination of these layers represents the state of the world as perceived by the robot team; individually, they provide insight that may be relevant on a particular aspect of the mission. PMs can contribute to different layers of the LVG, *e.g.* with a people detector contributing to a people occupancy layer and a mapping technique contributing to an occupancy layer. The PPM complements the LVG, representing entities without volume, *e.g.* robot poses or human joint configurations.

MoDSeM aims to introduce non-linearity in the traditional data flow used in perception (Figs. 2 and 3), allowing PMs to access current and past percepts through the SM: PMs are allowed to use the SM and previous version of it as input. Indeed, some PMs are expected to use solely the SM as input; *e.g.* a traversability detector could estimate the traversability of the map using only occupancy and vegetation information. Thus, a history of SMs is kept during operation,

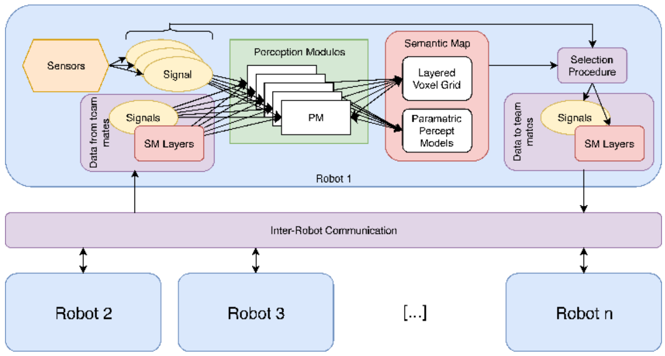

Figure 4: An overview of a robot team operating with MoDSeM. Each team member has its own sensors, perception modules and semantic map. These are shared with the rest of the team as needed, with each robot being able to receive signals and SM layers from other robots, fusing them to achieve a unified SM.

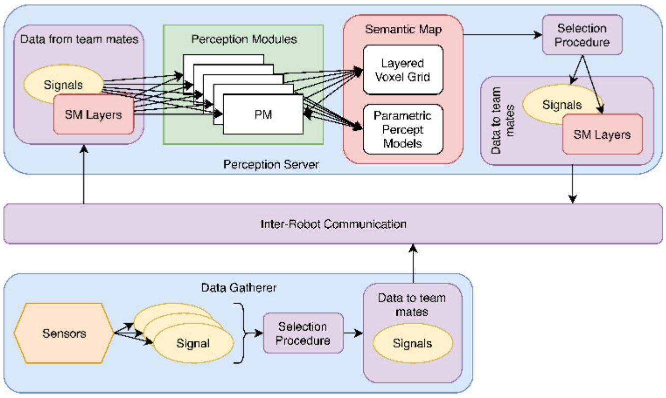

Figure 5: Different topologies for multi-robot perception using MoDSeM. Top: a perception server, which receives information and SM layers from the team and executes the most computationally expensive perception modules. Bottom: a data gatherer agent, which collects and sends data for processing in other agents.

which could quickly make its storage infeasible. This can be mitigated, for instance, by storing the successive differences in time between the PMs as they are generated, as done in video compression algorithms and source control systems, or by intelligently choosing which snapshots of the SM should be saved, using information-theoretic techniques.

B. Instantiation Examples

Traditionally, multi-robot perception is achieved in one of two ways: by propagating raw signals from each robot to a centralized perception server, which then replies with percepts; or by endowing each team member with perceptive abilities, as well as the ability to decide when percepts should be propagated among the team. Both of these approaches are valid in their own conditions, and it is important that MoDSeM support all of these perceptual topologies, as they allow for greater implementation flexibility.

Distributed perception is the appropriate technique when bandwidth is limited, when robots have heterogeneous needs and capabilities, and when each individual robot can be endowed with perception abilities that fit its needs. Fig. 4 illustrates an overview of MoDSeM implemented on a robotic team performing distributed perception, with each team member implementing the full architecture. In this case, each agent contains additional specialized PMs that are used to fuse

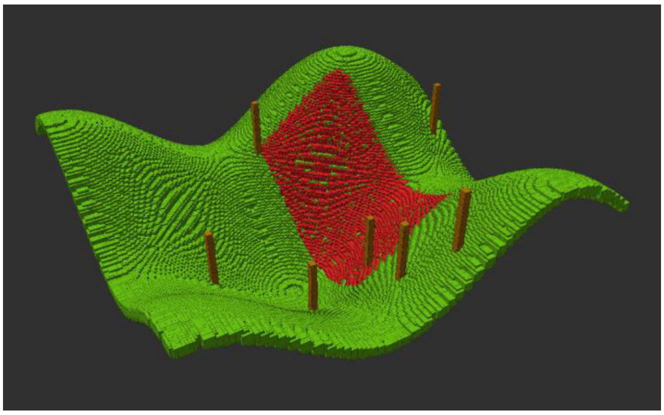

Figure 6: An illustration of the semantic map used in these tests. Green voxels represent the terrain, brown voxels represent trees and red voxels represent dry shrubbery.

information received from other agents, to achieve consensus, and selection procedures, which select information for sharing with other agents. Specific PMs in each robot can then fuse these representations, achieving consensus in representation and allowing all robots to plan with the same information. These can be implemented using the same formalism as regular PMs, with no necessary particularity, and would only depend on the SM itself to function.

Centralized perception can be useful when the robots in the team carry much less processing power than the necessary perception modules and when the communication infrastructure is always available and can support the necessary bandwidth. Fig.5 illustrates the usage of MoDSeM on a centralized topology, with a data gatherer collecting and selecting signals, which are then sent to a centralized server for processing and dissemination.

Other topologies can be achieved with the framework by mixing-and-matching the necessary components, such as PMs and sensors and their configurations, to achieve different use cases. For instance, a hybrid approach can be used with heterogeneous teams, when for example one of the robots is significantly more powerful in computational terms than other team members, which in turn can therefore unload part of their perceptual load to this team mate, while still executing basic PMs.

III. Experiments and Results

Tests were conducted with the goal of assessing the appropriateness of OpenVDB [12] and ROS[4] as back-end modules for MoDSeM, exploring two main functions: data insertion into the semantic map, and data retrieval from the semantic map. These constitute the two main operations that the semantic map server is expected to perform during runtime, and should operate efficiently enough to allow real time operation. To this end, a 100-by-100-by-100 meter map was generated in simulation, at a resolution of 5cm/voxel (Fig. 6[5]), containing three semantic layers with a total of 18 million voxels. The map was sent piece-by-piece over ROS to the semantic map server, operating on OpenVDB, simulating the operation of a mapping node that advances through the terrain

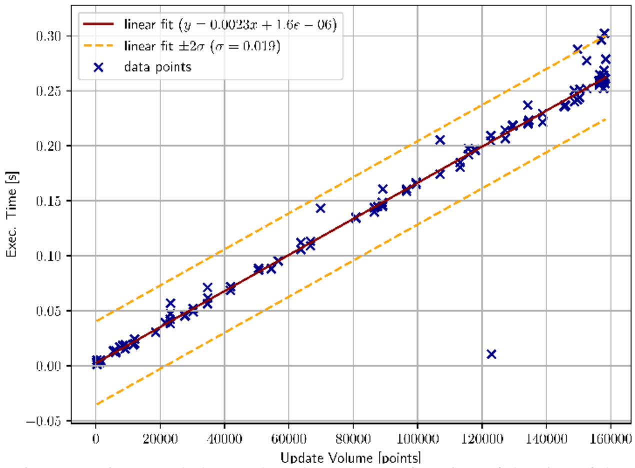

Figure 7: Time needed to update the map as a function of the size of the update, in occupied points. The clear outlier corresponds to the very first insertion of the map, wherein the received grid itself is used.

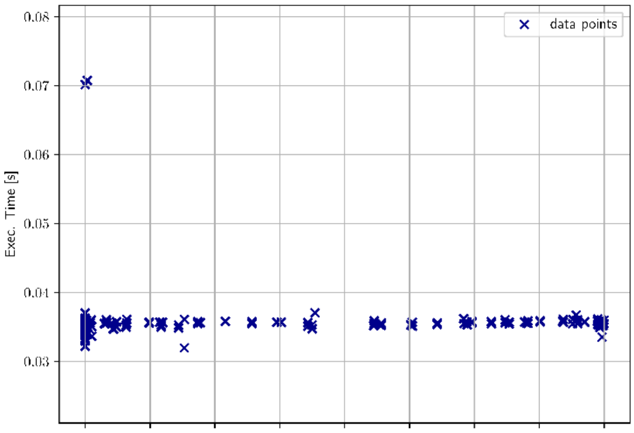

Figure 8: Time taken to retrieve a sub-map (or sub-grid) as a function of the number of voxels contained in the sub-map.

and iteratively updates the global map. At each update, the server was asked for the retrieval of the same portion of the map, testing its ability to deliver data. The whole experimental procedure took place on a computer running Ubuntu 16.04, equipped with an Intel Core i7-7700 and 16GiB of RAM.

Fig. 7 illustrates the time it took to update the map as a function of the size, in occupied points, of the respective update. A linear trend is observable in the data: the update time of the map is predictable given the size of the update, and can be accounted for. In the worst-case scenario, the update procedure took around 0.3 seconds, for an update of 160,000 points.

Fig. 8 illustrates the performance of the semantic map server when retrieving a subsection of the map. We can observe no undesirable relationship between the voxel structure of the original grid and the time it takes to retrieve the grid; for a constant sub-grid volume, the retrieval time is almost constant.

Fig. 9 illustrates the semantic map server's usage of memory as the experiment progresses. We can observe that memory usage grows linearly with the size of the updates that

[4] http://www.ros.org

[5] Aliasing artifacts are caused by downsampling applied for visualization. It is not possible to represent the map's near-20-million voxels on rviz.

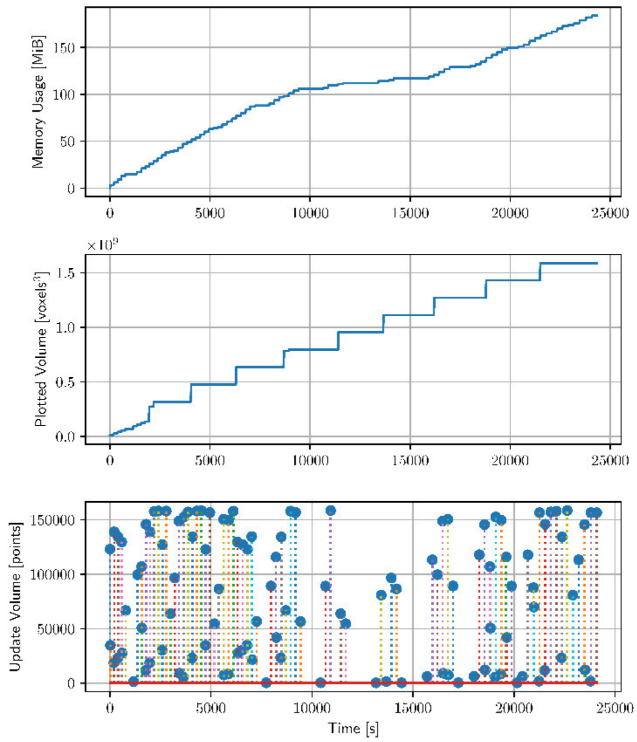

Figure 9: Evolution of memory usage as updates are received by the server. (Top) represents the total memory usage of the map; (middle) illustrates the volume, in cubic voxels, of the map; (bottom) shows the update times of non-zero updates, as well as their size in points.

are received, not with the mapped volume itself. This means that the map is capable of storing information independently of the volume mapped, which is one of the greatest advantages of tree-based maps such as OpenVDB or Octomap [6].

IV. Discussion

Generally, the current results are promising. Map update and retrieval speeds are fast enough for our application: updates up to 160,000 voxels, equivalent to a completely full $3m^3$ volume, can be processed at 3 to 4Hz. Given that a time complexity below *O(n)* was unlikely , this is a positive result: the update time of the map is easily predictable given the size of the update, and measures can be taken to account for it.

As seen in Section III, system performance is acceptable for the worst-case scenario. An update as large as those described therein is a relatively unlikely event; it may correspond to an update to the map produced by a mapping node or eventually to a bulk update from another perception node which has produced a large calculation. It is unlikely that such updates would be produced frequently, or at a high enough frequency to overload the server. This work demonstrates that basic functionality is possible, and that MoDSeM's future development should involve OpenVDB and ROS: they seem able to support the operation of the semantic map server and can provide a stable framework for future development.

V. Conclusion and Future Work

This paper presents the design and the ongoing development of MoDSeM, a software framework for spatial perception supporting teams of robots. Preliminary experiments confirm the appropriateness of our design choices.

We present only a preliminary study of the functionality that is being designed and implemented. It will now be extended in several ways, namely to further evaluate the framework's limitations, and to apply it in real use cases in several current research projects. Additional testing will be conducted in semi-realistic scenarios, involving several robots, to develop the inter-robot communication and data transmission facilities that will propagate SM layers across team mates. MoDSeM will then be implemented in teams of patrolling robots[6] for surveillance and inspection, allowing the team of robots to synchronize and fuse perceptual information, promoting coordinated action. In later follow-up work, MoDSeM will also support the perceptual mechanisms of heterogeneous teams of robots for automated forestry tasks [13][7].

References

[1] J. C. Mankins, “Technology Readiness Levels,” *White Pap. April*, vol. 6, no. 2, p. 5, 1995.

[2] J. F. Ferreira and J. Dias, *Probabilistic Approaches for Robotic Perception*. Springer International Publishing, 2014.

[3] T. Hellström, A. Ostovar, T. Hellström, and A. Ostovar, “Detection of Trees Based on Quality Guided Image Segmentation,” in *Second International Conference on Robotics and associated High-technologies and Equipment for Agriculture and forestry (RHEA-2014)*, 2014.

[4] P. Lottes, R. Khanna, J. Pfeifer, R. Siegwart, and C. Stachniss, “UAV-Based Crop and Weed Classification for Smart Farming,” in *IEEE International Conference on Robotics and Automation (ICRA)*, 2017, pp. 3024–3031.

[5] R. Oberti, M. Marchi, P. Tirelli, A. Calcante, M. Iriti, and A. N. Borghese, “Automatic detection of powdery mildew on grapevine leaves by image analysis : Optimal view-angle range to increase the sensitivity,” *Comput. Electron. Agric.*, vol. 104, pp. 1–8, 2014.

[6] A. Hornung, K. M. Wurm, M. Bennewitz, C. Stachniss, and W. Burgard, “OctoMap: An efficient probabilistic 3D mapping framework based on octrees,” *Auton. Robots*, vol. 34, no. 3, pp. 189–206, 2013.

[7] M. Labbé and F. Michaud, “RTAB-Map as an open-source lidar and visual simultaneous localization and mapping library for large-scale and long-term online operation,” *J. F. Robot.*, no. May, 2018.

[8] M. Quigley, K. Conley, B. Gerkey, J. Faust, T. Foote, J. Leibs, E. Berger, R. Wheeler, and A. Mg, “ROS: an Open-Source Robot Operating System,” in *ICRA workshop on open source software*, 2009.

[9] P. Fitzpatrick, E. Ceseracciu, D. E. Domenichelli, A. Paikan, G. Metta, and L. Natale, “A middle way for robotics middleware,” *J. Softw. Eng. Robot.*, vol. 5, no. September, pp. 42–49, 2014.

[10] A. Mallet, C. Pasteur, M. Herrb, S. Lemaignan, and F. Ingrand, “GenoM3 : Building middleware-independent robotic components,” in *2010 IEEE International Conference on Robotics and Automation (ICRA)*, 2010, no. May 2014.

[11] T. Hellström and O. Ringdahl, “A software framework for agricultural and forestry robotics,” in *International Conference on Robotics and associated High-technologies and Equipment for agriculture*, 2012, pp. 171–176.

[12] K. Museth, “VDB: high-resolution sparse volumes with dynamic topography,” *ACM Trans. Graph.*, vol. 32, no. 3, pp. 1–22, 2013.

[13] M. Couceiro, D. Portugal, J. F. Ferreira, and R. P. Rocha, “SEMFIRE: Towards a new generation of forestry maintenance multi-robot systems,” in *IEEE/SICE International Symposium on System Integrations (SII 2019)*, 2019.

[6] http://stop.ingeniarius.pt/

[7] http://semfire.ingeniarius.pt/

Controlling a Bipedal Robot with Pattern Generators Trained with Reinforcement Learning*

Christos Kouppas, Qinggang Meng, Mark King and Dennis Majoe

Abstract — **Herein, the use of reinforcement learning and pattern generators for balancing a bipedal robot, is described. SARAH (Silent Agile Robust Autonomous Host) is an underactuated robot designed by Motion Robotics LTD and aims to become an everyday bipedal robot that has fast, humanlike response. By utilizing V-Rep simulator, a simulated model of the robot was constructed and controlled with pattern generators. Then, those pattern generators were optimized by using reinforcement learning and a neutral advantage function agent. The training results are presented through graphs with respect to training steps, to show how the parameters converge to the optimum values.**

I. Introduction

Bipedal robots are becoming more sophisticated over the years however, their structural design remains the same. The majority of bipedal robots demonstrate a human-like mechanical structure which was established from the early 70s [1]. A full humanoid, like ASIMO of Honda [2] and ATLAS of Boston Dynamics [3], usually consists of at least 23 Degrees of Freedom (DoF) that can be categorized as: 3 for the head, 3 for each shoulder joint, 1 for each elbow joint, 2 for each hip joint, 1 for each knee joint and 3 for each foot joint. They can further be grouped into the upper part (head, shoulders, elbow – 11 DoFs) and the lower part (hip, knee, foot – 12 DoFs).

Our research focuses on the lower part of the bipedal robot because it is more challenging compared with the upper part which has similar structure as industrial robots and is well studied and optimized. In this paper, we designed an underactuated bipedal host which has 6 actuators and 10 DoFs [4]. The control of the robot was achieved by combining Central Pattern Generators (CPG) and Reinforced Learning (RL). As it was demonstrated, CPG are used by humans [5] and they are suitable for bipedal robots [6]. Reinforced Learning on the other hand, proved suitable for real-time applications [7].

The robot model was implemented in V-Rep Simulator [8] and the basic characteristics of the simulation were evaluated with the physical robot. Combining the simulator with reinforced learning, two set of parameters of the robot were optimized. The first set was to optimize to increase the number of steps per minute, in respect of the overall movement in the transverse plane. The second set of parameters was to adjust small movements in hip joints to modify flexion/extension and abduction/adduction during steps. These movements are aiming to keep a stable position, in the transverse plane, for as long as possible.

Figure 15: Ankle joints of SARAH with and without shoe.

II. Mechanical Structure

SARAH has four underactuated DoFs, two on each foot. These joints were responsible for the lateral movement of the forefoot and the hindfoot parts. They were free to rotate but limited by the shank, where they were touching on a pressure sensor, and a shoe was holding them from moving downwards thus, they could flex inside the shoe like a human foot. Figure 1 demonstrates the actual ankle joint with and without the shoe.

As shown in Figure 2, the physical model of the developed bipedal robot can be divided into three main groups. The first includes the main top compartment with the right and left hips, as well as four actuators for the adduction/abduction and flexion/extension of the robot. The other two main groups are the two legs, each one having one actuator (“knee”) and two passive joints on the foot. The total weight of the robot was 30kg, with each group weighing 10kg. These specifications were also considered in the simulated model in order to achieve realistic dynamics.

III. Controlling Architecture

Balancing was provided from a CPG using information from an Inertial Measurement Unit (IMU) that was fixed in the

*Research was partially founded from EPSRC, funding from the Engineering and Physical Science Research Council Centre for Doctoral Training in Embedded Intelligence (grant no. EP/L014998/1).
Christos Kouppas is with Loughborough University, Loughborough, LE11 3TU, UK (corresponding author, e-mail: c.kouppas@lboro.ac.uk)

Qinggang Meng and Mark King are with Loughborough University, Loughborough, LE11 3TU, UK (e-mails: Q.Meng@lboro.ac.uk, M.A.King@lboro.ac.uk)
Dennis Majoe is with Motion Robotics LTD, Southampton, SO30 3DS, UK (e-mail: dennis.majoe@motion-robotics.co.uk)

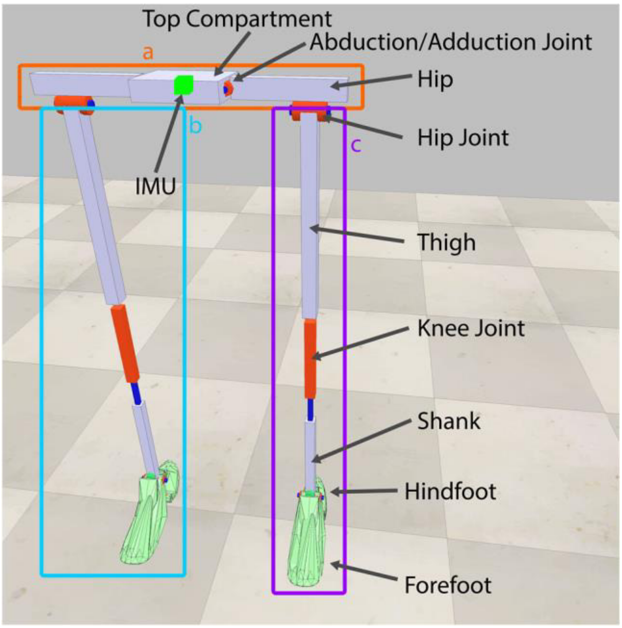

Figure 16: SARAH's simulated model in V-Rep with annotations. (a) top groups, (b) right leg, (c) left leg

center of the top compartment. From that, 6 axis IMU, only 4 pieces of information were used as the angular rate on the x and z axes were not necessary (for this stage of balancing). The Y-axis angular rate shows the speed at which the robot will jump from one leg to the other. From the x-y-z axes accelerations, a quantitively postural angle of the robot can be determined by dividing the correspondent (to the angle that was examined) axis with the total acceleration. Additionally, the four pressure sensors that are located on the ankle, were giving information if the forefoot and the hindfoot were on the ground. With the addition of the feedback from the actuators (six signals), the observations from the simulation sum up to 16. Figure 3 shows the complete CPG schematic with the equations for each condition and the actions that take place after each condition.

Additionally, in Figure 3 two sets of variables are noted, the P1-5 and the V1-4. These variables were extracted after two consecutive reinforced learning trainings using keras-rl library [9] and the normalized advantage function (NAF Agent) [10]. Under this agent, the calculation of the Q-value variant took place in a continuous form with experience replays. Model-free reinforcement learning with continuous outputs, uses raw inputs from the system (e.g. raw sensor data) and outputs a float number as a result in all the outputs. Those outputs can be used raw, in the inputs of the real/simulated system. The reason for two consecutive trainings and not one is based on the future exploration of the balancing problem. The first training was focusing more on the response speed than the stability and the second training was the opposite.

The models that were used as actor (mu_model), critic (V_model) and Q-maximizer model (L_model) were simple neural networks and the interaction between them achieved a complex non-linear result. The V_model had three layers of neurons with each layer having neurons equal to the square of the number of the observation signals (256). The L_model had four layers of 5 times the number of the observation signal (80) and the mu_model had four layers too, but with the number of observation signals (16). The layers had a sigmoid as an activation function and the output layer of each model had a linear activation to rectify the decisions in a continues space. Because, heuristically, it was observed that the parameters must be positive, the actor's rectification bias was initialized at 1, instead of 0.

The main difference between the reinforced learning and the supervised learning is the way that the data were collected, as the first one is collecting the data during training while the latter is using a pre-collected dataset. Another difference is that, reinforced learning needs to define a cost (if it is negative) or a reward (if it is positive) function based on the performance of the robot in the simulator or real world. This function will act as the "correct option" and the reinforced learning will maximize it. For the training of SARAH's model, the equation (2) was used as a reward function. Its value was calculated in every step of the simulation and their summation wes presented as a reward in the end of each simulation.

$$R = (0.5 - c_x) \cdot (0.5 - c_y) \cdot 2^{-(f-3)^4} \cdot c_z \qquad (2)$$

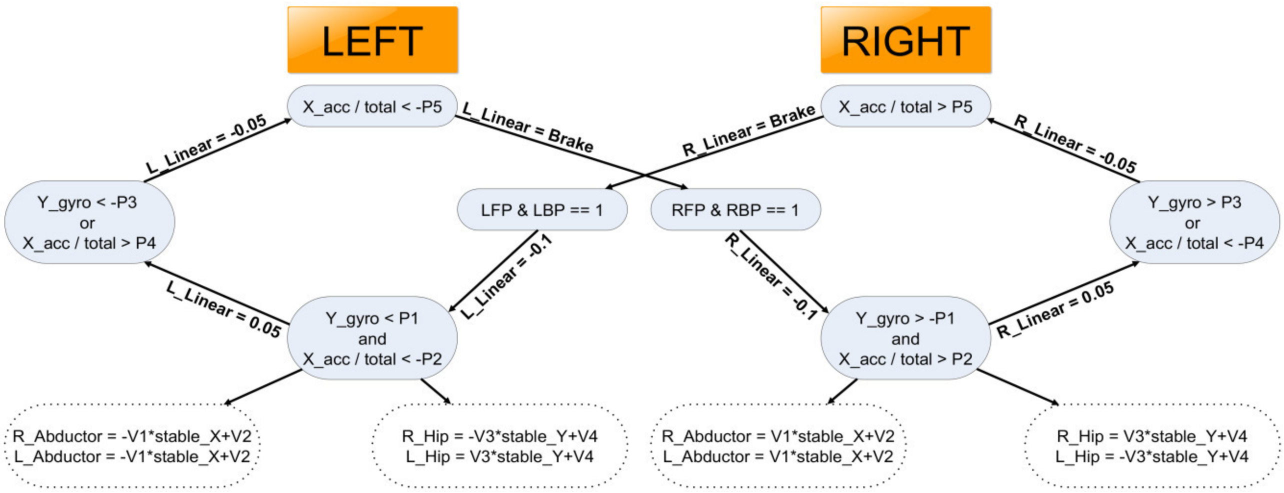

Figure 17: Central Pattern Generator for balancing the bipedal robot. P1-5 were the parameters that were trained during the first training. V1-4 were the parameters that were trained during the second training. Colored rectangles represent condition's statements and colorless (or having =) represents actions. LFP, LBP, RFP and RBP are the forefoot and hindfoot pressure sensors of the left and right foot, respectively. stable_Y and stable_X are the lowpass accelerations in y and x axes. total is the squared acceleration in the three axes.

where, R is the reward, f is the number of steps per second and $c_x/c_y/c_z$ is the position of the top compartment in 3 dimensions x-y-z, respectively.

First Training

During the first training the model was initialized standing upwards and stable. After one second, the CPG started moving the legs based on the parameters P1-5, which were the trained parameters. Meanwhile the movement of abduction/ adduction and extension/flexion was locked, requiring no training. The parameters were set in the beginning of each simulation, once by the outputs of the neural network and were not changed during the simulation. The aim of the first training was to find the best parameters for the CPG in order to have similar steps per second as a human (3-5 steps per second) but without sacrificing a lot of the planar stability.

The output of each model was 5, 1 and 15 for the actor, critic and Q-maximizer, respectively. The Q-maximizer outputs formed a 5x5 lower triangular matrix (L) and it was used for calculating the Q-value of the network based on the equations (3). The number of the outputs matches the number of parameters that must be trained.

$$Q_{(i)} = V_{(i)} - \frac{1}{2}(u - M_{(i)})(L \cdot L^T)(u - M_{(i)})^T \qquad (3)$$

where, Q(i) is the Q-value, V(i) is the output from V_model, u is the predicted actions with the addition of a random exploration value [1x5 matrix], M(i) is the predicted action [1x5 matrix] and L is the outputs of the L_model in a lower triangular matrix like equation (4).

$$L_{(i)} = \begin{bmatrix} L1 & 0 & 0 & 0 & 0 \\ L2 & L3 & 0 & 0 & 0 \\ L4 & L5 & L6 & 0 & 0 \\ L7 & L8 & L9 & L10 & 0 \\ L11 & L12 & L13 & L14 & L15 \end{bmatrix} \qquad (4)$$

Second Training

The second training was similar to the first one, as it was starting with the robot standing stable for one second. However, after that point, a random planar force was acted on the top compartment and had an amplitude up to 100 N. This force was displacing the robot by a few centimeters and during the steps, the robot was trained to return to its initial position by changing the parameters V1-4 in the CPG.

The network was the same as with the first training, except that the outputs of the actor and Q-maximizer were 4 and 10, respectively. The reward function stayed the same as the amount of step per second was not changing drastically from V1-4 parameters. Also, both trainings were stopped under three criterions. First, criterion was that the simulation will not stop after 30 second even if they performed well. The other criterion was a virtual 3D limit of movements by 25 cm. When those limits were reached, the simulation was stopped. Last criterion was if the parameters did not make the robot oscillate in the first 5 seconds, then again, the simulation was stopped. The criterions were implemented thus, the simulations that will produce low reward, will end sooner and reserve resources.

IV. Results And Discussion

First Training

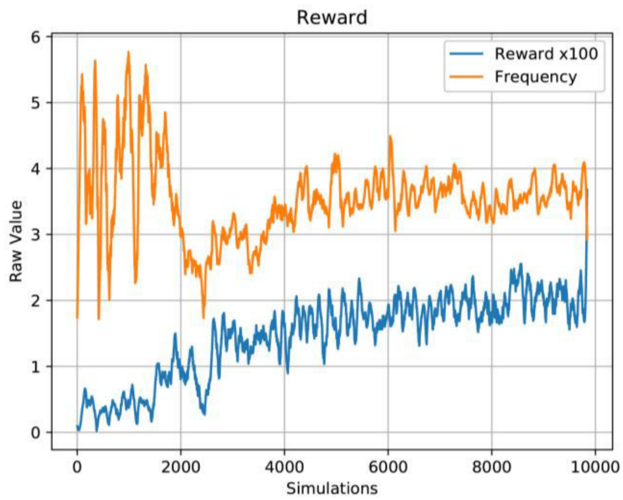

Figure 18: Reward and Frequency during First Training.

Figure 4 shows the performance of the NAF agent finding the parameters P1-5 to balance SARAH in V-Rep simulator. The objective of the training was to increase the number of steps per second without sacrificing the stability of the robot. It was observed that all parameters, P1-5, must be positive in order to have a stable and continues response. If the parameters were negative, small changes resulted in unexpected results.

Examining the parameters and how they changed in respect with the performance, the key parameters were determined. Figure 5 demonstrates the changes of parameters P1-P5 during training. Figure 3 shows that, the parameters P1-P3 were responsible mostly for the performance of the simulation, as the other two parameters were increasing rapidly but the reward was not. Those results were confirmed by manually varying those variables, after the training and showed that they do not change the reward/performance proportionally. Those parameters control the timing of each step so, if they were too big, the step cycle never finishes and if they were to small, the step finishes abnormally fast. Alternating the feet on the floor, was making the robot rotate in Y-axis and the faster the steps, the bigger the rotation speed. The parameters P1 and P3 were responsible to limit this rotation and they stabilized around 0.4

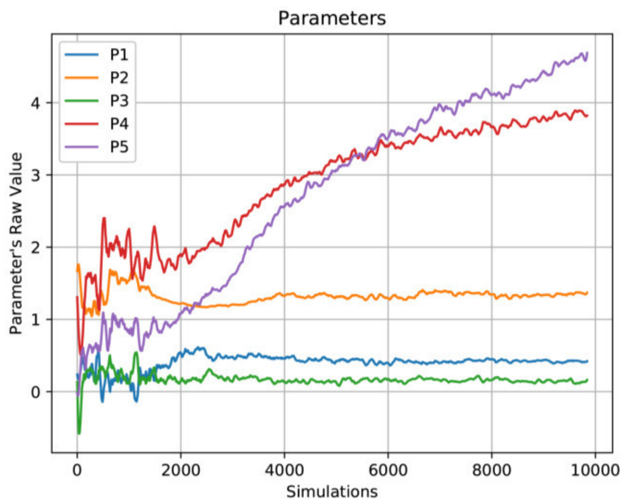

Figure 19: Parameter (P1-5) results during First Training.

and 0.1, respectively. The variable P2 was responsible for the amount of tilt, sidewise, and was stabilized at 1.3 which can be translated to ~7.5°.

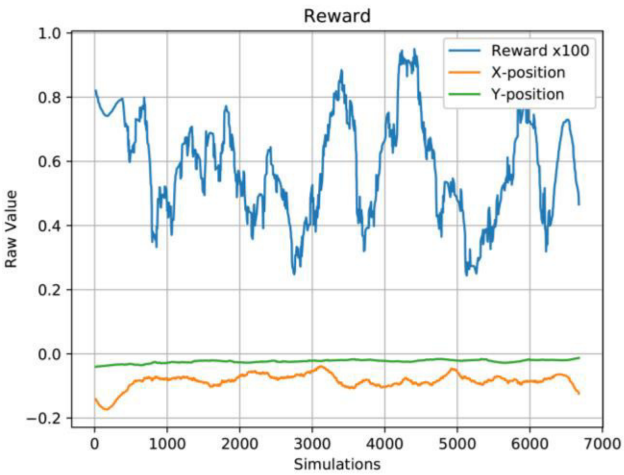

Figure 20: Reward and X-Y final position of the top compartment during Second Training.

Second Training

During the second training, the parameters V1-4 were trained to minimize the movements in the planar plane. Those variables were adjusting the angles for the abduction/adduction and flexion/extension based on X and Y axes accelerations, respectively. Figure 6 demonstrates the performance of the simulation and the movements in X-Y axes as the training got trained. The performance, as reward, was based on the same equation as before (equation (2)). However, because the steps per second were limited by the parameters P1-5, the reward was controlled mainly by the position of the top compartment.

Figure 7 presents the parameters V1-4 and it is noteworthy that, the variables V1 and V3 were more important than V2 and V4. The important variables were multiplying the acceleration of the X-axis and Y-axis, respectively, since they were changing the sensitivity of the respond as they were linear to the response. The variables V2 and V4, were responsible for the constant value that may be needed to keep the center of mass in the center of the robot. The randomness of the force added a great difficulty in the training algorithm. The variables

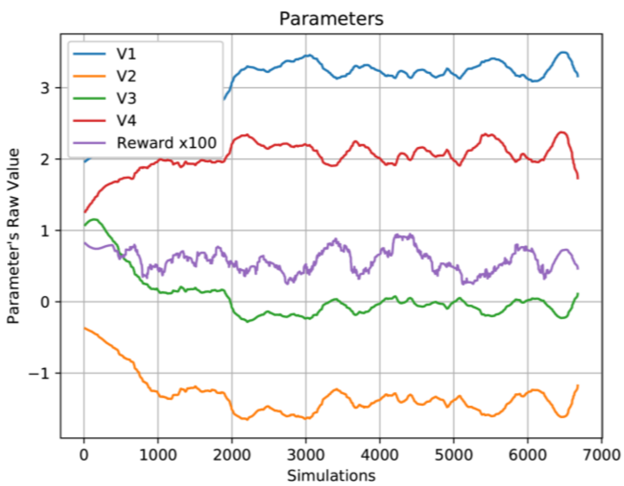

Figure 21: Parameter (V1-4) results during Second Training.

did not show a logical relation with the reward as V1 was following V4 trends and V2 was following V3 trends.

V. Conclusion

The use of neural networks with CPG in bipedal robots for balancing is not new [11], however the use of NN to optimize values of a CPG is novel. Utilizing reinforcement learning, the network is optimized to provide a parameter set solution that will replace certain variables in the CPG in order to balance SARAH. Reinforcement learning with NAF agent, offers exploration of the parameters and the ability of learning through experience.

The CPG used to drive the robot, works independently from the NN. The CPG increases the response rate of the system, as they can be executed faster than a neural network as each cycle is executed in few processor cycles but NN needs few cycles for each layer. However, the use of CPG with NN that we propose, includes the ability of learning from the robot as the NN can be trained offline from events while the robot was used. Afterwards, using NN trained classifiers, new CPG parameters can be pushed through and update movements appropriately based on real time sensors.

Future work of this project includes, the finalization of SARAH and to integrate the balance with this technique as well as to train it from its own experience, online. Finally, the algorithm will be tested in different terrains, with different slopes, friction or texture.

Acknowledgment

The authors would like to thank Motion Robotics LTD and all the employees for the assistant that they provided for this project. Also, the reviewers for their time and helpful feedback.

References

[1] S. Behnke and S. Behnke, “Humanoid Robots - From Fiction to Reality?,” *KI-Zeitschrift*, vol. 4, no. December, pp. 5–9, 2008.

[2] American Honda Motor Co. Inc., “ASIMO Specifications | ASIMO Innovations by Honda,” 2018. [Online]. Available: asimo.honda.com/asimo-specs/.

[3] Boston Dynamics, “ATLAS - The World’s Most Dynamic Humanoid,” 2018. [Online]. Available: www.bostondynamics.com/atlas. [Accessed: 20-Jun-2018].

[4] C. Kouppas, Q. Meng, M. King, and D. Majoe, “S.A.R.A.H.: The Bipedal Robot with Machine Learning Step Decision Making,” *Int. J. Mech. Eng. Robot. Res.*, vol. 7, no. 4, 2018.

[5] J. B. Nielsen, “How we Walk: Central Control of Muscle Activity during Human Walking,” *Neurosci.*, vol. 9, no. 3, pp. 195–204, Jun. 2003.

[6] S. Kolathaya and A. D. Ames, “Achieving bipedal locomotion on rough terrain through human-inspired control,” *2012 IEEE Int. Symp. Safety, Secur. Rescue Robot. SSRR 2012*, 2012.

[7] K. Doya, “Reinforcement Learning In Continuous Time and Space,” vol. 245, pp. 1–28, 1999.

[8] Coppelia Robotics GmbH, “V-Rep Pro Educational,” 2018. [Online]. Available: http://www.coppeliarobotics.com/. [Accessed: 12-Jul-2018].

[9] M. Plappert, “keras-rl,” *GitHub Repos.*, 2016.

[10] S. Gu, T. Lillicrap, I. Sutskever, and S. Levine, “Continuous Deep Q-Learning with Model-based Acceleration,” Mar. 2016.

[11] S. F. Rashidi, M. R. S. Noorani, M. Shoaran, and A. Ghanbari, “Gait generation and transition for a five-link biped robot by Central Pattern Generator,” *2014 2nd RSI/ISM Int. Conf. Robot. Mechatronics, ICRoM 2014*, pp. 852–857, 2014.

Development of a Debris Clearance Vehicle for Limited Access Environments*

Craig West, Wei Cheah, Vijaykumar Rajasekaran, Andrew West, Farshad Arvin, Simon Watson, Manuel Giuliani, Rustam Stolkin, and Barry Lennox

***Abstract* — The need for nuclear decommissioning is increasing globally, as power stations and other nuclear facilities reach the end of their operational life. Currently a lot of decommissioning tasks are carried out by workers in protective air fed suits, this is slow, expensive and dangerous. The work that is described here aims to develop a flexible mobile manipulator platform, combining a Clearpath Husky and a Universal UR5, that can be used for exploration of contaminated environments, building maps to aid in task planning, but also be used for manipulation and to sort waste. The aim is to develop a system that can be used in real world tasks but also function as a research platform to allow continued research and development. As well as developing a hardware platform, a detailed simulation model is also being developed to allow testing of algorithms in simulation before being deployed on hardware. This article focuses on the planned work for developing the system, as well as discussing the progress so far on the simulation model.**

I. Introduction

Nuclear decommissioning often involves working in areas contaminated with high levels of radiation, where human entry is only possible with the use of protective air fed suits. The use of air fed suits require a team of people to put on and take off, and following the use of the suit it becomes contaminated waste which needs to be disposed of accordingly. Besides being costly and time consuming, the working time for the operators wearing these protective suits are limited due to the radiation risk [1]. These are contributing factors to why nuclear decommissioning is expensive, slow and dangerous. Nonetheless, nuclear decommissioning remains a critical task that needs to be undertaken.

The need for decommissioning is in fact increasing as more facilities are approaching the end of their operational life. One such example is the Sellafield site in the UK, where the Thermal Oxide Reprocessing Plan (THORP) has been recently shut down, and the Magnox reprocessing plant is due for closure before 2020 [2]. These facilities are highly radioactive and contain many rooms and work areas that will require radiation cleanup and materials to be removed, processed and sorted. For these reasons the industry wants to improve safety, reduce costs and improve productivity. This is where robotic systems can come in, there are many tasks within the nuclear industry and decommissioning in particular that can benefit from robots and automation [3].

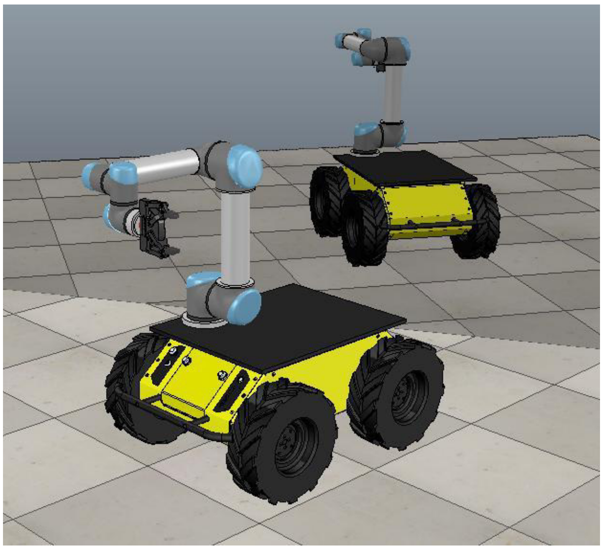

Fig. 1. V-REP simulation of a Clearpath Husky robot with a UR5 robot arm mounted to it.

With this in mind, this work aims to develop a mobile manipulator platform for remote operation in these hazardous areas. By combining a mobile base with a manipulator, namely a Clearpath Husky robot [4] with a Universal Robots UR5 robot arm [5], a platform that can operate remotely, indoors, and perform a variety of useful tasks will be created.

The Husky was chosen for being a good compromise between its small size and maneuverability for operating in confined or cluttered spaces, whilst still large enough to mount a manipulator and other sensors. For example, its small size allows it to traverse through doorways, under tables, and also over small obstacles or uneven terrain that may be encountered in a nuclear facility. The Universal UR5 arm is a widely supported manipulator, compact enough to be mounted on the Husky (see fig. 1) with a payload of 5 kg, making it useful for real-world manipulation tasks.

Applications for this system will range from visual inspection and mapping, to manipulation and waste sorting. This will give operators a view inside these hazardous facilities, some of which have not been entered for many years, allowing necessary tasks to be identified and a plan

*Research supported by EPSRC RNE (No. EP/P01366X/1) and TORONE (No. EP/P018505/1).

C. West and M. Giuliani are with the Bristol Robotics Laboratory, University of the West of England, Bristol, BS16 1QY, UK. (email: craig.west@uwe.ac.uk)

W. Cheah, A. West, F. Arvin, S. Watson, B. Lennox are with the Robotics for Extreme Environments Lab at the School of Electrical & Electronic Engineering, The University of Manchester, UK.

R. Stolkin and V. Rajasekaran are with the Extreme Robotics Laboratory, School of Metallurgy and Materials, University of Birmingham, UK.

created. Then using the same system some of these tasks can be completed, such as moving and sorting waste material, or collecting samples. This would allow for example, an inspection to be carried out and then the clearing of a path for a larger more specialised system to enter the area exactly where it is needed, with a work plan in place.

The challenges presented by these environments extend beyond the obvious radiation risks, and include:

- Chemical hazards
- Operating in confined spaces
- Operating in potentially unknown environments as some facilities have been closed for many years
- Communication challenges presented by thick steel reinforced concrete walls
- Materials may have perished over time e.g. metal rusting which may affect the handling of objects

In a robotics context the communication challenges are one of the most important. Due to the work environment wireless communication would be unreliable, and as such a tether is proposed to allow communication between the operator and the robot. This also gives the advantage of extending operation time beyond the limited on-board battery. The downside is that using a tether presents its own challenges, especially in a cluttered environment where there are lots of obstacles for the tether to catch on. As such, part of this work is to develop a tether management system that will consider the tether during path planning and limits the cable deployed, for example back tracking to allow the cable to be wound in then travelling around obstacles.

Another challenge that has to be considered with the deployment of robots in radiation contaminated environment is what happens to the robot post operation, or if it breaks. The robot will have become radiologically contaminated and thus requires a complete radiation cleanup which is very difficult and often deemed not worth the time and cost, or more commonly disposed of creating more contaminated waste that needs dealing with. This forms part of the motivation for making a flexible system that can perform a variety of tasks rather than making a highly specialised robot for one particular task.

With this in mind, we chose to make use of proven off-the-shelf components to create the mobile manipulator platform, rather than building a bespoke solution. This approach yields a highly reliable system, extending the mean time between failure (MTBF), which is of high importance for the target application. We will also design the system to be modular, allowing parts such as sensors to be easily replaced if they get damaged. Although the replacement of parts requires human intervention, this approach extends the lifetime of the system, reducing both cost and further contaminated waste.

II. Originality

The use of mobile robots in the nuclear industry is not a new idea, [6] gives a detailed review of mobile robots deployed in the nuclear industry over the last few decades. Many robots used previously have been used in response to accidents such as at Chernobyl or Fukushima, with relatively few robots being used in decommissioning tasks. A similar platform to the one discussed here has also been developed by the nuclear and applied robotics group at the University of Texas at Austin, called Vaultbot [7]. Their system combines a Husky with dual UR5 manipulators. However their system required extensive modification of the Husky platform to allow 2 manipulators to be fitted, and is also battery powered so has a short run time. In contrast our system requires almost no modification and so is kept modular and retains the MTBF of the off the shelf hardware. It will also utilise a tether with a novel tether management system, allowing extended periods of operation and maintain communication in environments where wireless communication is unreliable.

The main contributions of this work is the combination of expertise from The University of Manchester, Bristol Robotics Lab and The University of Birmingham to create a reliable mobile platform with semi-autonomous grasping abilities, a tether management system to prevent cable tangling with obstacles and an intuitive user interface that is effective and simple to control the platform. The platform will be developed focusing on real world challenges but will also allow novel research into areas such as grasping, manipulation and human robot interfaces. The aim is to develop a system that in the short term can be deployed in the real world, and with minimal operator training be used by nuclear industry workers, whilst simultaneously in the longer term be used as a research platform to develop industry relevant functionality.

The authors are aiming to develop the platform and participate in ENRICH 2019 [8], a robotics trial scheduled in summer 2019 for testing robots in a hazardous materials response operation. This involves testing of the robot inside a real nuclear facility that was built in Austria but never went online, giving a real world test but in a safe environment.

There is also scope to use it as a platform for research, for example, into human factors experiments, studying the effects of different cameras on ease of tele-operation, or different input methods and levels of automation. This would involve carrying out a series of tests with different cameras attached, e.g. a fixed camera, fixed stereo cameras, pan-tilt camera system, fish eye or 360 camera, and also comparing between on screen images with the use of a VR headset. To investigate different input methods and levels of automation, a study comparing e.g. keyboard tele-operation, game pad control and point and click interactive target markers could also be carried out. These two areas overlap, as the control method has a direct impact on the information required by the operator.

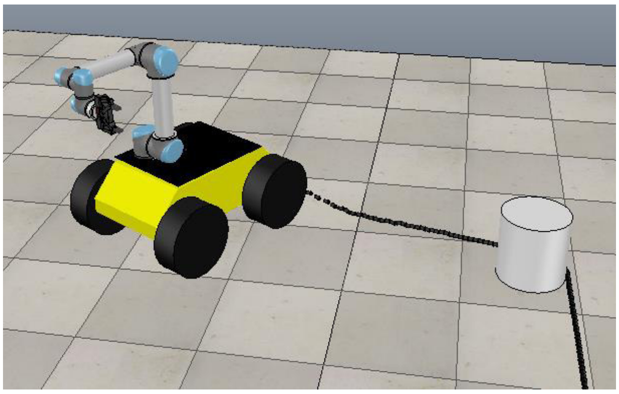

Fig. 2. Simplified model of Clearpath Husky in V-REP with UR5 mounted and power/communication tether attached.

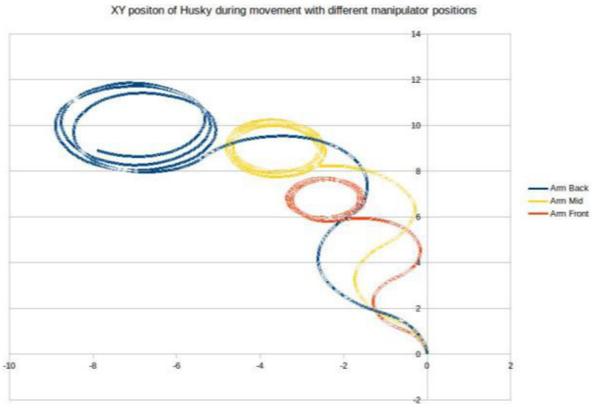

Fig. 3. Initial results showing XY position of the platform, with the same motor input, for 3 different manipulator mounting locations.

III. SIMULATION

Whilst the hardware is purchased and assembled to create the mobile manipulator, a simulation model has been created in the V-REP simulation software [9]. The Clearpath Husky model was not included in V-REP hence the simulation model was created using the CAD file Clearpath provided as a base, and the finished model has a UR5 manipulator attached as shown in fig. 1. Due to the detail in this model, particularly the geometry of the tyres, the physics based simulation runtime was very slow, and so a simplified version was also created as shown in fig. 2. While this version has simplified geometry, properties such as mass and friction are maintained so the dynamics of the real system is still represented closely.

Both of these models can be integrated through V-REP with ROS, eliminating code porting between the real and simulated robot. This allows new algorithms to be quickly and safely developed in simulation before being deployed on the hardware. It also allows the possibility of operator training on a simulated robot, using the same control interface, before using the hardware. This is particularly useful whereby following the mapping of the environment, the environment can be simulated allowing manipulation tasks to be evaluated prior to executing the same tasks in the real world.

As part of the simulation, a tether has also been created, shown in fig. 2 (note that the tether can be added to the detailed model also). Again, V-REP does not provide available cables hence it has been developed from the ground up. The tether is fixed to the rear of the platform and has both mass and friction so acts realistically as it is dragged along the floor. Including the tether allows the effect it has on the system to be investigated, for example the effect of tether length and weight on performance, and the effect of the tether being caught on objects. Including the tether in the simulation also allows the tether management solution to be evaluated as it is developed, reducing the chances of potential damage the hardware. There has also been work done on simulating a rotating drum for winding the cable in and out, which would be needed for the tether management, however it is not shown here for brevity.

During the development of the simulation model it became apparent that the placement of the manipulator has a noticeable effect on the performance of the system. Results of an initial investigation placing the manipulator at the front, middle and rear of the simulated Husky and monitoring the XY position of the robot when given identical motor inputs are shown in fig. 3. This is an area that needs further investigation as the difference seems much larger than would be expected. It is assumed that the difference is caused by the change in the robot's centre of mass affecting traction. To determine whether this is exaggerated in the simulation a test using the real Husky will be carried out when the hardware is available. This may have an impact on the control of the system when objects are being carried, so understanding if this is as noticeable on the real robot is important. It will also help to improve the simulation model if the effect is not observed on the hardware.

Another area that is currently being investigated is what sensors are needed on the robot. It is desirable to keep the system as simple as possible whilst also making it capable enough to be easily controllable and with some semi-autonomous behaviours. It is anticipated that at a minimum a 2D Lidar, a camera and a radiation sensor will be needed. The 2D Lidar will allow SLAM (Simultaneous localisation and mapping) so that the environment can be navigated. A camera on the Husky will allow the operator to see what the robot can see, this is essential for tele-operation. Additionally using stereo or depth cameras would allow a 3D point cloud of the environment to be created which would aid planning of tasks and visualizing the area. It is also likely a second camera would be needed on the manipulator, to act as an eye in hand camera to allow grasping. A radiation sensor would allow both monitoring of the environment to identify radiation level and also aid in separating items into high and low level waste. Date from the radiation sensor could potentially be combined with a 3D point cloud, to give a 3D environment map showing areas of contamination.

The simulation model being integrated with ROS allows different combinations of sensors to be tested in simulated environment and the output displayed in RVIZ, as it would be with real hardware sensors. This allows quickly testing

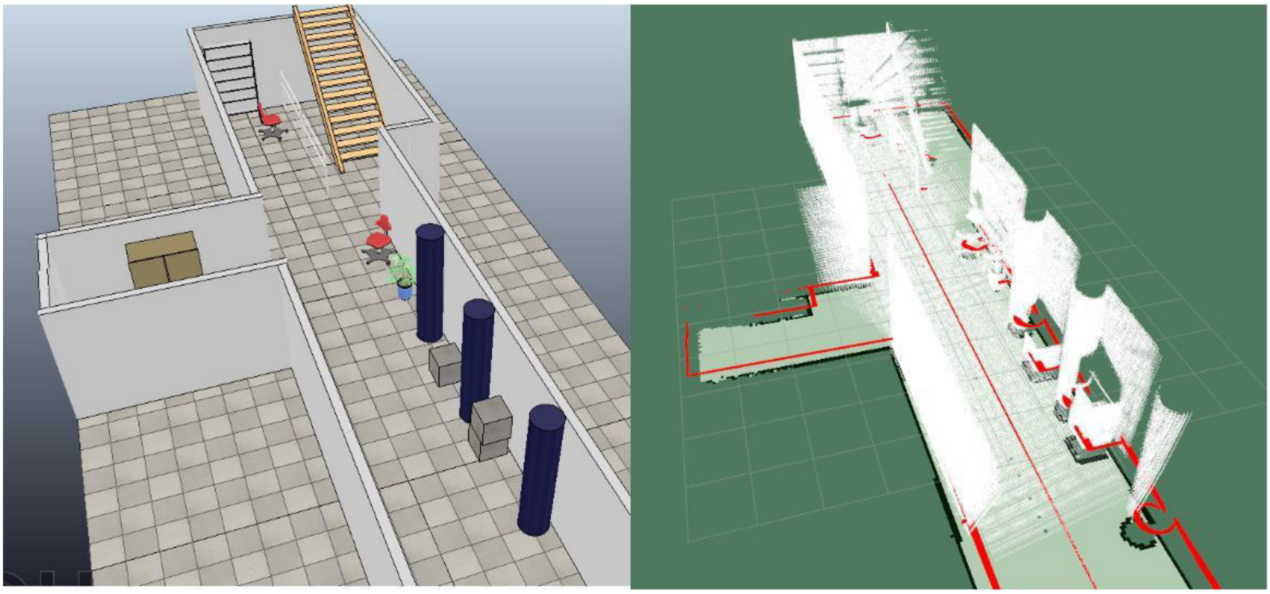

Fig. 4. (left) initial test scene created in VREP (right) Simulated 2D Lidar and depth sensor data combined in Rviz. Created by the mobile platform moving in a straight line in a single direction in simulation.

different sensor combinations and seeing the output on the user interface before implementing with expensive hardware. An example of this is shown in fig. 4, which shows the combined output of a simulated 2D Lidar and a low resolution depth camera (64x64 pixel) in a simulated corridor. The 2D Lidar data is used with a SLAM algorithm to produce a 2D map of the area and the depth camera creates a 3D point cloud. This example was created by driving in a straight line in one direction, as such the point cloud is lacking detail but still gives a good indication of what is in the environment, the columns and boxes on the right are all clearly identifiable as are the staircase and railing at the end of the corridor. The investigation into different sensor combinations is ongoing, and more work is required to identify suitable sensors. A user study may be carried out to identify what data the operators want which can then help identify necessary sensors.

IV. Conclusion

A need for reliable flexible robotic systems within the nuclear industry is clear, with the number of facilities requiring decommissioning continuing to rise and current methods being slow, expensive and dangerous. This paper has focused on the plans for the development of a mobile manipulator platform for use in nuclear decommissioning tasks, which is currently in the early stages of development. The platform will combine a mobile base with a manipulator and multiple sensors for visualising the environment.

Currently the work is at a simulation stage whilst the various hardware components are obtained and assembled. Details of the simulation model, which was developed by the present author, are given and some initial results of testing the simulation presented, including a simulated tether and visualisation of combined sensor data. This model will allow testing of different sensor combinations in simulation so the right choice can be made when implemented on hardware,

Next steps include investigating tele-operation interfaces such as joystick or game-pad controllers and implementing one for the simulation model, this together with the sensor output will allow work on the user interface to begin. At the same time the hardware can be assembled to make the platform and testing can begin, making use of the same algorithms as well as testing of new control algorithms and novel tether management systems. There is also potential to use the model for training of new operators as it will share a control interface with the hardware platform.

References

[1] C. Bayliss and K. Langley, Nuclear decommissioning, waste management, and environmental site remediation. Elsevier, 2003.

[2] NDA and Innovate UK, “Robots compete in nuclear decommissioning challenge.” https://www.gov.uk/government/news/robots-compete-in-nuclear-decommissioning-challenge, Jan 2018. Accessed: 2018-12-10.

[3] D. W. Seward and M. J. Bakari, “The use of robotics and automation in nuclear decommissioning,” in 22nd International Symposium on Automation and Robotics in Construction ISARC, pp. 11–14, 2005.

[4] Clearpath Robots, “Husky-unmanned ground vehicle.” https://www.clearpathrobotics.com/husky-unmanned-ground-vehicle-robot/, 2013. Accessed: 2018-12-14.

[5] Universal Robots, “Ur5 technical specifications.” https://www.universal-robots.com/media/50588/ur5en:pdf, 2014. Accessed: 2018-12-14.

[6] I. Tsitsimpelis, C. J. Taylor, B. Lennox, and M. J. Joyce, “A review of ground-based robotic systems for the characterization of nuclear environments,” Progress in Nuclear Energy, vol. 111, pp. 109–124, 2019.

[7] A. Sharp, K. Kruusamae, B. Ebersole, and M. Pryor, “Semiautonomous dual-arm mobile manipulator system with intuitive supervisory user interfaces,” in Advanced Robotics and its Social Impacts (ARSO), 2017 IEEE Workshop on, pp. 1–6, IEEE, 2017.

[8] Enrich, “Enrich 2019.” Theenrich.european-robotics.eu, Jul 2019. Accessed: 2018-12-10.

[9] M. F. E. Rohmer, S. P. N. Singh, “V-rep: a versatile and scalable robot simulation framework,” in Proc. of The International Conference on Intelligent Robots and Systems (IROS), 2013.

Model based 3D point cloud segmentation for automated selective broccoli harvesting*

Hector A. Montes, Grzegorz Cielniak, and Tom Duckett**

Abstract— **In this paper we address the topic of feature matching in 3D point cloud data for accurate object segmentation. We present a matching method based on local features that operates on 3D point clouds to separate crops of broccoli heads from their background. We have implemented our approach and present experiments on datasets collected in cultivated broccoli fields, in which we analyse performance and matching capabilities and evaluate the usefulness of the system as a point feature-based segmentation method.**

I. INTRODUCTION

Segmentation of 3D objects in noisy and cluttered scenes is a highly relevant problem. Given a 3D point cloud produced by a depth sensor observing a 3D scene, the goal is to separate objects of interest in the foreground from other elements in the background. This has been extensively investigated in various research fields, such as computer vision, robotics, and pattern matching [14]. In this paper, we focus on 3D point clouds obtained with a structured light 3D camera and favourably compare our results to previously published experiments where sets of points where extracted based on the local proximity of the points. Our approach to this problem uses 3D classification based on point-to-point matching of estimated local 3D features. These features capture information of the local geometry of each point and are compared to the features of its surrounding points. The objective of the work reported in this paper is to research 3D imaging methods to accurately segment and identify broccoli plants in the field. The ability to separate parts into different sets of sensor readings is an important task towards this goal. This research is focused on the broccoli head segmentation problem as a first step towards size estimation of each broccoli crop in order to establish whether or not it is suitable for cutting.

The paper starts by a brief contextual introduction of automated solutions for broccoli harvesting as well as a concise review of related work in Section II. Section III describes the methodology and the data acquisition, while Section IV describes the experimental results along with the evaluation metrics used to assess the overall performance. Section V concludes the paper.

II. HARVESTING BROCCOLI CROPS

Broccoli is a vegetable in the cabbage family that belongs to the Brassica Oleracea plant species. The interest in its cultivation has grown in recent years due to genetic improvement programmes developed in several countries, and to the healthy compounds contained in the crop that have increased its consumption [1]. A consequence of the methods used to breed broccoli is that the heads grow at different rates. This makes them difficult to harvest [2]. Moreover, almost all broccoli is currently harvested by hand, relying on visual grading of size to estimate whether a head can be cut [2]. As a result, only around 50% of broccoli heads can be harvested economically. Two approaches can be readily compared when harvesting crops, namely, slaughter harvesting, i.e. cutting everything in one pass, and selective harvesting, i.e. cutting individually each crop [4]. Slaughter harvesting is not a productive option as it potentially produces large quantities of unmarketable broccoli heads, whereas selective harvesting presents its own challenges as it relies on a subjective assessment by each person cutting the broccoli as to which head is ready. Additionally, labour has become increasingly scarce and more expensive due to a variety of factors ranging from political pressures to migration dynamics [4]. The goal of growing fresh fruit and vegetables is to keep the quality high while minimising costs. It is therefore desirable to find a method to harvest more frequently, more quickly, more accurately, with less waste, and that reduces labour and overall operation costs [3]. Thus, developing an automated method for selective harvesting capable of accurately identify and separate broccoli crops from the background would help to increase productivity and to better control production costs.

A. Related work

Automated harvesting systems usually consist of three independent systems: a recognition system to identify and locate the product, a picking system to perform grasping and cutting operations, and a navigation system to allow the robot to move around the cultivated crop plants [4]. One major challenge in autonomous harvesting is the recognition and segmentation of the crop from the rest of the plant. One of the first and common approaches has been to detect crops using 2D images. This can be promptly perceived in the wealth of techniques based on computer vision available in the literature [4,5,6]. For the particular case of broccoli, some approaches have used colour images to separate the broccoli head from the soil and other plant parts. We address the most relevant work below.

Ramirez [7] developed an algorithm to locate the broccoli head within an image of an entire broccoli plant. To locate the head, first the method finds the leaf stems using a threshold, a Canny edge detector, and a Hough transform to extract geometric features that approximate lines that can be fit to the stems. Then the broccoli head can be located based on contrast texture analysis at the intersection of the stems. The method also determined the maturity of the crop using statistical texture analysis. Tu *et al.* [10] published results of a method to grade broccoli heads. The goal was to assess the quality decay of the

* This research has been supported by the UK Agriculture and Horticulture Development Board (AHDB), https://ahdb.org.uk.
** Hector A. Montes, Grzegorz Cielniak, and Tom Duckertt are with the School of Computer Science, University of Lincoln, Brayford Pool, Lincoln, LN6 7TS, UK (corresponding author e-mail: hmontes@lincoln.ac.uk; tduckett@lincoln.ac.uk; GCielniak@lincoln.ac.uk).

Figure 1. Top: Data acquisition with the 3D sensor mounted at the rear of the tractor. The sensor is fixed inside a purpose-built “black box” enclosure to block direct sunlight and other external incidences. Bottom: 3D point cloud images of broccoli plants (far left) are analyzed offline based on local angular features (middle frames) to segment broccoli heads (far right).

harvested crop based on a set of colour and shape parameters. The system determined the area and roundness as the shape parameters and extracted the colour features using standard vision techniques. The resultant quality of the broccoli head was then decided by a neural network classifier. More recently, Blok *et al.* [8] presented a method for detecting and sizing broccoli heads based on computer vision techniques. The method segmented an image based on texture and colour of the broccoli head buds. Firstly, the contrast of the image was enhanced to emphasise high frequency areas, followed by a series of filters and several morphological operations to fine-tune the image. Then, pixel connectivity was used to generate connected green-coloured components. Lastly, a shape-based feature selection on the connected area was conducted to separate small non-connecting components from the foreground. The segmented heads were sized using circle templates, and the mean image processing time took a little less than 300 ms. The system was part of a prototype harvesting device attached to a modified tractor and was tested in cultivated broccoli fields reaching an accuracy of 94%. Kusumam *et al.* [9] documented a system for detecting and locating mature broccoli heads in cluttered outdoor field conditions based on depth images acquired by a low-cost RGBD sensor. The paper evaluates a combination of Viewpoint Feature Histograms (VFH), a Support Vector Machines (SVM) classifier, and a temporal filter to track the detected heads. Their results showed a precision rate of 95.2% and 84.5% on datasets collected from fields in the UK and Spain, respectively.

Although 2D imagery is clearly important, this paper focuses on effective 3D depth features. However, 2D features is an interesting addition to 3D data worth studying in future work.

III. METHODOLOGY

A. *Point cloud data acquisition*

The 3D point cloud data for our experiments was captured in outdoor fields under different weather conditions using the well-known Kinect 2 sensor (1920×1080 RGB, and 512×424 depth resolution). The sensor was fixed inside a specially constructed enclosure to block direct sunlight and to protect during rainy conditions. The point cloud data was collected with the camera enclosure mounted on the rear of a tractor, as shown in 0

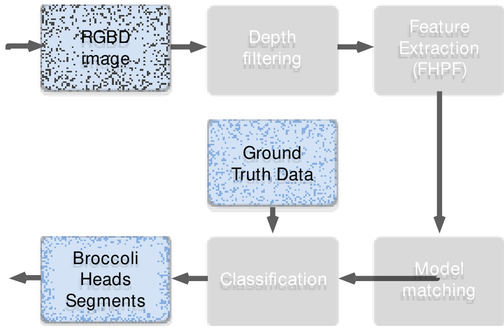

Figure 2. 3D point cloud segmentation pipeline. The frames of 3D point cloud data are first filtered by depth. Then features are extracted from each point and matched to the reference models. The points are then classified using a decision function. The points with the same target class are grouped to form the final segments.

B. *Model based 3D point cloud segmentation*

Two approaches are common in 3D object segmentation methods. In the first approach, the scene is segmented into smaller regions and *global* features are computed for each segment. These features are then matched to the descriptors of a model. In contrast, *local* methods commonly locate a list of appropriate points, often referred to as *interest points* or *key points*, and extract a set of features in the vicinity of those points. The points are then matched to a model and the correspondences are grouped according to the geometry of the model. This paper applies a local recognition method for segmenting broccoli heads in sets of 3D point cloud images collected in planted broccoli fields. The method processes the depth data in a pipeline of four stages: point cloud depth filtering, feature extraction, model matching, and classification, as shown in 0

The point cloud data captured by the sensor is first filtered to remove visible parts of the soil and other noisy points that are too distant from the surface of the scene. Feature descriptors are then computed in the remaining points and matched with the model references to finally determine if the points belong to a broccoli head. We use the algorithms available as part of the PCL C++ library [12] for processing point clouds.

B.1 *Depth filtering*

Depth filtering of the soil and other distant points is achieved through a simple depth range thresholding of the input point cloud. The points that lie outside the desired range are simply discarded. The depth threshold is defined to be of *1 m* and is based on the distance of the sensor to the ground measured during data collection.

B.2 *Feature extraction*

We use a set of local 3D feature descriptors that are extracted for individual input points. Local descriptors are often used for object recognition and image registration. Even though descriptors have no notion of what object the points belong to, they do describe how the local geometry is around

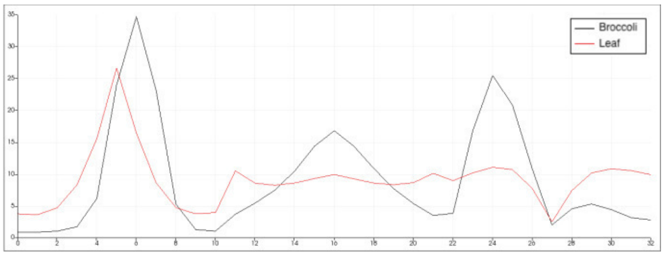

Figure 3. Histograms of the reference models used in our algorithm. A FPFH descriptor is computed for each data point. The descriptor is then matched to both reference models and the difference provides the final classification score.

that point. Every feature descriptor should be discriminative with respect to the two given reference models, i.e., broccoli and non-broccoli points. To this end, we use the *Fast Point Feature Histogram* (FPFH) descriptor introduced by Rusu *et al.* [13].

B.2.1 Fast Point Feature Histogram

We briefly summarize here the structure of the FPFH descriptor. The interested reader is referred to [13] for extended details on the descriptor and a discussion on its relevant properties. The FPFH captures information of the local geometry of the point by analysing the difference between the directions of the normals in its surrounding area. The distribution of the surface normal directions should encode the underlying geometry of the broccoli heads and be discriminative compared to that of other elements in the scene. The FPFH derives from a more computationally expensive descriptor called Point Feature Histogram (PFH) [13]. To calculate the FPFH, the algorithm pairs the current point to all the points in the vicinity, and for each pair, a fixed coordinate frame is computed from their normals. The direction differences between the normals can then be encoded into three angular variables between the normal and the three axes of the fixed frame. These variables are then binned into a histogram when all pairs have been computed. The histograms of the neighbours are merged with the current point histogram, weighted according to their distances. The final FPFH descriptor is the concatenation of the histograms of each angular variable.

B.3 Classification

To compare two FPFH descriptors, we use a fast but effective measure between the descriptors of two points: the *histogram intersection*. Given a query point and its corresponding histogram H (its descriptor), and a reference histogram h calculated from the descriptors of sets of known models, the histogram intersection is defined as:

$$d(H,h) = \sum_{i=1}^{n} min(H_i, h_i) \tag{1}$$

where n is the number of histogram bins. For the histogram intersection, higher values are better. After the intersections are calculated between the query and the reference descriptors, the difference between both intersections is used to make a choice as to which model is the best match and provides the final classification score. This score is computed with point-to-point correspondences obtained by matching local descriptors of feature points to a set of known reference models. Consecutive cloud points with similar high score are part of the same point cloud segment.

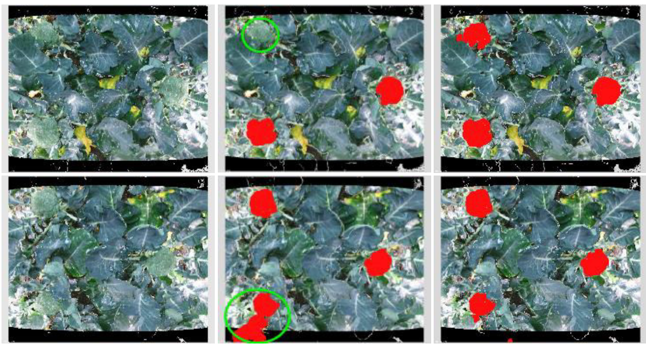

Figure 4. Two segmentation samples on different frames. First column: The original frame. Center column: circled in green, under segmented (missed one head) and over segmented objects (not only the head) using the Euclidean Clustering method from [9]. Right column: Samples of our model-based segmentation method.

C. Reference models

We construct models for the 3D point cloud objects that we are interested in. The reference models are two FPFH descriptors calculated from the histograms of sets of known models. These models are sets of selected 3D points that are already labelled to be part of either a *broccoli* head or a *leaf* (although labelled as *leaf*, the points also include other elements in the scene that are not part of a broccoli head). 0shows a plot of the FPFH reference descriptors selected for our experiments. These two descriptors suffice for our segmentation purposes as the angular distributions of a broccoli head is more relevant for the classification and segmentation tasks.

IV. EXPERIMENTAL RESULTS

The experimental evaluation aims to determine the overall performance and the accuracy of the method. To evaluate our results, we use a set of the same point cloud dataset used in the experiments reported by Kusumam *et al.* [9]. We particularly focus on frames where those experiments produced either *under segmentation*, i.e., some of the target broccoli heads were missed, or *over segmentation*, i.e., the extracted segments were larger that the broccoli heads seen in the scene frame. A sample of these two cases is shown in 0

The frames of a 3D point cloud are first filtered by depth and the FPFH descriptors are computed for each point and then matched to the reference models. These initial steps already show the areas of the point cloud that are more likely to contain broccoli heads. This allows to classify every point using a simple decision function that takes the current point matching score and determines the best label class. A function that examines nearby points of the same class forms the final segments and helps to eliminate false positives. An illustration of the broccoli segmentation steps is shown in 0

A. Classifier evaluation

We evaluated the classifier of the 3D system pipeline for segmenting broccoli heads using individual FPFH descriptors. For each point in the current frame a classification score is produced. If the point is part to a broccoli head, according to

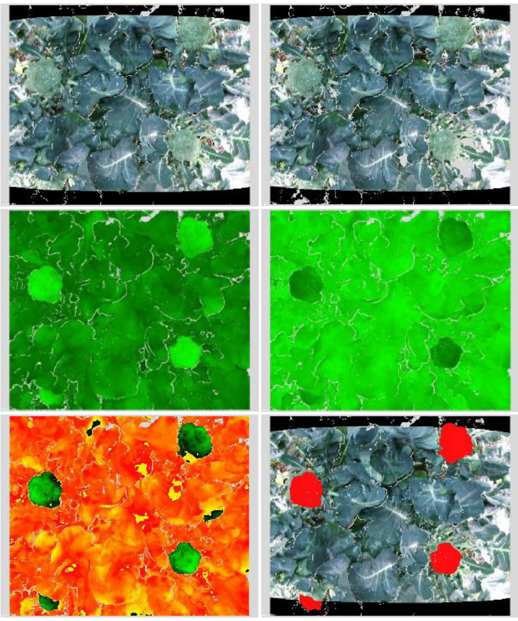

Figure 5. Broccoli segmentation steps. Top row: The original frame on the left, and after been depth filtered on the right. Mid row: matched points of broccoli heads shown in bright green on the left, and other points shown on the right. Bottom row: The difference of the two reference models shown in contrasting colors on the left and, on the right, the extracted segments in red.

ground truth data, it is labelled as a positive sample; otherwise it is labelled negative. The resultant sample sets are highly unbalanced, i.e. there is a significant difference in the number of positive and negative samples. In this case, the negatives notably outnumber the positives as large portions of each point cloud frame are from leafs, soil or other elements. Classification results were evaluated using precision-recall curves (PRC), as they provide a more accurate interpretation of a classifier performance on unbalanced samples [11]. *Precision* represents a ratio of true positive detections to the total number of positive detections (true and false), whereas *recall* is a ratio of true positive detections to the total number of both true positive and false negative detections. The precision and recall values are computed over a range of discrimination threshold values across the classification scores. 0shows the performance evaluation on a PRC plot on the set of classified points. The plot shows the average precision results on the scores computed for every point. The results show a precision rate of 92.22% on the datasets examined by our model-based method, versus a precision rate of 73.20% of the results published in [9]. Originally the EC method was applied on clusters of points and global features were extracted. The PRC plot shows the performance of the same method reflected on all the points that form the same clusters.

V. CONCLUSION

In this paper, we discussed a method for 3D point cloud segmentation based on 3D feature descriptors matching. Comparative experimental results show that our method performed favourably against an existing 3D broccoli detection algorithm based on the Euclidean proximity of 3D points when tested on the same dataset. The results showed a promising precision score. Moreover, our results also showed that the segmentation method can be used to detect broccoli heads, as a first step in the development of a fully autonomous selective harvester. Interesting future research directions include a more principled selection of key points to be examined by, for instance, performing a point cloud compression that retains the original perceived distribution of 3D points. Another research direction is to adopt strategies to find or even synthesize descriptors for the reference models, so they better encode the properties of the broccoli heads we are interested to segment. Future work will also address the issues of developing a real-time implementation of the presented approach for deployment on open field conditions.

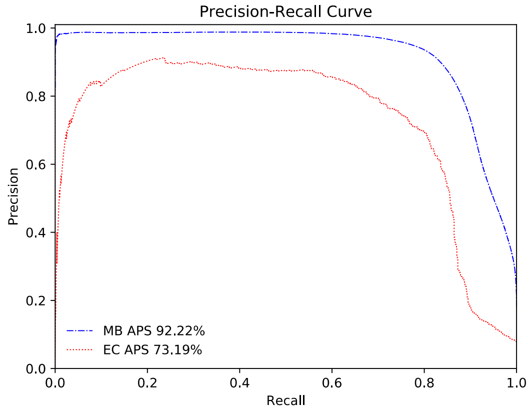

Figure 6. Precision-Recall curve showing the classification performance of the segmented points. The value shown is the average precision score (APS) at various discrimination threshold settings. The plot shows the performance of Euclidean Clustering (EC) from [9] and our Model Based (MB) approach.

REFERENCES

[1] L. Maggioni, R. von Bothmer, G. Poulsen, and F. Branca. Origin and domestication of cole crops (Brassica oleracea L.): linguistic and literary considerations. Economic botany, 64(2):109–123, 2010.

[2] M. D. Orzolek, W. J. Lamont, L. F. Kime Jr., and J. K. Harper. Broccoli production. In Agricultural Alternatives series, Agricultural Alternatives series. Penn State Cooperative Extension, 2012.

[3] C. Wouter Bac, Eldert J. van Henten, Jochen Hemming, and Yael Edan. Harvesting robots for high-value crops: State-of-the-art review and challenges ahead. Journal of Field Robotics, 31(6):888–911, 2014.

[4] S. Bachche. Deliberation on design strategies of automatic harvesting systems: A survey. Robotics, 4(2):194–222, 2015.

[5] A. R. Jimenez, R. Ceres, and J. L. Pons. A survey of computer vision methods for locating fruit on trees. Trans. ASAE, 43(6):1911, 2000.

[6] Y. Zhao, L. Gong, Y. Huang, and C. Liu. A review of key techniques of vision-based control for harvesting robot. Computers and Electronics in Agriculture, 127:311–323, 2016.

[7] R. A. Ramirez. Computer vision based analysis of broccoli for application in a selective autonomous harvester. Master thesis, Virginia Polytechnic Institute and State University, July 2006.

[8] P. M. Blok, R. Barth, and W. van den Berg. Machine vision for a selective broccoli harvesting robot. IFAC-PapersOnLine, 49(16):66–71, 2016. 5th IFAC Conference on Sensing, Control and Automation Technologies for Agriculture AGRICONTROL 2016.

[9] K. Kusumam, T. Krajník, S. Pearson, T. Duckett, and G. Cielniak. 3D-vision based detection, localization, and sizing of broccoli heads in the field. Journal of Field Robotics, 34(8):1505–1518, 2017.

[10] K. Tu, K. Ren, L. Pan, and H. Li. A study of broccoli grading system based on machine vision and neural networks. In Intl Conference on Mechatronics and Automation, pp 2332–2336. IEEE, 2007.

[11] T. Saito and M. Rehmsmeier. The precision-recall plot is more informative than the ROC plot when evaluating binary classifiers on imbalanced datasets. PLoS ONE, 10(3), 2015.

[12] R. B. Rusu and S. Cousins. 3D is here: Point Cloud Library (PCL). In Proc. ICRA. Shanghai, China: 2011.

[13] R. B. Rusu, N. Blodow, and M. Beetz. Fast Point Feature Histograms (FPFH) for 3D Registration. In Proc. IEEE ICRA, Kobe, Japan. 2009.

[14] U. Castellani, M. Cristani, S. Fantoni, and V. Murino. Sparse points matching by combining 3D mesh saliency with statistical descriptors. In Computer Graphics Forum, 27:643–652.

Enabling functional resilience in autonomous multi-arm and multi-vehicle cooperative tasks

Amar Kumar Behera, *Member, UKRAS*

***Abstract*— This paper presents results from experiments aimed at creating a framework for designing functionally resilient multi-robot systems. This is achieved by embedding functional information in motion planning algorithms and linking it to the robot's morphology. Two specific use case scenarios are discussed, one pertaining to multi-arm co-operative tasks and the other involving multi-vehicle tasks. Initial experimental results for each use case scenario are presented. The results indicate that the speed of response in the event of a disaster is dependent on the noise in the environment, processing power and intelligent mapping of functions to morphologies.**

I. Introduction

A team of robots or robotic manipulators performing tasks jointly either co-operatively or competitively have come to be defined as multi-robot systems. These systems can be thought of as complex engineered systems as they tend to display complex behavior, have a life of their own and can be hard to interpret analytically [1]. As such, there is often limited understanding regarding how such systems will function and behave in the real world and this can lead to operational difficulties in the form of cost overruns, delays in project completion and delivery, unplanned repair and maintenance and total system failure [2].

The design of multi-robot systems to meet performance specifications given by measures of predictability, reliability, stability, controllability and precision requires enabling resilience in these systems as they function under myriad environmental conditions and perform different tasks. Resilience can be defined as the ability of a system to autonomously recover when subjected to change, especially from disastrous events [3]. This, in turn, requires addressing the twin attributes of reliability and restoration [4]. While current robotic systems may exhibit resilience to a certain degree, systematic studies that discuss and enable functional resilience are lacking in literature and have been limited to very specific topics such as security [5] and coordination [6].

This work seeks to create an initial framework for functional resilience in multi-robot systems by taking an experimental approach where the requirements for resilience are derived from specific experimental scenarios involving change and disaster. These requirements are then used to embed intelligence within the software algorithms in the multi-robot system that enable the multi-robot system to function in a resilient manner.

*Research is supported by Engineering Complexity Resilience (ENCORE) Network+ grant.

A.K.Behera is with the Centre for Intelligent Autonomous Manufacturing Systems (i-AMS), Queen's University Belfast, Belfast BT9 5AH (phone: +44 28 9097 4769 e-mail: a.behera@qub.ac.uk).

II. Methodology

Functional resilience was explored in the context of two types of multi-robot systems: i) multi-arm and ii) multi-vehicle. These are discussed below.

A. *Multi-arm experiment*

A multi-arm experiment was set up on a Baxter collaborative robot. The task given to the robot was to pick and place pegs and rings on a Bytronic Industrial Control Trainer (ICT3) conveyor belt. The trainer is designed to assemble the pegs and rings. The pegs are made of aluminium alloy while the rings are made of white-colored polymeric material. The pegs and rings are placed in separate red and green bins respectively, as shown in Fig. 22. The task given to the left arm was to place the pegs on the conveyor, while the right arm was required to place the rings on the conveyor. Pick and place operation on the Baxter can be performed using visual servoing using cameras on the robot. A specific demo example on golf balls was calibrated for use in this study.

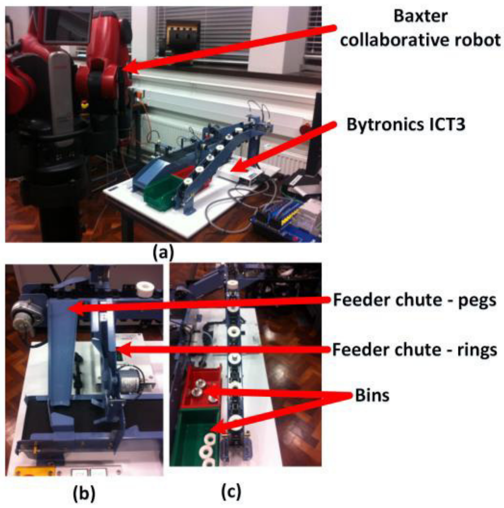

Fig. 22. Multi-arm experiment showing (a) entire setup (b) feeder chutes of Bytronic ICT3 (c) bins with conveyor belt

The following scenarios for functional resilience were conceived:

- If the left arm fails, then the right arm takes over the entire pick and place operation for both pegs and rings
- If the right arm fails, then the left arm takes over the entire pick and place operation for both pegs and rings

- If both arms fail, then an error message is displayed stating that both arms are dysfunctional
- If any one or both of the arms are functional again, the robot returns back to working with one or both arms

An algorithm was written to realize the above scenario that enables functional resilience by embedding intelligence into the code for the pick and place of pegs and rings.

B. *Multi-vehicle experiment*

A multi-vehicle experiment was set up using a commercially available unmanned ground vehicle (UGV) platform, Diddyborg together with an unmanned aerial vehicle (UAV) platform, CoDrone Pro, as shown in Fig. 23. A search and inspect experiment was designed where the UAV-UGV combination is sent out to autonomously search an area for a red ball and once the ball is found, the drone takes off to inspect the area. The Diddyborg is equipped with a Raspberry Pi 3 model B+ board and camera. The autonomous following of the ball is achieved using a Python code, adapted from a demo example, that uses the OpenCV library to process the images from the Raspberry Pi camera and detect objects of a specific color and shape. A disaster scenario is introduced in the shape of a blue obstacle that appears suddenly in the field of view of the UGV. Resilience is to be achieved so that the obstacle can be identified in real time, the multi-robot system stops a certain distance before the obstacle and the drone takes off to inspect the area following which a new path is charted for achieving the task of finding the red ball.

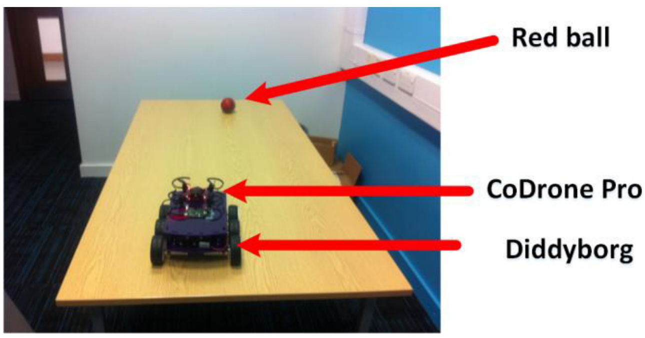

Fig. 23. Multi-vehicle experiment with an UAV and UGV performing a search and inspect operation

III. Results

This section discusses i) how the scenarios for functional resilience were embedded in the code of the robots and ii) the robustness of the algorithms embedding the resilience.

A. *Enabling functional resilience in multi-arm experiment*

A careful survey of programming techniques that would be suitable for enabling resilience led to the conclusion the key to enabling functional resilience is to be able to run multiple processes in parallel. For instance, while a robot is carrying out a certain task using a function or a set of functions called from the main function, if a simultaneous check could be run using another function whether all the manipulating arms are functional by processing sensor data, then if it found that one of the arms is failing, the other manipulating arms could take over the task or a remedial measure be put in place for the faulty arm. Having identified multi-threading as the technique to be used to enable resilience, the next step was to artificially inject one of the four scenarios identified in Section II.A. This was done by using a mouse click. A click of the left mouse button was meant to indicate that the left arm was non-functional while a click of the right mouse button made the right arm non-functional. The pseudo code that enables resilient operation is listed below –

Algorithm: Multi-arm resilience using multiple threads

Input: Adverse and repair events as mouse button clicks

Output: Pick and place using functional arm(s) or display error message

```
Obtain current state of mouse buttons as 'state_left' and 'state_right'
Define global variables 'count_left_mouse', 'count_right_mouse' that count the number of clicks made with each mouse button so far
Define start_robot as a flag for thread that kickstarts robot with both arms functioning

# Define a function for pick and place with both arms
def pick_place_both():
  count = 0 # variable to keep track of maximum number of rings that can be fed to feeder chute
  while count < max_feed and count_left_mouse % 2 == 0 and count_right_mouse % 2 == 0:
      count += 1
      pick_bin_B1(left_arm)
      pick_bin_B2(right_arm)
      time.sleep(10) # time required to perform pick and place operations

# Define a function for pick and place with left arm
def pick_place_left():
  count = 0
  while count < max_feed and count_left_mouse % 2 == 0 and count_right_mouse % 2 != 0:
      count += 1
      pick_bin_B1(left_arm)
      pick_bin_B2(left_arm)
      time.sleep(10)

# Define a function for pick and place with right arm
def pick_place_right():
  count = 0
  while count < max_feed and count_left_mouse % 2 != 0 and count_right_mouse % 2 == 0:
      count += 1
      pick_bin_B1(right_arm)
      pick_bin_B2(right_arm)
      time.sleep(10)

# Define a function for both arms dysfunctional
def pick_place_error():
  count = 0
  while count < max_feed and count_left_mouse % 2 != 0 and count_right_mouse % 2 != 0:
      count += 1
      print("Both arms dysfunctional \n")
      time.sleep(10)

while True: # loop that enables continuous pick and place
  Obtain current state of left and right mouse buttons as 'a' and 'b'

  if a != state_left:  # Button state changed
    state_left = a
    count_left_mouse += 1
      if count_left_mouse % 2 != 0 and count_right_mouse % 2 == 0:
                  print("Left arm not functioning")
                  start_new_thread(pick_place_right,())
      elif count_left_mouse % 2 == 0 and count_right_mouse % 2 != 0:
                  print("Right arm not functioning")
                  start_new_thread(pick_place_left,())
      elif count_left_mouse % 2 == 0 and count_right_mouse % 2 == 0:
                  start_new_thread(pick_place_both,())
      elif count_left_mouse % 2 != 0 and count_right_mouse % 2 != 0:
                  start_new_thread(pick_place_error,())

  if b != state_right:  # Button state changed
    state_right = b
    count_right_mouse += 1
      if count_right_mouse % 2 != 0 and count_left_mouse % 2 == 0:
                  print("Right arm not functioning")
                  start_new_thread(pick_place_left,())
      elif count_right_mouse % 2 == 0 and count_left_mouse % 2 != 0:
                  print ("Left arm not functioning")
                  start_new_thread(pick_place_right,())
      elif count_right_mouse % 2 == 0:
                  start_new_thread(pick_place_both,())
      elif count_left_mouse % 2 != 0 and count_right_mouse % 2 != 0:
                  start_new_thread(pick_place_error,())

  if start_robot == 0:
      start_new_thread(pick_place_both,()) # Runs only when kickstarting robot with both arms
      start_robot +=1 # Stops this thread from running after adverse events kick in
```

A series of timed tests were performed with a stop watch to assess the robustness of the multi-threading algorithm. Results from one such test are presented below in Table I.

TABLE I. STATISTICS FROM DISASTER EVENTS IN MULTI-ARM PICK AND PLACE USING A MULTI-THREADING ALGORITHM

Total time for experiment	5min 28 s
Time between events	16.4 s
Number of disaster events	21
Number of events with 0 subsequent error	2
Number of events with 1 subsequent error	17
Number of events with 2 subsequent errors	2

It may be noted that every pick and place event has a delay time of 10 s as mentioned in the pseudo code. This delay time is the time it takes to perform the operation. When a disaster event occurs, a pick and place event is already occurring and the thread performing it is running. Hence, even after the disaster event occurs, the operation is shown to being done and hence, an error occurs. This explains the 17 errors for the 21 disaster events. However, if two disaster events occur in close proximity of one another and negate the effect of each other (e.g. power supply fluctuations), then no error may be recorded. This explains the 2 cases with no subsequent errors. Another possibility is that the same thread is started twice due to such fast fluctuations leading to 2 subsequent errors.

B. *Enabling functional resilience in multi-vehicle experiment*

The first step was to pair the drone and the raspberry pi and fly it. Although the bluetooth chip on the pi (Bluetooth 4.2 chip Cypress CYW43455) communicates with the bluetooth chip on the drone (bluetooth 4.0 BLE), it was found that only pairing is feasible and flying the drone could not be enabled. Hence, the bluetooth board from CoDrone Pro had to be carried onboard and plugged in to the USB port of the pi. Next, the CoDrone library was imported within the diddyborg Python code, creating an instance of the drone, pairing it, and then having the drone take off after the diddyborg arrived at the red ball. The diddyborg has a thread where it prints a message "Close enough" on reaching the ball and this is where the drone take off event was created. A youtube video of the successful experiment is available at https://youtu.be/-Lo_2z0fhMg. The code was then modified to be able to detect blue objects in addition to red object, treat the blue objects as obstacle and inspect them. The pseudo code for the same is given below –

Algorithm: Multi-vehicle resilience using color-space based rules

Input: Streaming video of area being navigated
Output: Search and inspect red balls and blue obstacles

1. Instantiate an object of type CoDrone as "drone"
2. # Pair drone and bluetooth module connected to Raspberry Pi by specifying USB port
3. drone.pair (drone.Nearest, USB port connected to Bluetooth module)
4. Blur image obtained from raspberry pi using the function 'medianBlur'
5. Change the image definition from RGB to HSV colorspace using the function 'cvtColor'
6. Find the portion of the image in the red and blue channels using the function 'inRange' between numpy arrays
7. Use the function 'findContours' to segment the image into red contours and blue contours
8. Find the center of each set of contours and the area
9. Determine distance to blue obstacle and red ball using the centers and area
10. if (distance of obstacle to robot < distance of ball to robot)
11. if (obstacle is in the path to the red ball)
12. navigate close to obstacle
13. fly drone to inspect obstacle
14. else if (obstacle in not in the path to the red ball)
15. navigate to red ball
16. fly drone to inspect red ball
17. else if (distance of obstacle to robot > distance of ball to robot)
18. navigate to red ball
19. fly drone to inspect red ball

The algorithm used to estimate the distance of an object from the robot is based on an area calculation. The speeds of the motors on the robot are adjusted according to the location of the centers in two axes in the plane of the camera of the robot and the area calculation. While the threshold values for the red ball worked for the demo diddyborg code available from the manufacturer, the use of the drone necessitated an upgrade from Python 2.7 to Python 3 as the drone's libraries are written in Python 3. This meant the older Open CV libraries no longer worked and needed a fresh install. When this was done, the area thresholds for objects needed changing. Fig. 24 shows the new calibration that was done for blue objects. While earlier, the ball following code for the diddyborg worked well with a value of 10, 000 for autoMaxArea corresponding to a ball 65 mm in diameter, the new value for the same was re-adjusted to 1, 000 based on the below calibration. This produced satisfactory results for identifying both obstacles and balls.

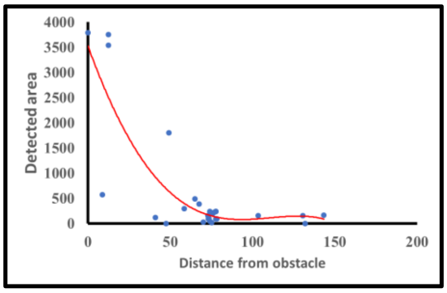

Fig. 24. Area of a blue object as a function of distance from camera; the red line shows a polynomial fit through the measured data points

IV. DISCUSSION

A discussion on the interpretation of the results from the multi-arm and multi-vehicle experiments is presented below.

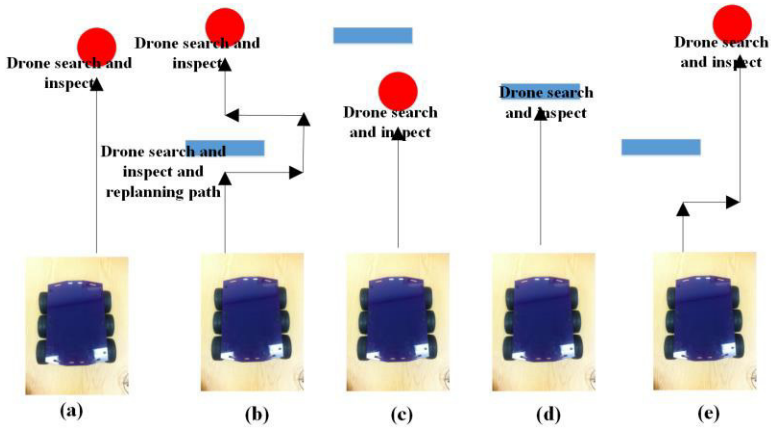

Fig. 25. Scenarios for obstacle emergence and associated path planning strategies a) no obstacle b) obstacle in line of sight of ball c) ball in front of obstacle d) only obstacle and no ball e) both ball and obstacle visible to the multi-vehicle team

A. Discussion on multi-arm resilience experiment

The introduction of a disaster scenario during the functioning of the multi-arm bin-picking experiment revealed that threads need to be handled with efficiency for the system to be resilient. Else, two situations may occur: i) delay in task allocation to the functional arm, ii) repetition of activities by a specific arm due to multiple instances of the same function running.

The first situation is hard to remedy as the non-functional arm may come in the way of the functional arm and an active collision avoidance algorithm between the two arms is necessary. Further, the thread for the non-functional arm needs to be interrupted immediately. Human intervention may be essential for the functional arm to take over the tasks or an intelligent algorithm to re-position the non-functional arm needs to be in place, which may be hard to realize, especially if the disaster scenario involves a power supply issue to the motors operating the non-functional arm.

The second situation can be remedied by introducing a waiting time between activities where the thread sleeps. Hence, a new pick and place activity does not start until the disaster scenario has kicked in. However, this will reduce the productivity from the multi-arm tasks and hence, was not pursued within this work.

A few hardware related issues need to be kept in mind before a fully resilient operation can be illustrated. One of these is being able to perform visual servoing on different types of objects with accuracy. These include the effects of color, size and shape, especially in different ambient conditions. Secondly, the placement of pegs and rings in the slots on the conveyor belt is not an easy task, and the positioning accuracy of the Baxter needs to be improved for the task to be performed precisely every time.

B. Discussion on multi-vehicle resilience experiment

The multi-vehicle experiment required the robot to identify new obstacles in its path as they emerge and inspect them. While an active collision avoidance algorithm can enable this, doing this based on color is significantly more challenging. Additionally, several scenarios for path planning can be envisaged as shown in the Fig. 4 below.

For the drone and the diddyborg to continuously operate as a team autonomously, the diddyborg must carry the drone with it at all times. This requires the drone to land on top of the diddyborg, after performing its search and inspect operation. This is easy to do using a joystick, however, achieving this autonomously requires the drone to run additional algorithms for detecting the diddyborg and making a stable landing on its top plate.

V. CONCLUSIONS

Functional resilience was explored experimentally in the context of multi-arm and multi-vehicle scenarios. The use of multi-threading in enabling resilience was outlined and algorithms for achieving this were successfully tested. Key challenges in achieving resilience in autonomous co-operative tasks were discussed, which provide the motivation for further research. Improvements in hardware and improved efficiency in the underlying algorithms can help create resilient multi-robot systems of the future.

ACKNOWLEDGMENTS

The author wishes to acknowledge the contributions of Conor Burrows and Sarka Klimkova in building the robots and setup of experiments.

REFERENCES

[1] A.A. Mina, D. Braha, Y. Bar-Yam, Complex engineered systems: A new paradigm, Springer, 2006.
[2] C. Ivory, N. Alderman, Can project management learn anything from studies of failure in complex systems?, Project Management Journal, 36 (2005) 5-16.
[3] R.J.T. Klein, R.J. Nicholls, F. Thomalla, Resilience to natural hazards: How useful is this concept?, Global Environmental Change Part B: Environmental Hazards, 5 (2003) 35-45.
[4] B.D. Youn, C. Hu, P. Wang, Resilience-driven system design of complex engineered systems, Journal of Mechanical Design, 133 (2011) 101011.
[5] S. Gil, S. Kumar, M. Mazumder, D. Katabi, D. Rus, Guaranteeing spoof-resilient multi-robot networks, Autonomous Robots, 41 (2017) 1383-1400.
[6] M.B. Dias, M. Zinck, R. Zlot, A. Stentz, Robust multirobot coordination in dynamic environments, in: IEEE International Conference on Robotics and Automation, 2004. Proceedings. ICRA'04. 2004, IEEE, 2004, pp. 3435-3442.

In process monitoring and control of automated TIG welding processes

James Dobrzanski, Daniel De Becker, Dr Laura Justham, *UKRAS*

***Abstract* - TIG (Tungsten Inert Gas) welding is utilised in industry as a preferred choice due to its high quality, coupled with the ability to control the shape of the weld bead. In any thermal based material processing, in-process control of the melt zone is essential to achieve optimal process conditions. However, due to the harsh environments during the joining process, including high temperatures and plasma emissions, it remains difficult to monitor the process and react to any conditions which may prove detrimental to the desired properties of the joint. In most cases, the input current and/or arc voltage are monitored during the process to guarantee integrity of the finished joint, backed by destructive testing of sample joints to confirm the output. This research develops a closed-loop adaptive control system based on thermal imaging to address the fluctuations observed during the TIG welding process. The experimental setup comprised of a robotic TIG welding system, single wavelength IR (Infrared) thermal camera, a data acquisition system and an NI (National Instruments) based DAQ controller. The results show that the online monitoring and closed loop control of the TIG welding process can help to minimise defects and the proposed system can be readily adapted to any thermal based manufacturing techniques.**

I. INTRODUCTION

Tungsten Inert Gas (TIG) welding is required in applications where a high-quality joint is necessary. However due to the heterogeneous nature of this type of joint there are yield limitations associated with productions of such joints. Typically, within literature, four major variables are synonymous with the creation of high-quality joints; welding current, arc voltage, welding electrode speed across the workpiece, and shielding gas composition [1]. A high level of interdependence between these variables adds further complexity to the process. An increase in electrode speed requires a corresponding increase of current to satisfactorily melt the material to be welded. This subsequently increases both the pressure within the welded joint and the flow of molten material, creating a periodic irregular surface profile of the joint. This leads to defects within the joint, which can affect its integrity [2 - 3].

Thus far, the focus on utilization of infrared thermography (IRT) has been for its use as a monitoring tool. A variety of industries opt to utilize this equipment due to the non-contact non-destructive means of operation. Temperature has been identified as one the most common indicators of structural health of both plant and components, with the ability to monitor a system's condition and therefore health in real-time [4]. Condition monitoring is an in process monitoring technique of plant and procedures. In the case of TIG welding, condition monitoring refers not only to the structure and visual condition of the welded joint but also the equipment behavior during the welding cycle. This may include heat build-up within the welding electrode, heat shield, and gas nozzle; which may help to identify deterioration in equipment before a failure occurs, resulting in both damage to the plant and a compromise to the joint integrity. Previous work on how the introduction of an IRT unit is able to help in a multivariable control system can be used in welding control has been primarily focused on MIG welding processes. With modern process control focusing on the development of laser-based material processing.to understand [5-7]. This work looks to expand the scope of this to TIG welding. TIG welding differs by using a non-consumable electrode which may obscure or influence the ROIs (Region of Interest) of the IRT system. Careful placement of the camera with respect to the melt pool is required to mitigate these effects.

During the welding process, undesirable signals from specular reflection of the hot electrode on a metallic surface or from heat accumulation within the torch heat shield may occur. The use of an IRT (Infrared Thermographic) camera offers greater flexibility than the use of single spot infrared sensor technologies used in the testing processes of Wikle [8} The two-dimensional area monitoring offered by IRT cameras allow for the observation of multiple areas of emission. Whilst masking areas where unwanted signals may occur.

The aim of the work presented in this paper was to develop a robust adaptive control system based on thermography for automated control of the HAZ shape and width in the TIG welding process. Event based control offers a method of filtering the signal response to slow the system's reaction to the current input.

II. EQUIPMENT AND METHODOLOGY

The material chosen for the task was stainless steel 316, with a filler wire of 0.52 mm² CSA (Cross sectional Area) matching the material type. The blanks for welding dimensioned 150 mm x 50 mm x 1.5 mm and a gap spacing of 0.2 mm was used during the welding procedure. This gap allows for some small thermal expansion of the material during the welding operation and is appropriate as the gap should not exceed the diameter of the filler wire, which was 0.8 mm, to ensure the filler wire can successfully bridge the gaps between the parts being welded. A jigging fixture to stop the blanks from moving during the welding process was also used.

The welding power source is a Fronius Magicwave 4000 capable of operating in a fully autonomous mode, receiving its control signals during operation. A Fronius Robacta PTW 1500 torch handle, welding currents up to 150 A (with suitable

J Dobrzanski is with the Intelligent Automation Centre at Loughborough University, LE11 3QZ, UK (email: J.Dobrzanski@lboro.ac.uk).
D De Becker is with the Intelligent Automation Centre at Loughborough University, LE11 3QZ, UK (email: d.de-becker@lboro.ac.uk).
L Justham is with the Intelligent Automation Centre at Loughborough University, LE11 3QZ, UK (email: L.Justham@lboro.ac.uk

shielding nozzle and gas flow) was also used. The electrode used was a 2.6 mm diameter tungsten electrode doped with 2% thorium. The welding torch was attached to the end effector of a KUKA kr16-2 6 axis robot controlled by a KRC2 robot controller. A custom robot program ensured the repeatability of the robot path during the experiments. A national instruments PXI module handled communication to the robot and control signals to the welding unit. Expansion modules allow for the transmission of both analogue and digital signals. An image of the robotic welding setup can be seen in Figure 1. The IRT is place in an isometric chase position to stop the reflection of the Tungsten influencing the recorded temperature of the melt pool.

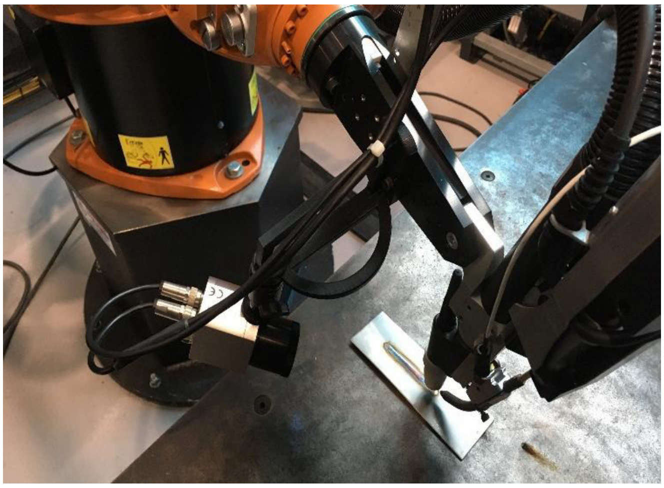

Figure 1. The welding components on the end effector of the robotic arm

A Micro Epsilon thermaIMAGER TIM M1 managed the thermography elements. A 16mm 12 ° field of view (FOV) lens allowed the entire melt pool during the welding process to be captured when coupled with the thermal camera. A custom program offers NI LabVIEW the ability to monitor and control the process during operation. This program used closed loop feedback to facilitate temperature data from the IRT controlling the welding current during operation.

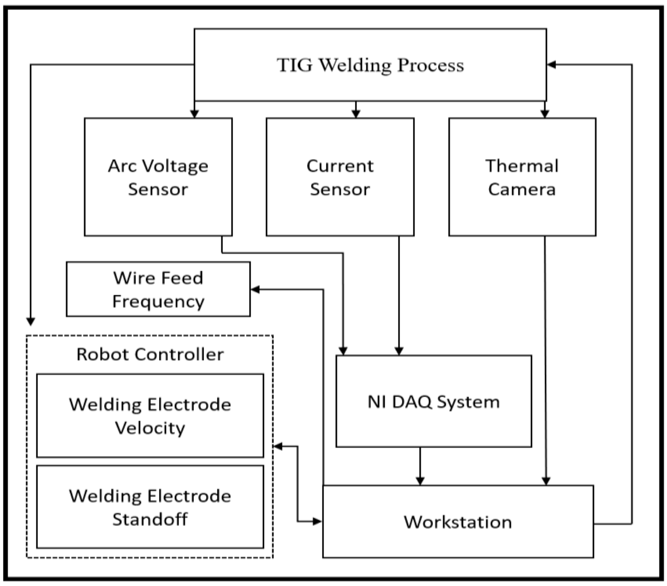

Figure 2 System diagram of the experimental set up

The main components of the developed adaptive control system are shown in Figure 2. The arrows highlight the communication between each of the devices.

D-optimal methodology of experimental design is used with the aid of design expert software; this design allows for the use of pre-defined central core values with incremented and decremented steps from the chosen core values to help identify the true optimal equipment settings and how their interaction affects one another. |Interviews of skilled TIG welders provided the initial choices for the number and values of the parameters used as a base for the initial runs of the robotic welding. These settings are in Table 1 row 5.

The TIG welded samples were tested and analysed with two different methods. The first means of testing the welded samples was by performing tensile testing. The Second test involved geometric analysis of the joint. The first test will show if the welded joint's tensile strength is equal to that of the base material. If the joint fails prematurely then we must assume the welded joint to have a lower tensile strength than that of the base material; stainless steel 316l. The machine used for this testing was an Instron 234 tensile testing machine. Firstly, the welded samples were laser cut into an ISO standard size, as shown in Figure 3a, and this cut sample was placed into the centre of the jaws, which are then locked in place around the sample. The load was then increased until fracture occurred on the specimen. The output from the tensile testing machine is in graphical form showing load vs extension. We can expect to see the UTS of either the joint or the material from this graph, which should occur shortly before fracture. The Instron 234 tensile testing machine is an electromechanical tension-testing machine, which is often referred to as a pull testing machine. As well as tension testing these machines are also able to perform shear, peel, tear, cyclic and bend tests. The Instron 234 tensile testing machine is able to perform tensile tests of up to 100kN, at a maximum pull speed of 500mm/min, with a load accuracy of 0.05%, and data acquisition rate of 500Hz.

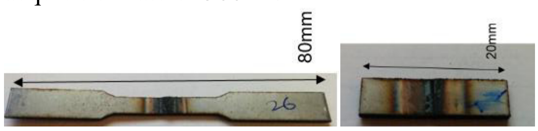

(a) *(b)*

Figure 3. Samples used for (a) mechanical and (b) Geometric analysis

Figure 3b shows a laser cut sample for use in microscopic analysis of the welded joint. The sample is cut from the HAZ (Heat Affected Zone) of the weld, then encased in a resin block. Finally, the edge of the sample was machined upon its edge to remove any processing of the material via the laser cutting process and analysed for imperfections and joint geometry.

III. Results and Discussion

The initial set of experiments were devised to identify the KPVs of TIG welding and the effect of parameters on TIG welding quality. This information was used as a baseline to find the optimal settings for further experimentation related to automation. The primary KPV's selected for analysis were welding current, welding voltage, electrode standoff, electrode angle, and electrode velocity. Penetration and joint strength were taken as the key output quality parameters Table 1 shows a selection of the parameters used in the welding study.

	Welding Current (A)	Electrode Speed (mm/s)	Electrode Angle (°)	Electrode Standoff (mm)	Wire Feed Rate (mm/s)
Test A	90	5	0	2	2
Test B	50	1	40	5	0
Test C	50	3	0	2	0.5
Test D	50	1	40	2	0
Human Selection	70	3	20	3.5	1

Table 1. Welding parameters

Figure 4 shows the effect of TIG welding parameters on the weld shape and size. Figure 4a shows a high-quality joint with no voids, good penetration and width. Figure 4c shows good penetration but a reduced amount of wire feed during the process has resulted in under filling of the top face of the joint. Low current input to the joint has allowed fusion to occur but has resulted in the formation of voids within the joint. Figure 4b shows a severe lack of material in the joint, this has resulted in a very narrow joint. Figure 4d shows good penetration and depth. Poor fusion has resulted in the formation of an undercut in the joint which would seriously compromise the joint strength.

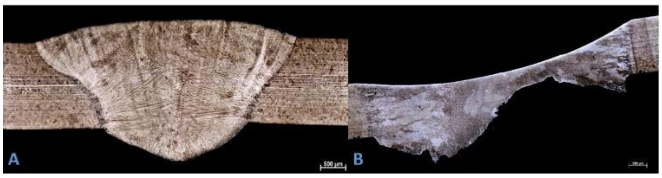

(a) Current=90A; speed=5mm/s ; Electrode angle=0° ;Electrode Standoff = 2mm ;Wire Feed Rate=2mm/s

(b) Current=50A; speed=1mm/s ;Electrode angle=40° ;Electrode Standoff=5mm ; Wire Feed Rate=N/A

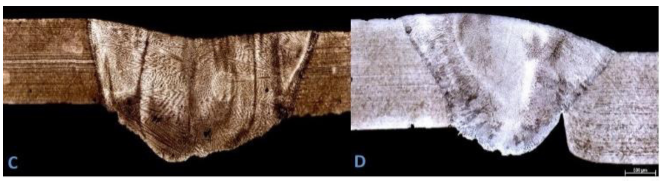

(c) Current=50A; speed=3mm/s ;Electrode angle=0° ;Electrode Standoff=2mm ; Wire Feed Rate=0.5mm/s

(d) Current=50A; speed=1mm/s ;Electrode angle=40° ;Electrode Standoff=2mm ;Wire Feed Rate=N/A

Figure 4. Cross-sectional view of the TIG welded samples

Figure 5 shows a force vs extension graph for each of the four samples tested within the experiment where a cohesive joint was formed. From these results, the following setting as a baseline for the control inputs were determined: Current=90A; Electrode speed=5 mm/s; Electrode angle=0 °; Electrode Standoff=2 mm; Wire Feed Rate=2 mm/s. These settings produced the strongest, most ductile weld. Stainless Steel 316l has a Solidus temperature of 1375 °C, with the material becoming liquid at a temperature of approximately 1400 °C. A weld is unable to be formed until the material of the 2 halves to be joined are molten and have mixed to form one cohesive joint. Due to this, a temperature of 1450 °C was selected as the initial target temperature for the melt pool. This was then set as the control point for the system to maintain during operation to control the width of the HAZ

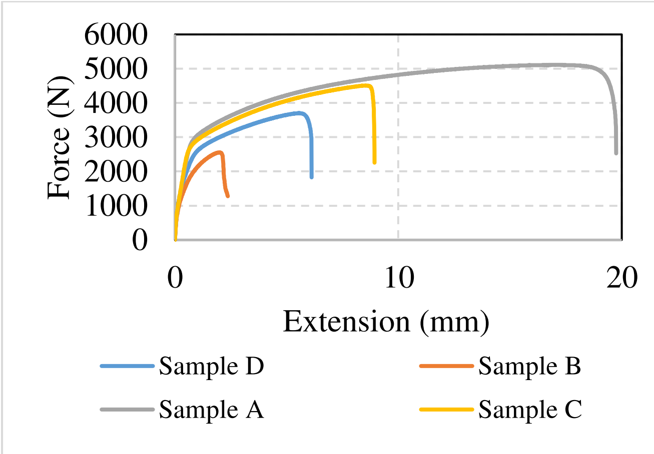

Figure 5. Force vs Extension on for various TIG welded samples ((a)90 A; 5 mm/s; 0°; 2 mm; 2 mm/s; (b) 50 A; 1 mm/s; 40°; 5 mm; 0 mm/s; (c) 50 A; 3 mm/s; 0°; 2 mm; 0.5 mm/s;(d)50 A; 1 mm/s; 40°; 2 mm; 0 mm/s)

With the optimal parameters established for the welding of 316l with the equipment; optimization of the HAZ was undertaken using thermography as a control input. Images from the adaptive control system can be observed from Figure 6. The aim of the control system was to maintain a melt pool temperature of 1450 °C. Figure 6a shows an initial condition of 1440 °C, this is too low and the current input into the joint is raised (and therefore also the power input). The result is the temperature in 6B of 1459 °C. The control system recognizes this as having excess heat within the joint and therefore reduces the input current. The reaction time to each of the changes in power input is 100 ms, with the current step change of 0,1 A.

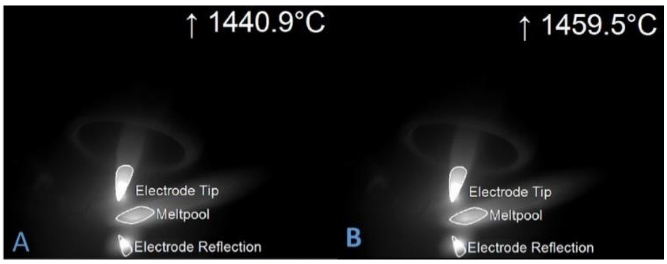

Figure 6. Image (A-B) showing the measurement phase of the melt pool temperature

To determine the benefits 2D thermography for control rather than just condition monitoring, visual analysis of the welded samples was undertaken. Images of the welded samples can be viewed in Figure 7, with blob analysis coupled with Matlab functions created to apply a best-fit line to the edges of the HAZ boundaries and the deviation from it measured in mm from the boundaries. Table 1 shows that thermographic control helps to establish a HAZ with greater uniformity with closed loop control vs the open loop system. The mean error of the HAZ boundary has decreased from 0.18 to 0.14mm on the upper boundary, an improvement of 22%. The lower boundary shows a greater improvement in linearity with an improvement from 0.21mm to 0.12mm, just over 82%. Whilst also controlling the shape of the HAZ, the width can also determine how stresses concentrate around a joint to help identify potential weaknesses in the joint. Ideally the width of the joint will be as narrow as possible with only the edges of the joint affected by the joining process. The average width of the HAZ showed a decrease in width of 5%. Typically, to reduce the width of the HAZ, welding at increased current coupled with increased electrode speed across the melt pool is required. The benefit of a HAZ is the subsequent reduction in residual stresses internal to the welded joint. Therefore, control over the current has also allowed for greater uniformity of the HAZ boundary with a significant improvement in the standard deviation observed.

	Mean Error of upper HAZ	Mean Error of Lower HAZ	Average HAZ Width (mm)	S.D. (δ) of Upper HAZ	S.D. (δ) of Lower HAZ
Without Control	0.18	0.21	10.67	0.22	0.26
With Control	0.14	0.12	10.14	0.06	0.05
Improvemen t	22.28 %	82.20 %	5.19%	0.16	0.21

Table 2. Results

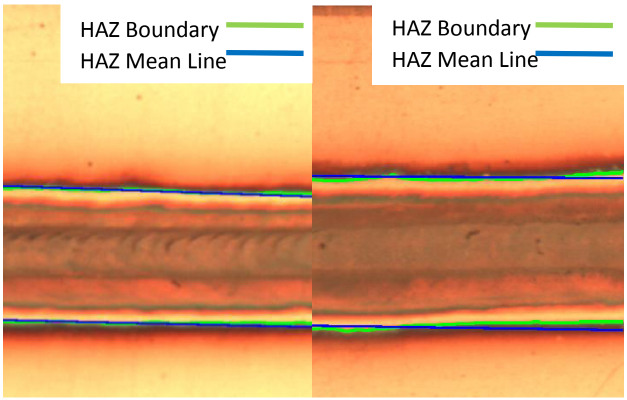

Figure 7. The welded samples

IV. CONCLUSION

Traditional methods of closed loop control for welding systems rely on sending a control signal to the power source reading the current supplied by the primary side of the transformer to control the welding current. The system developed and presented here aims to compliment this with the addition of a weld pool monitoring system which can send a control signal to the power source to modify the welding current and maintain the melt pool temperature for optimal joining conditions. The output from the system utilizing an event based thermographic control shows improvement over the open loop system. The introduction of signal feedback allows for finer control of the HAZ shape than offered simply via the power source alone. In addition, the system is able to react to heat build-up within the material caused by the welding process and impurities within the material creating hot spots in the joint. Further study into the use of more advanced control techniques using PID (Proportional, Integral, Differential) control and image processing techniques coupled with machine learning hope to offer decreased response times of the system and further control of the HAZ.

ACKNOWLEDGEMENTS

This research was carried out with the help of funding from the EPSRC. The authors would also like to IA-CIM for the use of equipment and lab space to conduct these experiments.

REFERENCES

[1] Pires, J.N., Loureiro, A., Bölmsjo, G., 2006. Welding Technology In: Welding Robots: Technology, System Issues and Applications. Springer Science Business Media, Germany, pp. 31–34.
[2] Zhao, C.X., Steijn, V.van, Richardson, I.M., Kleijn, C.R., Kenjeres, S., Saldi, Z., 2009. Unsteady interfacial phenomena during inward weld pool flow with an active surface oxide. Sci. Technol. Weld. Join. 14 (2), 132–140
[3] Lin, M.L., Eagar, E.T.W., 2005. Influence of Surface Depression and Convection on Arc Weld Pool Geometry, vol. 10. Transport Phenomena in Materials Processing, USA, pp. 63–69.
[4] Bagavathiappan, S., Lahiri, B.B., Saravanan, T., Philip, J. and Jayakumar, T., 2013. Infrared thermography for condition monitoring–a review. Infrared Physics & Technology, 60, pp.35-55.
[5] C. C. Doumanidis and David E. Hardt, 1988. Multivariable Adaptive Control of Thermal Properties During Welding: Journal of Dynamic Systems, Measurement, and Control 113, pp. 22-92.
[6] Mansoor A. Khan, Nels H. Madsen, Nels H. Madsen, John S. Goodling, John S. Goodling, Bryan A. Chin, Bryan A. Chin, "Infrared Thermography As A Control For The Welding Process," Optical Engineering 25(6), 256799 (1 June 1986). , 113, pp.228-233.
[7] Gade, R. & Moeslund, T.B. Thermal cameras and applications: a survey: Machine Vision and Applications (2014) 25: 245. https://doi.org/10.1007/s00138-013-0570-5
[8] H.C Wikle S.Kottilingam, R.H Zee, B.A Chin., 2011. Infrared sensing techniques for penetration depth control of the submerged arc welding process, 113, pp.228-233.

Dynamic, Anytime Task and Path Planning for Mobile Robots

Cuebong Wong, Erfu Yang, Xiu-Tian Yan, and Dongbing Gu

***Abstract*— The study of combined task and motion planning has mostly been concerned with feasibility planning for high-dimensional, complex manipulation problems. Instead this paper gives its attention to optimal planning for low-dimensional planning problems and introduces the dynamic, anytime task and path planner for mobile robots. The proposed approach adopts a multi-tree extension of the T-RRT* algorithm in the path planning layer and further introduces dynamic and anytime planning components to enable low-level path correction and high-level re-planning capabilities when operating in dynamic or partially-known environments. Evaluation of the planner against existing methods show cost reductions of solution plans while remaining computationally efficient, and simulated deployment of the planner validates the effectiveness of the dynamic, anytime behavior of the proposed approach.**

Keywords—robotics, autonomous systems, task planning, path planning, combined task and motion planning, dynamic planning

I. INTRODUCTION

The study of task planning and path planning for applications in robotics has largely been conducted in isolation. Task planning is carried out using a symbolic representation of the world consisting of a finite set of discrete states. In this domain, geometric relationships of objects in the world are, in general, highly abstracted to reduce the size of the state space. Thus task planners are rarely able to consider geometric constraints of the planning problem. Path planning (a purely geometric *motion planning* problem [1]) on the other hand seeks to find an admissible path in $\mathbb{R}^d$ space to transition a robot from a start configuration to a goal configuration by exploiting the geometric representation of the environment. While trivial problems may be efficiently solved by performing task planning in isolation and subsequently calling a path planning instance for each movement action, applying the same approach to more complex problems may produce sub-optimal plans, or in the worst case be unsolvable.

An emerging concept in literature called combined task and motion planning (CTMP) seeks to address this by integrating the process of path planning and task planning. The authors in [2] proposed a hierarchical approach that interleaves planning with execution. The FFRob [3] is a CTMP planner that extends FastForward heuristics used in symbolic planning to robot motion planning, while [4] performs CTMP by precomputing motion graphs and collision tables for a mobile manipulator. The Task-Motion Kit (TMKit) [5], which addresses probabilistic completeness and generality, is a general-purpose framework that interfaces the symbolically-defined task domain with the geometric relational properties of the motion domain through a domain semantics layer. These aforementioned work focus on feasibility planning for high complexity problems involving object manipulation. However, far fewer works have applied CTMP concepts to planning for lower-complexity problems consisting of mobile robots. Yet CTMP can provide improvements to the optimality of long mission plans, or adapt task plans in response to failures or perceived dynamic changes to the world. We highlight the UP2TA framework [6], which integrates task and path planning for applications to exploration mission planning. However, UP2TA does not consider general cost spaces in path optimisation, nor facilitates dynamic re-planning. Thus the contributions of this work is two-fold: (i) we compare a base planner, which integrates task and path planning to enable optimal task planning in continuous cost spaces by making use of a multi-tree T-RRT* algorithm [7], against UP2TA and a *planning-in-isolation* approach, and (ii) we extend the base planner with dynamic, anytime capabilities to enable high-level re-planning and low-level path corrections in dynamic environments. We collectively refer to the proposed planner as the Dynamic, Anytime Task and Path Planner (DA-TPP).

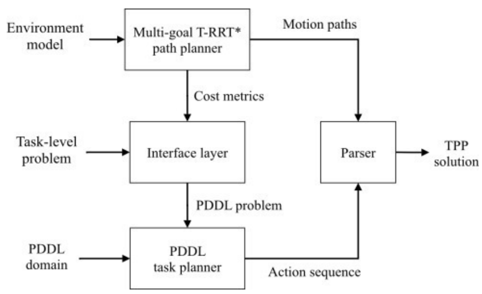

Figure1. The proposed base planner architecture

II. PROBLEM DEFINITION

This paper addresses task and path planning (TPP) problems for autonomous mobile robots. As a minimum, this consists of a robot in an environment containing a set of landmarks L. These landmarks represent locations in space where a robot must perform some actions. A movement action consists of traversing between any pair of landmarks $l_a, l_b \in L$. A valid planning problem within this domain consists of an initial landmark from which the robot starts from, and a set of tasks that must be performed at each landmark. These may be defined as a discrete action within the planning domain. A goal landmark for which the robot must be located at the end of the plan may also be specified. For consistency, we assume that the robot must begin and end at a root landmark l_0, referred to as the robot base, throughout this paper.

C. Wong, E. Yang and X. T. Yan are with the Department of Design, Manufacture and Engineering Management, University of Strathclyde, Glasgow, G1 1XJ, UK. (e-mails: {cuebong.wong, erfu.yang, x.yan}@ strath.ac.uk).

D. Gu is with the School of Computer Science and Electronic Engineering, University of Essex, Wivenhoe Park, Colchester C04 3SQ, UK (e-mail: dgu@essex.ac.uk).

III. DA-TPP Approach

In DA-TPP, the base planner (Fig. 1) pre-plans all possible paths before the execution of a task planner. The resulting path costs are then configured into the task planning problem as discrete movement action costs. This enables optimal task planning as true path plans are considered in the task planning phase. Indeed it can be inefficient to run an individual planning instance for each possible movement action. This is addressed through our previously developed multi-goal path planning algorithm based on T-RRT* trees [7], which simultaneously and efficiently finds feasible paths between all landmark pairs.

Given a continuous cost space mapping function, c, from which a cost value can be derived for all robot configurations, we define the path cost function, c_p, of a path σ as a weighted sum of integral cost and path length:

$$c_p(\sigma) = l(\sigma)\left(\frac{w_a}{n}\sum_{k=1}^{n} c\left(\sigma\left(\frac{k}{n}\right)\right) + w_b\right) \qquad (1)$$

Where n is the number of subdivisions of σ, $l()$ is the path length and w_a and w_b are weight factors for c and $l(\sigma)$, respectively. This formulation enables consolidation of both the cost function and path length as a weighted sum multi-objective optimisation problem. When a termination criteria is met, the planner returns the best set of paths and corresponding costs found for each of these actions ($c_p = \infty$ if no solution is found). In the interest of anytime planning, we note that a TPP solution can be found if all landmarks form a fully-connected graph such that any landmark $l_i \in L$ can be reached from every other landmark $l_j \in L | i \neq j$ by traversing the graph.

The task planning layer employs PDDL representation [8], and is solved using the openly available planner Local Planning Graphs (LPG-*td*) [9]. We chose to represent the planning problem in PDDL due to its wide acceptance as a standard for representing classical symbolic planning problems. This enables interchangeable use of other heuristic planners (such as Metric-FF [10]) developed for PDDL so long as they are compatible with *fluents* as a minimum requirement.

A. Anytime extension

Anytime planning supports a request for an initial solution after a fixed allotted time, which minimises idle time at the start of a task. This is supported by the base planner under the condition that sufficient paths are found to form a connected graph across all landmarks. Once an initial TPP solution is obtained, the path planning layer continues to iterate the path planning algorithm while the robot executes the initial solution. Suppose that the initial path cost for an action a is c_p. Following the work in [11], an upper cost bound C_s^+ is defined as:

$$C_s^+ = (1 - \eta_a) \cdot c_p. \qquad (2)$$

Where η_a is a constant. When the path planning layer finds a new path for a with $c_p < C_s^+$, a new instance of task planning is called and c_p is updated to the new path cost. This mechanism guarantees that the task planning layer is called only when a guaranteed improvement to an action cost is found.

When running this anytime planner alongside robot execution, it is also necessary to consider the goals that have been met thus far. This is addressed by updating the initial state of the planning problem at each instance of task planning to reflect the next state of the world after executing the current action of the latest plan. In this way the robot always commits to the first action of each plan.

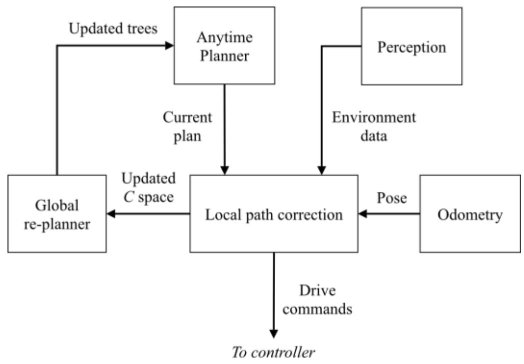

Figure 2. DA-TPP architecture

B. Dynamic anytime extension

The complete DA-TPP architecture is shown in Fig. 2. The key extensions are the local path correction and the global task re-planner modules. Each time an obstruction to a currently executed path is detected, a local path correction procedure is performed to find a new optimal path to the goal configuration. The DA-TPP then determines whether an instance of global re-planning should be called using (3). Letting c_p' be the path cost of the remaining segments of the original path, a lower cost bound is defined as

$$C_s^- = (1 + \eta_d) \cdot c_p'. \qquad (3)$$

Where η_d is a constant. When the cost of the corrected path exceeds C_s^-, global re-planning takes place. This permanently updates all planning trees with the detected obstruction, and lazily finds a path to the robot's current location, if it exists, from every landmark. A new TPP solution is then produced from the updated path plans to generate a new optimal sequence of movement actions. The benefits of applying (3) as a re-planning condition is briefly discussed in section V. B.

Accordingly the DA-TPP provides the following behaviours in dynamic environments. When minor obstructions are encountered, only small adjustments to the planned path is required. This, in general, does not affect the optimality of the task plan from a high-level perspective. It is sufficient then to correct paths locally each time the same obstruction is encountered. However, in situations where an obstruction causes significant diversion for a particular traverse (e.g. from road blockages), the likelihood of the obstruction affecting other paths are high and thus re-routing may produce new optimal task plans. In these situations it is necessary to update the entire plan to maintain optimality.

IV. Path Planning

The path planning layer of the base planner is implemented following the approach described in [7]. Readers are directed to this initial work for a detailed description of the multi-tree T-RRT* algorithm. This section briefly discusses the dynamic algorithms for local path correction and global re-planning.

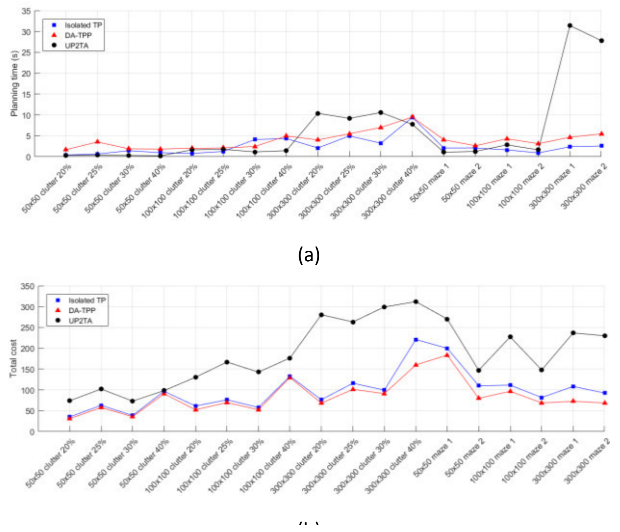

Figure 3. DA-TPP benchmarking results. (a) planning time, (b) overall plan cost

A. *Dynamic path correction (local)*

The local path re-planner corrects any single path according to procedures based on elements of the RRT^X algorithm [12]. At the start of any movement action, a new tree T_{new} is generated from two trees T_0 and T_g corresponding to the start and goal landmarks l_0 and l_g, respectively. T_{new} is rooted at the goal configuration q_g and consists of all the vertices of T_0 and T_g rewired to minimise path cost according to the new tree root. This step eases the dynamic re-planning procedure as the root of the tree does not need to be updated at each time step as the robot advances along the path. As the robot traverses along this path, new environmental information is used to temporarily update the configuration space *C*. A feasibility check is used to determine if the updated configuration space invalidates the current path plan. If it does, the algorithm proceeds to update the path. Otherwise, the changes to *C* are discarded.

The algorithm invalidates all vertices that lie in the collision region of new obstacles. All descendant vertices that remain valid are then updated as *orphans*. This closely resembles the *propagateDescendants* function in [12]. Following this, the algorithm updates the connecting edges of the tree by iterating through a queue of vertices consisting initially of the neighbours of orphaned vertices (see *reduceInconsistency* function in [12]). For each of these vertices, the algorithm updates the parent of the current vertex, and then runs a rewiring procedure on its neighbouring vertices. Any vertices that are rewired at this step are then added to the queue. This continues until no further improvements can be made. Finally, a new path from the tree root to the robot configuration q_{rob} is found by attempting to connect q_{rob} to neighbouring vertices.

B. *Dynamic path correction (global)*

The global re-planner provides an update to all solutions of the path planning layer. When the condition in (3) is met, the optimality criteria for the current action-motion sequence may no longer hold and a new action-motion sequence must be determined by updating the costs of all movement actions. The algorithm first updates every tree by invalidating infeasible vertices, updating orphaned vertices and cascading a series of rewiring, as in section IV-A. New optimal paths between landmarks are obtained by finding new connecting vertices between corresponding pairs of trees. The set of best paths Σ_{best} are then updated accordingly. A temporary landmark l_{temp} is then inserted into the TPP problem at q_{rob}. An attempt to find an optimal path from each original landmark to l_{temp} is made by testing connections from neighbouring vertices of each tree to the root of l_{temp}. Σ_{best} is then expanded to include these paths. Indeed the planner may not initially find a feasible path for each of these movement actions. However, this does not prevent the planner from obtaining a solution by making use of the anytime attributes of DA-TPP to find action-motion sequences despite certain actions possessing infinite costs.

V. EXPERIMENTAL EVALUATION

A. *Base planner evaluation*

The base planner is benchmarked across a number of randomly generated cluttered and structured environments. We assess the performance of these approaches in 50 × 50, 100 × 100 and 300 × 300 environments. Note that in these experiments the cost function *c* in (1) for a given configuration *q* is given by $c = 1/\delta^2$, where δ is the distance to the nearest obstacle. Thus *c* describes the 'closeness' of *q* to an obstacle.

We compare the performance of the DA-TPP base planner with a simple planner consisting of task and path planning in isolation (isolated TP) and UP2TA. The isolated TP consists of a task planner that solves for an optimal action sequence by using the Euclidean distances between landmarks as movement action costs. For consistency in comparison, a single instance of a bi-directional T-RRT* algorithm is called for each movement action to obtain the final action-motion sequence. Our implementation of the UP2TA framework employs the greedy search algorithm [6] to obtain approximate cost metrics for each possible movement action. For consistency, LPG-*td* is then used to solve the task planning problem. An additional path planning layer based on Theta* [13] is required to obtain true paths for each movement action like in isolated TP.

Based on the results in Fig. 3, one may observe that the UP2TA fails to consider cost spaces and consequently performs notably worse than other planners when considering total path cost for the same planning instances. In terms of scalability, planning time highlights a key deficit of grid-based approaches: as the size of the problem increases, its performance generally decreases rapidly, as observed for environments of size 300x300. In particular, grid-based algorithms may become 'trapped' in enclosed regions that forces the algorithm to search through a large number of useless nodes needlessly. Isolated TP scales far better with the size of the problem and maintains a low computational cost across all trials. However, this approach finds solutions with overall costs that are generally greater than the DA-TPP approach. This is an expected observation as the task planning layer is ill-informed by misleading action costs. Without knowing the geometric relationships of objects in the world, costly (or even infeasible) movement actions are unknown to the symbolic planner.

In contrast, the DA-TPP consistently finds the lowest cost plans in all test cases. Although this sacrifices computational efficiency, the proposed planner scales well with the size of the problem and indeed finds a solution faster than UP2TA in almost all cases for 300 × 300 environments. Finally, the quality of DA-TPP solutions may be further improved over time as a result of anytime planning, as discussed below.

B. Anytime evaluation

To analyse the anytime component of DA-TPP, the base planner was first run until an initial solution was obtained. Following the planner description in section III, the planner continues to run with η_a set to 0.03. Then, at defined time instances a new solution is requested from the planner. The corresponding overall cost of the task sequence at each of these time instances are shown in Fig. 4.

These planning results show improvements made to the overall solution at two levels. The observable decreasing 'step' behaviour corresponds to changes at the action sequence level. Here the planner identifies a new optimal task sequence that provides larger quality improvements as a result of higher quality paths being found for previously expensive actions. On the other hand, more minute improvements to the solution cost is attributed to local path quality improvements that do not alter the high-level task sequence. This observation provides support for the behaviour of the dynamic components of DA-TPP: small local changes to a path do not, in most cases, change the optimality of the task-level action sequence. Hence it is unnecessary to re-plan an entire action-motion sequence for small local path changes.

C. Dynamic anytime evaluation

Finally, the complete DA-TPP approach is assessed through simulations in the environment shown in Fig. 5, with obstacles not known a priori shown in blue. Unlike the experiment conducted for anytime evaluation, the robot begins executing a plan after an initial solution is obtained. Hence as actions are performed, new task plans become shorter and shorter until the robot finally executes all actions and return to base. We simulate real-time execution on the Gazebo simulator using a Husky mobile manipulator. Perception of the environment is achieved using a laser scanner with a range of 30 meters, while η_d is set to 0.05.

From Fig. 5, we note the following observations. Normally, the anytime planner without the dynamic component would force the robot to commit to the first action of a plan under all circumstances. However, the global re-planning unit allows the robot to follow a new optimal task sequence even part-way through a movement action if changes are detected. Secondly, the robot efficiently navigates past new obstacles and maintains global optimality by preserving previous knowledge in the path planning layer. This is not possible with the UP2TA, which would require planning from scratch in each instance.

The solutions of DA-TPP may be subject to local minima according to the limitations of the heuristic planner used in task planning. For example, LPG-*td* may provide *locally*-optimal task plans but is always able to return solutions quickly. Other planners such as Metric-FF can provide *globally*-optimal solutions at the expense of lower efficiency. Conversely, the path planning layer maintains the asymptotic optimality property of RRT* and thus always converges toward globally-optimal solutions if sufficient time is allowed.

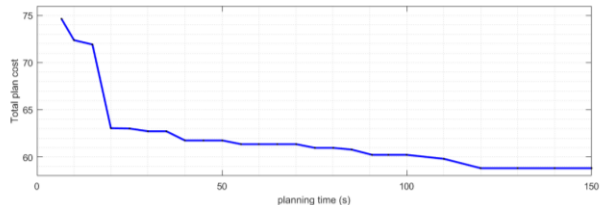

Figure 4. Anytime planning cost reductions

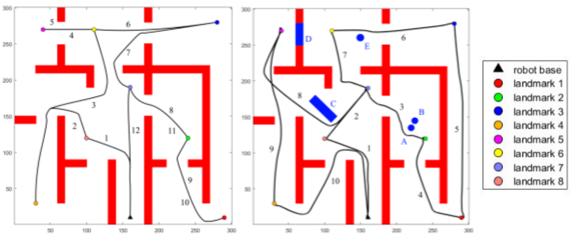

(a) (b)

Figure 5. DA-TPP dynamic replanning. (a) initial plan, (b) actual paths executed (unknown obstacles shown in blue)

ACKNOWLEDGMENT

This research is funded by the Engineering and Physical Sciences Research Council (EPSRC) under its Doctoral Training Partnership Programme (DTP 2016-2017 University of Strathclyde, Glasgow, UK).

REFERENCES

[1] A. Gasparetto, P. Boscariol, A. Lanzutti, and R. Vidoni, "Path planning and trajectory planning algorithms: A general overview," Springer, Cham, 2015, pp. 3–27.

[2] L. Pack Kaelbling and T. Lozano-Pérez, "Hierarchical task and motion planning in the now," in *2011 IEEE International Conference on Robotics and Automation*, 2011, pp. 1470–1477.

[3] C. R. Garrett, T. Lozano-Pérez, and L. P. Kaelbling, "FFRob: An efficient heuristic for task and motion planning," Springer, Cham, 2015, pp. 179–195.

[4] J. Ferrer-Mestres, G. Francès, and H. Geffner, "Combined task and motion planning as classical AI planning," Jun. 2017.

[5] N. T. Dantam, S. Chaudhuri, and L. E. Kavraki, "The Task-Motion Kit: An open source, general-purpose task and motion-planning framework," *IEEE Robot. Autom. Mag.*, vol. 25, no. 3, pp. 61–70, Sep. 2018.

[6] P. Muñoz, M. D. R-Moreno, and D. F. Barrero, "Unified framework for path-planning and task-planning for autonomous robots," *Rob. Auton. Syst.*, vol. 82, pp. 1–14, Aug. 2016.

[7] C. Wong, E. Yang, X.-T. Yan, and D. Gu, "Optimal path planning based on a multi-tree T-RRT* approach for robotic task planning in continuous cost spaces," in *12th France-Japan and 10th Europe-Asia Congress on Mechatronics*, 2018, pp. 242–247.

[8] D. McDermott, "The PDDL planning domain definition language," *AIPS-98 Plan. Compet. Comm.*, 1998.

[9] A. Gerevini, A. Gerevini, A. Saetti, I. Serina, and P. Toninelli, "LPG-TD: A fully automated planner for PDDL2.2 domains," *14th Int. Conf. Autom. Plan. Sched. Int. Plan. Compet.*, 2004.

[10] J. Org Hoomann, "The Metric-FF planning system: Translating 'ignoring delete lists' to numeric state variables," *J. Artiicial Intell. Res.*, vol. 20, pp. 291–341, 2003.

[11] D. Ferguson and A. Stentz, "Anytime RRTs," in *Proceedings of the 2006 IEEE/RSJ International Conference on Intelligent Robots and Systems*, 2006, pp. 5369–5375.

[12] M. Otte and E. Frazzoli, "RRT ^{X}: Asymptotically optimal single-query sampling-based motion planning with quick replanning," *Int. J. Rob. Res.*, vol. 35, no. 7, pp. 797–822, Jun. 2016.

[13] S. K. and A. F. K. Daniel, A. Nash, "Theta*: Any-angle path planning on grids," *J. Artif. Intell. Res.*, vol. 39, 2010.

An Information Theoretic Approach to Path Planning for Frontier Exploration

Callum Rhodes, Cunjia Liu and Wen-Hua Chen

Abstract— **Efficient path planning for autonomous robots to explore unknown areas is a critical area of research due to the requirements on mission times and problems that dictate as quick a solution as possible e.g. search and rescue scenarios. It also proves to be a difficult problem to solve due to its inherent NP-hard nature, which requires that an optimal (albeit not necessarily perfect) path is defined based on a set of defined principles. This gives rise to a wide variety of logical solutions. This paper proposes an information theoretic addition to the well-established Frontier Exploration in order to build a 2D spatial map of an area of interest as intelligently as possible. The informative method is then compared with a greedy approach toward information gain, as well as the traditional 'nearest frontier' approach to frontier exploration. The proposed method is shown to outperform other methods in terms of the total number of actions required to resolve the map, as well as being consistently the quickest method of reducing map entropy throughout the mapping procedure. We also discuss how, by exploiting an information theoretic framework, other quantities of interest can be mapped efficiently alongside a spatial map.**

I. Introduction

Autonomous exploration is an increasingly useful area of research as industry pushes for the autonomy of tasks perceived to be trivial or too dangerous for human undertaking. Environmental surveillance after dangerous incidents, such as that seen in the Fukushima nuclear power plant explosion, are a prime use case for autonomous exploration as the environment has become uncertain physically and is too dangerous for human intervention. In this scenario, the spatial mapping of the environment must be attained in cases where the localisation within the environment is unknown. Therefore, mapping and localisation must be performed simultaneously, commonly referred to as SLAM (Simultaneous Localisation and Mapping). However, trajectory planning must also be considered to reduce the uncertainty of the map, whether the map produced is spatial in nature or of another form (e.g. gas or radiation concentration mapping). An efficient trajectory is desirable as limitations may be imposed on the mission time or the number of actions capable of being performed by the robot. This paper seeks to explore the planning of the most efficient routes in typical spatial mapping missions.

For a robot to successfully and *efficiently* map an area autonomously, it must complete the *active SLAM* problem (coined by Leung et al. [1]). The SLAM portion of active SLAM is a vast area of research and there are many approaches to the issue which transcend the scope of work for this paper. The SLAM review by Cadena et al. [2] concludes that SLAM is *not* solved and therefore trying to address the path planning problem independently allows for evolving solutions to SLAM to not supersede work on the path planner. Therefore, we assume that the Localisation and Mapping are accurately handled by an appropriate SLAM algorithm and that the path planning portion can be dealt with independently of this (acknowledging that the performance of the path planner is entirely dependent on the SLAM algorithm). This assumption requires that the robot does not need to perform specific loop closure activities to provide high fidelity mapping. This is, however, dependent on the SLAM package used and the environment it is operating in, as shown in [3]. The independence assumption becomes insignificant as the performance of various SLAM packages improves.

Frontier Exploration, proposed by Yamauchi [4], has been chosen as the goal setting technique due to its simplistic nature and successful application within the exploratory mapping domain. Frontier Exploration functions by defining naive targets for a robot to navigate by stating that any unknown areas of a map that border free space are points of interest. Traditionally, Frontier Exploration simply chooses the closest frontier of a minimum size and plans an obstacle free trajectory to resolve said frontier. The process then eventually terminates when all frontiers have been resolved. While effective, this approach does not consider the possible information gain at the target and therefore may not choose the most efficient route. By considering information gain at points of interest, the path planner will make informed decisions on where to navigate and therefore provide an overall mapping trajectory that is more efficient than that of an uninformed technique.

Recent sampling-based path planning methods that have exploited information gain have not used a goal setting method such as frontier exploration. They have instead used a horizon based approach wherein the prediction is either a set number of steps ahead of the current state [5] (finite horizon) or is subject to a total budget constraint [6] (infinite horizon). Using Frontier Exploration allows the horizon consideration to be ignored and narrows the focus of the path planner to specific trajectories. This reduces the total number of path considerations, reducing the computational load at the expense of planned path generality.

II. Information Theory

A. *Definition of Information Gain*

Information Gain when trying to resolve a variable of interest can be defined as how variable uncertainty is reduced via an action or observation. Uncertainty is mathematically characterised by the term *Entropy*. For an occupancy grid, where the occupation probability of a cell P_{cell} is defined:

$$0 < P_{cell} < 1 \tag{1}$$

$$P_{cell} = 0 \quad \text{if free} \tag{2}$$

$$P_{cell} = 1 \quad \text{if occupied} \tag{3}$$

The entropy of a single cell H_{cell} is given by:

$$H_{cell} = -(P_{cell}\log(P_{cell}) + (1 - P_{cell})\log(1 - P_{cell})) \tag{4}$$

Due to the assumption that each cell's occupation probability is independent of each other cell [7], the total map entropy H_{map} can be defined as a simple summation of the entropy of the total number of cells, N, such that:

$$H_{map} = \sum_{i=1}^{N} H_{cell}(i) \tag{5}$$

The change in entropy between two states can be considered as the information gain over a step. When comparing multiple states to the same reference state, this provides a suitable measure of the information gain. However, the value returned is predicated on the reference state entropy and therefore cannot be used to compare the change in entropy over time. The relative entropy between consecutive distributions shows how different the two distributions are and therefore can be thought of as the relative information gain. The Kullback-Liebler divergence [8] is a method of calculating the relative information gain between two distributions. For calculating the information gain between the current map state (P_1) and a comparison map state (P_2) in this manner, the

$$D_{KL}(P_1||P_2) = -\sum_{i=1}^{N} P_1(i)\log\left(\frac{P_2(i)}{P_1(i)}\right) \tag{6}$$

following equation is used:

where i denotes the i-th cell, N is the total number of the cells and both map occupancy probability matrices are discrete probability distributions of the same probability space.

B. Predicting Information Gain

In order to predict the information gain at a point of interest using an occupancy grid, an inverse sensor model [9] can be employed which takes key parameters of the sensor that is being used by the robot (in this case a RPLIDAR A2 lidar scanner). The inverse sensor model casts rays in an occupancy grid at a given location as if the scanner were to be deployed at said location. It then returns any obstacle hits by the rays, based on the current occupancy status of the cells within range. If no obstacles are hit by the beam, then a blank distance reading is returned. The occupancy status of cells within range are then updated based of the parameters of the inverse model. In this case a hit cell is updated with probability 0.7 and any free cells along the path with 0.3.

If unreturned rays are ignored, then this gives the lower bound of the possible information gain at a location and is often unrealistic to the actual gain when the sensor is at the location of interest. If unreturned rays are treated as not hitting any obstacles and cells along the ray updated with the free probability until the maximum range of the sensor, then this gives the maximum possible information gain i.e. upper bound. Using the Information gain upper bound, whilst optimistic, is a better predictor of the information gain at a point and therefore is used for future map state estimation.

III. Path Planning

A. Frontier Exploration

A general issue in autonomous exploration is that of setting the next goal point for the robot to navigate towards. Frontier exploration sets bounds between free space and unknown space as targets using an edge detection method. In this study, the Canny edge detection method [10] is used to abstract frontiers from the occupancy grid. The midpoint of a frontier is generally used as a goal point [4] but this possibly ignores several viewpoints along the frontier which could yield more information. This becomes increasingly important with longer frontiers. Hence, an equal distribution of viewpoints along the frontier are selected at a set distance. This gives rise to a tunable parameter that is specific to the scale and resolution of the environment being mapped.

The minimum length of frontier is also specific to the environment and is required in order to avoid needlessly attempting to resolve frontiers which are insignificant or erroneous due to noise in the scanner or mapping procedure.

B. Path Selection

The path selection problem rises once all possible obstacle free trajectories to all frontier points have been established. Traditional frontier exploration simply states that the closest frontier point should be chosen however this does not take into account any information about the future state of the map at that point.

By employing the inverse sensor model at each of the frontier points and then using the Kullback-Liebler divergence between the current map state and the predicted map state, the information gain for each path is established. By selecting only the end point of the path to employ the sensor model, rather than predicting across the entire trajectory, computational time is reduced dramatically. Further, since the robot is moving across known free space to navigate towards the frontier, the information gain during traversal to the frontier is insignificant compared to the gain at the frontier itself.

It can be naively stated that the path which exhibits the most information gain should be selected, the Next Best View (NBV). This however does not take into account the cost involved in travelling to a frontier, which is important for scenarios which either have a limited endurance e.g. UAVs, or in a time-limited scenario e.g. search and rescue operations. Therefore, a tradeoff between the path length and the information gain must be established. Whilst this can be scaled depending on which variable is more desirable, a reward function that simply calculates the path with the largest information gain per metre travelled is used for testing purposes (NBV/m).

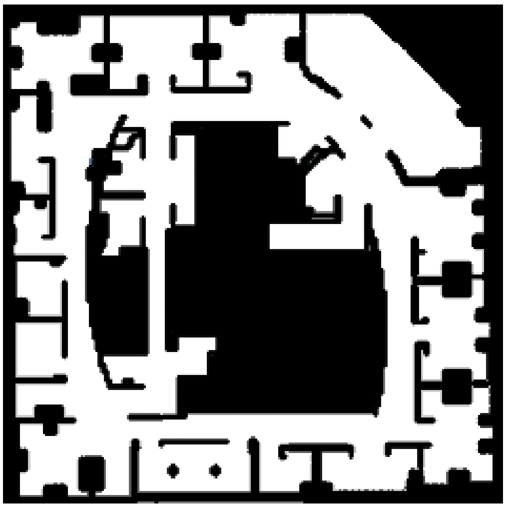

Figure 2. Intel research lab, Seattle.

$$T^* = \underset{T}{\operatorname{argmax}} \left(\frac{I_{UB}(T)}{T_{length}} \right) \qquad s.t. \quad T_{length} > r_{min} \qquad (7)$$

where T are the possible trajectories, $I_{UB}(T)$ is the upper bound information gain of a trajectory and r_{min} is a minimum radius around the robot as to avoid the robot getting stuck in local minima.

IV. Simulation Study

A. Simulation Setup

For simulating the performance of the information theoretic addition, the *Mobile Robotics Simulation Toolbox* available for *Matlab* is used with a LIDAR equipped robot. Perfect SLAM is assumed for simulation (mapping with known poses) and noise is added to the LIDAR scan readings to allow for anomalous readings in the map. The scenario used is the Intel research lab map which is often used for testing similar mapping and SLAM algorithms due to its high amount of clutter, making the mapping task more realistic and difficult than other simpler scenarios [11].

In order to test the algorithm within a full autonomous system, a simple probabilistic roadmap (PRM) is employed with a path following function that takes advantage of a differential drive system such as that seen on the Turtlebot.

For performance comparison, the 3 path selection strategies previously described (closest frontier, NBV \& NBV/m) are run under the same conditions. The rate of map entropy reduction as well as the final map entropy after 300s are logged and used as metrics to analyse the performance of each strategy. It should be noted that the simulation is set so that the robot is constantly performing actions and therefore, limiting the simulation time to 300s means that all 3 strategies will have performed the same number of movement actions.

B. Simulation Results

Figure 2 shows the Entropy of the map against time for all 3 strategies. The initial information gain for all 3 strategies is comparable as, regardless of the path chosen, the map is in a high state of uncertainty and therefore any action resolves the map significantly. As the robot moves through the environment, the difference in strategies becomes apparent as

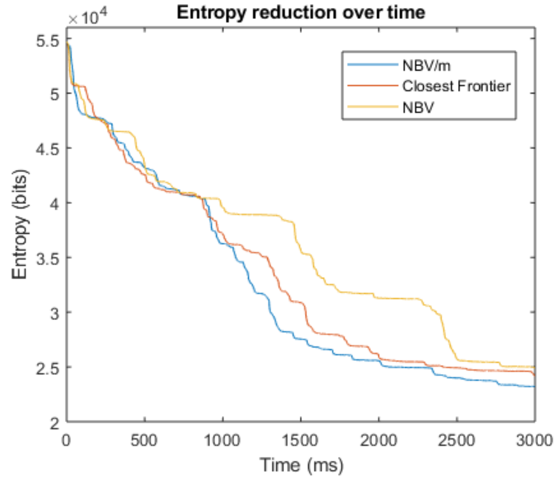

Figure 1. Entropy reduction over time for each path selection strategy.

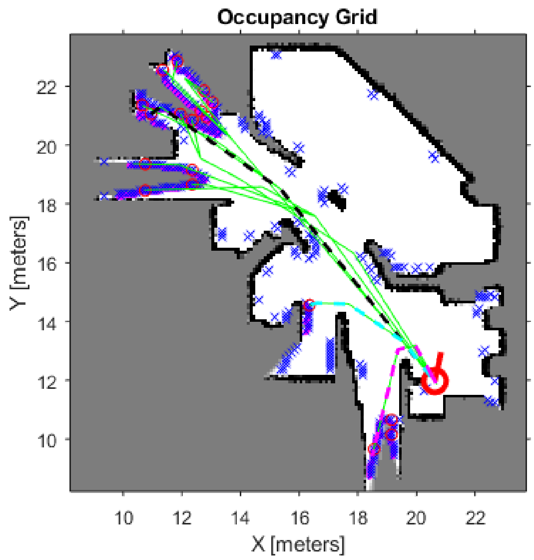

Figure 3. Comparison of path selection by NBV (black dash), NBV/m (magenta dash) and closest frontier (cyan dash) strategies. Frontier cells are represented by a blue X, frontier targets by a red O and all possible trajectories by green lines.

displayed in Figure 3. This snapshot is a prime case of the algorithm choosing the intuitively correct path. The proposed algorithm successfully ignores the closest frontier, as there is little to no information to be gained at this location and it is only deemed a frontier due to the noise in the LIDAR scanner not resolving the wall properly. It also does not greedily go to the frontier with the most information which would require a large traversal of the map. Instead, it chooses the frontier that will allow the robot to continue down the corridor thus optimising the future information gain the robot can achieve without prior knowledge of the rest of the map.

TABLE I
PERFORMANCE COMPARISON BETWEEN THE 3 STRATEGIES.

Strategy	Closest Frontier	NBV	NBV/m
Final Entropy (kbits)	24.31	24.94	23.22
Calls to function	50	27	34
Time to complete (s)	200	249	182

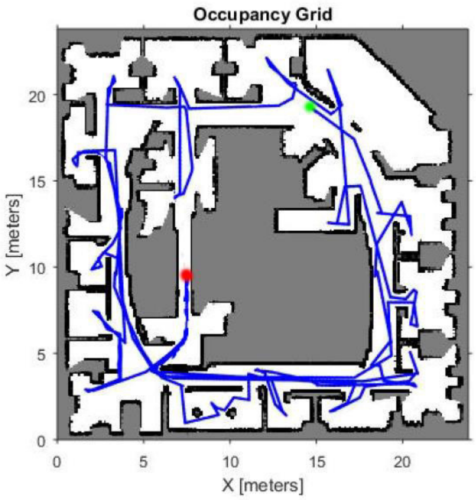

Figure 4. Completed occupancy map with total trajectory. Green dot indicates start point and red dot indicates end point.

As more of the map is resolved, Figure 2 shows that the greedy NBV approach becomes increasingly inefficient at reducing map entropy due to long traversals over areas of low uncertainty. However, the NBV/m and closest frontier approach remain relatively similar in their ability to reduce entropy, performing better than the NBV method due to their more efficient short path lengths. Where the performance of NBV/m becomes apparent is in the later stages of the mapping process where large areas of uncertainty are less common. In this instance, whereas the closest frontier approach may attempt to resolve very small frontiers (which add little information) purely because they are close by, the NBV/m algorithm intelligently deduces areas where uncertainty can still be significantly reduced despite the larger path cost.

Final mapping performance is seen when the relative entropy is reduced to a significantly low value, that the map can be deemed complete. For the intel map this was judged to have occurred when:

$$argmax\,(D_{KL}(T)) \leq 400bits \tag{8}$$

Table 1 shows the numerical performance of each strategy. Analysing the time taken to complete, NBV/m shows an improvement of 27% over the greedy approach and 9% improvement over the traditional approach. The final entropy value of the NBV/m approach is also lower, which accentuates the fact that it performs significantly better than the traditional approach in the latter stages of the mapping procedure.

Figure 4 shows the final occupancy grid created by the simulated robot in the NBV/m case and it is clear that all major structures of the environment have been adequately resolved, thus showing that the stopping criterion of 400 bits is suitable for the Intel Lab environment. The overall trajectory consisted of one anticlockwise loop of the main corridor followed by a second half loop to suitably resolve some of the smaller rooms that weren't resolved adequately during the first loop.

V. CONCLUSIONS AND DISCUSSION

The addition of an intelligent information theoretic path planner adds significant benefits to the traditional frontier exploration approach to autonomous exploration. The use of a greedy approach is proven to be disadvantageous compared to the traditional approach and provides evidence that efforts must be made so that the reward function takes into account the path cost effectively. In this regard, whilst the reward function presented provides better performance for a simulated SLAM mission of an office environment, it may not be optimal for all mapping scenarios and should be investigated further.

Using uncertainty as the primary consideration for path planning also adds flexibility to its application, as uncertainty is a universal metric when mapping any unknown quantity (such as temperature, gas concentration etc.). This means that not only spatial mapping can be planned efficiently using this technique but theoretically, given an appropriate sensor prediction model, any quantity that requires the reduction in its uncertainty can be used. Further to this, if multiple quantities are in the same information framework, they can be mapped simultaneously with weightings on whichever quantity is of greater interest to the mission.

REFERENCES

[1] C. Leung, S. Huang, and G. Dissanayake, “Active SLAM using model predictive control and attractor based exploration,” IEEE International Conference on Intelligent Robots and Systems (IROS), pp. 5026–5031, 2006.
[2] C. Cadena, L. Carlone, H. Carrillo, Y. Latif, D. Scaramuzza, J. Neira, I. Reid, and J. J. Leonard, “Past, present, and future of simultaneous localization and mapping: Toward the robust-perception age,” IEEE Transactions on Robotics, vol. 32, no. 6, pp. 1309–1332, 2016.
[3] W. Hess, D. Kohler, H. Rapp, and D. Andor, “Real-time loop closure in 2D LIDAR SLAM,” Proceedings - IEEE International Conference on Robotics and Automation, vol. 2016-June, pp. 1271–1278, 2016.
[4] B. Yamauchi, “A Frontier Based Approach for Autonomous Exploration,” Proceedings of IEEE CIRA, pp. 146–151, 1997.
[5] S. S. Geoffrey Hollinger, “Proofs and Experiments in Scalable, Near-Optimal Search by Multiple Robots,” Proceedings of Robotics: Science and Systems IV, pp. 206–213, 2008.
[6] G. A. Hollinger and G. S. Sukhatme, “Sampling-based robotic information gathering algorithms,” International Journal of Robotics Research, vol. 33, no. 9, pp. 1271–1287, 2014.
[7] S. Thrun, “Learning occupancy grids with forward models,” Proceedings 2001 IEEE/RSJ International Conference on Intelligent Robots and Systems. Expanding the Societal Role of Robotics in the the Next Millennium (Cat. No.01CH37180), vol. 3, pp. 1676–1681, 2015.
[8] S. Kullback and R. A. Leibler, “On information and sufficiency,” The annals of mathematical statistics, vol. 22, no. 1, pp. 79–86, 1951.
[9] A. Elfes, “Sonar-Based Real-World Mapping and Navigation,” IEEE Journal on Robotics and Automation, vol. 3, no. 3, pp. 249–265, 1987.
[10] J. Canny, “A Computational Approach To Edge Detection,” IEEE Transactions on Pattern Analysis and Machine Intelligence, vol. 8, no. 6, pp. 679–714, 1986.
[11] S. Owald, M. Bennewitz, W. Burgard, and C. Stachniss, “Speeding-up robot exploration by exploiting background information,” IEEE Robotics and Automation Letters, vol. 1, no. 2, pp. 716–723, July 2016.

Underwater Scene Segmentation by Deep Neural Network

Yang Zhou, Jiangtao Wang, Baihua Li, Qinggang Meng, Emanuele Rocco and Andrea Saiani

Abstract— **A deep neural network architecture is proposed in this paper for underwater scene semantic segmentation. The architecture consists of encoder and decoder networks. Pre-trained VGG-16 network is used as a feature extractor, while the decoder learns to expand the lower resolution feature maps. The network applies max un-pooling operator to avoid large number of learnable parameters, and, in order to make use of the feature maps in encoder network, it concatenates the feature maps with decoder and encoder for lower resolution feature maps. Our architecture shows capabilities of faster convergence and better accuracy. To get a clear view of underwater scene, an underwater enhancement neural network architecture is described in this paper and applied for training. It speeds up the training process and convergence rate in training.**

I. Introduction

The scene understanding of the underwater environment is an appealing topic among marine researchers and the public too, as underwater and especially undersea domains highly capture its attention. Many applications benefit from underwater scene information such as seafloor survey and marine object detection[1]. Conventional methods for underwater scene understanding fall into multi-sensor data fusion. Castellani et al.[2] proposed to reconstruct 3D underwater environment with the aid of multiple acoustic views given by underwater acoustic sensors, but the trade-off between speed and accuracy limits this method for the real-time use. Moroni et al[1] instead proposed to use both acoustic and stereo camera sensors, but the additional data fusion process for mapping has to be carefully considered. Moreover, it could be difficult to calibrate a stereo camera in underwater environment because the refractive effects lead to non-linear distortion effects that depend on the seawater density and incidence light rate. Furthermore, depth image only cannot provide the straightforward information for object recognition task in the current camera view. To achieve the object recognition task without considering depth information, an alternative approach is to use image semantic segmentation based on monocular camera.

Image semantic segmentation is one of the key fields in computer vision, to which deep learning has been giving many contributions during the past three years[3]. It is successfully used for indoor scene segmentation and outdoor scene segmentation[4]. The development of semantic segmentation benefits an increasing number of applications including autonomous driving, human-computer interaction and augmented reality, to name a few[3]. Compared with conventional semantic segmentation methods such as Markov Random Field (MRF), Conditional Random Field (CFR)[5] and SVM [6] as classifiers, deep neural network can achieve higher accuracy with the ability of learning from high level representations Moreover, deep neural networks enable end-to-end image semantic segmentation with simpler procedures.

Autoencoder is a popular network structure for image semantic segmentation in deep neural network application field [3]. The encoder part is a convolutional neural network (CNN) for generating the feature maps by applying pooling operator. On the other hand, the decoder network is a reverse convolutional neural network based on the un-pooling operator.

As in the successful cases of image semantic segmentation on indoor scene and road scene applications[4], our work focuses on end-to-end underwater scene semantic segmentation by using deep neural network with monocular camera only. In this paper, a network structure is proposed for underwater scene segmentation, which can be used for real-time inference. The neural network architecture proposed in this paper enhances the generalization ability compared with using SegNet[4] when applying to real-time videos and needs less memory during training process compared with U-Net[7]. The underwater data used in this paper are collected by Witted Srl, Italy.

Furthermore, considering the color distortion and underwater optical effects on underwater images, we apply Generative Adversarial Network (GAN) for underwater image enhancement to transform the original bluish images into surface-like ones. This approach aids to speed up the training process as it highlights the boundaries of the objects.

This paper is organized as follow. Sec. 2 describes the deep neural network structure we proposed. Sec. 3 illustrates the experiment of training on underwater images and comparisons with other network architectures. To get a better view of underwater environment for training, Sec. 4 shows the methods we used for underwater image enhancement. Finally, we conclude in Sec. 5.

II. Underwater Scene Understanding

Fully Convolutional Network (FCN) [8] was the first work for pixel-wise semantic segmentation enabled by deep neural network. Instead of using decoder process, FCN applied *backwards convolution* (known as *deconvolution*) to connect coarse output with dense pixels [8]. U-Net [7] introduced instead the decoder network to expand the feature maps for medical image segmentation, adopting the idea of

Yang Zhou is with Loughborough University, Loughborough, The United Kingdom, LE11 3TU (e-mail: Y.Zhou5@lboro.ac.uk).
Jiangtao Wang is with Loughborough University, Loughborough, The United Kingdom, LE11 3TU (e-mail: J.Wang4-18@student.lboro.ac.uk).
Baihua Li is with Loughborough University, Loughborough, The United Kingdom, LE11 3TU (e-mail: B.Li@lboro.ac.uk).
Qinggang Meng is with Loughborough University, Loughborough, The United Kingdom, LE11 3TU (e-mail: Q.Meng@lboro.ac.uk).
Emanuele Rocco is with Witted Srl, Piazza Manifattura, 1 38068 Rovereto (Tn) Italy (e-mail: emanuele@witted.it).
Andrea Saiani is with Witted Srl, Piazza Manifattura, 1 38068 Rovereto (Tn) Italy (e-mail: andrea@witted.it).

concatenating the feature maps from encoder to decoder. However, the number of parameters in the deconvolution operator and of gradients in the back propagation, both generated by the feature map concatenation, slows down the training process. To reduce the number of parameters, SegNet [4] applies a new up-sampling method without learnable filters when expanding the feature maps, and removes the concatenation to reduce the gradients to be calculated during the back propagation.

A. Network architecture

Typical neural networks for classification task such as LeNet [9] and AlexNet [10] take fixed-sized inputs because of the requirement of the fully-connected layers. However, both U-Net [7] and SegNet [4] remove these layers so that the input can be of any size. To this extent, the architecture we propose for underwater scene segmentation removes the fully-connected layers and consist of an encoder network followed by a decoder network. This architecture is showed in figure 1.

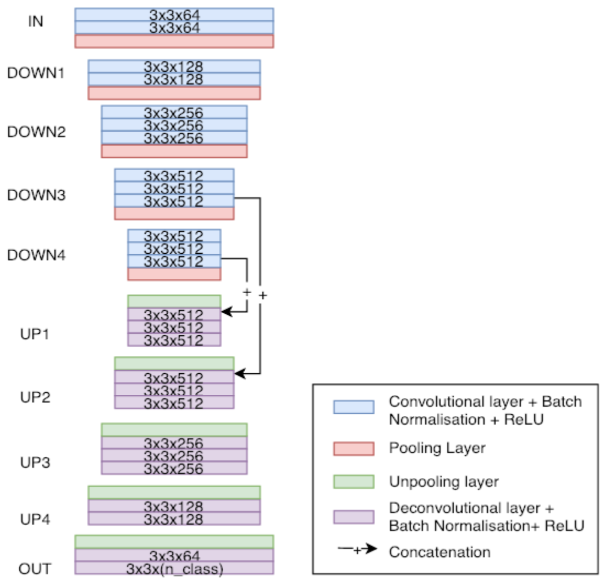

Network architecture for underwater scene segmentation.

Our encoder network includes 13 convolutional layers from VGG-16 [11], pre-trained on the ImageNet dataset, where each layer is followed by a batch normalization layer[12] and a ReLU layer [13] to speed up the training process. These layers are grouped in 5 blocks, each ending with a max-pooling layer to reduce the size of feature maps. The decoder network is the mirror reverse structure of our encoder network, being made of 5 blocks each with one un-pooling layer followed by deconvolutional layers.

B. Un-pooling layer

Current research [4][3] has shown that, instead of using learnable filters with large number of learnable parameters, un-pooling operators without learnable parameters can achieve similar performances. Our architecture follows this approach, and, it applies the max un-pooling method which records the max value indices of the pooling layers to the decoder network. The corresponding un-pooling layers use these indices to define the output position for their inputs, while leaving zero to the undefined positions. With this approach, the architecture keeps the spatial information of the feature maps.

C. Concatenation

As from U-Net [7], in our architecture shown in Figure 1, we use the concatenation operator to transfer the feature map from the encoder to the decoder network. Furthermore, to reduce the size of the needed memory during training, we keep such concatenations for final two blocks of the encoder network, responsible for generating the dense feature maps.

Concatenation helps preserves the information learned from encoder, and lets the decoder directly learn from the feature maps. For deep neural network, the concatenation operator also alleviates the gradient vanishing problem [14].

III. Experiment

We use PyTorch to implement our architecture. The training dataset were selected from the frames of two underwater videos recorded by Witted Srl; 70 images were manually labeled with 4 categories: seagrass, rocks, sand and seawater. The images were at 1920×1080 resolution, resized at 640×360 for training to reduce the number of parameters. Over the training dataset, the numbers of pixels in each category are as follow: seagrass of 6.5M, rocks of 53.2M, sand of 22.2M and seawater of 63M. As the seagrass and sand mostly appear in the central of the view, we use augmentation methods to increase pixels numbers for sand and seagrass and the dataset size. After augmentation, the number of training data increases to 140 images by randomly rotating, and cropping. As for testing, we applied the model to those two raw underwater videos which include the 70 frames for training. These two raw underwater videos consist of thousands of frames, but some of the frames are new to the model.

During training, to increase speed, we do not alter the pre-trained weights of the VGG-16 pretrained model used as a feature extractor and we initialize the decoder parameters as describe in [14]. The network is trained by stochastic gradient descent (SGD) algorithm with learning rate as 0.01 and momentum as 0.9. The learning rate schedule is based on step decay with 0.1 decay rate for every 100 epochs.

To make full use of dataset, we use cross-validation methods to train the model: the whole dataset of 140 images are divided into 28 segments by batch size as 5. Then, only 1 segment is selected as validation data while another 27 segments are used for training. Each epoch, the validation segment is sequentially selected to statistically balance the whole dataset. That means every segment has the same probability to be elected as validation segment. As the task for semantic segmentation is a classification problem, each pixel in label image is a one-hot vector and cross-entropy loss is chosen. We calculate the overall accuracy as the number of correctly predicted pixels over the total pixel number for each epoch.

Table I illustrates the loss and overall accuracy on training images during training process and shows that our network makes the training process convergent faster than U-Net and SegNet. The training results show also that our network outperforms U-Net with a large gap of loss and accuracy and is slightly better than SegNet

TABLE I. TRAINING PROCESS

Network	Training (%)					
	100 epochs		*200 epochs*		*300 epochs*	
	Loss	*Acc*[a]	*Loss*	*Acc*	*Loss*	*Acc*
U-Net	0.215	0.930	0.080	0.971	0.078	0.972
SegNet	0.116	0.957	0.055	0.979	0.053	0.980
Ours	**0.100**	**0.961**	**0.045**	**0.983**	**0.036**	**0.986**

a. Training accuracy (%)

For validation process, we used the metrics of mean accuracy and mean intersection over union (mIoU). The mean accuracy is the mean of predictive accuracy over all classes in the dataset which is slightly different from overall accuracy because it considers the balance among the accuracies between different classes. Mean intersection over union (mIoU) is the metric used in [15] and penalizes the fault predictions. Table II presents the results of validation after 300 training epochs. It shows that our network outperforms U-Net and is slightly better than SegNet too. However, for memory use, SegNet is more efficient than ours when training, as the concatenation operators of our network require more memory during back-propagation, although our network shares the same number of trainable parameters with SegNet.

TABLE II. VALIDATION PROCESS

Network	Validation				
	Parameters	*Memory used*	*Accuracy (%)*	*Mean Accuracy (%)*	*mIoU (%)*
U-Net	16.08M	8G	0.976	0.718	0.670
SegNet	**14.7M**	**4G**	0.985	0.742	0.705
Ours	**14.7M**	7G	**0.994**	**0.744**	**0.707**

Figure 2 shows the example results predicted from these three networks. It shows that the three networks all work well with on the dataset.

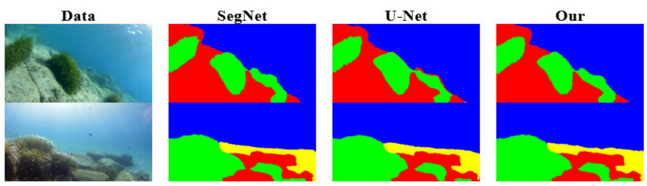

Predictions on different network architectures

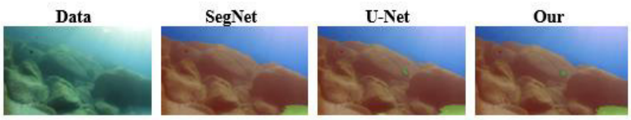

Real-time video frame testing

For real-time video testing, our model can achieve nearly 25 frames per second, which is close to the standard real-time frame rate. The results are shown in figure 3, our work and U-Net have a better generalization ability to recognizing unseen scenes on new videos than SegNet[4]. E.g. The seagrass in the centre can be recognized by U-Net and our architecture. This improved performance is given by the concatenation operation in U-Net and in the last two blocks in encoder network of our architecture.

IV. UNDERWATER IMAGE ENHANCEMENT

The undersea images are of a blue green tinge, mostly blurry and unclear because of the light absorption in water and diffusion due to suspended particles [16]. Moreover, the color distortion and blur effects change during seasons. In this situation, the visual model trained with raw images may not perform well. Hence, we consider an image enhancement process to standardize all images in a clear view.

The algorithms for underwater image enhancement can be classified into two categories: physics-based technique and deep learning technique. For example, the work of Luz [16] applies an energy minimization formulation using a Markov Random Field. Deep learning models instead, such as WaterGAN [17], UGAN and UGAN-P [18] used Generative Adversarial Network (GAN) to enhance the underwater images.

A. *Method*

We use GAN architecture as well, which consists of a generator network and a discriminator network. The U-Net structure is used for the generator network and it is responsible for learning the image style by matching blurry images to clear ones. The discriminator network uses instead the same module described in PatchGAN [19] with four convolution layers and calculates the loss from enhanced images and clear images. During inference, the generator network predicts clear images from blurry images as input.

B. *Dataset*

The training of the enhancing GAN requires training data of paired clear and unclear images. Such pairs are collected by using clear images from ImageNet [20] and using unclear synthetic images generated by the UGAN of [18] from the clear ones.

C. *Result*

Underwater image enhancement result (left column shows original images, righ column shows enhanced iamges)

After training, the enhancing GAN architecture is verified with our underwater image dataset. A sample result is showed in figure 4, where the left image shows the original frame before processing, while the right column shows the enhanced one. Not only the enhanced image is not bluish anymore, but also the scene details like edges of stone, sand and sea grass are better defined. However, the color of sand and stones in enhanced image is more yellowish.

D. *Segmentation experiment with enhanced images*

To verify if the image enhancing method helps the training process of our scene segmentation architecture, we separately train our network with two datasets: one model with the original underwater images; the second one with the enhanced ones. Figure 5 shows sample results from such dual training processes, while the recorded loss and overall accuracy are showed in Table III. The model trained on the enhanced image dataset is more accurate at 100 epochs than the original one with a faster convergence rate.

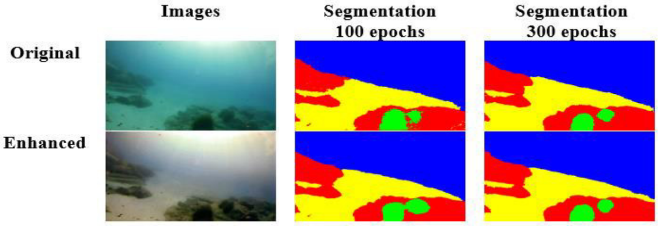

Compared image segmentation result with enhanced iamges

TABLE III. ENHANCEMENT

• Dataset	• Training (%)					
	50 epochs		*100 epochs*		*200 epochs*	
	Loss	***Acc*** [a]	***Loss***	***Acc***	***Loss***	***Acc***
Original	0.211	0.925	0.148	0.929	**0.041**	**0.984**
Dehazed	**0.185**	**0.932**	**0.064**	**0.976**	0.043	**0.984**

a. Training accuracy (%)

In conclusion, GAN architecture shows potentials for underwater image enhancement from blurred saturation, recovering the images into ground-like images and helping to convergence of the segmentation training process.

V. CONCLUSION

This paper shows deep neural networks can be effective for underwater semantic segmentation and underwater image enhancement. Our proposed segmentation network achieves better performances according to different metrics than U-Net [7] and is slightly better than SegNet [4] too. The tested GAN architecture for image enhancement is showed to help the training convergence rate of our segmentation architecture. In future our segmentation method could be extended to used jointly with depth information for further underwater vision tasks.

ACKNOWLEDGMENT

The authors are grateful to the EPSRC Centre for Doctoral Training in Embedded Intelligence under grant reference EP/L014998/1 for financial support sponsored by Witted Srl, Italy.

REFERENCES

[1] D. Moroni, M. A. Pascali, M. Reggiannini, and O. Salvetti, “Underwater scene understanding by optical and acoustic data integration,” in *Proceedings of Meetings on Acoustics*, 2013, vol. 17, no. 1, p. 070085.

[2] U. Castellani, A. Fusiello, and V. Murino, “Registration of multiple acoustic range views for underwater scene reconstruction,” *Comput. Vis. Image Underst.*, vol. 87, no. 1–3, pp. 78–89, 2002.

[3] A. Garcia-Garcia, S. Orts-Escolano, S. Oprea, V. Villena-Martinez, and J. Garcia-Rodriguez, “A Review on Deep Learning Techniques Applied to Semantic Segmentation,” 2017.

[4] V. Badrinarayanan, A. Kendall, and R. Cipolla, “SegNet: A Deep Convolutional Encoder-Decoder Architecture for Image Segmentation,” *IEEE Trans. Pattern Anal. Mach. Intell.*, vol. 39, no. 12, pp. 2481–2495, 2017.

[5] H. Zhu, F. Meng, J. Cai, and S. Lu, “Beyond pixels: A comprehensive survey from bottom-up to semantic image segmentation and cosegmentation,” *Journal of Visual Communication and Image Representation*, vol. 34. Academic Press, pp. 12–27, 01-Jan-2016.

[6] M. Thoma, “A Survey of Semantic Segmentation,” 2016.

[7] O. Ronneberger, P. Fischer, and T. Brox, “U-net: Convolutional networks for biomedical image segmentation,” in *Lecture Notes in Computer Science (including subseries Lecture Notes in Artificial Intelligence and Lecture Notes in Bioinformatics)*, 2015, vol. 9351, pp. 234–241.

[8] J. Long, E. Shelhamer, and T. Darrell, “Fully Convolutional Networks for Semantic Segmentation,” *IEEE Conf. Comput. Vis. Pattern Recognit.*, pp. 3431–3440, 2015.

[9] Y. Le Cun *et al.*, “Handwritten Digit Recognition with a Back-Propagation Network,” *Dermatologic SurgeryAdvances Neural Inf. Process. Syst. 2 (NIPS 1989)*, 1990.

[10] A. Krizhevsky, I. Sutskever, and G. E. Hinton, “ImageNet Classification with Deep Convolutional Neural Networks Alex,” *Proceeding NIPS’12 Proc. 25th Int. Conf. Neural Inf. Process. Syst.*, vol. 1, pp. 1097–1105, 2012.

[11] K. Simonyan and A. Zisserman, “VERY DEEP CONVOLUTIONAL NETWORKS FOR LARGE-SCALE IMAGE RECOGNITION,” *CORR*, 2014.

[12] S. Ioffe and C. Szegedy, “Batch Normalization: Accelerating Deep Network Training by Reducing Internal Covariate Shift,” *Proc. 32nd Int. Conf. Mach. Learn.*, vol. 37, 2015.

[13] X. Glorot, A. Bordes, and Y. Bengio, “Deep Sparse Rectifier Neural Network,” *Proc. 14th Int. Con- ference Artif. Intell. Stat.*, vol. 15, 2011.

[14] K. He, X. Zhang, S. Ren, and J. Sun, “Deep Residual Learning for Image Recognition,” *IEEE Conf. Comput. Vis. Pattern Recognit.*, pp. 770–778, 2016.

[15] M. Everingham, S. M. A. Eslami, L. Van Gool, C. K. I. Williams, J. Winn, and A. Zisserman, “The Pascal Visual Object Classes Challenge – a Retrospective,” *Int. J. Comput. Vis.*, vol. 111, no. 1, pp. 98–136, 2015.

[16] L. A. Torres-Méndez and G. Dudek, “Color Correction of Underwater Images for Aquatic Robot Inspection,” in *Energy Minimization Methods in Computer Vision and Pattern Recognition*, 2005, pp. 60–73.

[17] J. Li, K. A. Skinner, R. M. Eustice, and M. Johnson-Roberson, “WaterGAN: Unsupervised Generative Network to Enable Real-time Color Correction of Monocular Underwater Images,” 2017.

[18] C. Fabbri, M. J. Islam, and J. Sattar, “Enhancing Underwater Imagery using Generative Adversarial Networks,” 2018.

[19] A. Radhakrishnan, C. Durham, A. Soylemezoglu, and C. Uhler, “Patchnet: Interpretable Neural Networks for Image Classification,” 2017.

[20] D. Jia, D. Wei, S. Richard, L. Li-Jia, L. Kai, and F.-F. Li, “ImageNet: A large-scale hierarchical image database,” *2009 IEEE Conference on Computer Vision and Pattern Recognition*. IEEE, Jun-2009.

Exploiting System Capacity with a Distributed Routing Strategy for UAVs*

W. Bonnell, *Member, UKRAS*

Abstract — **This paper presents a routing strategy for UAVs that can be applied in conjunction with lower level navigation and collision avoidance methods. The strategy presented draws inspiration from traditional road vehicle routing where some cars are directed down less busy routes even if it results in a longer path. Our strategy will allow individual UAVs to route themselves in 2D space in order to avoid areas of high-density traffic.**

The proposed approach is then explored in simulation. Details of the simulation set-up are provided. The results demonstrate that the traffic is safer when the routing strategy is used compared with just a simple collision avoidance method.

I. Introduction

This paper demonstrates that by implementing higher level routing on top of simple navigation algorithms, it is possible to ensure Unmanned Aerial Vehicles (UAVs) more fully exploit the airspace capacity, providing system-wide benefits. Here we investigate the BeeJamA routing algorithm [1], previously applied to road traffic networks, represented as graphs where intersections are nodes and roads between them are links. At each node, cars score neighbouring nodes according to a weighted sum of their distance from the intended destination and a penalty related to traffic congestion. Simulations showed that by proceeding to the node with the lowest score, cars achieve higher levels of stable throughput than by other routing methods.

In contrast to cars, UAVs have a greater degree of freedom in their maneuverability. Although they can fly in three dimensions, the airspace in which they operate may be restricted to a 2D plane or several such layers. This is due to 1. restrictions on how close UAVs can fly to traditional airspace, 2. that some minimum vertical separation is required between UAVs and 3. that UAVs will have some minimum operating altitude. Therefore, building on the idea of using routing as a means to exploit system capacity, this paper explores using the BeeJamA algorithm to route UAVs through a 2D airspace.

Navigation through 2D spaces is a well studied problem and a number of methods have been developed for large multi-agent systems that may be applicable to UAVs. Examples include those based on the Social Force Model (SFM) [2] or using Reciprocal Velocity Obstacles (RVO) [3]. These paradigms incorporate robust collision avoidance. However, collision avoidance becomes more computationally expensive and/or less effective/efficient when agents are densely packed. For example, depending on the set-up of an RVO-based navigation strategy, the entire system can become gridlocked if agents are too close, see [3].

The routing strategy presented in this paper is intended to be implemented in conjunction with a navigation method, such as SFM or RVO, in order to ensure that extreme traffic densities do not arise. While these scenarios may seem unlikely to happen due to the inherent extra capacity afforded by relatively unrestricted 2D airspace, there are some obvious bottlenecks such as landing zones. It is also likely that in the near future there will be a significant increase in the density of UAV traffic, especially in and around large population centers. According to the Single European Sky ATM Research Programme (SESAR) in 2016 [4], there were an estimated 1–1.5 million leisure drones and 10,000 commercial drones in use in Europe. These numbers are expected to rise to near 7 million and 400,000 respectively by 2050, exacerbating existing pinch points.

A further problem with the roll-out of UAVs is the lack of an appropriate air traffic management infrastructure. Thus, distributed traffic management strategies are desirable. The routing method presented here is therefore implemented so that each UAV generates its route dynamically based on the environment. This way UAVs can be flown autonomously without the expense of developing bespoke communication and control infrastructure.

The rest of this paper is divided in to three sections. Section II will provide details on how the routing method is implemented along with some details of the underlying navigation mechanisms. Section III will then describe how this method has been implemented in simulation. Section IV will present the results from a representative traffic scenario for a variety of simulation parameters. Finally, Section V will provide some concluding remarks, including possible future work based on this paper.

II. Methods

While the main contribution of this paper is the routing method described below, this section will begin with a brief overview of the underlying navigation and collision avoidance

*This work was supported by an EPSRC grant EP/R0047571 and by Thales SA.

W. Bonnell is with the University of Bristol, Bristol, BS8 1QU, UK (phone: +44117 985 8759; e-mail: Wb17716@bristol.ac.uk).

scheme. The UAVs move using a method inspired by the SFM, comprised of two parts. The first part causes the UAV to move toward its goal, with an acceleration toward the goal that is proportional to the deviation away from a desired velocity in the direction of the goal. The second part is the collision avoidance. When a UAV comes within a certain range of another UAV or is on a collision course within a given time window, then the two UAVs will accelerate away from one another with a magnitude that is inversely proportional to their separation. These two component accelerations are then combined in such a way as to ensure that the UAV does not exceed a maximum acceleration (a physical bound).

The routing developed for this paper was inspired by [1]. The BeeJamA algorithm uses a graph representation of the road network to decide on which node, i.e. intersection, to move to next. In order to extend this to a 2D space, the UAV will generate candidate intermediary goals that we call waypoints, and then choose one to travel toward. This enables the routing method to be layered on top of any individual navigation regime as each waypoint becomes the goal of that particular section of the overall journey. Also, as each UAV generates and ranks its own waypoints, this allows the UAV to operate without centralised control.

The routing method works by first generating a set number of candidate waypoints at a distance R_{wp} away from the UAV, i.e. all the waypoints are on a circle of radius R_{wp}, see Fig. 1. Each candidate waypoint, c, is then assigned a dimensionless score Q_c according to

$$Q_c = N_c + (R_{cg} - R_{UAVg})\,\gamma, \tag{1}$$

where N_c is the number of other UAVs within a distance R_c of the candidate waypoint, R_{cg} and R_{UAVg} are the distances from the candidate waypoint and the UAV to the end goal respectively, and γ is a parameter with units m^{-1}. All distances in (1) have units m. The candidate with the smallest score Q_c

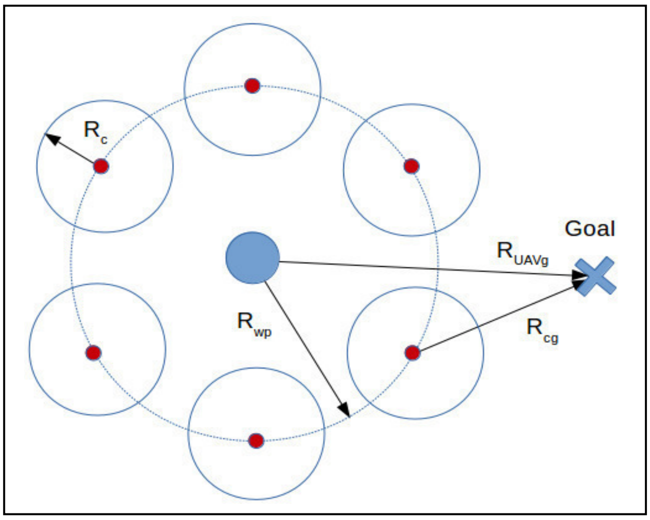

Figure 1. Shows a UAV (blue circle), candidate waypoints (red circle) and the UAV's goal. The radius at which candidate waypoints are generated R_{wp}, the radius out to which the candidate waypoints count other UAVs R_c, the distance from the UAV to its goal R_{uavg} and the distance from a particular candidate waypoint to the goal R_{cg}.

is then chosen as the next waypoint to move toward. Once the UAV reaches that waypoint it then generates new candidate waypoints and chooses again. Also, if the end goal is within R_{wp} of the UAV then it is also added to the list of candidate waypoints.

The waypoint that has the least traffic in its local vicinity and is closest to the end goal is therefore chosen according to (1). The parameter γ can be used to decide which of these two factors is more important. A UAV with a high γ will prioritise heading toward their end goal while a UAV with a small γ will prioritise avoiding areas with lots of other UAVs present. For this paper, γ is the same for all UAVs throughout a simulation run, but this assumption could be relaxed in future work.

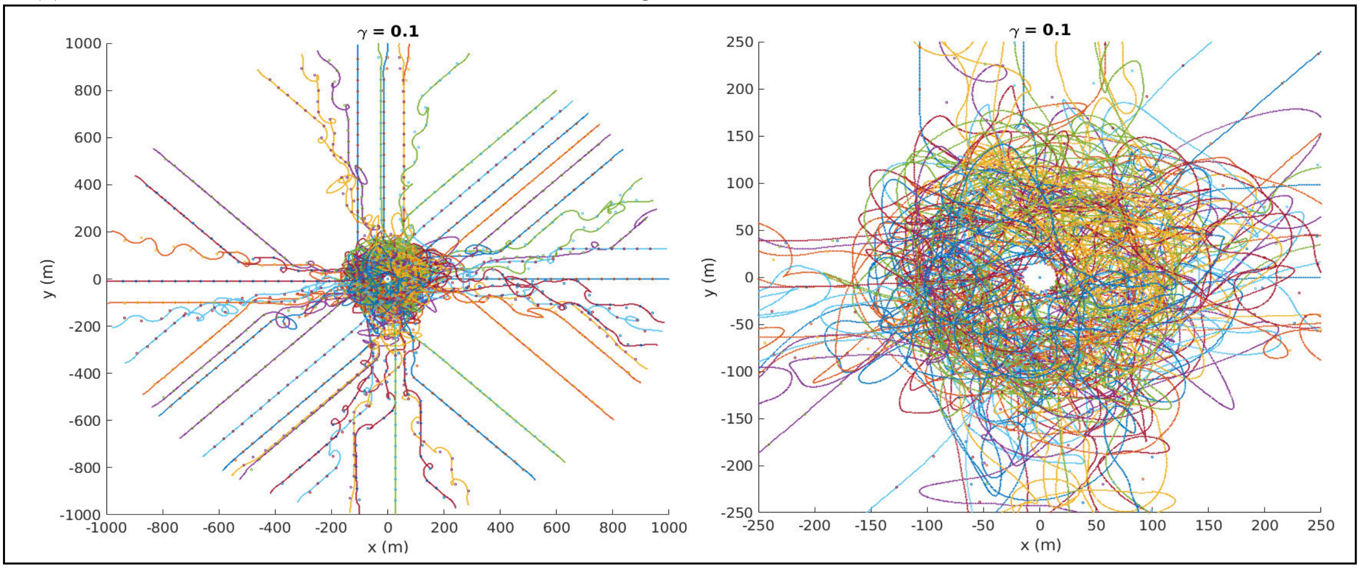

Figure 2. An example simulation run for 50 UAVs where γ is 0.1m^{-1}. Each line is the trajectory taken by a UAV and each point is a waypoint. On the right is a zoomed in view.

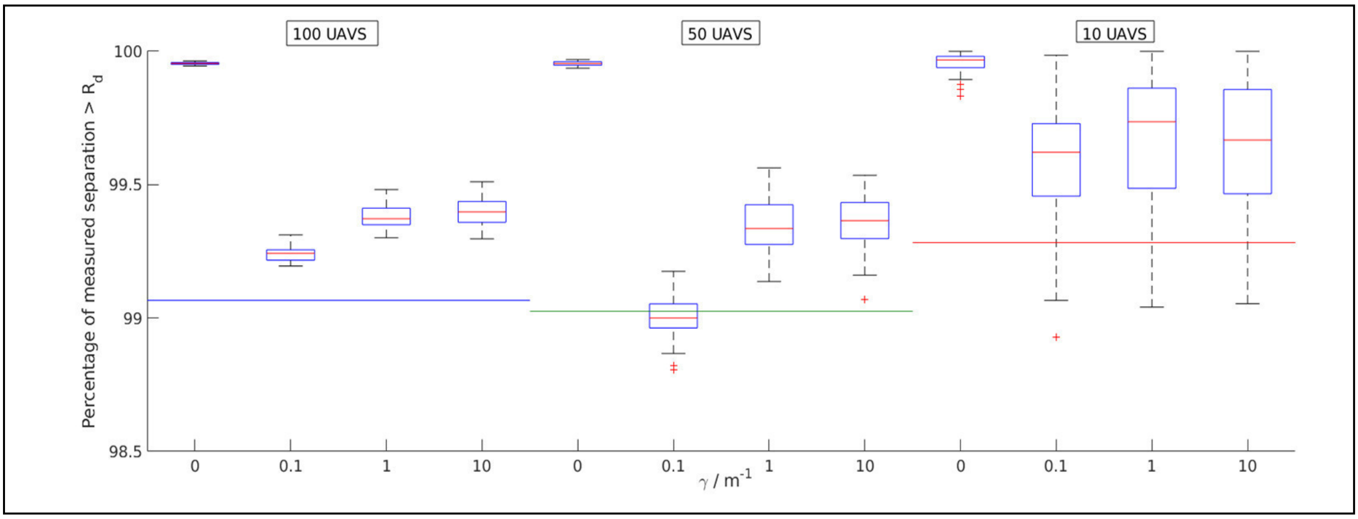

Figure 3. The percentage of UAV displacements that are greater than or equal to R_d for different values of γ and numbers of UAVs. The solid lines show the average percentage for that number of UAVs when there is no routing. The red line in each box shows the mean value.

III. Simulation Procedure

This section provides details about the simulation. In order to ensure that the routing method was tested in a scenario with high traffic density, all the UAVs share an end goal in the center of the simulation. Thus, the scenario is an approximation of a depot or similar landing area that all the UAVs are converging on.

The number of UAVs is set before the simulation starts and all UAVs are instantiated at the first time step at random points along the circumference of a circle with radius 1000m. Each UAV's starting velocity is 20ms^{-1} pointing toward the central goal. Two simplifications for this work are that the simulation is restricted to 2D and that UAVs are considered to have landed if they come within a set radius, 15m, of the end goal. This same criterion is used to determine when a UAV has reached its next waypoint and therefore when to generate the next one.

The UAVs simulated in this paper are also quadcopter-like as they can hover. As such there is a certain minimum desired separation that UAVs should try to maintain in order to not adversely affect one another, referred to in this paper as R_d. This defines the idea of a conflict, when two UAVs have a separation that is less than the desired minimum.

See Fig. 2 for example trajectories. Each simulation run is for 500s and statistical results are derived by averaging over 50 runs. Some of the UAVs exhibit an unexpected behaviour where they loop around waypoints. This was not intended and hopefully can be eliminated in future work through refinements to simulation parameters.

IV. Results

This section will provide results from simulation and explore the effect that the routing method has on the safety of the system. Using the concept of the conflict as described in the previous section, the percentage of recorded UAV separations that are greater than or equal to the desired minimum separation, R_d, provides a metric to understand the safety of each simulation. If the percentage is 100%, then no conflicts are recorded for that particular run of the simulation (perfect safety).

This metric is recorded in Fig. 3 for a variety of values of γ and number of UAVs. The solid line shows the average percentage for that number of UAVs when there is no routing. There are two main results to note. Firstly, in almost all scenarios the average percentage of UAV separations compliant with the minimum separation increases for all values of γ compared with the average for simulations where no routing is used. Thus, the system is safer when the routing method is implemented. Secondly, the system becomes safer as gamma increases from 0.1m^{-1} to 10m^{-1}. This is the opposite of the expected behaviour as smaller values of γ should correspond to traffic that prioritises avoiding areas of higher density.

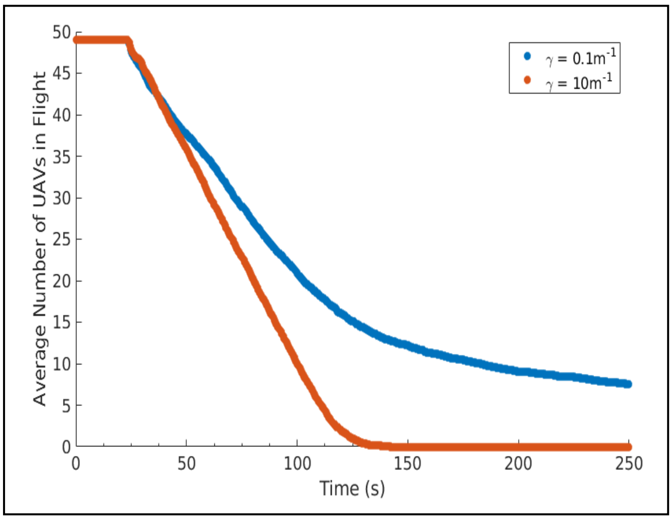

Figure 4. The number of UAVs still in flight versus time step for γ = 10m^{-1} (orange) and γ = 0.1m^{-1} (blue).

It is also worth considering how γ can affect other characteristics of the system. Fig.4 shows how the average number of UAVs still in flight changes over time. It shows that for a larger value of γ, the number of UAVs in flight decreases more rapidly in time, as traffic prioritises reaching the landing zone more strongly.

V. Conclusion

This paper has presented a new routing strategy for UAVs that attempts to improve performance by avoiding areas of high traffic density. The routing strategy has been implemented in a distributed manner so that it can be used on UAVs without centralised control or the development of new infrastructure. The results presented are for a simulation scenario inspired by a UAV depot or other landing zone in order to force UAVs to form an area of high density traffic. Despite this bottleneck, the safety of the system has been shown to increase when the routing strategy is applied on top of some simple navigation rules.

As was expected, the value of γ for which there were the fewest conflicts on average was 0m^{-1}. This is when UAVs will always pick a waypoint based on which waypoint has the least neighbouring UAVs. However, the relationship between γ and the system safety did reveal an unexpected behaviour.

As γ increases from 0.1m^{-1} to 10m^{-1}, the average safety of the system increases as well, see Fig. 3. Also, from Fig. 4, it can be seen how the rate of UAVs landing is higher for higher values of γ. Since no analysis of the severity of each conflict has been conducted, i.e. a conflict of 25m is not as severe as a conflict of 1m, it is possible that though the rate of conflicts is lower for larger γ, the severity of those conflicts is worse. In other words, for large values of γ, the UAVs converge quickly on the central goal and rapidly increase the local density. While this results in severe conflicts, they also manage to land quickly which in turn decreases the local density allowing other UAVs to move more safely.

There are several directions that future work might take. The strategy presented here is agnostic about what method the UAV uses to detect other UAVs and the landing mechanics are extremely simplified. Both aspects could be modelled more accurately in future iterations. As for the routing strategy itself, there are two adaptations that might be of interest to explore. These are a stochastic version where Q_c is used as a weight and a version where γ is dynamic. By introducing a stochastic element to (1), we obtain a more extreme version of the routing strategy by ensuring that some amount of the UAVs pick sub-optimal routes, ensuring a lower local density around the goal. Alternatively, a dynamic γ that is related to the total number of UAVs in the simulation could allow UAVs to change their risk appetite, by prioritising avoidance when there are many UAVs still flying, and prioritising landing when there are fewer.

With conflicts as defined in Section III, it is acceptable for a traffic system to have some conflicts provided they are short lived and are close to the desired minimum separation. However, this paper recognizes that actual collisions will need to be entirely prevented before any routing strategies can see real world aviation applications. Although we have shown how routing strategies can achieve performance gains over simple collision avoidance and navigation methods, our future aims are to establish how these gains might still be achieved, with the minimisation of conflicts and elimination of undesirable behaviours such as spiralling.

References

[1] H. F. Wedde et al., "A novel class of multi-agent algorithms for highly dynamic transport planning inspired by honey bee behavior," in *2007 IEEE Conference on Emerging Technologies and Factory Automation* (EFTA 2007), 2007, pp. 1157–1164.

[2] D. Helbing and P. Molnár, "Social force model for pedestrian dynamics," *Phys. Rev. E*, vol. 51, no. 5, pp. 4282–4286, May 1995.

[3] J. Van Den Berg, S. J. Guy, M. Lin, and D. Manocha, "Reciprocal n-body collision avoidance," *Springer Tracts Adv. Robot.*, vol. 70, no. STAR, pp. 3–19, 2011.

[4] "European Drones Outlook Study, Unlocking the value for Europe," *SESAR*, 2016.

Towards Symbiotic Human-Robot Collaboration: Human Movement Intention Recognition with an EEG

Achim Buerkle, Niels Lohse, Pedro Ferreira

Intelligent Automation Centre, The Wolfson School of Mechanical, Electrical and Manufacturing Engineering, Loughborough University

***Abstract*: In order to meet the trend of customers demanding more customised and complex products, human workers and robots need to collaborate in closer proximity. Working in shared environments raises safety concerns of humans getting injured by robots. Current safety systems are mostly vision based and detect movement after it has started. This work proposes the use of an electroencephalography (EEG) which measures the brainwaves in order to detect a worker's intention to move. This is expected to provide 0.5 seconds gain for the system to react in advance of the actual movement. In this paper the details on how EEG sensors can be integrated to detect intentions and how these can be extrapolated using machine learning techniques, are presented. The ultimate vision is to deliver an early warning system to enhance existing safety systems.**

***Keywords*: Human-Robot Collaboration, Symbiotic Assembly Systems, Robot Safety, EEG, Movement-Intention Recognition, Machine Learning**

I. Introduction

The consumer market for manufactured goods is currently following a trend from mass produced goods towards individual and highly customised products. Simultaneously due to shorter lifecycles of products and a higher product variety, manufacturing goods becomes more complex [1].

Conventional robots are designed for low mix production repeatedly coping with a high payload at a high speed while providing consistent quality. This, however, conflicts with the aforementioned trend towards manufacturing highly customised goods [1] [2].

Human workers strengths, on the other hand, are the cognitive skills, adaptability to changes and the ability of making difficult decisions with incomplete data [3].

An opportunity to cope with the demands of high adaptability and high complexity in manufacturing can be the symbiosis of robots and human workers in a confined workspace. A symbiosis typically combines the benefits of two systems. This, however, requires clear and transparent communication channels and awareness of all members in the system [3].

While most research focuses on robots replicating human activities and movements, in a human-robot collaboration environment both parties are expected to perform tasks simultaneously which are related to their characteristic strengths. Fully automated systems, on one hand, can achieve a high production volume at a low-level product complexity. Manual systems, on the other hand, typically produce complex products at a low volume. Therefore, human-robot collaboration could change manufacturing towards producing high complexity goods at a high production volume [3].

Consequently, human workers and robots need to work in close proximity to each other. These "fenceless", shared manufacturing environments raise safety concerns, as robots lack abilities to detect humans, whilst being able to operate at high speed and at high levels of torque. In order to ensure human worker's safety, there are video-based systems available which will stop/slow down a robot once a human worker is approaching the robot and at risk of getting injured [4]. Shutting down a robot as a safety feature, however, should be seen as 'ultima ratio' – the final argument/solution. A better approach is to react beforehand by communicating the intention meaning the willingness of performing a task before the actual execution [5].

There are concepts for Robot-Human communication such as using Augmented Reality glasses to show robot movement animations to human workers in advance, in order to highlight the robot's intentions [1].

However, communicating human intentions to a robot is rather difficult. Therefore, a concept to apply electroencephalography (EEG)-based (Brainwave-measuring) systems to detect human intentions to perform motor-movements is investigated. Instead of replicating the movement intention with a robotic arm, the measured intention will be used as means of communication. In order to validate, that EEG-based sensors can be integrated in a system, it is essential to accurately detect human movement intentions. The idea is to establish a new mechanism to enhance current video-based safety systems, by taking advantage of detecting intentions before the actual execution.

II. Background

Robots seem to be an essential part of today's manufacturing industry with 2.6 million robots in operation worldwide in 2019 and increase of 13% every year [2].

However, the level of human-robot interaction in such systems is still fairly low, despite recent advances in robot technology [6]. The interactions between humans and robots range from working in parallel, in sequence or jointly. Thus, one can argue that the interactions are dependent on the level of expected proximity between the two. A very low-level interaction is the **human-robot coexistence**. Both share the same working environment while performing different tasks which do not interfere. In such situations, safety systems are required to avoid collisions, however human-robot communication is restricted to “START” / “STOP”-commands only [7]. In a **human-robot assistance** scenario the activities of both humans and robots need to be synchronised. Also, a communication needs to be established to enable interoperability. The relationship of humans and robots can be viewed as Client and Server interaction. Robots are supposed to serve workers without cognitive capabilities, hence they’re human-guided. [4] The highest level of interaction is the **human-robot collaboration** by jointly executing tasks. This is also due to the fact that it’s the most intense and challenging way of interaction. Since both workers and robots do not only share the same task but also interact within the same process, interoperability is required on a detailed level [3].

Apart from both workers and robots needing to be aware of each other, timing of each task is also essential. This leads to the need of situational, goal-oriented planning as well as being aware of each member’s current and future tasks or intentions. Possible interferences of tasks need to be anticipated and solved in order to establish a safe collaboration. Therefore, robots are also required to have cognitive skills [7].

In order to establish safety during a collaborative operation, ISO 10218-1 distinguishes between four levels of collaboration and associated means of risk reduction [8]. The first one is a safety-rated monitored stop, meaning that there will be no robot motion once a human operator is entering in a collaborative work space. A second operation is hand-guiding which will only allow robot motion through direct input of the operator. The third clause contains the definition of speed and separation monitoring. Therefore, robot motion is enabled when the separation distance is above minimum separation distance. Finally, there is power and force limiting by design or control. In that case robots are designed to only impart limited static or dynamic forces in the event of a human-robot contact [9]. However, these safety features are the ‘ultima ratio’ - the final solution to prevent hazards. Organising tasks and communicating intentions from operators to robots and robots to operators beforehand could avoid creating high risk-scenarios which would trigger the safety systems to interfere.

According to Gustavsson et al. (2018) there are three main approaches to robot-human communication. One is augmented reality (AR) which overlays digital information onto camera-captured real-world objects. The technology provides information where it’s needed. A second approach is Text-To-Speech (TTS) which allows robots to provide understandable audible messages for human workers. While this technology is mostly used in devices such as satellite-navigation, there are also opportunities to use it in a manufacturing environment. A third approach is Pick-by-light. A small lamp installed on each storage container indicates which part or tool a human worker should pick. Although this system is not very flexible, it has been in use in modern warehouses [6].

Human-to-robot communication, on the other hand, often focuses on natural or intuitive human communication channels. While haptic controls such as a joystick to guide a robot were used in assistance or coexistence scenarios, they are less applicable in human-robot collaboration. Automatic speech recognition (ASR), on the other hand, allows humans to communicate in a natural way with the robot, similar to human-human interactions. In contrast to haptic controls, humans communicate without removing hands or their focus from their current task. Gesture recognition is not only restricted to hands but can also mean nodding the head in order to indicate an affirmative decision. Both vision-based, and glove-based technologies allow the system to locate a human worker’s position as well as receiving commands such as highlighting an object by pointing at it. Overall, best results were achieved when combining different channels [10].

Safety systems tend to rely on vision-based systems in human-robot collaborative manufacturing [4]. Their main purpose is to help avoiding collisions or limiting impact forces to a level that they won’t cause injuries. The reason why vision-based safety systems are so popular is because of their affordable price, high flexibility and easy tailoring[4].

While electroencephalography (EEG) has been used to analyse brain behaviour for a few decades, due to recent developments regarding mobility, it can now also used in an industrial environment [5]. Mohammed and Wang (2018) established training sessions for human operators to think of commands. The measured brain activity-patterns were translated into robot commands. Similar to vision based communication, this allows an operator to perform an individual task, while at the same time controlling the robot in a human-robot assistance scenario [11].

III. Problem Description

As described in Section II, there is a trend towards human-robot collaboration in industrial assembly processes. Human-robot collaboration is more than human-robot coexistence and human-robot assistance. Human-robot collaboration requires both to share the same working environment while performing tasks which are assigned according to the required, characteristic strength of either humans or robots [4].

The main advantages of human-robot collaboration will be the ability of coping with high production volume while assembling increasingly more complex products [3].

However, these shared working environments raise safety concerns due to the close proximity. Therefore, human workers and robots need to be in a constant feedback loop which ensures awareness of each member in the system in order to avoid collisions or any negative interference. The main purpose of these safety system is to keep human workers safe and to prevent possible injuries. Current safety systems solutions are mostly vision-based. They detect the current location of a human worker as well as the performed movement. Typically, movements are detected after their execution has started, which is only possible after certain timespan which is required to process the images.

The question that arises is if it is possible to predict movements before they occur. This would provide the safety system with faster reaction times and allow for higher leeway on robot operations. Based on the processed images, there are approaches to predict future motions by using statistical methods and estimated probabilities. The accuracy of these predictions, however, decreases with the complexity of the assembly task [4].

An opportunity to physically measure human arm movement intentions and therefore enhancing/extending existing vision-based safety system can be the usage of EEG-measured brain waves. Liu and Wang (2017) state that the human brain is always analysing and evaluating motions before executing them [12].

Therefore, it is possible to detect intentions such as human arm movement by recognising patterns in the EEG, as highlighted in Figure 1 [5].

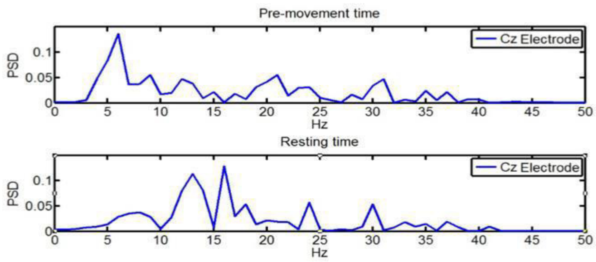

Figure 1 Pre-movement patterns [13]

Generally, there are two neuro-physiological phenomena that can be detected before a voluntary action occurs. The first one, sending weak signals, is called *Bereitschaftspotenzial* (readiness potential) and occurs up to 1.5 seconds before the actual movement. The second one, sending a stronger, more easily measurable signal through EEG, can be detected up to 0.5 seconds before the movement [13]. In order to gain a time-related advantage, the time to process the EEG data, including feature-extraction, classification, evaluation by contextualising and finally, giving the feedback command, needs investigation whether it is faster than video-based systems. However, the data-stream transferred by EEGs is presumably smaller than the data-stream which is processed in video-based safety systems. This could also offer the opportunity of achieving a faster processing performance.

Another challenge that should be considered apart from processing and reaction time is accuracy. Safety systems typically require a high Recall (retrieving all intentions) and then a high accuracy. The main purpose of this bias is to avoid False Negatives, meaning that the safety system should rather cause a false alarm, than missing an actual hazardous situation. Therefore, the safety systems should consider this bias when modelled to ensure a similar behaviour to existing systems. There is a clear potential to assess EEG as a potential solution for predicting motion, which can be used in safety system, but would also have wider applications on human-robot collaborations, as it would provide an interfacing path that currently does not exist. Nevertheless, it is also important to state that EEG-based experiments are mostly performed in quiet and sterile laboratories which are intended to protect an experiment from external influences as good as possible. In an industrial environment, on the other hand, there are various sources of external stimuli such as a high noise level, machines performing movements and other sensor-disturbing influences. Typically, an EEG is measuring micro-voltage levels whereas a human worker could stand next to a machine running at thousands of volts. These influences also need further investigation and considered before an EEG-based system can be applied in an industrial environment.

IV. METHODOLOGY FOR DETECTING HUMAN INTENTIONS TO MOVE

In order to extend existing safety systems, it is essential to measure worker's movement intentions. An EEG allows to detect patterns; however, these need to be mapped with actions to differentiate between being idle, having the intention to move and finally the movement itself. Therefore, the main approach is first, to detect movement intentions before then optimising classification accuracies. Finally, the time-related advantage over video-based systems needs to be validated. The general process for an integrated movement intention recognition with an EEG would be (1) measuring brainwaves at certain locations before (2) pre-processing the signal by using filters to reduce the noise. Bousetta et al. (2017) examined channels (Figure 3) to detect movement intentions. The channels AF3, AF4, F3 and F4 were used[13].

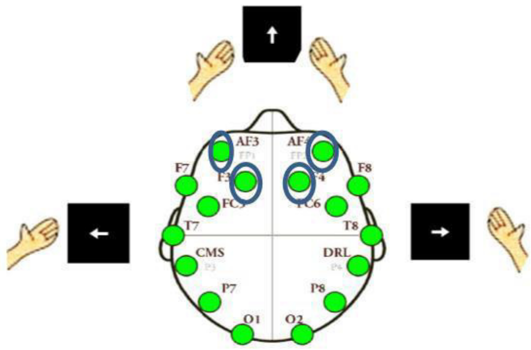

Figure 2 Responsible EEG-channels [5]

In a third step, a feature extraction needs to be performed to reduce the dimensionality of the features. Typically, sensorimotor rhythms that can be measured before and during an arm movement, are frequency bands of 8 Hz – 12 Hz and 12 Hz – 22 Hz which can be filtered with a Butterworth-filter. After applying a Fast Fourier Transformation, distinct signals can be detected [5], [13].

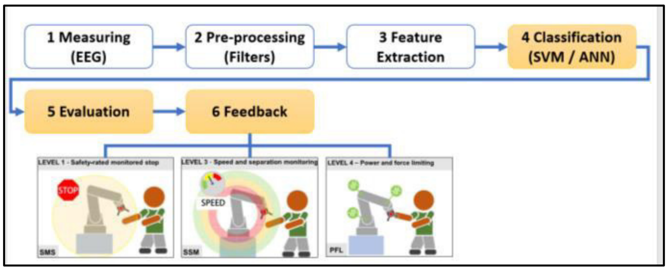

Figure 3 Integrated EEG-measurement in Process

Finally, a classification is performed (4). For each arm there are the aforementioned classes: Idle, intention and movement.

Bousetta et al. (2017) used a Support-Vector Machine (SVM) as a state of the art-classifier [5]. Planelles et. Al. (2014) also obtained highest accuracies with SVMs compared to other statistical methods such as k-nearest neighbours [13]. Either classification algorithm requires a training phase before it can be used in the process shown in Figure 3. However, instead of passing along the commands to the robot in order the replicate the human movement. The human intention of moving a left / right arm in combination with the current context of the worker's position and task can be evaluated (5). Then it can be integrated into the safety-system. While vision-based safety-systems must detect differences in arm positions and therefore reacting relatively late, the main advantage of the EEG-intention recognition is that the processing of brainwave signals can already begin before the actual movement is executed. After the evaluation-phase (5), there is the opportunity to follow up with a reaction (6). Based on Villani et al. (2018) there are three possible feedback options. The first option is to fully stop the robot. The second alternative is to reduce speed. A third possibility is to reduce power and force in order to not injure human workers [9]. While the first three steps within the process stay the same (measuring, filtering and feature extraction), there are opportunities to train and later to use different classification algorithms. Bousseta et al. (2017) measured the arm-movement intentions for four participants. The overall mean accuracy achieved is 84.18%. In their paper similar results presented had an accuracy of 78% up to 88%. However, in each case the method for performing a classification was based on SVM's [5].

Due to the rapid development of machine learning algorithms including artificial neural networks and deep learning, there are more advanced classifiers available than SVM's.

Jiao et al. (2017) compared different classifiers for EEG-measured data. Their accuracy for the SVM with 84.66% is close to the aforementioned 84.18%. In their paper, a model based on a Convolutional Neural Network increased the accuracy up to 92.37% [14]. However, according to Géron (2017), there are two main approaches of deep learning: Recurrent Neural Networks (RNN) and Convolutional Neural Networks (CNN). CNN's are typically used for image recognition and visual feature based identification, RNN's, on the other hand, are typically used to identify time-based data series such as stock-market rates and language recognition [15]. Due to EEG-signals for arm-movements also being time-based series and since they can, similarly to language recognition, be seen as a means of communication there is also the opportunity of increasing accuracy and recall by using RNN's [15]. In the context of safety in a human-robot collaboration scenario, it is important to implement bias towards high recall over high accuracy when training the classifiers to recognise all movement intentions. On the other hand, a false-alarm-scenario is a False-Positive intention recognition leading to an unnecessary interruption of the robot movement. This is also desired to be prevented or kept as low as possible, since it will slow down the assembly process.

V. Conclusion

In shared manufacturing environments, human-robot communication becomes more important. While robot movements are predefined, human intentions are difficult to detect. Video-based safety systems can only react to human movement after it started. A novel concept of measuring human movement intentions and integrating them into a safety system is presented. It is expected to provide additional reaction time to safety systems. The proposal is to use existing approaches that demonstrated the use EEG-measured brainwaves to replicate human movements with robotic arms. By using a similar approach to use the brainwaves as a means of communication by detecting human intention to move. The main goal is to validate the possibility to detect human intentions and by providing this information to the robot enable the vision of symbiotic human-robot collaborations.

References

[1] R. Palmarini *et al.*, "Designing an AR interface to improve trust in Human-Robots collaboration," *Procedia CIRP*, vol. 70, pp. 350–355, 2018.

[2] I. F. of R. (IFR), "IFR. Executive summary world robotics 2016 industrial robots. Technical Report.," 2016.

[3] P. Ferreira, S. Doltsinis, and N. Lohse, "Symbiotic assembly systems - A new paradigm," *Procedia CIRP*, vol. 17, pp. 26–31, 2014.

[4] R. J. Halme, M. Lanz, J. Kämäräinen, R. Pieters, J. Latokartano, and A. Hietanen, "Review of vision-based safety systems for human-robot collaboration," *Procedia CIRP*, vol. 72, pp. 111–116, 2018.

[5] R. Bousseta, I. El Ouakouak, M. Gharbi, and F. Regragui, "EEG Based Brain Computer Interface for Controlling a Robot Arm Movement Through Thought," *Irbm*, vol. 39, no. 2, pp. 129–135, 2018.

[6] P. Gustavsson, M. Holm, A. Syberfeldt, and L. Wang, "Human-robot collaboration - Towards new metrics for selection of communication technologies," *Procedia CIRP*, vol. 72, pp. 123–128, 2018.

[7] G. Weichhart, M. Åkerman, S. C. Akkaladevi, M. Plasch, Å. Fast-Berglund, and A. Pichler, "Models for Interoperable Human Robot Collaboration," *IFAC-PapersOnLine*, vol. 51, no. 11, pp. 36–41, 2018.

[8] International Organization for Standardization, "ISO 10218-1:2011," *Safety requirements for industrial robots*, 2011. [Online]. Available: https://www.iso.org/standard/51330.html. [Accessed: 13-Dec-2018].

[9] V. Villani, F. Pini, F. Leali, and C. Secchi, "Survey on human-robot collaboration in industrial settings: Safety, intuitive interfaces and applications," *Mechatronics*, no. June 2017, pp. 1–19, 2018.

[10] P. Gustavsson, A. Syberfeldt, R. Brewster, and L. Wang, "Human-robot Collaboration Demonstrator Combining Speech Recognition and Haptic Control," *Procedia CIRP*, vol. 63, pp. 396–401, 2017.

[11] A. Mohammed and L. Wang, "Brainwaves driven human-robot collaborative assembly," *CIRP Ann.*, vol. 67, no. 1, pp. 13–16, 2018.

[12] H. Liu and L. Wang, "Human motion prediction for human-robot collaboration," *J. Manuf. Syst.*, vol. 44, pp. 287–294, 2017.

[13] D. Planelles, E. Hortal, Á. Costa, A. Úbeda, E. Iáñez, and J. M. Azorín, "Evaluating classifiers to detect arm movement intention from EEG signals," *Sensors (Switzerland)*, vol. 14, no. 10, pp. 18172–18186, 2014.

[14] Z. Jiao, X. Gao, Y. Wang, J. Li, and H. Xu, "Deep Convolutional Neural Networks for mental load classification based on EEG data," *Pattern Recognit.*, vol. 76, pp. 582–595, 2018.

[15] A. Géron, *Hands-On Machine Learning with Scikit-Learn and TensorFlow*. O'Reilly Media, 2017.

Development of a Multi-robotic System for Exploration of Biomass Power Plants

Sihai An, Farshad Arvin, Simon Watson, and Barry Lennox

Abstract—**Biomass Integrated Gasification Combined Cycle (BIGCC) is a power generation technology which has been vastly used in past years. Maintaining those power plants are very crucial due to having various risk of hazards. In order to increase workers safety and reduce property losses, common faults which are reported in BIGCC based power plants were investigated in this paper. Also, a fault detection methods using multi-robot system was proposed. Therefore, autonomous group of robots were used for achieving continuous inspection in BIGCC power plants. The inspection scenario and implementation of the proposed scenario were conducted with simulation software, V-rep. Two types of mobile robots, ground and flying robots, have been deployed.**

Index Terms—**Exploration, Autonomous System, Mobile Robots, Extreme Environments**

I. Purpose of the Research Study

Inspection using robotic platforms has become an important research topic in recent years. Particularly, some patrolling robots have been developed for smart industry in petroleum [1], chemical industry [2], power plant [3] and other applications [4]. With regard to single robot inspection, the robot for visual inspection of nuclear plants were proposed in [5] [6]. The proposed robot can reduces human involvement in inspection of nuclear radioactive area. In a recent study [7], an aircraft fuel tank inspection robot was developed. It decreases the workload of aircraft crew and improves the maintenance efficiency. Although using single robot for inspection is an efficient approach, multi-robotics has shown better performance to solve exploration tasks in complex and unknown environments [8]. As an example, an inspection of jet engine turbine using miniature swarm robots were proposed in [9]. In another study, an application of swarm robotics in crops inspection for precision agriculture was proposed in [10]. The custom robotic systems can be the one main reliable solutions for industry.

BIGCC is an advanced power system to extract energy from renewable biomass sources. There are nearly 2000 biomass power plants producing a total of 22.5 GW in over 40 countries [11]. BIGCC usually containing 13 key sub-systems as listed in Table I. It can achieve zero emission to offer good performance on environmental protection [12]. However, several flaws remained in BIGCC. The gasification is a dangerous process and it may pose issues of Occupational Safety and Health (OSH) for workers and environmental damage [13]. In August 2017, a man had multiple injuries of serious burns after an explosion in a gasification plant [14]. Six weeks later, two men were badly hurt in another gasification plant again [14]. In addition to the reported accidents, various risks exist in the power system. To identify the dangerous causes of BIGCC power plant, some general faults of power plants were listed in Table I. These issues of the power system have drawn a great risk to the 1.2 million workers [15]. Numerous people have to face a series challenge on their works for each family's well-beings.

Monitoring of power system equipment is an indispensable process for their sustainability and continuous maintenance. Some invention has been proposed and implemented. Wall-climbing robot was proposed for inspection of nuclear plants equipment [16]. Application of robots for tank inspection in power plant was proposed in [17]. Recently, a multi- function pipe inspection robot was proposed in [18]. These robots have helped engineers for inspection and maintenance in some extent. These inspection robots were most suitable for static environments and it has to cooperated with human operator. An advanced way for monitoring dynamic power system is using an automated guided vehicle (AGV). It have been utilized to follow a certain path [19] and integrated sound, light, electricity and computer [20]. In addition, another forward research that is using robot service to renewable wind- farm was developed in [21].

In summary, inspection using mobile robots still has a room for improvement in the dynamic power system. Single robot deployed for large scale energy system has limitations by its ability, such as running speed, power capacity of unmanned aerial vehicle (UAVs), multi inspection tasks, inspection frequency etc. Multi-robotics system has strong robustness which made robotics system becomes flexible and scaleable. However, inspection using autonomous multi-robots for the renewable energy system is demanding research area. The project has broad prospects and generality that is focused on to solve real-world problems by integrating robotic technology into the renewable energy system, it also contributes to the body of knowledge in the multi-robotics technology. This work aims at providing a reliable autonomous multi-robot system to carry out continuous patrolling tasks, specifically to help to inspector keep away from hazard areas of a power system. The proposed multi-robotic solution in this study will be able to cover inspection tasks of full-scale biomass power plant.

II. Methodology

A. Research Question

BIGCC technology has several immaturities as listed in Table I. Any faults in BIGCC power plant will result in

All the authors are with the Robotics for Extreme Environments Lab at the School of Electrical & Electronic Engineering, The University of Manchester, UK. (email: sihai.an@postgrad.manchester.ac.uk).

TABLE I
LIST OF SUBSYSTEMS AND GENERAL FAULTS IN BIOMASS-IGCC

BIGCC-Subsystem	Functionality	Problem, Running Condition	Consequence
Biomass Raw Material Handling System	also called pulverization stage, which convert the raw biomass material to the small pellets	dust explosions, self ignition, off-gassing of bacteria, fungi	fire, explosion, worker fatalities, loss of production, poisonous, power plant destruction, operator OSH, gas/steam turbine or generator damaged, electricity black-out in large scale, terminal user unsatisfied, power plant maintenance
Biomass Storage System	for storage the wet biomass pellets, general its a circular shapes tank.		
Biomass Feeding System	for delivery of the treated pellets to the carbonization system. Typically, it's a closed screw feeder.	noise	
Carbonization System	remove the different moisture content (MC%) from biomass pellets for reduce the gasification system primilary energy cost.	self ignition	
Air Booster System	pump the compressed air to gasification and gas power system.	high temperature, pressure	
Gasification System	which is the key part of the BIGCC power technology, the function of gasifer is transfer the solid fuel to gases fuel after a series gasification process.	syn-gas leakage, explosion-prone	
Tar Remove System	for remove the tar from syn-gas, this process will start after gasification transfer process.	high temperature, pressure	
Syn-Gas Purification System	remove the ash and impurities from syn-gas. such as: C, SiO2, COS, NH3, H2S etc.	combustible leakage	
Gas Power System	for electricity generation, which is decide the entire power system energy utilization factor.	generator excessive vibration and overheating, tube corrosion, leakage, noise, output voltage level over accepted level	
Steam Power System	Heat Recovery Steam Generator (HRSG) system was the main part of steam power system, which is used for recovery thermal energy from hot flue-gas, this process is for highly system net thermal efficiency.		
Heating System	recovery the bleeding from power cycle for supply hot water to terminal user.	output water temperature higher/lower than accept level	
Refrigeration System	recovery waste heat from power cycle for support cold requirements.	refrigerator fault	
Back-up System	support power to user when the BIGCC system maintenance or fault happening.	back up system start time delay	

injuries to workers and property losses. It is essential to provide continuous monitoring of the facilities using intelligent devices. Multi-robotic solutions will improve the performance of monitoring for this kind of long-term exploration of large facilities.

B. *BIGCC Scenario Development*

BIGCC system generally containing different sub-systems, the detail was as listed in Table I. Each sub-system have been built in V-Rep software. The primary model work was as shown in Fig. 1. The BIGCC model developed from raw biomass material handling process, main energy converting process, power generation cycles etc until the electricity output processes. General and faulty, two modes will be conducted in to the experimental. Such as: steam leakage, tube overheat, switching operation, parameter calibration with control center, self ignition, cable trench inspection etc.

C. *Multi-Robotics System*

1) Flying Robot – Trailbreaker: Trailbreaker is a four-axis UAVs robot as shown in Fig. 2. The Trailbreaker robot was allowed in six degree of freedom (DOF) flying. For gathering data from BIGCC, sensing equipment will be attached to group of Trailbreaker robots.

Energy radiation around everywhere in BIGCC, which provides good opportunities for monitoring the temperature of each subsystem. While, each sub-system of BIGCC running in a constant state. The temperature values of each pipelines or subsystems will exist in a constant value. Thermal camera will be employed into the robot system for detect the energy emission of BIGCC. A thermal map therefore can be generated in time, while a set of normal threshold value will be added in the robot system. Thus, monitoring of temperature fault will be achieved Trailbreakers. In another hand with regard to others issues of BIGCC, for example leakage, open flames or some instrument parameter reading etc, is indispensable tasks to the inspection robot as well. Additional vision system will be equipped on-board of Trailbreaker robots for guarantee more redundancy of inspection process.

2) Ground Robot – Wheeljack: Wheeljack, is an unmanned ground vehicle (UGV) robot as shown in Fig. 3. The Wheeljack is designed to cover the missing inspection points from Trailbreaker. In the other hand, the main contribution of Wheeljeack is fix general issues of Biomass-IGCCs.

Road boundary detection and obstacle avoidance are essential task to the robot inspection. Unknown environmental and multi obstacles of BIGCC has made inspection process more complexity. A high-resolution camera and radar system has designed and employed in Wheeljack robots. The Wheeljack robot was able to directly measure the range, velocity, and azimuth angle of obstacles [22]. With these equipment deployed, the inspection of robot system performed with excellent quality on problem judgement. Different accessories will be employed with regard to debug process of Wheeljack, such as a cooling tank for overheat problem, a fire extinguisher for ignition or an additional manipulator for transfer the wounded operators, etc.

3) Multi-Robotics system control mechanisms: A hybrid architecture (combine centralized and distributed) will be

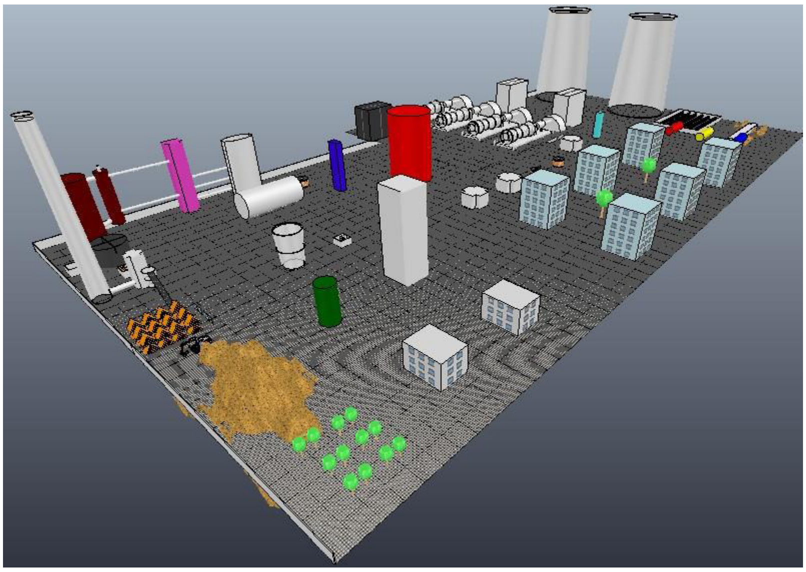

Fig. 1. A model of Biomass-IGCC Power Plant developed in V-rep

attempted to deployed in Heterogeneous robot system. The Trailbreaker, Wheeljack and base station will cooperate with each others to conduct the exploration tasks. The tasks for robot system will be classified to different priority levels. Trailbreaker and Wheeljack will be allowed to command each other. Wheeljack collective behaviours will judged by Trailbreaker. Feedback mechanism will be deployed when an unreasonable command received. Each robot will broadcast a signal of itself current status to its own team, as well as around robot. The signal information, such as current position, inspection missions and priority levels, fault information, state of power etc. Additionally, heterogeneous robot system will be separated into different small teams. Wheeljack and Trailbreaker will be treated to different agent groups. Each groups will performing inspection in autonomous and worked at a specified area.

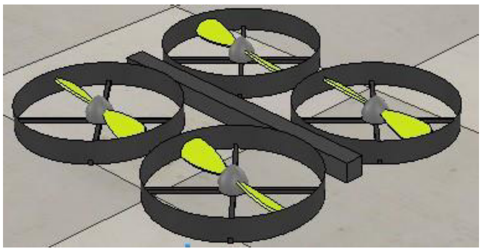

Fig. 2. A model of Trailbreaker Robot

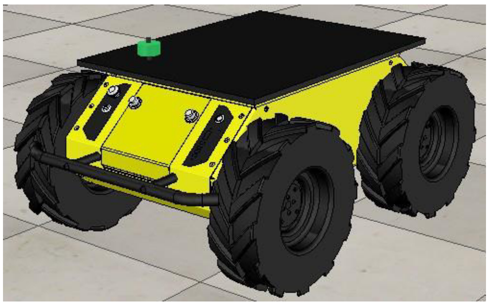

Fig. 3. A model of Wheeljack Robot

D. V-Rep Implementation

V-Rep is a free simulator for education with versatile and scaleable framework for modelling robotics. It is vastly used in the academic as well as industrial applications [23]. In this project, V-Rep will be employed for carrying out the entire system modelling work. The simulation process will be split into four steps:

- Building a biomass power plant model. This will be achieved by utilizing the various physics and graphics libraries in the V-Rep. Some of sub-systems will be specially designed compared with real case, for example ignition of storage system, feeding water temperature of power systems.
- Building and control heterogeneous multi-robot model. To utilizing the V-Rep robot simulator and controller. Such as a robot motion control: (a) define the desired robot position (b) using V-Rep to calculate the kinematics for each motor (c) assigning the calculated motor positions to be used as target positions by the dynamics module [24]
- Group robot inspection synergy design. This relative on architecture, communication, the collective mechanism (multi-task allocation, multi-robot path planning), collective localization and mapping and target following etc. More detail can be check in [24]
- The entire system modelling and implementation. Calibrating the power plant and robot model to general states. Dynamic experimental of proposed system under different modules calling. The modules detail can be found in [23]

III. Research Limitations

- The representative of data has various limitations, e.g. simulation random fault cannot represent the real situation.
- A large scale scenario is difficult to develop in simulators, e.g. details may be ignored or results may contain unrealistic values.
- In a real-world experiments, robots are not be able to conducted complex task probability due to their processing or communication limits.

IV. Originality

The project has broad prospects and generality that is focused on to solve real-world problem by integrating advanced robotic technology in the renewable smart grid. Three originality details are as follow:

- This project has a wide range of applications. The proposed robot system has ability to performing inspection in any power or similar power plant, such as gas, thermal or nuclear.
- Monitoring a large scale facility using a group robot. This is inspired by the collective behaviour of ants or honeybees. This project will improve the inspection performance, and propose new applications for group robotic systems
- Integrating heterogeneous multi-robot and smart renewable grid together. This project will help in building the first world smart autonomous renewable energy system

V. Further Works

Two objectives will be the main research direction of this project:

- Exploration of a BIGCC using the heterogeneous multi-robot system
- Development of collective control mechanisms for multi-robot system

Acknowledgement

This work was supported by EPSRC RNE (No. EP/P01366X/1) and EPSRC RAIN (No. EP/R026084/1) projects. The Wheeljack robot's V-rep model was developed by Craig West at the Bristol Robotic Lab.

References

[1] H. Schempf, B. Chemel, and N. Everett, "Neptune: above-ground storage tank inspection robot system," *IEEE Robotics & Automation Magazine*, vol. 2, no. 2, pp. 9–15, 1995.

[2] K. Suzumori, T. Miyagawa, M. Kimura, and Y. Hasegawa, "Micro inspection robot for 1-in pipes," *IEEE/ASME transactions on mechatronics*, vol. 4, no. 3, pp. 286–292, 1999.

[3] S. Yamamoto, "Development of inspection robot for nuclear power plant," in *IEEE International Conference on Robotics and Automation*, pp. 1559–1566, 1992.

[4] C. Jun, Z. Deng, and S. Jiang, "Study of locomotion control characteristics for six wheels driven in-pipe robot," in *International Conference on Robotics and Biomimetics*, pp. 119–124, IEEE, 2004.

[5] M. Nancekievill, A. Jones, M. Joyce, B. Lennox, S. Watson, J. Katakura, K. Okumura, S. Kamada, M. Katoh, and K. Nishimura, "Development of a radiological characterization submersible rov for use at fukushima daiichi," *IEEE Transactions on Nuclear Science*, vol. 65, no. 9, pp. 2565–2572, 2018.

[6] B. Bird, A. Griffiths, H. Martin, E. Codres, J. Jones, A. Stancu, B. Lennox, S. Watson, and X. Poteau, "Radiological monitoring of nuclear facilities: Using the continuous autonomous radiation monitoring assistance robot," *IEEE Robotics & Automation Magazine*, 2018.

[7] G. Niu, J. Wang, and K. Xu, "Model analysis for a continuum aircraft fuel tank inspection robot based on the rzeppa universal joint," *Advances in Mechanical Engineering*, vol. 10, no. 5, 2018.

[8] D. Wang, H. Wang, and L. Liu, "Unknown environment exploration of multi-robot system with the fordpso," *Swarm and Evolutionary Computation*, vol. 26, pp. 157–174, 2016.

[9] N. Correll and A. Martinoli, "Multirobot inspection of industrial machinery," *IEEE Robotics & Automation Magazine*, vol. 16, no. 1, pp. 103–112, 2009.

[10] C. Carbone, O. Garibaldi, and Z. Kurt, "Swarm robotics as a solution to crops inspection for precision agriculture," *KnE Engineering*, vol. 3, no. 1, pp. 552–562, 2018.

[11] C. Juntarawijit, "Biomass power plants and health problems among nearby residents: A case study in thailand," *International journal of occupational medicine and environmental health*, vol. 26, no. 5, pp. 813–821, 2013.

[12] R. M. Shrestha and R. Shrestha, "Economics of clean development mechanism power projects under alternative approaches for setting baseline emissions," *Energy policy*, vol. 32, no. 12, pp. 1363–1374, 2004.

[13] O. Alves, M. Gonçalves, P. Brito, E. Monteiro, and C. Jacinto, "Environmental impact and occupational risk in gasification plants processing residues of sewage sludge and refuse-derived fuel: a review," *International Journal of Occupational and Environmental Safety*, vol. 2, no. 2, pp. 50–63, 2018.

[14] A. N. Rollinson, "Fire, explosion and chemical toxicity hazards of gasification energy from waste," *Journal of Loss Prevention in the Process Industries*, vol. 54, pp. 273–280, 2018.

[15] A. Freiberg, J. Scharfe, V.C. Murta, and A. Seidler, "The use of biomass for electricity generation: A scoping review of health effects on humans in residential and occupational settings," *International journal of environmental research and public health*, vol. 15, no. 2, p. 354, 2018.

[16] L. Briones, P. Bustamante, and M. A. Serna, "Wall-climbing robot for inspection in nuclear power plants," in *International Conference on Robotics and Automation*, pp. 1409–1414, IEEE, 1994.

[17] K. Sato, Y. Fukagawa, and I. Tominaga, "Inspection robot for tank walls in nuclear power plant," in *Proceedings of the international topical meeting on remote systems and robotics in hostile environments*, 1987.

[18] O.-H. Kwon, S.-w. Lee, D.-H. Won, and J. Y. Kim, "In-pipe inspection robot," May 29 2018. US Patent 9,982,830.

[19] R. Guo, L. Han, Y. Sun, and M. Wang, "A mobile robot for inspection of substation equipments," in *International Conference on Applied Robotics for the Power Industry (CARPI)*, pp. 1–5, IEEE, 2010.

[20] L. Shengfang and H. Xingzhe, "Research on the agv based robot system used in substation inspection," in *International Conference on Power System Technology*, pp. 1–4, IEEE, 2006.

[21] M. Barnes, K. Brown, J. Carmona, D. Cevasco, M. Collu, C. Crabtree, W. Crowther, S. Djurovic, D. Flynn, P. Green, M. Heggo, K. Kababbe, B. Kazemtabrizi, J. Keane, D. Lane, Z. Lin, P. Mawby, A. Mohammed, G. Nenadic, L. Ran, A. Stetco, W. Tang, and S. Watson, *Technology Drivers in Windfarm Asset Management*. Home Offshore, 6 2018.

[22] J. Han, D. Kim, M. Lee, and M. Sunwoo, "Enhanced road boundary and obstacle detection using a downward-looking lidar sensor," *IEEE Transactions on Vehicular Technology*, vol. 61, no. 3, pp. 971–985, 2012.

[23] E. Rohmer, S. P. Singh, and M. Freese, "V-rep: A versatile and scalable robot simulation framework," in *IEEE/RSJ International Conference on Intelligent Robots and Systems (IROS)*, pp. 1321–1326, IEEE, 2013.

[24] M. Freese, S. Singh, F. Ozaki, and N. Matsuhira, "Virtual robot experimentation platform v-rep: a versatile 3d robot simulator," in *International Conference on Simulation, Modeling, and Programming for Autonomous Robots*, pp. 51–62, Springer, 2010.

Transfer Learning in Assistive Robotics: From Human to Robot Domain

David Ada Adama, *Graduate Student Member, IEEE,* Ahmad Lotfi, *Senior Member, IEEE,*
Robert Ranson and Pedro Trindade

***Abstract*— Transfer Learning (TL) aims to learn a problem from a source reference to improve on the performance achieved in a target reference. Recently, this concept has been applied in different domains, especially, when the data in the target is insufficient. TL can be applied across domains or across tasks. However, the challenges related to *what to transfer, how to transfer* and *when to transfer* create limitations in the realisation of this concept in day to day applications. To address the challenges, this paper presents an overview of the concept of TL and how it can be applied in human-robot interaction for assistive robots requiring to learn human tasks in Ambient Assisted Living environments. The differences in feature spaces between a human (source domain) and robot (target domain) makes it difficult for tasks to be directly learned by robots. To address the challenges of this task, we propose a model for learning across feature spaces by mapping the features in the source domain to the target domain features.**

I. Introduction

Assisted living environments are incorporated with different technological solutions to improve the quality of life and wellbeing. In recent years, there has been a growing interest in the research community on how to develop evolving solutions to aid assisted living. Different techniques have been studied to address the need for technological systems which are intelligent enough to evolve their knowledge to solve task which have not been previously encountered. One of such approach is Transfer Learning (TL), for example, between humans and robots.

TL in computational intelligence is a branch of learning adopted from a concept in psychology concept 'transfer of learning'. TL involves developing computational models which are capable of mimicking humans' ability to learn and reuse knowledge in different but related tasks. For example, the knowledge acquired while learning to eat with a spoon can be applied in learning to use 'chopsticks'. This knowledge is transferred across related tasks. Traditional machine learning techniques work under the assumption that both source and target data are drawn from a similar distribution of information or similar data domains. This assumption holds in situations where the machine learning model is applied in classification of data which occur in both source and target information. However, in situations when source and target data are drawn from different information distribution, the traditional machine learning techniques struggle to correctly identify the target data [1]. This poses a limitation to machine learning techniques being used in such situations [1]. To address the limitation of traditional machine learning techniques, TL models seek to apply knowledge learned from a previous/source information to a new, but related target information to improve the performance achieved and to reduce time needed in training the model from scratch [2].

Practical implementations of TL aim to transfer as much knowledge from a source task or domain over to the target task or domain. The knowledge transferred varies depending on the application and data from the source available. According to authors in [3], the key challenge in TL is defining the metrics related to *what to transfer*, *how to transfer* and *when to transfer*. This is mainly due to the fact that there are various algorithms that can be applied in TL. In trying to solve this challenge, TL algorithms used so far have focused on three main steps namely.

- Given a target task, select an appropriate source task or sets of tasks from which to transfer knowledge.
- Learn the relationship between a target task and source task, and.
- Transfer knowledge effectively from source task(s) to target task.

These steps have been used by researchers in proposing TL models [3] [4] .

TL has recently attracted interest in recent years due to the potential benefits it offers in artificial intelligence applications including assisted living [1], computer vision [5] and robotics [6]. It has not recorded as much success as the long existing traditional machine learning methods partly due to the challenges which yet remain unresolved in the research community [2]. It has potential to become a fundamental driver for the success of machine learning in the coming years [7] [8].

In relation to assisted living, different applications of TL have been studied. The authors in [1] proposed a model called Fuzzy TL which was applied in an intelligent environment. Data from the source domain was learned by constructing a fuzzy inference system from generated fuzzy rules. The constructed fuzzy inference system is then applied to a new domain referred to as the target domain through stages of adaptation of the generated fuzzy rules with the target data. Results from the model tested on real datasets from two intelligent environments (source and target environments) which were different but related showed the model achieves better performance in the target with transfer of knowledge when compared to performance attained without transfer.

TL has been used in other applications. Of interest to this work is its application in assistive robotics. In [9], the authors proposed a method for improving robot learning manipulation

*Research is funded by Nottingham Trent University Research Scheme.

D. A. Adama, A. Lotfi & R. Ranson are with the Computational Intelligence and Applications Research Group, School of Science and Technology, Nottingham Trent University, Clifton Lane, Nottingham, NG11 8NS. (corresponding author e-mail: ahmad.lotfi@ntu.ac.uk).

P. Trindade is with Critical Software Technologies Ltd, 4 Benham Road, Southampton Science Park, Chilworth, Southampton, SO16 7QJ.

tasks from data obtained from the robot performing other tasks or from similar robot architectures. The method used in [9] is an attempt to address the challenge of *how to transfer* by considering two steps which include, dimensionality reduction of data obtained from the robot to a low dimensional space and manifold alignment of source and target robot dimensions through a transformation function. The work in [6] also follows a similar approach of finding *how to transfer* between multi-robots. Even though these works achieve impressive performances, the challenges of *what to transfer* and *when to transfer* prove to be difficult in transfer learning applications. Addressing these challenges require consideration of properties related to spatial and temporal occurrences of both source/target domains. In this paper, we consider the case of TL from human to robot domains in trying to address some of the challenges of TL.

Figure 1 shows an illustration of TL between a human and an assistive robot in which the robot learns to perform a similar task by extracting relevant properties from the activity source (a human). In this work, we aim to follow a similar approach to TL in the context of transfer of human activity between a human and a robot by: 1) identifying requirements for TL in applications using human/robot as source/target domains respectively, 2) propose a method to address the differences between both domains through a remapping of feature spaces. From the review of related works [1] [9], it is evident that once an optimal mapping between source and target domains is known, *what/when to transfer* would be achievable.

II. METHODOLOGY FOR TRANSFER LEARNING BY FEATURE SPACE REMAPPING

From the introduction to TL presented in Section I, consider a source domain D_S with a feature space F_S and a target domain D_T with a feature space F_T such that $D_S \neq D_T$. TL aims to learn a task in D_S and the knowledge acquired is used in solving a different but related task in D_T. An overview of the method proposed to address the challenges of TL discussed in this work for TL by a remapping of feature spaces between source and target domains is presented in Figure 2. Information from both domains is required as inputs from which the feature spaces are constructed. For a model applied in a domain to be effectively transferred to a different domain, the features related to both domains need to be studied. The proposed approach assumes transfer is achieved when an effective mapping of F_S is obtained in D_T.

In the case where $F_S = F_T$ there can be a direct mapping from source to target to achieve transfer. This case is a much simpler case of TL where the challenges of *what/when to transfer* can be addressed with less computational effort. However, for example in applications such as human-robot interaction where a robot is required to learn an action from a human, this can be activities like *pick and place objects* in assisted living environments. The human and robot are considered as the source and target domains respectively. The differences in both feature spaces makes it not feasible for a direct mapping of features across the robot/human domains. This work assumes the robot domain needed for transfer of knowledge differs in feature space from that of a human, that is, $F_S \neq F_T$ and therefore for TL across such domains we

Figure 1. An illustration of Transfer Learning with an Assistive Robot.

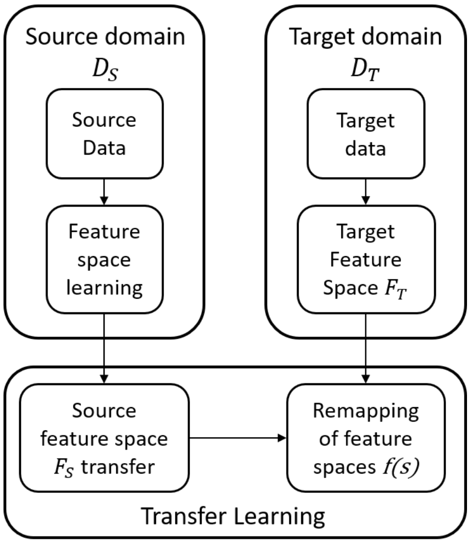

Figure 2. Transfer learning overview by a remapping of features in both source and target domains

Algorithm 1. TL by feature space remapping from source to target domains.

Input: Source domain feature space F_S and Target domain feature space F_T.
Output: Mapping function $f(s)$ from F_S to F_T.

1. Check and remove all duplicate features in F_S and F_T.
2. For every observation in the source domain D_S^i, a weight W_S^i is estimated for each feature – for $i > 0$.
3. Similarly, weights are constructed for the target features and represented by a matrix W_T.
4. For identical features in F_S and F_T, return corresponding weights W_S and W_T.
5. For the non-identical features in F_T, find correlation between weights W_S and W_T.
6. $f(s)$ is obtained by running a similarity function on weights W_S and W_T obtained, and a transformation of learned model to the target domain.

propose a remapping of feature space from source to target domains.

The proposed method for a remapping of feature spaces is summarised in Algorithm 1. The method requires both source and target domain feature spaces as inputs and the output obtained is a mapping function *f(s)* which is a transformation of source features into relevant target features. Duplicate features within the feature spaces are discarded and weights W_S and W_T are assigned to features through a measure of feature importance in both domains. Identical features are extracted in a matrix while a method of correlation is applied to the weights of non-identical features to deduce a relationship between the features. Once this stage is completed, a mapping function is defined which is used in the transformation from F_S to F_T. It is worth noting that the proposed TL by feature remapping method is generalizable to different applications. This is possible if the feature spaces for transfer of knowledge are identified and not specific to an application or information distribution.

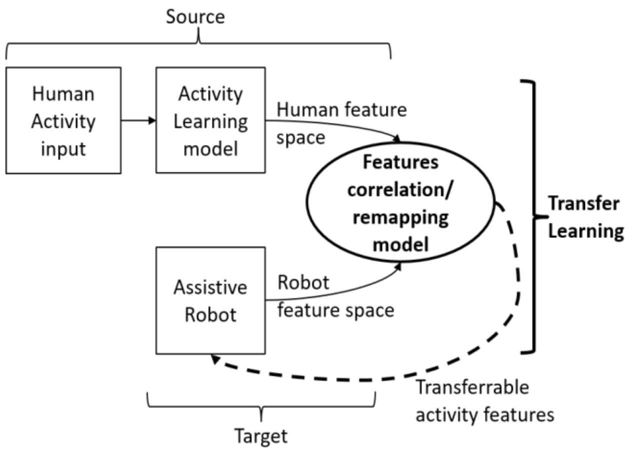

Figure 3. Human activity TL from human to robot domains by features remapping

III. Application of Methodology for Transfer Learning of Human Activities from Human to Robot Domains

The application of the method discussed in the previous section is applied in TL of human activities in an assisted living environment. A human performing an activity is assumed to be the source domain D_S with feature space F_S and an assistive robot needed in learning to perform a similar activity is assumed to be the target domain D_T with feature space F_T. The goal is to be able to learn an activity from a human and transfer the knowledge acquired to an assistive robot which would be capable of learning similar activity within an assisted living environment such as the example presented in the illustration in Figure 1.

Obtaining sufficient data from a robot to train a model for performing activities is a daunting task with a lot of complexities. However, sufficient data for a model to learn an activity can be obtained as humans perform activities and transferred to a robot. This would also enable assistive robots learn human activities by observing while a human performs activities. As shown in Figure 3, human activity data is obtained from visual cues as activities are performed. This could be information such 3D skeleton joint information, RGB or depth frames. The position and orientation features of joints of the human body are extracted. In addition, features of temporal occurrence, velocity, space and motion energy are formulated from the visual information of the activity performed. These features from D_S are used in a learning model for identifying the task performed within the activity.

For a robot to be able to learn to replicate a similar activity, it needs to understand the feature space of the activity source and how it can be transformed into its own space. The TL model requires the robot feature space F_T as input as well. This feature space can be in the form of joint positions and orientations, forward or inverse kinematics of the robot being used. The process of finding the mapping function *f(s)* for the transformation of F_S to F_T following the algorithm described in Algorithm 1 is followed. The features learned from this step are used by the assistive robot in performing the learned activity.

IV. Discussion and Conclusion

In this paper, the concept of TL and its applications in an assisted living environment is discussed with a proposed application in assistive robotics - which is increasingly being incorporated in assisted living environments and explored by the software industry to provide meaningful services to the end-users. Although we propose a model for TL by learning the relationship between source and target features which is the basis of the knowledge being transferred, the key challenges of TL mentioned in Section I leave a gap in the ability to adequately model this concept. More applications of TL in technology could be a potential driver of the next revolution in artificial intelligence as seen from the benefits discussed earlier in this work which should not be underestimated. More research needs to be done on improving TL models to generalize across various applications. For future work, experiments will be carried out to validate the concept of TL and how it can successfully be applied to assistive robots. We also plan to investigate algorithms such as deep neural networks and domain adaptation methods in addressing the challenge of *what to transfer*.

V. References

[1] J. Shell and S. Coupland, "Fuzzy Transfer Learning: Methodology and application," *Information Sciences,* vol. 293, pp. 59-79, 2015.

[2] D. J. Cook and K. D. Feuz, "Transfer Learning across Feature-Rich Heterogeneous Feature Spaces via Feature-Space Remapping (FSR)," *ACM Transactions on Intelligent Systems and Technology,* vol. 6, no. 1, p. 27, 2015.

[3] S. J. Pan and Q. Yang, "A Survey on Transfer Learning," *IEEE Transactions on Knowledge and Data Engineering,* vol. 22, no. 10, pp. 1345-1359, 2010.

[4] D. Cook, K. D. Feuz and N. C. Krishnan, "Transfer learning for activity recognition: a survey," *Knowledge Information Systems,* vol. 36, no. 3, pp. 537-556, 2013.

[5] MathWorks, "Transfer Learning Using AlexNet," MathWorks Inc, 2018. [Online]. Available: https://www.mathworks.com/help/deeplearning/examples/transfer-learning-using-alexnet.html. [Accessed 30 12 2018].

[6] M. K. Helwa and A. P. Schoellig, "Multi-robot transfer learning: A dynamical system perspective," in *IEEE/RSJ International Conference on Intelligent Robots and Systems (IROS)*, Vancouver, BC, 2017.

[7] DTAI - Ku Leuven, "Deep Transfer: Generalizing Across Domains," EU FP7 - People, 2012 - 2015. [Online]. Available: https://dtai.cs.kuleuven.be/projects/deeptransfer. [Accessed 30 12 2018].

[8] European Commission, "Transfer Learning within and between Brains," FP7-IDEAS-ERC, 2014 - 2019. [Online]. Available: https://cordis.europa.eu/project/rcn/191311/factsheet/en. [Accessed 30 12 2018].

[9] B. Bócsi, L. Csató and J. Peters, "Alignment-based transfer learning for robot models," in *International Joint Conference on Neural Networks (IJCNN)*, Dallas, TX, 2013.

Towards a Dataset of Activities for Action Recognition in Open Fields

Alexander Gabriel, Nicola Bellotto, and Paul Baxter

Abstract— **In an agricultural context, having autonomous robots that can work side-by-side with human workers provide a range of productivity benefits. In order for this to be achieved safely and effectively, these autonomous robots require the ability to understand a range of human behaviors in order to facilitate task communication and coordination. The recognition of human actions is a key part of this, and is the focus of this paper. Available datasets for Action Recognition generally feature controlled lighting and framing while recording subjects from the front. They mostly reflect good recording conditions but fail to model the data a robot will have to work with in the field, such as varying distance and lighting conditions. In this work, we propose a set of recording conditions, gestures and behaviors that better reflect the environment an agricultural robot might find itself in and record a dataset with a range of sensors that demonstrate these conditions.**

I. Introduction

There are quite a number of datasets available that provide sensor readings of humans performing various activities. These usually come in the form of RGB videos, with ground truth in the form of action labels [1,2,3] or human skeletons (a set of joint positions organized as a graph) [2]. Today's datasets cover a wide variety of human actions, but mostly contain videos recorded by human camera operators under controlled lighting conditions. This results in videos where the subject is usually frame filling, conveniently oriented and illuminated well.

These conditions are not met in an agricultural setting where the camera operator is a robot, the camera can not be zoomed in on far-away targets or adjusted in direction, and the lighting conditions change with weather and the time of day. Additional problems can be caused by occlusions due to vegetation, infrastructure or machinery.

As a result of this mismatch, the researchers in [4] created a computer vision dataset with focus on the specific challenges for autonomous navigation in orchards like occlusions and poses uncommon in existing datasets.

Our research is carried out in the context of the RASberry project [5], which aims to develop autonomous fleets of robots for in-field transportation to aid and complement human fruit pickers.

In our setting, an agricultural robot has to cooperate with human field workers efficiently and comfortably. The workers pick berries into crates either in an open field or in a poly-tunnel. Once a crate is full, the robot will collect the crate and transport it to a destination outside the field for further processing.

This application requires basic communication between humans and robots. The robot has to learn where to go when, how far away from a picker it should stop and when it should leave again.

There are a number of interaction modes to choose from. Voice recognition, haptic interaction using buttons or touch screens, and gesture recognition either through remote observation or worn sensors have all been used in the past. We settled on remote gesture/behavior recognition as voice recognition is made infeasible by windy conditions and worn movement sensors as well as haptic interaction over distance rely on a wireless communication infrastructure that cannot be relied upon to be present in fruit fields.

Figure 1 shows how we are recording this dataset of action and behavior videos suitable to this task, i.e. in an open field at various distances and lighting conditions. We further extract skeletons using OpenPose [8,9] and investigate the influence of sensors and distances on extraction performance.

In other work, OpenPose has been applied in a gait recognition task [10] and for human pose matching [11].

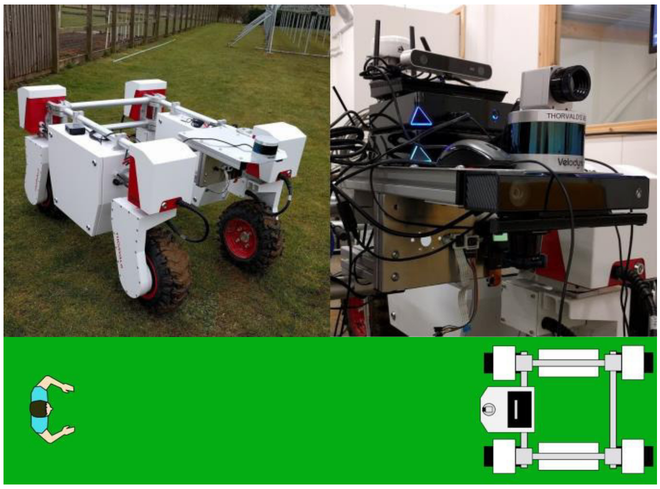

Figure 1: On the left: Our robot (SAGA Robotics Thorvald [6]) in front of our poly-tunnels. On the right: The sensor setup used in the recording. The figure at the bottom shows our experiment setup: An actor performing actions and behaviors at various distances to the robot.

In Section II we will introduce the dataset in detail and motivate the design choices we made. In Section III we will give insight into the features of the dataset with special emphasis on the performance of different sensors at various distances, before concluding in Section IV.

A. Gabriel, N. Bellotto, and P. Baxter are with the Lincoln Centre for Autonomous Systems, University of Lincoln, Lincoln, UK
E-mail: agabriel@lincoln.ac.uk, nbellotto@lincoln.ac.uk, pbaxter@lincoln.ac.uk.

II. Dataset Features

The choice of activities and decision to record at various distances are inspired by our application, the collection of fruit crates from human field workers and transportation of said boxes to a cooling facility outside the field [5]. The dataset was recorded outside, on a piece of grassland, under varying lighting conditions (sunny, cloudy, morning to afternoon) and at distances ranging from 5m to 50m, at 5m intervals. Recording at different distances allows us to determine the performance of sensors and algorithms over the interaction range that the robot will face in action.

We recorded 10 actors, performing every activity once at each distance. Behaviors were performed from the front, back and side for a basic coverage of different directions.

The gestures were chosen for their relevance in basic communication between human and robot, the activities as a sample of interesting behavior displayed by human fruit pickers.

Thereafter each frame up to 25m distance was labeled with distance, actor ID, action and the direction the actor was facing. Labeling at further distances was hampered due to the actor being too small in the frame. The following list gives a short overview of dataset features:

- Distances: 5m – 50m at 5m intervals
- Actors: 10 actors, recorded individually
- Sensors: ZED stereo camera (RGB video and depth video), Optris thermal camera (thermal video), Velodyne VLP-16 (stream of 3D point clouds)
- Gestures: Waving, beckoning, indicating to stop, shooing, thumb up, thumb down, lower arm up, lower arm down, pointing
- Activities: Walking*, turning*, crouching down, standing up; with a crate in hand, (marked classes also without crate)

We chose a range of behaviors observable from human fruit pickers at work, and a set of gestures we deem helpful for basic communication over distances between 10 and 50 meters in the context of our application (i.e. directing a robot to collect and transport crates). The following two subsections will give a short overview of the gestures and activities.

A. Gestures

To direct the robot's attention to the worker in need of support, we selected a waving and a pointing gesture.

Waving: With the upper arm stretched out to the side, a rhythmic side to side motion of the lower arm.

Pointing: With the upper arm stretched out to the front, fist clenched except for the index finger which is also outstretched. We recorded this gesture at 0°, 45°, 90°, 135°, 180°, 225°, 270°, and 315° for basic directional coverage.

To facilitate comfortable and efficient loading of the robot, we want to direct it to a preferred stopping distance. For this we selected the beckoning, stop and shoo gestures.

Beckoning: With the arm partly stretched out to the robot and the palm facing the body, a sometimes circular fanning motion of the hand.

Indicating to stop: With the arm stretched out to the robot, the palm facing away from the body, fingers pointing up.

Shooing: With the arm partly stretched out to the robot and the palm facing the body, a fanning motion of the hand with emphasis (higher speed) on the motion away from the body.

For basic feedback purposes, we included a thumbs up/down gesture and a variant using the lower arm instead of the thumb, which should be easier to detect at further distances.

Thumbs up: With the arm partly stretched out to the robot, fist clenched and thumb sticking out, pointing up.

Thumbs down: With the arm partly stretched out to the robot, fist clenched and thumb sticking out, pointing down.

Lower arm up: With the upper arm stretched out to the side, the lower arm pointing straight up.

Lower arm down: With the upper arm stretched out to the side, the lower arm pointing straight down.

For sample stills of the recorded gestures, please refer to Figure 2 at the bottom of this page.

B. Activities

The most common activities in our domain are - besides the picking of berries - walking and turning around, crouching down, and standing up. Each of these activities occurs with free hands and while carrying a crate.

Being able to detect different behaviors allows the robot to learn activity models, specific to each individual worker, which allows it to predict the timing of future support requests.

Walking 5m with/without crate: Recorded from the front, the back, the right and left side.

Turning 90° with/without crate: Recorded from the front, the back and the right side.

Figure 2: A sample of the gestures we collected for the dataset. From left to right: wave, come, stop, shoo, thumb up, thumb down, lower arm up, lower arm down, pointing anti-clockwise at 45° intervals. The skeletons shown are 2D skeletons back-projected from 3D skeletons generated by the 'Lifting from the Deep algorithm' [7] run with OpenPose [8,9] 2D skeletons as input.

Turning 180° with/without crate: Recorded from the front.

Crouching down with crate: Recorded from the front, the back and the right side.

Standing up with crate: Recorded from the front, the back and the right side.

Table 1 shows the average duration for each action and behavior. The individual actions have a relatively short (<4s) duration and many of them like waving, shooing or the 'come' gesture consist of many, much shorter movements. A system running motion-based Action Recognition on this dataset will have to perform at a challenging framerate in order to capture these movements correctly.

TABLE I. AVERAGE DURATION PER ACTIVITY

Activity	Average Duration	Activity	Average Duration
Wave	3.73	Come	2.20
Shoo	2.22	Stop	2.25
Thumb up	1.71	Thumb down	1.90
Arm up	1.92	Arm down	2.09
Crate down away	1.83	Point 0	1.92
Crate up away	1.29	Point 45	1.91
Crate down side	1.21	Point 90	2.00
Crate up side	1.30	Point 135	1.82
Crate down toward	1.34	Point 180	1.81
Crate up toward	1.11	Point 225	1.88
Walk away	3.20	Point 270	1.99
Walk away (crate)	2.20	Point 315	3.20

III. DATASET CHARACTERIZATION

For the characterization of the dataset we combined the hand gesture classes (wave, come, stop, shoo, thumb up, thumb down) into a single class (hand gesture), as the skeleton models we use [7,8,9] do not support hand detection. Detection of individual fingers at longer distances is further complicated and ultimately prevented by sensor resolution.

The dataset was recorded outside which allows us to record at a wider range of distances and provides a natural variety in lighting conditions. The flat grassland, on which the dataset recording took place, is a well enough approximation for the flat ground we find in poly-tunnels, but does not feature enough occlusion of feet and lower legs or variations in ground level to model conditions in open fields.

Our data does not contain occlusions of the upper body except for self-occlusions from body parts/held items (crates). In this respect it is less challenging than the intended domain.

Recording outside allowed us to examine how larger distances affect skeleton extraction in our setup. Skeletons were extracted using OpenPose [8,9] from the RGB video as well as a color-coded version of the thermal camera feed. An example of the extracted skeletons is shown in Figure 3.

The confidence scores for skeleton extraction shown in Figure 4 are averages of the confidence scores produced by OpenPose for each skeleton. They are averaged over the duration of actions for different sensor sources individually.

The data shows significantly better skeleton extraction for action classes where the actor is facing the camera (arm down, arm up, wave, hand gestures, 'towards' gestures) compared to classes where the actor is facing to the side or away ('side' and 'away' gestures). This stems from self-occlusion of the further body side occurring in side views and self-occlusion of the arms by the torso when the actor is performing some action while facing away from the camera.

To note are also differences in scores for skeleton identification between the two sensors (see Figure 4), with the thermal source providing better skeleton identification for certain actions – a result that can be taken advantage of in the varying field conditions likely to be encountered.

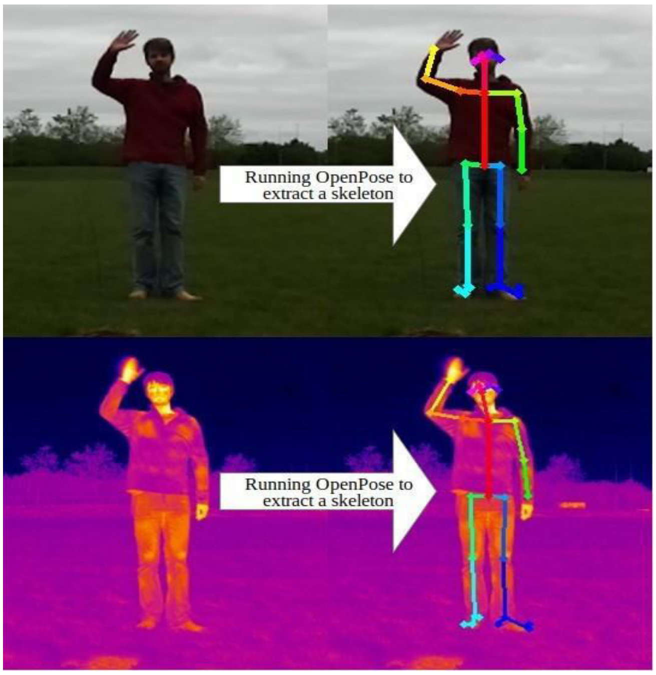

Figure 3: Results of running OpenPose on RGB video (top) and color-coded thermal video (bottom).

Another interesting result are the generally higher scores for skeletons generated from RGB at close range combined with the lower scores for these skeletons at long range. This validates our initial intuition that the wide-angle lens on the RGB-D camera would prove beneficial at short range but a disadvantage at long range compared to the thermal camera. In general, skeleton extraction confidence tends to deteriorate at large distances for both sensors.

IV. CONCLUSION

Our experiments show a difference in skeleton extraction performance over the two sensor types based on the distance of the subject to the sensor. We expect additional differences based on the lighting and temperature conditions as the regular RGB video will lose contrast in the evening hours and turn to a black video in a night setting while the thermal sensor should continue to function well. In another setting like for example a humid green house, the atmospheric temperature might be close to the body temperature of a person and thus reduce the detection performance of the thermal sensor. As would be expected, subject orientation further has a big influence on detection performance.

These considerations show us that datasets fitting the task area, sensor setup, and recording scenario are crucial to the development of algorithms applicable in real life.

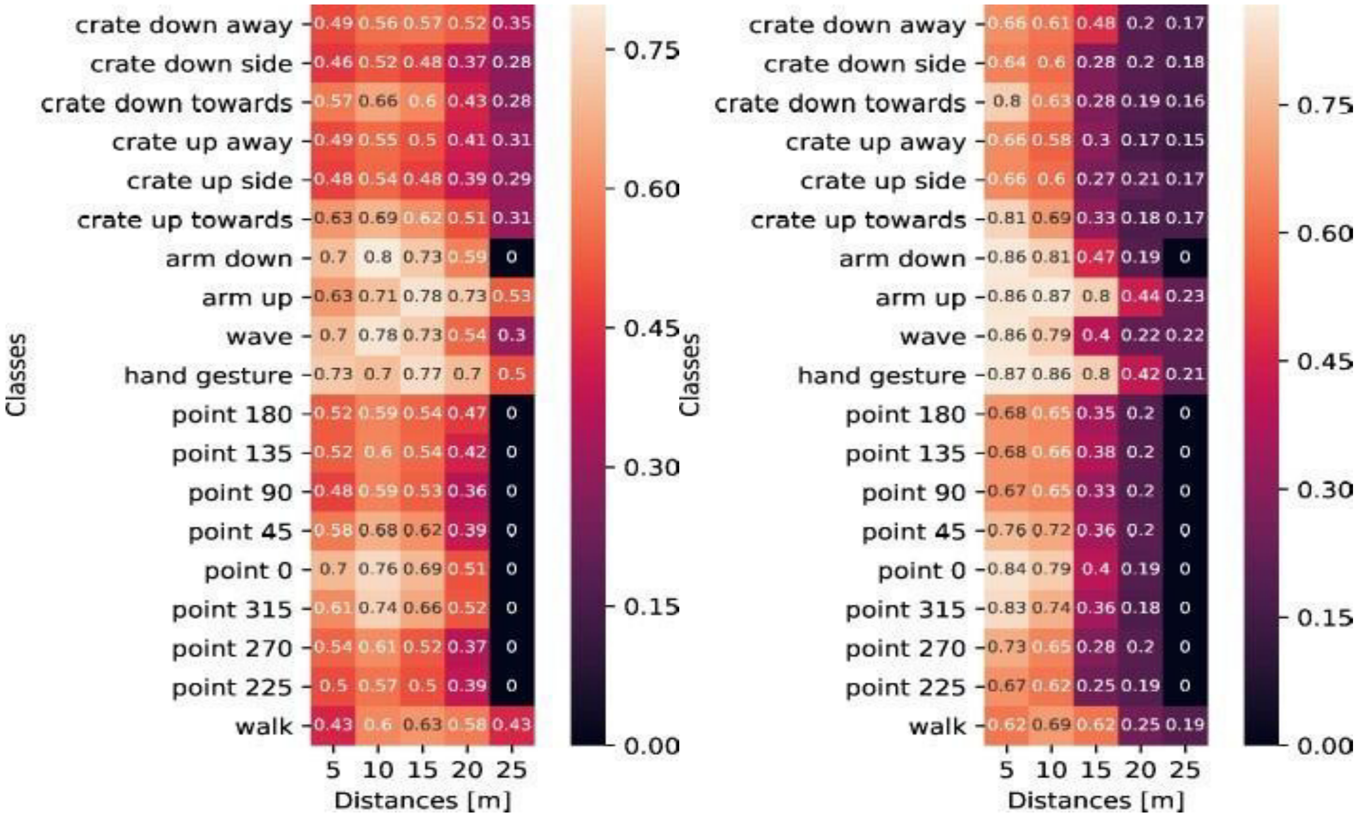

Figure 4: Average Skeleton detection confidence for Optris thermal sensor on the left and ZED RGB-D sensor (single RGB video) on the right. Distances on the X-axis from 5m to 25m, confidence values ranging from 0 to 1. Notable is the higher performance of the ZED camera at short range, but lower performance at long range. Also notable is the performance dependence on viewpoint. Actions facing the camera are generally captured better.

The recognition of actions is an important aspect of interacting with humans. However, this only encompasses the overt behavior of the humans in the vicinity of the autonomous robots. Equally important is the identification of the (covert) intentions of the humans when acting. It is from these that the robots would be best able to plan an appropriate response, whether this is providing physical assistance (e.g. moving to the appropriate location) or enhancing safety (e.g. proactively moving out of the way). Our goal in establishing the data processing pipeline, whose beginning is introduced in this paper, is to provide the data to address the issue of intention recognition. We will proceed to integrate more sensors which should lead to more robust pose estimation over a greater variety of conditions. In the case of the 3D LIDAR, we expect to gain approximate pose estimation for subjects outside the field of view of the directional sensors. The pipeline will further be supplemented with contextual information drawn from other robot systems, such as navigation, mapping, scheduling, etc.

The completed system should react to commands given by workers, track individual worker progress towards a full crate to preemptively navigate toward the next task, and learn individual worker's preferences when it comes to a comfortable stopping distance.

ACKNOWLEDGMENT

We thank the RASberry project (https://rasberryproject.com) [5] and its researchers as well as our voluntary actors for their support and cooperation.

REFERENCES

[1] W. Kay, K. Simonyan, B. Zhang, C. Hillier, F. Viola, T. Green, T. Back, P. Natsev, and A. Zisserman, "The Kinetics Human Action Video Dataset.", 2017.

[2] A. Shahroudy, J. Liu, T.-t. Ng, and G. Wang, "NTU RGB+D: A Large Scale Dataset for 3D Human Activity Analysis," 2016.

[3] F. Caba Heilbron, V. Escorcia, B. Ghanem, and J. Carlos Niebles, "Activitynet: A large-scale video benchmark for human activity understanding." in CVPR, pp. 961–970, 2015.

[4] Z. Pezzementi, et. al., "Comparing apples and oranges: Off-road pedestrian detection on the National Robotics Engineering Center agricultural person-detection dataset," Journal of Field Robotics, vol. 35, no. 4, pp. 545–563, 2018.

[5] P. From, L. Grimstad, M. Hanheide, S. Pearson, and G. Cielniak, "RASberry - Robotic and Autonomous Systems for Berry Production." Mechanical Engineering Magazine Select Articles, vol. 140, no. 6, pp. 14-18, 2018.

[6] L. Grimstadt, and P. From, "The Thorvald II agricultural robotic system." Robotics, vol. 6, no. 4, p. 24, 2017.

[7] D. Tome, C. Russell, and L. Agapito, "Lifting from the deep: Convolutional 3D pose estimation from a single image," CVPR, pp. 5689–5698, 2017.

[8] S. Wei, V. Ramakrishna, T. Kanade, and Y. Sheikh, "Convolutional pose machines," CVPR, pp. 4724–4732, 2016.

[9] Z. Cao, T. Simon, S. E. Wei, and Y. Sheikh, "Realtime multi-person 2D pose estimation using part affinity fields," CVPR, pp. 1302–1310, 2017.

[10] X. Gu, F. Deligianni, B. Lo, W. Chen, and G. Yang, "Markerless Gait Analysis Based on a Single RGB Camera," IEEE 15th International Conference on Wearable and Implantable Body Sensor Networks, pp. 42–45, 2018.

[11] J. Wilms, G. Beckers, T. Callemein, L. Geurts, and T. Goedemé, "Human Pose Matching", Dortmund International Research Conference, pp. 65–69, 2018.

Semantic enhanced navigation among movable obstacles in the home environment

Nico Sun, Erfu Yang, Jonathan Corney, Yi Chen and Zeli Ma

***Abstract*— An autonomous household robot has to be able to navigate through a variable environment and perform common household tasks. Additionally, in cluttered and narrow homes movement can become impossible unless obstacles are moved out of the way. Both challenges involve the manipulation of objects and a planning algorithm that can integrate the function of regions and objects to avoid the creation of new safety hazards during robot movement. We present a semantic detection method during path planning using a gridded semantic map to improve navigation among movable obstacles (NAMO) and support for simple household sub-tasks like cleaning a table and moving obstructing objects to another location. In our tests, the spatial planning was completed well within human reaction time, which is important for a natural interaction between a human and a robot.**

I. Introduction

Today's mobile robots navigate on a binary map, often scanned using Simultaneous Localization and Mapping (SLAM), dividing the workspace into free space and fixed obstacles. Some algorithms explored Navigation Among Movable Obstacles (NAMO), creating a ternary map (fixed obstacles, movable obstacles and free space). But robots operating in a human environment need to have a more complex understanding of their environment for autonomous navigation due to random temporary obstacles being placed in their way (e.g. chairs, bags) and it is frequently not possible to re-plan a new path (e.g. apartments with only one corridor).

Humans can easily identify what obstacles are movable and require the least effort to clear a path. However, obstacles are not always moved to a position which would require the least amount of effort, because this position would block another path which would need clearing at another time e.g. a doorway or a hazardous location (like right behind a corner). While a corridor. traditionally is empty space in navigation it isn't suitable to place an obstacle there because other people need to move through it. Perhaps the most dramatic example is a fire escape. This space needs to be encoded as free to move through, but not free to leave obstacles in it.

The main focus in robotic navigation has been getting from point a to point b. Rather than moving to a specific x/y coordinate humans move to a region or an object which have a dimension and multiple adjacent points as a valid goal location. Navigational planners could emulate this behaviour by checking a semantically annotated map.

In this paper, we use a semantic encoded map to improve the NAMO quality by considering the functions of space. The remainder of this paper is structured as follows: Section II gives an overview of related work in navigation and semantic mapping. Section III describes our semantic detection for navigational planning. Section IV presents our experimental results. Section V discussion and finally we conclude our findings in Section VI.

II. Related Work

There exists an extensive literature on robot navigation however given the compactness of this paper we discuss only the two closest aspects.

A. *Navigation Among Movable Obstacles*

Existing NAMO algorithms can solve very complex environments with a large number of obstacles, but typically these environments are rooms with random obstacles and don't resemble a household or office. e.g. one room with 20 chairs, tables and a few sofas[1][2][3]. The obstacle placement decision is also devoid of any function of space or the blocking of other paths. Additionally, an execution time of a few seconds is perceived as too long for a typical human interaction.

Algorithms that divide the space into free connected space regions and occupied regions won't be useful for 3D maps because in 3D there will be only one free space region for most objects which could theoretically be moved along the ceiling. This, however, is not a practical approach to deal with obstacles.

B. *Semantic Mapping*

Semantic mapping has been developed to give sensor data a meaning similar to the human perception of the environment. Simple semantics exists as a topological map, circles representing rooms and lines connecting rooms without metric information [4]. A more direct encoding of semantics into a navigation map with bounding boxes has been done in [5]. By using an RGB-D camera and convolutional neural network (CNN) semantic mapping has been done pixel by pixel on a 3D point cloud map from a SLAM algorithm [6][7]. Further research is needed to evaluate each semantic mapping method and their usefulness for autonomous navigation and household task performance.

In order to use the maps spatial semantic knowledge for complex household tasks, it needs to be combined with action-related and common-sense knowledge as in a semantic network [8][9]. The knowledge relates objects to another or to regions e.g. “microwave located in the kitchen” and their function e.g. “microwave can cook food”.

III. Our Approach

In order to encode different functions in a home environment, we utilize three layers for a 2D floor map, visualized as an RGB image with some predefined pixel by pixel encoded semantics. One layer for objects & obstacles, one for dynamic entities (humans, pets) and one for the room property or function.

For the robot pathfinding (start to goal) we use a bi-directional rapidly exploring random tree (Bi-RRT) algorithm (Figure 2) with a 5% goal bias. Bi-RRT is a variant of the simple RRT [10]. Simple RRT is great at exploring a large region of free space, but one single RRT can get stuck against a wall and have a hard time finding a gap like a doorway. In our tests, bi-directional RRT proved to be 3-10 times faster than a single tree, which is similar to findings in [11]. Due to the nature of a home robot environment – the interaction with humans. A solution should be found within human reaction time. Previous robots have been found to be too slow and unresponsive [12]. This gave preference of simple RRT over RRT*. After a solution is found we employ local path smoothing (Figure3) for a more natural motion.

The path planning and semantic detection (includes collision check) are done in Cartesian space instead of configuration space to avoids the recalculation of the space every time the robot moves an obstacle. The semantic detection of objects for the planner is done with OpenCV by finding the specified semantic value on the map and extracting its dimensions (contours). During path planning in the RRT algorithms, the semantic detection checks the map with the bounding box of the robot or movable obstacle and disregards a point when the bounding box touches another obstacle.

When the robot path is blocked by an obstacle the NAMO RRT, a simple modification to the RRT algorithm (see code) searches for a new collision free position that doesn’t obstruct the robot's path or collide with other obstacles. The improvement of NAMO quality is done by excluding regions encoded on the semantic map as valid goal positions. This semantic check is only done after a new node is added to the RRT and not every time a node is checked against permanent obstacles. In our tests, for example, we excluded doorways as valid goal positions.

Algorithm 1 Semantic detection during RRT

```
Map definitions
Op = permanent obstacles
Om = movable obstacles
Rf = free region
Rb = blocked region

Robot navigation
map = SemanticMap(Op,Om,Rf,Rb)
goal = map(x,y)
while True do
    rnd = random(map)
    if rnd in Op then
        continue
    else
        add rnd to path
    if rnd in goal then
        break
    if smoothed path in Om then
        add Om to NAMO task

    Movable obstacle goal check
    if rnd in goal then
        if rnd in Rb then
            continue
        else
            break
```

IV. Test/Evaluation

We perform the evaluation in Python 3.6 and single threaded on an Intel Core i5 2400 (3.1GHz). Ram usage is 60MB to load the 1000x800 three-layer test map + simple UI interface. During path planning, an additional 20MB is used for the computation of the robot path and new obstacle positions. The map resolution is 1cm/pixel, hence representing an apartment of 10m x 8m. The spatial semantic knowledge data is stored in NumPy arrays and visualized with matplotlib as an RGB image.

Pre-defined semantics and their visualization:

- Regions (red layer): unknown, sink, sinkstorage, TVcarpet, doorway, foodtable
- Dynamic Entities (green layer): unknown
- Objects (blue layer): unknown, plate, cutlery, TVtable,TVstool,plant,chair,foodtable, bed, shower

After an object is moved the map gets automatically updated (old position encoded as free space in object layer and new location encoded with the value of the object) For a better illustration of the skills we use the unused green layer (dynamic entities) to enhance the contrast between the objects original and new position and dimensions.

As expected, checking a point against a list of semantic values takes longer than checking against a single value representing all obstacles. The time increase depends on the number of total semantic values. In our tests with 1000 known semantic values, the calculation time increased by a factor of 15-30. From 0.213s for one million single value to 3.1-6.7s for the same number of multiple value checks. So any path planning algorithm should still perform single value collision detection against unmovable obstacles to reduce the number of slower semantic checks.

A. *Move to region or object*

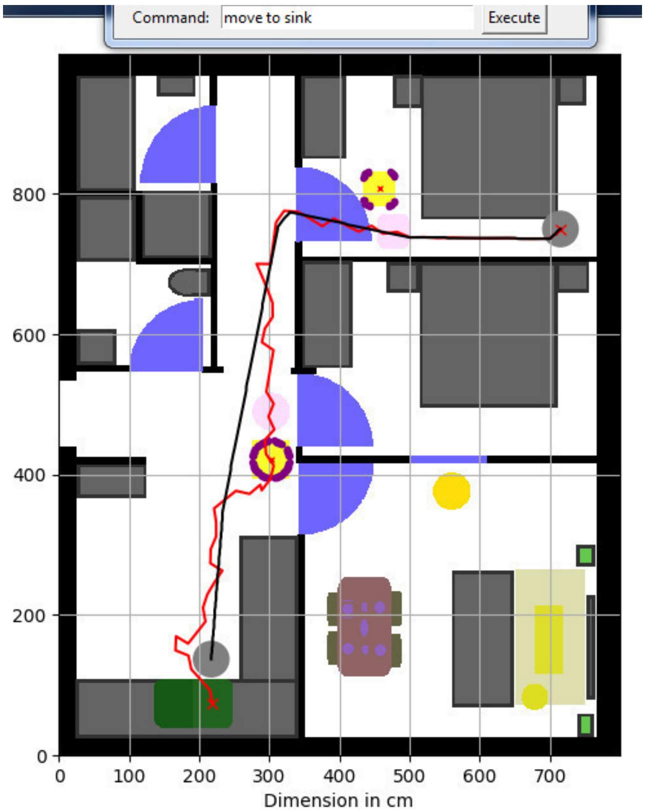

Figure 1: Robot skill: “Move to region/object” The robot (light grey) is in the upper right is instructed to move to the sink(green). The red line shows the raw path found by the Bi-RRT algorithm and the black line shows the smoothed path. In light red are the original obstacle positions & the purple dots outline the new positions for any moved obstacle.

Metric	Bi-RRT time in seconds	NAMO-RRT (seconds)	Robot Path cost	Obstacle path cost
Average	0.099	0.095	1049	199.0
Standard deviation	0.043	0.055	10.44	136.9

Table 1: Performance analysis for the task "move to sink". For our two-obstacle example, the planning time for the obstacles is the same as for the robot pathfinding. While the robot path with a fixed goal region shows very little variations in length the obstacle movement shows high variation due to a flexible goal position.

B. *Movable obstacle placement of semantic NAMO algorithm*

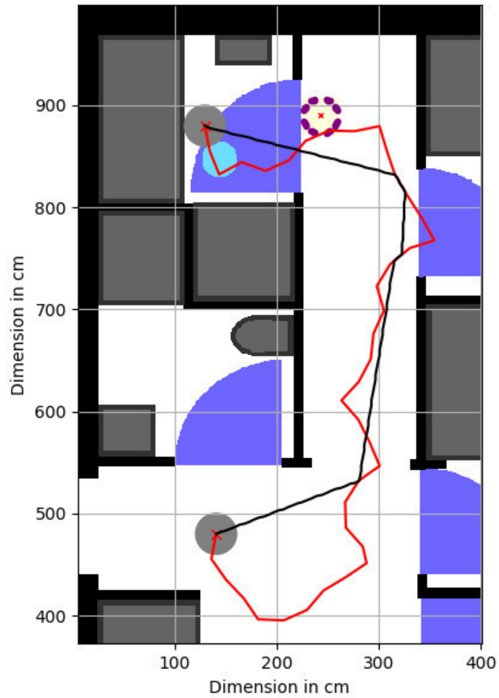

Figure 2: obstacle placement when considering semantics. The robot (light grey) is instructed to move from the lower left to the bathroom. The red line shows the raw path found by the Bi-RRT algorithm and the black line shows the smoothed path. The NAMO algorithm avoids placing the washing basket (light blue/purple dots) into the doorway (blue)

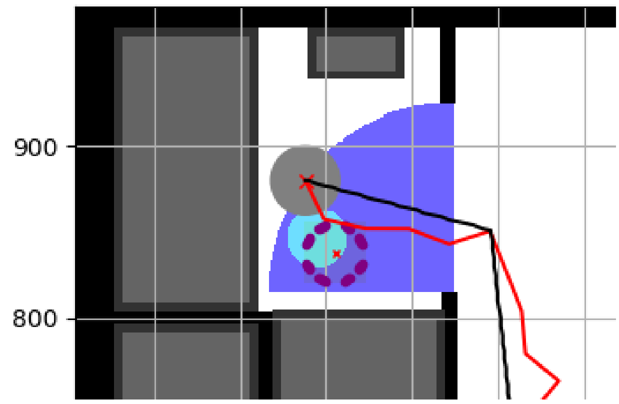

Figure 3: The same navigation task as in Figure 2 without exclusion of the door space(blue) as a valid goal position.

The obstacle movement cost (Table1) includes the cost of moving the robot and the relative size of the object compared to the robot. Small objects will have a negligible cost and large objects will have a high cost of moving. The performance analysis was done with 1000 samples in each test, a robot with a round base of 25 cm radius and an RRT expand distance of 20cm. For obstacles, the RRT expand distance is 10cm.

Equations for path cost:

$$C_R = d \tag{1}$$
$$C_o = (1 + A_o/A_r) * d \tag{2}$$

$C_R = Cost\ of\ moving\ robot, d = distance$
$\mathrm{C_o} = \mathrm{Cost\ of\ moving\ obstacle, A = Area}$

C. Moving objects to another region

When moving many small objects compared to the robot's size, the objects don't need additional collision detection. With the previously shown path cost calculation it's possible to calculate when it's more efficient to move the objects individually or to get a known container from a nearby place and move multiple objects at the same time. The semantically encoded map already includes the location and dimension of the goal region, therefore eliminating the need to compute a path for each individual object between its origin and goal position. Instead we only need to compute one path for the robot between the two regions and a short path for each object from the goal region to the objects final position.

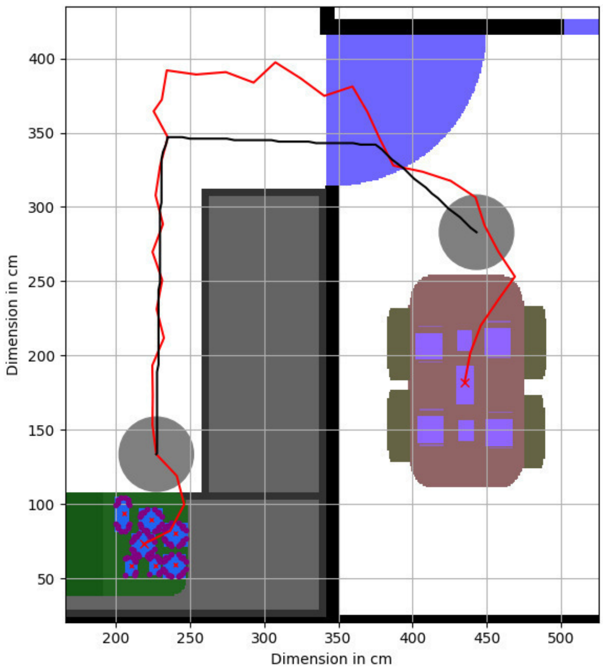

Figure 4: Robot skill: "move objects to a region". The robot moves all cutlery and plates (purple & purple dots) from the table(brown) to the sink(green). The robot path uses the same colours as before.

V. Discussion & future development

The use of semantics in navigational planning isn't restricted to the RRT algorithm, for us the general nature of RRT allowed an easy combination of A to B navigation and spatial task planning for some household tasks.

A real household robot would greatly benefit from a 3D semantic map, especially for small stackable objects. The performance of our currently un-optimized 2D representation was still well within human reaction time and an optimized version has the potential to work in 3D within reasonable human reaction time as well. Further evaluation needs to be done on a scanned semantic map instead of a pre-defined one.

VI. Conclusion

We have presented a semantic detection method during path planning for a gridded semantic map and how it can be used in a cluttered home with movable obstacles. With execution times of well below half a second, the semantics consideration can improve the navigation quality without adding significant computation time. By combining the planning for object placement and robot navigation into one system the system could also be used for practical household tasks, which are not yet well developed and needed in health care. In the future, these spatial planning tasks have to be combined with general knowledge of object functions and their usage/grasping to create household tasks that can be executed without specific prior knowledge of the exact environment.

References

[1] M. Levihn, J. Scholz, and M. Stilman, "Hierarchical Decision Theoretic Planning for Navigation Among Movable Obstacles," Springer, Berlin, Heidelberg, 2013, pp. 19–35.
[2] M. Stilman and J. J. Kuffner, "NAVIGATION AMONG MOVABLE OBSTACLES: REAL-TIME REASONING IN COMPLEX ENVIRONMENTS."
[3] A. Akbari, Muhayyuddin, and J. Rosell, "Task planning using physics-based heuristics on manipulation actions," in *2016 IEEE 21st International Conference on Emerging Technologies and Factory Automation (ETFA)*, 2016, pp. 1–8.
[4] A. Pronobis and P. Jensfelt, "Large-scale semantic mapping and reasoning with heterogeneous modalities," in *2012 IEEE International Conference on Robotics and Automation*, 2012, pp. 3515–3522.
[5] H. Deeken, T. Wiemann, K. Lingemann, and J. Hertzberg, "SEMAP - a semantic environment mapping framework," in *2015 European Conference on Mobile Robots (ECMR)*, 2015, pp. 1–6.
[6] R. Li, D. Gu, Q. Liu, Z. Long, and H. Hu, "Semantic Scene Mapping with Spatio-temporal Deep Neural Network for Robotic Applications," *Cognit. Comput.*, vol. 10, no. 2, pp. 260–271, Apr. 2018.
[7] H. Sun, Z. Meng, and M. H. Ang, "Semantic mapping and semantics-boosted navigation with path creation on a mobile robot," in *2017 IEEE International Conference on Cybernetics and Intelligent Systems (CIS) and IEEE Conference on Robotics, Automation and Mechatronics (RAM)*, 2017, pp. 207–212.
[8] M. R. Petr Masek, "A Task Planner for Autonomous Mobile Robot Based on Semantic Network in Advances," *Adv. Intell. Syst. Comput. 393*, pp. 634–639, 2016.
[9] M. Tenorth, L. Kunze, D. Jain, and M. Beetz, "KNOWROB-MAP - knowledge-linked semantic object maps," in *2010 10th IEEE-RAS International Conference on Humanoid Robots*, 2010, pp. 430–435.
[10] S. M. LaValle, "Rapidly-exploring random trees: A new tool for path planning," 1998.
[11] A. H. Qureshi and Y. Ayaz, "Intelligent bidirectional rapidly-exploring random trees for optimal motion planning in complex cluttered environments," *Rob. Auton. Syst.*, vol. 68, pp. 1–11, Jun. 2015.
[12] E. Martinez-Martin and A. P. del Pobil, "Personal Robot Assistants for Elderly Care: An Overview," Springer, Cham, 2018, pp. 77–91.

A Mixed Reality Approach to Robotic Inspection of Remote Environments

Elisabeth Welburn[1], Thomas Wright[2], Conor Marsh[2], Sean Lim[1], Ananya Gupta[1], William Crowther[2] and Simon Watson[1]

***Abstract*— Currently, inspection of remote environments poses potential hazards to the human operator. Mixed reality presents the unique opportunity for the human operators & the piloted robots to co-exist within a virtual world that is then spatially mapped to the physical world. This can then act as a platform to conduct remote inspection, where the human operators could potentially possess heightened situational awareness and control.**

I. Introduction

Remote inspection and asset management of offshore wind farms and their connection to shore is an industry that will be worth £2 billion annually by 2025 in the UK alone [1]. Deploying human personnel in such environments is often dangerous and costly. In these circumstances, robotic platforms displacing human personnel removes these associated risks. However, the viability of such an endeavor is contingent upon the robot's ability to maneuver effectively around the associated space. It is also imperative that the sensory data gathered is appropriate and sufficient for inspection of the infrastructure.

It is challenging to endow a robot with the capability to perform high-level mission planning based on environmental cues [2]. As a result, human involvement to varying degrees is often a necessity during robotic operation. Remote human-robot interaction has been limited to a screen interface up until recent years; where there has been a shift to more involved mediums [3]. Here, the spatial awareness of the operator is limited by the sensing capabilities of the remote inspection robot.

Virtual reality (VR) is becoming increasingly more prevalent in human-robot interaction systems; an example of which is the construction of the surrounding three-dimensional space visualized in VR, that is based upon two-dimensional images taken by a camera mounted on a ground vehicle [4]. However, VR can be limited to interaction within the virtual world, resulting in a more passive role for the participant, such as walkthroughs and demonstrations.

Mixed reality (MR) environments are where both real and virtual world objects are presented together on a singular display [5]. Ideally, the mixed reality system is capable of real-time, bi-directional feedback between the virtual and physical worlds [6]. This concept is encompassed by the *Digital Twin* paradigm where a digital replica of a physical asset is constructed to aid real-time monitoring as well as mission forecasting. This could potentially boost safety and reliability through the creation of an immersive virtual environment that would be immediately reactive to any external disturbances [7].

MR presents the opportunity to use a virtual world to interact with real world physical environments, potentially increasing visibility of regions of interest. MR also presents a method to implement a simulated system alongside a real-world system. This could facilitate debugging by providing a direct comparison between simulated and physically deployed quadcopters during inspection.

This paper presents a novel Single Operator of a Singular Robot (SOSR) MR system that enables the operation of a physical quadcopter through the use of a digital twin that exists within a virtual world. This system forms the basis of a remote teleoperation system that will be developed within the future. It was developed as part of an outreach activity that was demonstrated at the Manchester Science and Industry Museum as part of the Manchester Science Festival 2018.

II. Literature Review

Perhaps the most engaging feature of MR is how it enables control of complex system via an intuitive interface. Rosen et al. sought to quantify this enhancement by directly comparing the use of a more traditional 2D display with MR. In this experiment, several participants were asked to decide whether a robot arm collided with certain obstacles using the two systems and no visualization mode. It was found that MR led to a reduction in task completion time by 7.4%, increased precision by 11% and increased accuracy by 16% on average in comparison to the 2D display. The lack of a visualization interface was found to produce the worst results on average [8].

Human-robot interaction can take many forms; perhaps the most intuitive of which is the use of natural gestures. Crespo et al. sought to improve the quality of life of the elderly populace through the creation of a mixed reality interface to operate a drone. Interaction was enacted through the use of Rasberry Pi and additional 'Sense HAT' boards attached to the participants' arms. The data from the sensors was transmitted via Bluetooth to a smartphone that then ran the virtual reality simulation. This was subsequently visualized with Google cardboard headsets [9].

Honig et al. presented several use cases where mixed reality could be employed. The first of which was drones following humans in close proximity. The humans were visualized within the virtual world to ensure clearances were maintained. The

[1] School of Electrical and Electronic Engineering, University of Manchester.
[2] School of Mechanical, Aerospace, and Civil Engineering, University of Manchester.

second was the creation of additional virtual agents to maximize area coverage of a physical, pre-existing robotic swarm. The third use case presented was the identification of Turtlebots using AR tags that are then read by a downward-facing camera mounted on a virtual quadcopter flying overhead. Both virtual and physical Turtlebots were tracked using the simulated on-board camera. In both of these use cases, the physical robots deviated from the goal trajectories more due to latency and external disturbances, such as air currents [6].

Phan et al. used a mixed reality interface to allow for closed-loop control of multiple Crazyflie drones from multiple human operators within the same vicinity. The Unity client received current pose information from the VICON and PhaseSpace motion tracker systems and sent new goal positions to ROS base stations via a Python TCP socket connection. Commands are then transmitted to the Crazyflie drones with the use of a radio frequency radio. The path planning was implemented within Unity with the use of a navigation mesh generated by an A* search algorithm. Markers were attached to obstacles, such as a physical door, as well as humans and drones. The markers are tracked and this data is utilized to inform rendering within the virtual world. Within the experiment, a pair of drones followed each human operator. As a human transversed through a door, the drones broke formation to follow suit. To ensure collision avoidance, a radius boundary of 0.5m was placed around the rendered obstacles [10].

The enhanced spatial awareness MR endows the human operator in the study performed by Rosen et al. [8] is particularly beneficial when maintaining clearances in the remote inspection scenario considered in this paper. The use of natural, intuitive gestures to control the robot, as in Crespo et al. [9], reduces the perceived workload for the operator. As a result, a point-and-click mechanism was implemented to designate the waypoints for the quadcopter trajectory.

Both Honig et al. [6] and Phan et al. [10] investigated several use cases where drones were operated using MR in the vicinity of the human pilots. Within these studies, the drones were successfully navigated. This MR system was developed with a view of extending this concept for use in remote inspection operations.

III. Methodology

This section details the software architecture involved within the MR system. The interactions between different software components have been depicted in Figure 1.

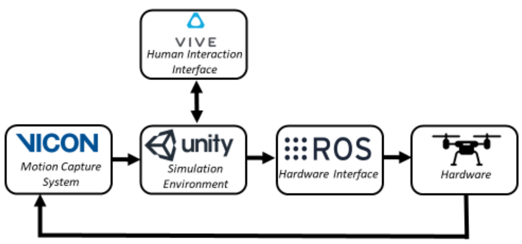

Figure 1: Software Architecture of the Mixed Reality System.

A. Robotic Platform

Remote environments are often difficult to access and navigate. In such situations, aerial robots enable superior coverage and flexibility during inspection. The selected morphology of the aircraft is a quadcopter due to their high maneuverability. A 27g Crazyflie drone was selected as an exemplar robotic platform due to its small size, low price and Robot Operating System (ROS) compatibility.

Figure 2: A Crazyflie Drone equipped with VICON markers.

B. VICON Motion Capture System

Markers were placed upon the Crazyflie drone as depicted in Figure 2. These were then selected and a rigid body object was created that represented the Crazyflie within the VICON space. The markers had to be placed asymmetrically in order to differentiate the axes of rotation of the Crazyflie. A ROS package, VICON bridge[3], identified the DataStream server as a separate machine based upon the specified IP address.

The ROS node VICON bridge published the object pose data from the VICON in the form of a *TransformStamped* ROS message. A ROS node was written that subscribed to this and converted it into a *PoseStamped* ROS message that was then published.

The VICON system was set up using nine cameras attached to a steel rig in the demonstration, as depicted in Figure 3.

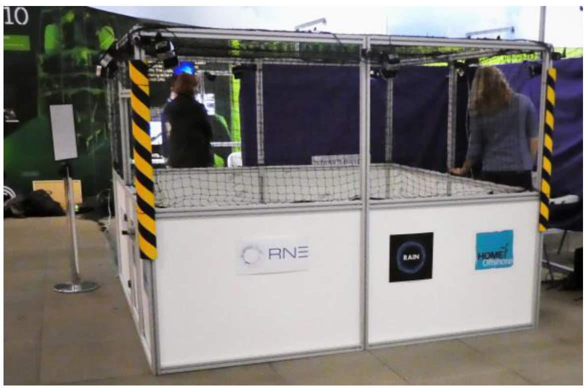

Figure 3: The VICON Cage to Capture the Crazyflie Movements at the Manchester Museum of Science and Industry.

[3] The ROS *VICON bridge* package is available online at http://wiki.ros.org/vicon_bridge

C. Virtual Reality World

The virtual reality system selected was the HTC Vive pro due to the pre-existing plugin, enabling compatibility with the game engine, Unity. The virtual world was constructed within Unity, utilizing the in-built physics engine. This consisted of a simulated quadcopter situated on an operational wind turbine. The operator was able to view the in-hand controllers within the simulation. A point-and-click mechanism was used to locate waypoints for the drone, where one waypoint exists at any one time. This method is intuitive for the human operator, reducing perceived workload. The current waypoint was represented by a red sphere in the virtual world. A red sphere was chosen because the stark contrast of the colour and morphology relative to the environment aids visualization of the waypoint within the 3D space. This was then published as the 'goal' position of the drone in the form of a *PoseStamped* ROS message.

An A* path planning algorithm was utilized within the Unity game engine. In order to enable a fast, on-the-fly remapping of the generated path, the target destination had to be relatively close of the current distance. This was ensured with the use of a Seeker component within Unity. This acted as an intermediate waypoint, accounting for the current trajectory and target destination. This mechanism had the effect of splitting the original trajectory into a series of segments. This Seeker component was published as a PoseStamped ROS message alongside the goal position.

D. ROS Interface

Both the goal and seeker component poses were visualized in Rviz alongside a Crazyflie URDF-generated robot model, animated using the VICON Bridge *TransformStamped* message. This was a useful debugging tool, and enabled fine tuning of the parameters of the seeker component within Unity.

The seeker component was published as the goal to the Crazyflie at a frequency of 120 Hz. An on-board PID controller and IMU performed the low-level control during flight.

IV. Evaluations

The Mixed Reality system outlined within this paper was demonstrated at the Museum of Science and Industry in Manchester, UK. It was observed that the Crazyflie drone successfully flew to the vicinity of the designated waypoint. A certain amount of overshoot was present within the trajectory. This may have been due to imperfect tuning of the PID values to account for the additional weight of the attached VICON markers. This could have also been affected by the constraint radius of the Seeker component being either too large or too small, not allowing for the application of sufficiently fast stabilizing torques.

The operators who, for the most part, had no experience in piloting drones, found the point-and-click mechanism intuitive to operate. However, some reported that the precise placement of the waypoints was difficult due to poor depth perception. This could be alleviated by offering an aerial view of the virtual space in conjunction to the current viewpoint based upon the operator's positioning. Unfortunately, implementation of this would potentially increase the perceived workload of the human operator, reducing the sense of presence.

V. Conclusions

In conclusion, the mixed reality system outlined within this paper is applicable to tele-operation of a multitude of mobile robotic platforms in remote environments. The additional scaling and rendering functionalities coupled with the enhanced situational awareness for the human operator result in mixed reality being an invaluable tool for remote inspection.

Future planned work includes qualitative studies of the performance of human operators using MR systems to control remote inspection robots. Both static and dynamic obstacles could be inserted into the mixed reality to ascertain the navigational capabilities within confined areas. This SOSR system could also be further extended into a Single Operator of Multiple Robots (SOMR) system that could facilitate the coordination of a robot swarm. This system utilizes only the exocentric perspective of the controlled agent. In the future, this could be compared to an egocentric control interface in terms of spatial awareness and ease of use.

Acknowledgments

The authors would like to thank the HOME-Offshore project (EPSRC reference: EP/P009743/1) and the Complex Autonomous Aircraft Systems Configuration, Analysis and Design Exploratory (CASCADE) project (EPSRC reference: EP/R009953/1) and the University of Manchester for the provided funding and support.

References

[1] E. M. Barnes *et al.*, "Technology Drivers in Windfarm Asset Management Position Paper," pp. 1–46, 2018.

[2] J.-C. Latombe, *Robot Motion Planning*. Springer US, 1991.

[3] T. Kot and P. Novák, "Application of virtual reality in teleoperation of the military mobile robotic system TAROS," *Int. J. Adv. Robot. Syst.*, vol. 15, no. 1, Jan. 2018.

[4] L. A. Nguyen *et al.*, "Virtual reality interfaces for visualization and control of remote vehicles," *Auton. Robots*, vol. 11, no. 1, pp. 59–68, 2001.

[5] P. Milgram and F. Kishino, "A Taxonomy of Mixed Reality Visual Displays," *IEICE Trans. Inf. Syst.*, vol. E77–D, no. 12, pp. 1321–1329, Dec. 1992.

[6] W. Honig, C. Milanes, L. Scaria, T. Phan, M. Bolas, and N. Ayanian, "Mixed reality for robotics," *IEEE Int. Conf. Intell. Robot. Syst.*, pp. 5382–5387, 2015.

[7] E. H. Glaessgen, D. T. Branch, D. S. Stargel, and M. Sciences, "The Digital Twin Paradigm for Future NASA and U . S . Air Force Vehicles," pp. 1–14, 2018.

[8] E. Rosen *et al.*, "Communicating Robot Arm Motion Intent Through Mixed Reality Head-mounted Displays," pp. 1–16, 2017.

[9] A. B. Crespo, G. G. Idrovo, N. Rodrigues, and A. Pereira, "A virtual reality UAV simulation with body area networks to promote the elders life quality," *2016 1st Int. Conf. Technol. Innov. Sport. Heal. Wellbeing*, pp. 1–7, 2016.

[10] T. Phan, W. Honig, and N. Ayanian, "Mixed Reality Collaboration between Human-Agent Teams," *25th IEEE Conf. Virtual Real. 3D User Interfaces, VR 2018 - Proc.*, pp. 659–660, 2018.

Multi-Cameras based Decision Making at Mini-Roundabouts for Autonomous Vehicles

Weichao Wang, Quang A. Nguyen, Paul Wai Hing Chung and Qinggang Meng, *Member, UKRAS*

***Abstract*— Safety driving in complicated traffic situations such as at roundabouts is crucial in autonomous vehicle design. Utilising multiple cameras for approaching vehicles detection in real-time has been determined the key challenge in this research area. This paper proposes a grid-based image processing approach that effectively learns the movement, position and direction of approaching vehicles, thus supporting an autonomous vehicle to make a human-like decision at mini-roundabouts. 230 video clips recorded in the UK were examined using three Machine Learning models (i.e. Support Vector Machines, Artificial Neural Network, k-Nearest Neighbours). Experiments indicated that SVM was outstanding with 91.32% accuracy rate in 0.7 seconds. This result suggests that the proposed system is reliable for autonomous vehicles to enter mini-roundabouts safely and smoothly.**

I. INTRODUCTION

Interaction provide challenge for autonomous vehicle in recently years, the autonomous vehicle is threated by many meeting-points in normal interaction when it merge a junction[5]. A roundabout is a useful circular design in improving safety in intersections, both in urban and rural areas. A roundabout is a looping junction where vehicles are restricted to go in one direction around a central island with priority is given to the ones have already entered the roundabout [1]. Roundabouts are widely applied in many countries' road systems and associated with a significant reduction of accidents [2] [3].

Traffic safety in roundabouts is an emerging topic in designing autonomous vehicles (AV). Facing a roundabout, the AV must normally handle a number of tasks including traditional vehicle controls (acceleration, deceleration, turning or braking) and situation awareness (approaching vehicles detection, speed evaluation or position keeping) [4]. Of which, the main issue should be judging the priorities and the behaviours of other vehicles around the roundabout [5]. Given that there could be a number of vehicles moving in various directions and speeds at a time, a roundabout can be considered a very complex driving environment. Enabling an AV to enter a roundabout smoothly and safety, therefore, remains a challenging question.

Many studies have been published in AV driving at roundabouts. For example, Gonzalez et al. [6] presented a path planning method that divided the driving process into three stages: entrance, driving within and exit the roundabout. By minimizing curvature steps, it avoided extensive manoeuver and increase smooth movements in roundabouts. Ziegler et al. [7] introduced a motion planning method for AV in roundabouts using camera recording, radar, and digital road maps. Dinh and Tang [8] proposed a Mixture of Gaussian algorithm to detect approaching vehicles in roundabouts using a single fix camera. Although some positive results have been reported, none of them really consider the mini-roundabout scenarios.

A mini-roundabout, as its name, is a smaller roundabout that built at sites lacking room for a conventional roundabout [9]. Mini-roundabouts even pose more challenges to AV than the normal roundabouts do [6]. Firstly, there is no physical centre island but a traversable painted circle (or a low dome) in a mini-roundabout, hence a higher chance of accidents. Secondly, the close gap between vehicles requires extra cautious in entering the mini-roundabout, especially in mini-roundabouts without a traffic light.

Figure. 1. A mini-roundabout (*source: Wikimedia Commons*)

In this paper, we propose a Grid-based system using multiple cameras to support AV in making the right decision at mini-roundabouts (GB-MC-MR). The system can evaluate the movement, position and direction of approaching vehicles at a

*Resrach supported by Computer Science, Loughborough University.

W. Wang is with the Computer Science department, Loughborough University, UK (corresponding author to provide e-mail: w.wang3@lboro.ac.uk).

Q. A. Nguyen is with the Computer Science department, Loughborough University, UK (e-mail: naquang@gmail.com)

P. W. H. Chung is with the Computer Science department, Loughborough University, UK (e-mail: p.w.h.chung@lboro.ac.uk).

Q. Meng is with the Computer Science department, Loughborough University, UK (e-mail: q.meng@lboro.ac.uk).

mini-roundabout and then decide whether when it is safe to join. To the best of our knowledge, it is the first study in AV path planning that exploited the use of multiple cameras and focused on the mini-roundabouts traffic. On the other hand, our system is fast and reliable to be applied in real-time traffic scenarios.

The rest of this paper is organized as follows: Section 2 describes the proposed GB-MC-MR system. Section 3 presents the detailed of experiments including data acquisition, preprocessing, feature extraction and classification stages. Important factors of the algorithm are highlighted in Section 4 whilst future work is discussed in the final section.

II. PROPOSED GB-MC-MR SYSTEM

This section presents details about the proposed GB-MC-MR. Basically, mini-roundabout traffic video that captured using two cameras is pre-processed to appropriate images (frames). Image processing techniques are applied to each frame to extract its features, which are the closest approaching vehicle attributes, including the position, the speed, and the direction. For training purpose, each frame will be labelled as safe or unsafe that indicates whether the AV should go or wait at the mini-roundabout. The feature vectors and the corresponding labels generated are fetched a machine learning model so that the system can make a local decision from each camera. The final decision will be an integration of two local decisions using a simple rule: it is safe to go if only all local decisions are Go.

In real-time traffic, it is possible to use the system to inform the AV about the moment it can join the mini-roundabout safely.

Key components of the system are illustrated in the following figure:

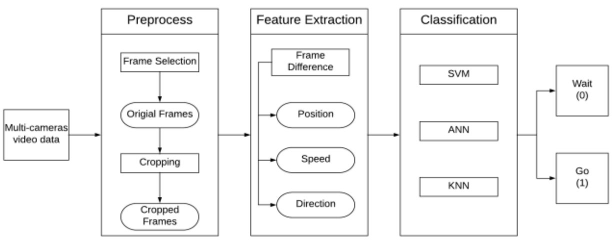

Figure. 2. The proposed system

A. *Data acquisition and preprocessing*

Two identical Nextbase 312GW cameras were utilised to record the traffic video in mini-roundabouts. To simulate the view from the UK driver seat, the cameras were installed on the frontal windscreen (camera A) and the right hand side window (camera B). The cameras worked synchronously, they started recording when the ego vehicle stopped (Wait) at a roundabout. When the ego vehicle started to enter the roundabout (Go), the recording was halted.

Figure. 3. Camera settings from inside the autonomous vehicle

230 pair of video clips were captured at 20 different mini-roundabouts in Leicestershire, UK. The video was recorded in different time frames in the day including peak hours (5 pm to 6 pm) to confirm the robustness of the system in busy traffic conditions.

Data were converted from video to images. In each second of an HD quality video 30fps, six frames were extracted (one in every five frames). Since there were two separated cameras used, each moment was represented by two single frames, frame A and frame B, respectively. The system should, based on the traffic condition showed in the two frames, inform the AV whether it is a safe moment to enter the roundabout.

Frames were manually labelled before passing to the next components. Each pair of frames were labelled as Wait (0) or Go (1) that reflect the decision the AV should make in facing a traffic scenario like what showed in the frames. It is noticed that the camera settings (car stops cameras on – car move cameras off) considerably simplify the labelling process. Only the last frame of each video clip was flagged as Go and the rest were all Wait.

From 230 pair of short clips, 632 samples pairs of frames were generated, providing 230 positive frame samples (Go), and 402 negative frame samples (Wait). Details about processed data are demonstrated in the following table.

TABLE 1. Learning sample statistics for 2 cameras at mini-roundabout (VN: The number of videos, RN: The number of roundabouts, SN: The number of samples, PSN: The number of positive samples, NSN: The number of negative samples, TR: Training sample, TR.P: Training positive sample, TR.N: Training negative sample, TE: Test sample, TE.P: Test positive, TE.N: Test Negative)

VN	RN	SN	PSN	NSN	TR		TE	
					TR.P	TR.N	TE.P	TE.N
230	20	632	230	402	506		126	
					182	324	45	81

B. *Feature Extraction*

That component discloses the descriptions of the closest vehicles to the AV in the pair of frames, including position, speed and direction of that vehicle.

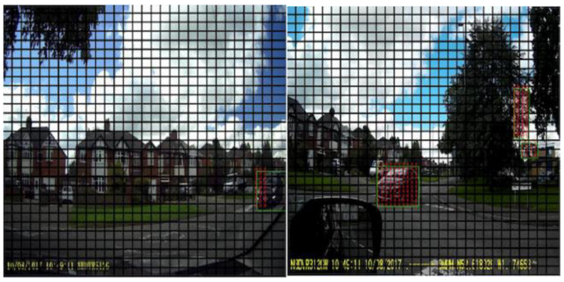

Figure. 4. Approaching vehicle detection in the frontal frame (frame A - left hand side) and the side view (frame B - right hand side)

Various ways of vehicles detection technologies are employed previously, for intense, frame difference method [13], average background method [13] and Gaussian mix method [6]. Gaussian mixture model works the best, but it works more slowly than difference frame algorithm [6]. Therefore, to detect the closest vehicle in each frame, the frame difference technique proposed in [10] was employed. The key advantage of that technique lies in its computational speed [11] which is important in maintaining the system's capability of performing in real-time situations. By applying the frame difference technique, the bounding box of the closest vehicle to the AV in each frame can be obtained. The centre point of the bounding box was used to represent that box.

After that, the position (Px, Py), the speed (S) and the direction (D) of the detected vehicle were computed. In the grid-based map, (Px, Py) denotes the coordinates of the above-mentioned centre point. S shows the distance between two centre points in that frame and the previous frame. D can be defined by the change of Px in that frame and the previous frame. D can take one value as follows:

- D = -1: Px current > Px previous. The direction of the closest vehicle was from left to right.
- D = 0: Px current = Px previous. The closest vehicle does not move horizontally.
- D = 1: Px current < Px previous. The direction of the closest vehicle was from right to left.

Finally, the closest vehicle in each frame can be described by a set of feature (Px, Py, S, D).

Samples of feature vectors generated using the frontal camera (camera A) are exhibited in the following table.

TABLE 2. Feature vector samples – camera A (frontal view) (FN: frame number, PxA: horizontal position. PyA: vertical position, SA: speed, DA: Direction)

FN	PxA	PyA	SA	DA
1	16	15	0	0
2	14	18	5	1
3	13	20	3	1
4	12	22	3	1

After that, the feature vectors and their corresponding labels are fetched a binary classifier. Signal from two cameras will generate to local decision DeA and DeB, each of which could either be 1 (Go) or 0 (Wait). The integrated final decision can be made using a simple logical AND rule: De = DeA *AND* DeB.

C. Classification and Results

The processed data were divided to 80% for training set (506 samples) and 20% for test set (126 samples).

Three classifiers were employed: Support Vector Machines (SVM), Artificial Neural Network (ANN), and k-Nearest Neighbours (kNN). To guarantee that our system is qualified in real-time traffic scenarios, the accuracy and the computational time must be balanced. In our experiments, we focus on reaching the highest accuracy within roughly one second.

Among the three, SVM achieved the highest accuracy rate at 88.44% in 0.9 seconds. ANN and kNN obtained various results based on different parameter settings, but none of them accomplished the tasks within 1 second. The fastest ANN spent 1.1 seconds to reach 85.12% accuracy rate. It only consisted of only 2 layers of 6 input nodes and 2 output nodes. Deepen the ANN by adding another layer lead to running time increasing. In kNN, the most reasonable outcome was 83.76% in 1.3 seconds, obtained with k=64. Adjust the value k would either decelerate the system or deteriorate the performance.

The three classifiers were re-examined using cropped frames. Realising that the closest vehicles almost never entered the top quarter of a frame (unless it was a big size vehicle such as a lorry), we removed the top 25% of each frame and repeated the experiments. Again, SVM was outstanding with 91.32% accurate after 0.7 seconds. The outputs for the above mentioned ANN and KNN were 87.05% in 1 second and 85.84% in 1.2 seconds, respectively.

The results of the experiments are demonstrated in the following table.

TABLE 3. GB-MC-MR output (Cla: classification, Acc: accuracy rate. TT(s): training time, TD: Average decision-making time, FNS/TS: False Negative rate)

	Original frames				Cropped frames			
Cla	Acc	**TT(s)**	**TD(s)**	FNS/TS	Acc	**TT(s)**	**TD(s)**	FNS/TS
SVM	88.44%	1401.13	0.9	7.14%	91.32%	1135.13	0.7	5.56%
ANN	85.12%	1396.26	1.1	9.52%	87.05%	1154.26	1.0	7.93%
KNN	83.76%	1529.71	1.3	10.32%	85.84%	1298.71	1.2	7.93%

Also, the result is compared with Cross Validation (K=10), the 632 samples is divided by 10 subsets. the highest accuracy are provided in table 3.

III. Discussion

In experiments with the two types of frames, SVM was the leading classifier that reaches approximately 90% accuracy rate within the 1-second threshold. That result is satisfactory in applying the system to real-time traffic scenarios.

Cropping the frames obviously improve the performance of the system. In our experiments, the most reasonable removal area was the top quarter of the frame. Exceeding that portion might reduce the reliability of the system since it was unable to effectively detect the approaching vehicles, especially big size vehicles such as Lorries, trucks or buses.

Using the logical AND rule significantly improve the safety in AV driving. It indicates that the AV is ready to go if only decisions made using each camera are all Go. Making the final decision in such way also reflect the way our system simulate the human driver's behaviour. At a mini-roundabout, the driver should always examine vehicles from the front and the right hand side (where other vehicles are given priority in the UK). Once it is safe in both sides, the drive can start entering the mini-roundabout.

One of the key factors in our algorithm is how to effectively and efficiently detect the closest approaching vehicle. Although there were several options, we recruited the frame difference technique [10] due to its simplicity and speed. However, it is not the most sensitive car detection technique, especially when the video quality is low [11]. For example, the poor lit condition in rainy weather can seriously interfere with its robustness. In such cases, other vehicle detection methods such as average background method [11] and Gaussian mix method [12] might be considered.

Another important factor in our algorithm is how to combine the frames captured by multiple cameras. In this study, we extracted features from each frame and accumulated them in a single feature vector. Initially, we also considered the well-known image stitching method which applied in handling multiple images [13] [14]. Image stitching can produce a wide-angle image whilst maintaining the quality of the source images. However, that method was rejected due to the fact that handling the distortion at the corners of the stitched image was a non-trivial task, and it significantly increases the computational cost.

Figure. 5. Image stitching distortion

IV. Conclusion

This paper proposed a grid-based decision-making system for an AV to safely enter a mini-roundabout (GB-MC-MR). It is the pioneer system that utilised multiple cameras in AV driving at roundabouts. Three classifiers were evaluated using 230 videos captured by multiple-cameras. SVM showed a promising result with a 91.32% classification accuracy in 0.7 seconds. That outcome suggested that the proposed system can support the AV to make a proper human-like decision when reaching a mini-roundabout in real-time. In the future, other complex driving scenarios including interaction and T-junction roundabouts will be investigated.

Acknowledgment

This work was supported by the National Natural Science Foundation of China under Grant 61703188

References

[1] C. Sustrans, "*Junctions and crossings: Cycle friendly design*", *SDMC,* Available at: http://www.sustrans.org.uk/sites/default/files/images/files/Route-Design-Resources/Junctions_and_Crossings_06_02_15.pdf. Accessed 15th Dec 2018.

[2] Elvik, R., 2003. Effects on road safety of converting intersections to roundabouts: review of evidence from non-US studies. *Transportation Research Record: Journal of the Transportation Research Board,* (1847), pp.1-10.

[3] Ambros, J., Novák, J., Borsos, A., Hóz, E., Kieć, M., Machciník, Š. and Ondrejka, R., 2016. Central European comparative study of traffic safety on roundabouts. *Transportation Research Procedia*, *14*, pp.4200-4208.

[4] B. Adler, J, Xiao, J. Zhang, "Autonomous exploration of urban environments using unmanned aerial vehicles". *Jour of Fie Rob*, *31*(6), pp.912-939. (2014).

[5] B. Okumura, M.R.James, Y. Kanzawa, M.Derry, K.Sakai , T .Nishi, and D.Prokhorov, "Challenges in perception and decision making for intelligent automotive vehicles: A case study". *IEEE Transactions on Intelligent Vehicles*, 1(1), pp.20-32. (2016).

[6] D. González, J. Pérez and V. Milanés, "Parametric-based path generation for automated vehicles at roundabouts". *Expert Systems with Applications*, *71*, pp.332-341, (2017).

[7] J. Ziegler, P. Bender, M. Schreiber, H.Lategahn, T.Strauss, C.Stiller, T.Dang, U.Franke, N.Appenrodt, C.Keller and E.Kaus, "Making Bertha drive—An autonomous journey on a historic route". *IEEE Intelligent Transportation Systems Magazine, 6(2)*, pp.8-20. 2014.

[8] H. Dinh, and H.Tang, "Camera calibration for roundabout traffic scenes". In Circuits and Systems (MWSCAS), *2012 IEEE 55th International Midwest Symposium* (pp. 674-677). (2012).

[9] Rhodes. B. "Frank Blackmore - Determined, maverick traffic engineer who invented the mini-roundabout". *The Guardian*. (2008). Available at: https://www.theguardian.com/theguardian/2008/jun/21/6. Accessed 17th Dec 2018.

[10] M. Cheon, W. Lee, C. Yoon and M. Park: "Vision-Based Vehicle Detection System with Consideration of the Detecting Location". *IEEE Transactions on Intelligent Transportation Systems 13(3)*, 1243-1252 .

[11] Kulchandani, J.S., Dangarwala, K.J.: "Moving object detection: Review of recent research trends". *In Pervasive Computing (ICPC) 2015*, pp. 1-5. IEEE. Pune (2015).

[12] A.K. Chauhan, P. Krishan: Moving object tracking using Gaussian mixture model and optical flow". *International Journal of Advanced Research in Computer Science and Software Engineering* 3(4), 243-246.

[13] M. Wang, S. Niu, and X. Yang. "A novel panoramic image stitching algorithm based on ORB". *Applied System Innovation (ICASI), 2017 International Conference* (pp. 818-821). IEEE. (2017).

[14] Y.J. Ha, H.D. Kang, "Evaluation of feature based image stitching algorithm using OpenCV". *Human System Interactions (HSI), 2017 10th International Conference* (pp. 224-229). IEEE. (2017)

Acoustic side-scan on enclosed underwater environment

Peng Yibin, Dr. Peter N Green, the University of Manchester, UK

***Abstract*— This paper brief introduces a ray tracing based mapping strategy that gathers the bottom information of an unknown enclosed water pond. This is done by an autonomous underwater vehicle, which equipped with acoustic transducer, performing acoustic Side-scans. The consequence of the mapping is a point cloud data.**

I. INTRODUCTION

Nowadays more and more industrial processes take place on liquid based environment, those industrial processes included but not limited to the undersea oil pipeline leakage detection, spent nuclear fuel storage pond monitoring, and chemical reagent synthesis in large-scale vessels. Unfortunately most of such processes take placed on risky and cluttered underwater environment they are difficult to access and monitor. Moreover, some environments pose additional hazards. For example, the spent nuclear fuel storage pond, it contains high radioactive metals such as Uranium and Plutonium [1] which are hazardous to human health, so such place is nearly impossible for human to work with even wearing a protection suite. In such circumstances, small-scale mobile underwater robots (micro-autonomous underwater vehicle or µAUV) could potentially be used to replace human to monitor the radiation level and explore the unknown underwater environment.

Underwater autonomous navigation is an important research topic in underwater robotics, whose purpose is to allow the robot to navigate and deploy safely from the starting position to the target position. A typical offline navigation process for a swimming pool sized underwater environment (nuclear storage pond) constitutes of 3 main procedures: environment mapping, occupancy map establishing, and path planning. Among them the environment mapping is the preliminary step, because the following procedures are relying on the data obtained by the environment mapping. In order to gather the bottom layout of the enclosed underwater environment, the acoustic side-scan is introduced. Other approaches such as Lidar or Radar are hard to implement in a cluttered underwater environment and too expensive or the instruments not fit to a small size AUV.

*

Y. Peng is a PhD student with the Electrical and Electronics Engineering School, the University of Manchester, UK (phone: (44)7871206251; e-mail: yibin.peng@manchester.ac.uk).

P.N.Green is a lecturer with the Electrical and Electronics Engineering School, the University of Manchester, UK (phone: (44)0161 306-3378; e-mail: peter.green@manchester.ac.uk).

II. METHOD

Acoustic side-scan uses sonar devices that produce a conical beam downward to the pond bottom with a wide beam angle perpendicular to the path of the sensor through the water to measure the depth of the bottom [2] [3]. In practice, µAUV will project a vertical beam from a plane with specified height toward an area by high-frequency acoustic pulse emission in order to capture depth information about the corresponding bottom surface. The movement plane is set above clutters and sampled in a uniformly spaced 2d grid (see Figure 1). The µAUV will move to each grid and measure the depth of the current grid by the received pulse that reflected off from the object's top surface. A routine of this survey is shown in Figure 2. The result of an aerial survey is an array of tuples, whose components are measurement positions and its corresponding height. This dense elevation point data is called "point cloud". See Figure 3 for the input and output of this method.

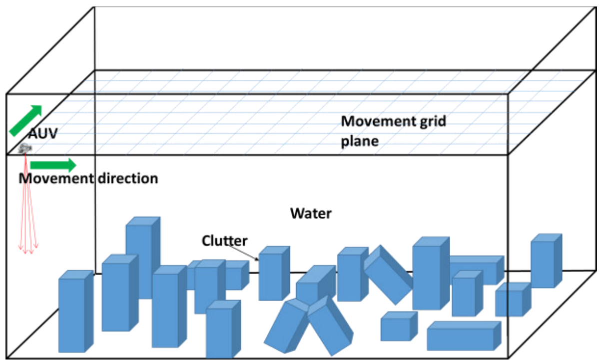

Figure 1: Regular grid acoustic side-scan

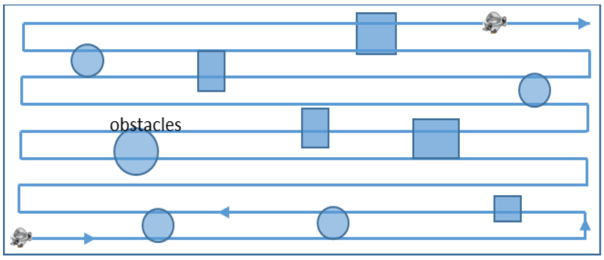

Figure 2: Scan itinerary

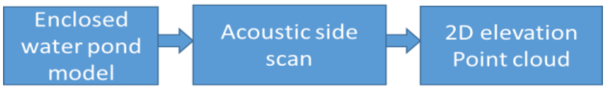

Figure 3: Diagram of input and output

The acoustic Side-scan is carried out by acoustic sensors which rely on modulating surface acoustic waves to sense a physical object. These devices transduce electrical signals to acoustic waves, receive reflected waves, and convert received waves back to electrical signal [4]. During the wave propagation, acoustic waves will be reflected, refracted, or attenuated by the medium. For the depth measurement the reflection is the main concern. In terms of analysis, the form of wave in depth measurement is not convenient, but the characteristic of the wave is approximate to a ray, so the ray tracing algorithm is introduced [5]. The acoustic wave propagations are regarded as rays, and the conical beam is constituted of finite number of rays. The depth can be calculated by knowing the time interval between the transmitted signal and received signal and the propagation speed of the acoustic ray.

The main problem is finding the correct signal (ray) from the received signal spectrum. Because there are unwanted signals and background noises in the received signal spectrum. The background noise includes reflections from small objects, reflections of sidelobes or part of reverberation (especially in shallow waters), the unwanted signal includes later reflections (signal that have multiple times of reflections) and diffuse reflections (signal that scatters in all direction when hits an object). Therefore, the useful signal is the normal reflection of the emitted ray, because a receiver and a transmitter combined in one device (transceiver), so the only first order specular reflection can be received is the normal reflection. Theoretically, it is reflected off the nearest obstacles and has the highest remaining energy [5]. Based on this property, 2 key factors can be used to estimate the normal reflection: time of flight (TOF) and response energy level. In the impulse response in time domain, the normal reflection signal is the pulse with the highest energy response and the shortest TOF. Once the TOF of the desired signal is known, the depth is given by the equation:

$$Depth = v * \frac{t}{2}$$

Where v is the speed of sound in water and t is the time of fight of the normal reflection signal.

For a horizontal surface, the transceiver will always receive the normal reflection signals. However, for the case of inclined surface, it is possible that normal reflection signal do not exist (no ray is perpendicular to the inclined surface see Figure 3.a). The way to address this problem is to propose a wide projection beam angle and ensure there is normal reflection. See Figure 3.b.

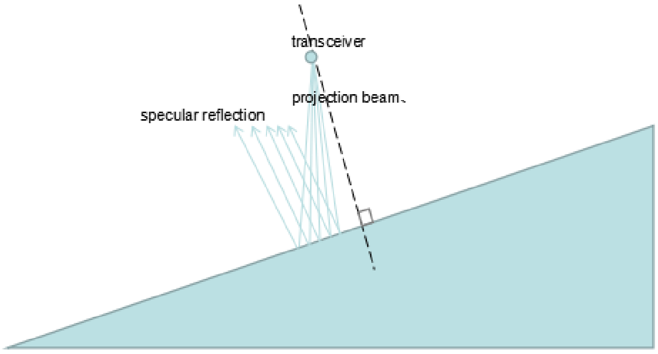

Figure 3(a): Small beam without normal reflection

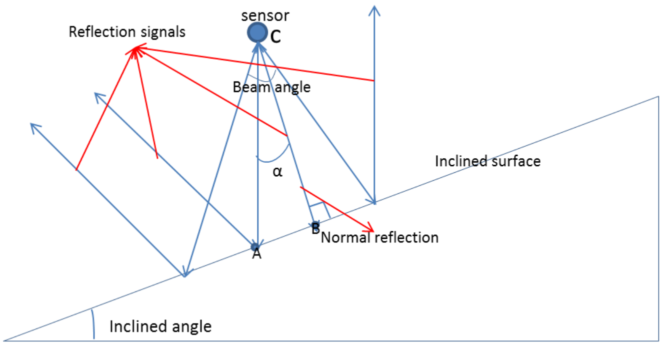

Figure 3(b): Wide Beam with normal reflection

III. RESULTS

A. *Depth measurement simulation*

There is a MATLAB model to illustrate how the depth can be calculated from received impulse response. See Figure 4(a): a scan above an obstacle. Assume this scanning beam is consisted of 21 rays (the beam angle is 20 degree, one ray for 1 increment degree). Assume each ray carried the same amount of energy (150 units), once the ray hit objects, its energy will be dissipated, assume the remaining energy of specular reflection signal is 50% of the total energy, and remaining energy of each diffuse reflection signal is 5% of the total energy. The corresponding energy impulse response of each received ray in time domain is shown in Figure 4(b). The signal that is useful to depth measurement is the first pulse, because it has the shortest TOF and highest impulse response, so it is the normal reflection ray. The TOF of this signal is 0.00696s; the depth can be calculated is 0.00696*1450/2=5.04657m.

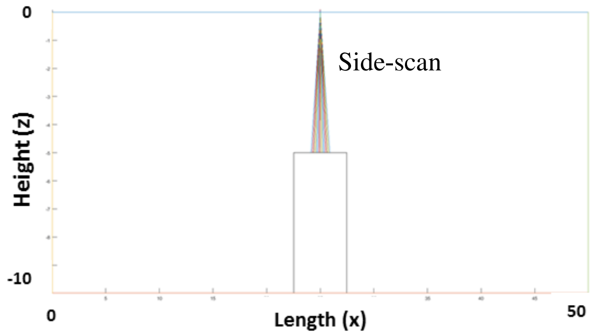

Figure 4(a): Acoustic scan with 20 degree beam angle

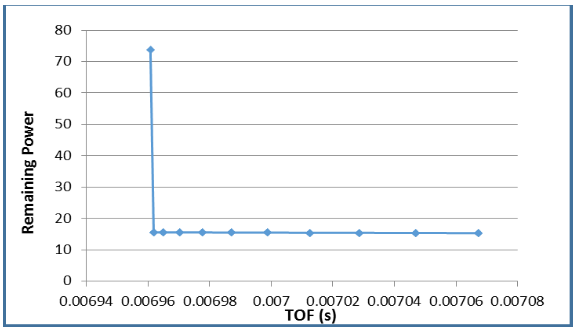

Figure 4(b): Energy impulse response of each received ray

B. *Well-organised modern nuclear storage pond*

The used nuclear fuel containers in modern storage pond are well-organised and regularly placed. They are equipped with storage racks designed to hold each container. An example of a modern nuclear storage pond is shown in Figure 5(a) and its geometry representation is shown in Figure 5(b).

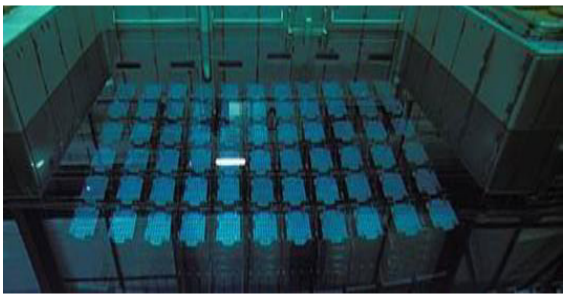

Figure 5(a): True pond

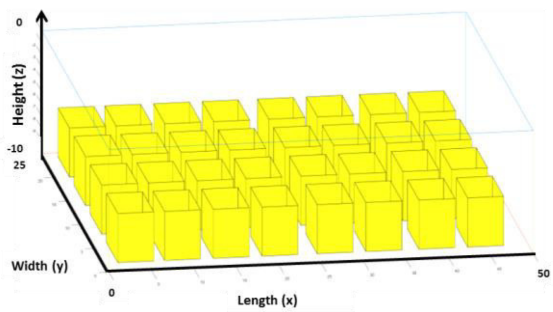

Figure 5(b) MATLAB pond model

Assume the pond is a 50m*25m swimming pool sized enclosure with a depth of 10m. Assume the side-scan sampling resolution is 0.5m*0.5m, the obtained point cloud data and its' corresponding surface plot are shown Figure 6(a) and 6(b) respectively.

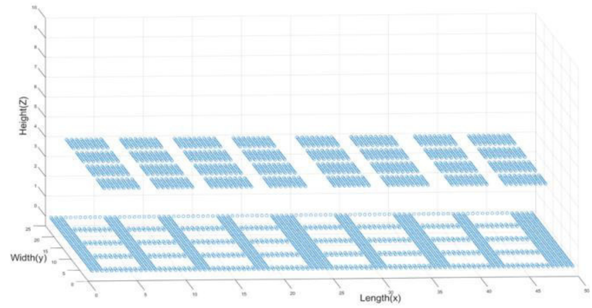

Figure 6(a): Point cloud model

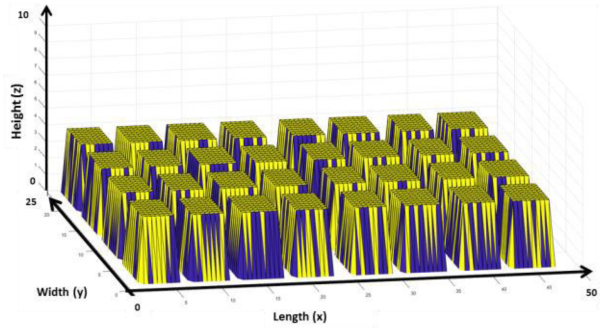

Figure 6(b): Surface plot

The surface plot is a MATLAB function which creates a continuous surface based on the obtained discrete sampling points. This simulation shows an image of what information is obtained by acoustic side-scans.

IV. Conclusion

Ray tracing based acoustic side-scan will follow the proposed route to measure the elevation of each measurement point. The consequence of the whole pond survey is a matrix of tuples (x, y, z coordinates) of the pond's bottom environment. This data is the 2D projection of the 3D clutter on to the measurement plane. This is a preliminary step of offline underwater navigation of μAUV. The scanning process must be performed on-line, while path planning might be performed off-line. The gathered point cloud data will be further processed with point interpolation to construct a 3D point cloud model (fill the gap between the ground and the top surface of measured objects), and then convert it to an occupancy grid map. Once competed, path planning algorithms can be applied to the reconstructed occupancy grid map in order to plan a collision free path.

References

[1] Nuclear Decommissioning Authority, "Radioactive Wastes in the UK: A Summary of the 2016 Inventory", *Department for Business, Energy & Industrial strategy*, March 2017.

[2] L. Paull, S. Saeedi, M, Seto and H. Li, "AUV Navigation and Localization: A Review", *IEEE J. Ocean,* Vol. 39, no. 1, Jan, 2014.

[3] J. Melo and A. Matos, "Survey on advances on terrain based navigation for autonomous underwater vehicles", *Ocean Engineering*, 2017, pp 250-264.

[4] J. Kirschner., "Surface Acoustic Wave Sensors (SAWS): Design for Application", *Micro-electronical Systems*. Dec 6, 2010.

[5] D. O. Elorza, "Room acoustics modeling using the raytracing method: implementation and evaluation". *University of Turku Department of Physics*, 2005.

Establishing Continuous Communication through Dynamic Team Behaviour Switching

Tsvetan Zhivkov[1], Eric Schneider[2], and Elizabeth I. Sklar[3]

Abstract— **Maintaining continuous communication is an important factor that contributes to the success of multi-robot systems. Most research involving multi-robot teams is conducted in controlled laboratory settings, where continuous communication is assumed, typically because there is a wireless network (wifi) that keeps all the robots connected. But for multi-robot teams to operate successfully "in the wild", it is crucial to consider how communication can be maintained when signals fail or robots move out of range. This paper presents a novel "leader-follower behaviour" with dynamic role switching and messaging that supports uninterrupted communication, regardless of network perturbations. A series of experiments were conducted in which it is shown how network perturbations effect performance, comparing a baseline with the new leader-follower behaviour. The experiments record metrics on team success, given the two conditions. These results are significant for real-world multi-robot systems applications that require continuous communication amongst team members.**

I. Introduction

Continuous communication, operating in real-time and uninterrupted, is vital for a *multi-robot team (MRT)* to perform effectively. Providing correct information to team members and having up-to-date local knowledge are only two of the critical functions that depend on networked communication facilities. However, if and when network infrastructure breaks down, risking the loss of mission-critical messages, MRTs may be required to create opportunistic *ad-hoc (AH)* networks in order to sustain performance levels. The long-term vision for multi-robot systems communication is real-time, low-latency, zero-outage networks; but wide availability of such capabilities are far into the future. In the meantime, multi-robot systems research must develop strategies for overcoming network problems.

Here, we propose an approach to responding to poor network performance in a multi-robot team. In earlier work, we applied a probabilistic message loss function to assess the impact of dropped messages on team performance [1]. Although limited, this study gave us an initial understanding of how a multi-robot team is affected by degrading communication quality. In this paper, we take a step forward in this line of research, by presenting a new MRT behaviour designed to adapt when communication fails and maintain better connectivity amongst team members.

We introduce *Leader-Follower (LF)* behaviour, described in Section III, a dynamic strategy that is inspired by the concept of AH networks. Experimental results show that our LF behaviour provides continuous communication regardless of network perturbations, as presented in Sections IV and V. This work takes a crucial step toward understanding how to assess and reduce the impact of unreliable communication depending on the network type and network perturbation that is experienced. Our long-term aim is to improve message passing capabilities in MRTs, by providing adaptive behaviours that respond to different network problems which arise during a mission.

II. Related Work

We are not the first to investigate aspects of communication in multi-robot systems. Murphy *et al* [2] use a remote-controlled robot agent to perform triage on a victim in a search-and-rescue scenario and thoroughly examine the impact of different sensors on communication (e.g., audio and video). Zadorozhny and Lewis [3] look at autonomous MRT collaboration with human assistants to perform search and rescue of victims in a simulated environment. Lujak *et al* [4] propose a model for integrating multiple different technologies (e.g., mobile robots or mobile phones/devices) to assist victims during an emergency. These works highlight the importance that certain types of messages have, particularly in search-and-rescue and emergency-response situations, which has helped us to prioritise certain message types for experimentation, as described in Section III.

Furthermore, we explore works that use the notion of *ad-hoc* networks for communication in multi-robot systems. Takahashi *et al* [5] investigate, in simulation, MRT formations with the aim to use an ad-hoc network. Witkowski *et al* [6] look at reestablishing infrastructure using robot teams and *ad-hoc* networks. Caccamo *et al* [7] demonstrate a novel robot navigation planner in an urban search-and-rescue (USAR) simulation environment that is communication-aware and can repair lost communication.

The first generation *Robot Operating System (ROS1)* [8] platform was originally designed for single robot academic experiments, with no real-time performance requirements and an assumption that wireless local area network connectivity is good. In the next generation, ROS2 [9][10] the communication middleware has been updated to support real-time messaging. Recent work within the MRT research community has produced a few ROS-based frameworks and tools for experimenting with multi-robot systems [11][12],

[1]Tsvetan Zhivkov is a Doctoral Student with the Department of Informatics Centre for Robotics Research (CoRe), King's College London University, Strand, London WC2R 2LS, England, United Kingdom.
tsvetan.zhivkov@kcl.ac.uk
[2]Eric Schneider is a Research Assistant with the Department of Informatics Centre for Robotics Research (CoRe), King's College London University, Strand, London WC2R 2LS, England, United Kingdom.
eric.schneider@kcl.ac.uk
[3]Elizabeth I. Sklar is a Professor of Robotics with the Department of Informatics, King's College London University, Strand, London WC2R 2LS, England, United Kingdom.
elizabeth.sklar@kcl.ac.uk

although there is no widely-adopted standard approach to facilitating multi-robot systems using ROS. As described below, we build on the MRTeAm framework [12] to implement and evaluate our Leader-Follower strategy.

III. Approach

We simulate *missions* where multi-robot teams are given a number of *tasks* to complete. Each task definition includes a location where the robot performs actions, such as *sensor-sweep* (collecting a series of images). In order to coordinate team activity, a centralised *assigner* agent determines which robots should perform which tasks and then mission execution begins. Thus the following types of messages occur:

1) the assigner agent sends messages that allocate tasks to robots;
2) the robots send messages to their teammates providing position information, which is used by the assigner for the task allocation process and by other robots to facilitate collision-free movement; and
3) the robots report task completion status, possibly accompanied by sensor data acquired as part of the task.

Our goal is to minimise the impact on team performance when some of these messages are not communicated.

A. Network type

We employ two different types of networks for our experiments: a baseline *wireless local area network (WLAN),* which uses our local "wifi", and *an ad-hoc (AH)* network.

We establish an *ad-hoc* radio communications network for our multi-robot system with the objective of maintaining continuous communication while performing normal operation. To create an AH network topology, devices connect directly to each other and rely on the close proximity of neighbouring devices to maintain connectivity. Devices can also leave and join the network freely; however, sharing of information is only possible as long as connections are maintained. The characteristics of our AH network are: no infrastructure, quick dissemination of information and distributed control (i.e., no single point of failure).

Radio signals have *theoretical* and *actual* limits. For our simulation, we measured the limitations of our *ad-hoc* network using Turtlebot2 robots and the type of IEEE 802.11n/ac wireless network cards which come standard with that platform. We measured the signal strength over various distances in order to construct a realistic model for our experiments, shown in Fig. 1. We employ these values in our LF behaviour, described below, as a guideline for maximum separation between any two robots in the team.

We impose further network limitations to make our problem tractable by assuming specific WLAN and AH network conditions: for both WLAN and AH it is assumed that SNR (signal-to-noise-ratio) experiences uniform loss and that interference from other devices is negligible, and additionally for WLAN we assume uniform radial coverage of the operational environment.

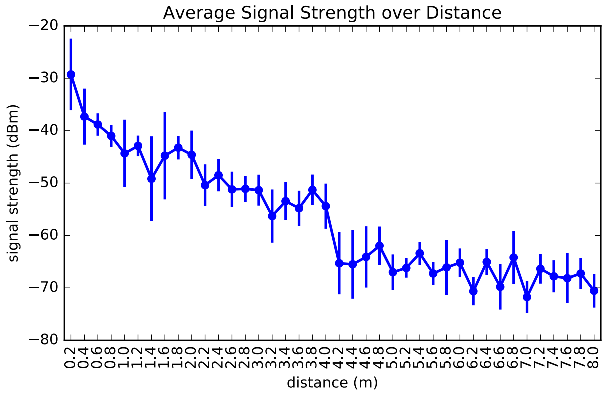

Figure 1. Signal strength vs. distance. Average values over 30 readings.

B. Robot behaviours

We compare two different robot behaviours: a baseline *no-behaviour (NB)* and our novel *Leader-Follower (LF)* behaviour, which is designed to maintain connectivity even when the network is unreliable. In NB mode, robot team members do not adjust their behaviour based on network quality. They attempt to complete their assigned tasks, disregarding network type or loss of communication quality, and perform standard navigation and obstacle avoidance behaviours.

In LF mode, robot team members detect changes in communication quality, such as when team members move outside of their close neighbourhood, requiring the team to regroup and move closer together again. This can be translated easily to react to change in network type as well, for example from WLAN to AH and back again.

When the robot agents use LF behaviour, they assume one of three *roles: not assigned (NA), leader* or *follower.* Initially, they all start with the NA role. Initially, they all start with the NA role. Upon the team detecting a loss of connection from any member, the robots dynamically assign themselves to either the *leader* or *follower* role, based on a utility score, defined as follows:

$$u = d\_score \times num\_incomplete \times recently\_completed$$

where $\boldsymbol{u}$ = utility score; ***d_score*** = distance score, computed as *1÷distance_to_goal* (task location); ***num_incomplete*** = number of incomplete tasks remaining on the robot's *agenda*[1], which is computed as the total number of tasks assigned less the number of tasks completed; ***recently_completed*** = 0.5 if the robot has just completed a task or 1.0 if it has not (this value is reset with every change in role and/or completion of a task). This last factor acts to balance out the priorities of tasks amongst the teammates. This is because the *follower* behaviour prioritises staying in communication with teammates over completing its allocated tasks, whereas the *leade*r robot prioritises completing its tasks. If a given robot is always a follower, it may never get an opportunity to prioritise completion of its tasks. Effectively, this factor ensures that all tasks are given priority at some point during the mission.

[1] The "agenda" is the list of tasks a robot has been allocated by the assigner agent.

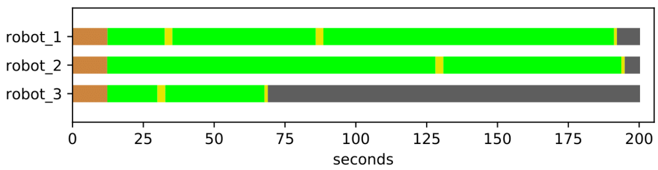

(a) no-behaviour (NB) with WLAN network type (AH is similar)

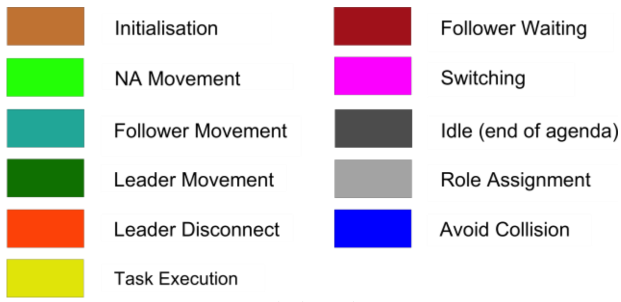

(b) legend

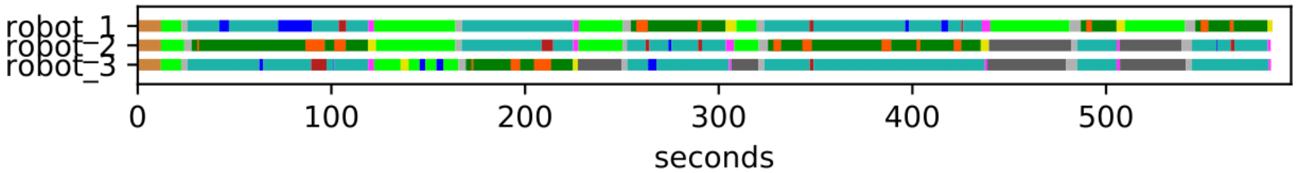

(c) Leader-Follower (LF) behaviour with AH network type

Figure 2. Sample Timelines. These plots illustrate the various activities undertaken by the robots during one representative experiment. Plot (c) shows that the three robots alternate between taking on leader and follower roles.

The robot with the highest ***u*** value is selected as *leader*. In our simulation, the leader is a proxy for the robot that initialises the *ad-hoc* network in a physical setup. Then the followers connect to this new network. The final stage of the behaviour clears all robots of their roles, i.e., NA, which we denote as switching. An illustration of role assignment and switching within the LF behaviour is shown in Fig. 2.

IV. Experiment Design

For our experiment scenario, we have chosen 3 robots to perform 7 exploration tasks starting in a clustered formation, where each task is independent from the next and requires a single robot to complete. We have purposefully chosen difficult task locations in narrow spaces and poor starting locations for the robot team (illustrated in Fig. 3). Tasks T_R are assigned sequentially to each robot R, and the assignments are fixed for all our experiments[2]. To demonstrate the effectiveness of LF in minimising the impact of network connectivity problems, we simulate network perturbation as *simulated packet loss (SPL)*. We compare four values: SPL_j where $j \in \{0, 25, 50, 75\}$ is a percentage of messages that are dropped.

Table I lists the set of experiment configurations. For each, we compared four different network conditions. Each experiment is performed 30 times.

network type	*behaviour*	*network perturbation*
WLAN	NB	{*SPL0, SPL25, SPL50, SPL75*}
AH	NB	{*SPL0, SPL25, SPL50, SPL75*}
AH	LF	{*SPL0, SPL25, SPL50, SPL75*}

Table I. Experiment configuration.

We collect a number of different metrics during each experiment. The most relevant metrics discussed here are: *number of successful tasks*, *distance travelled* and *movement time.* We expect that the number of successful tasks will decrease when the network is perturbed and connectivity is compromised, except when employing the LF behaviour, which attempts to maintain connectivity. However, we expect that the distance travelled and the amount of time robots spend moving will increase with LF, since they may travel extra distance in order to remain connected.

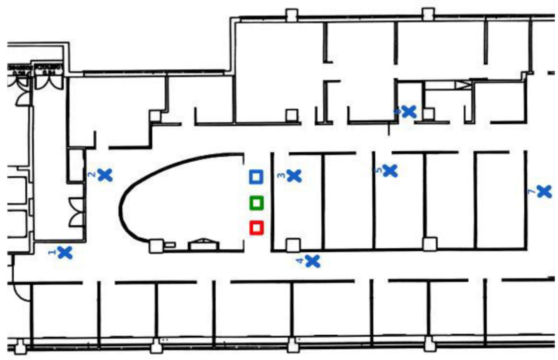

Figure 3. Office setting for experiments, crosses represent task locations and squares robots (based on actual floor plan of building).

V. Results and Discussion

Fig. 4a shows that LF maintains continuous communication and completes all tasks, whereas NB fails to maintain communication so does not manage to complete all the tasks.

There is a negative impact on using the LF behaviour due to the fact that each robot consistently needs to maintain communication. This leads to the results seen in Fig. 4b, which shows a three-fold increase in distance travelled. However, this is the expected behaviour (i.e., by design) of LF and can be improved in future work. Moreover, Fig.4c shows how LF's movement time is designed differently to that of NB. LF movement time is made up of three parts,

[2] Robot_1 (the red square in Fig. 3) is assigned tasks T_1 = {1, 4, 7}, robot_2 (green square) T_2 = {2, 5} and robot_3 (blue) T_3 = {3, 6}.

namely NA, leader and follower movement time. For NB movement time is made up of only NA movement time.

VI. Summary

We have presented a novel dynamic Leader-Follower behaviour that achieves perfect communication with a test set of network perturbations. The baseline MRT using only standard navigation and collision avoidance (NB behaviour) shows poor results in comparison. Our immediate next step is to demonstrate that our framework can easily reproduce the same results in a physical environment. Furthermore, it is inevitable that in the real world, environments are dynamic and conditions change, including the type of network and perturbation. We wish to analyse how our dynamic LF behaviour can deal with variable network conditions. In future work, we will expand the network perturbation to simulated signal strength degradation and effective signal strength, applied to physical robot experiments. Finally, we hope to explore if other strategies improve the performance of the dynamic behaviour while having less adverse impact on distance travelled and movement time.

Acknowledgements

This work was partially supported by a King's College London Graduate Training Scholarship and by the ESRC under grant #ES/P011160/1.

References

[1] T. Zhivkov, E. Schneider, and E. I. Sklar, "Measuring the effects of communication quality on multi-robot team performance," in *Towards Autonomous Robotic Systems: 18th Annual Conference (TAROS)*, Springer, 2017.

[2] R. Murphy, V. Srinivasan, Z. Henkel, C. Soto, M. Minson, J. C. Straus, S. Hempstead, T. Valdez, and S. Egawa, "Interacting with trapped victims using robots," in *International Conference on Technologies for Homeland Security, HST,* 2013.

[3] V. Zadorozhny and M. Lewis, "Information fusion for usar operations based on crowdsourcing," in *Proceedings of the 16th International Conference on Information Fusion*, Istanbul, Turkey, 2013.

[4] M. Lujak, N. Bouraqadi, A. Doniec, L. Fabresse, A. Fleury, A. Karami, and G. Lozenguez, "Towards robots-assisted ambient intelligence," in *5th International Conference on Agreement Technologies*, 2017.

[5] T. Takahashi, Y. Kitamura, and H. Miwa, "Organizing rescue agents using ad-hoc networks," in *Advances in Intelligent and Soft Computing (AINSC)*, vol. 156, 2012.

[6] U. Witkowski, M. El-Habbal, S. Herbrechtsmeier, A. Tanoto, J. Penders, L. Alboul, and V. Gazi, "Ad-hoc network communication infrastructure for multi-robot systems in disaster scenarios," in *Proceedings of IARP/EURON Workshop on Robotics for Risky Interventions and Environmental Surveillance,* Benicassim, Spain, 2008.

[7] S. Caccamo, R. Parasuraman, L. Freda, M. Gianni, and P. Ögren, "Rcamp: A resilient communication-aware motion planner for mobile robots with autonomous repair of wireless connectivity," in *International Conference on Intelligent Robots and Systems (IROS)*, 2017.

[8] M. Quigley, K. Conley, B. P. Gerkey, J. Faust, T. Foote, J. Leibs, R. Wheeler, and A. Y. Ng, "ROS: an open-source robot operating system," in *ICRA Workshop on Open Source Software*, 2009.

[9] E. Fernandez, T. Foote, W. Woodall, and D. Thomas, "Next-generation ros: Building on dds," *ROSCon*, Chicago, US, 2014.

[10] A. Dąbrowski, R. Kozik, and M. Maciaś, "Evaluation of ros2 communication layer," *ROSCon*, Seoul, Korea, 2016.

[11] T. Andre, D. Neuhold, and C. Bettstetter, "Coordinated multi-robot exploration: Out of the box packages for ROS," in *Published in IEEE Globecom Workshops (GC Wkshps)*, Austin, TX, USA, 2014

[12] E. Schneider, E. I. Sklar, and S. Parsons, "Evaluating multi-robot teamwork in parameterised environments," in *Towards Autonomous Robotic Systems: 17th Annual Conference (TAROS),* Springer, 2016

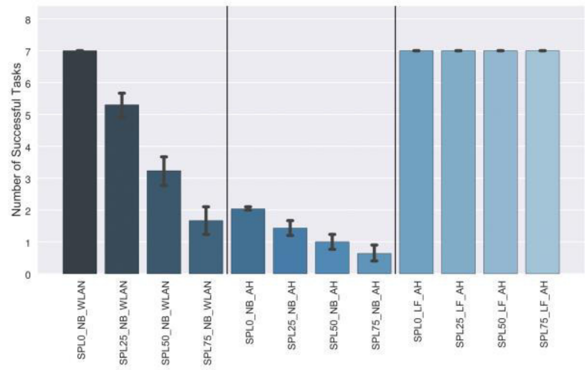

(a) number of successfully completed tasks (out of 7)

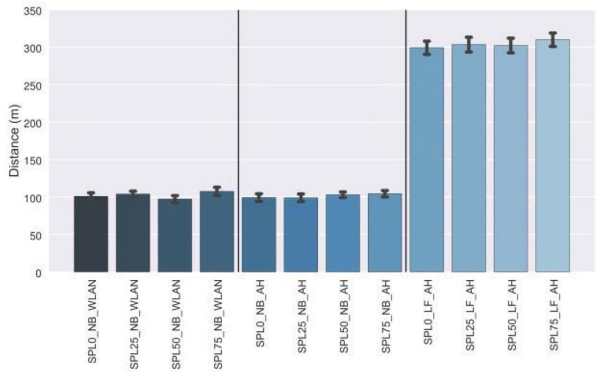

(b) total distance travelled

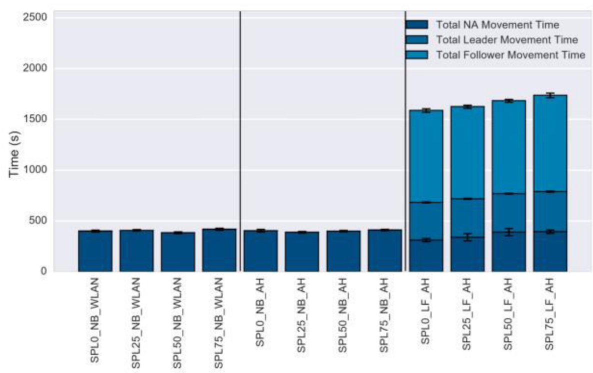

(c) total time spent travelling

Figure 4. Experiment Results

Trajectory Creation Towards Fast Skill Deployment in Plug-and-Produce Assembly Systems: A Gaussian-Mixture Model Approach

Melanie Zimmer, Ali Al-Yacoub, Pedro Ferreira, Niels Lohse

***Abstract*—In this paper, a technique that reduces the changeover time in industrial workstations is presented. A Learning from Demonstration-based algorithm is used to acquire a new skill through a series of real-world human demonstrations in which the human shows the desired task. Initially, the collected data are filtered and aligned applying Fast Dynamic Time Warping (FastDTW). Then the aligned trajectories are modelled with a Gaussian Mixture Model (GMM), which is used as an input to generate a generalisation of the motion through a Gaussian Mixture Regression (GMR). The proposed approach is set into the context of the openMOS framework to efficiently add new skills that can be performed on different workstations. The main benefit of this work in progress is providing an intuitive, simple technique to add new robotics skills to an industrial platform which accelerates the changeover phase in manufacturing scenarios.**

Keywords— Plug-and-Produce; Changeover; Learning by Demonstration; Fast Dynamic Time Warping; Gaussian Mixture Regression; Trajectory Learning.

I. Introduction

In today's manufacturing, the introduction of a new product or product variants is becoming more and more common. A change in product requirements, however, often leads to a modification to the manufacturing system. In order to do these changes, a certain amount of system downtime will result, which manufacturers are keen to keep as limited as possible. One way how manufacturers and research approach the problem of product variety is through the implementation of flexible manufacturing systems that allow handling various product types [1]. As an example of a project that falls into the category of flexible manufacturing systems and in which the presented work is also set is the European project 'open Dynamic Manufacturing Operating System for Smart 'Plug-and-Produce' automation components' (openMOS) [2]. The goal of the openMOS project is the development of an innovative, openly accessible plug-and-produce system platform, which facilitates a rapid and smooth ramp-up and changeover of equipment such as industrial robots.

Enhancements in robot technology increased the use of robots in industry with one area of interest in robot skill learning [3]. Learning from Demonstration (LfD) facilitates the acquisition of new skills for the robot as the motion can simply be demonstrated using motion sensors involving less programming [4]–[6]. An important field in LfD is trajectory learning. Here, advantage is taken from the strength of human motion planning. Humans will exemplify the trajectory considering special limitations and speed implications. However for humans, it is often difficult to keep a steady hand, and thus the produced trajectories might most certainly not be optimal so that a way of optimising the outcome is required.

This paper proposes an approach to reduce the changeover time for workstations in plug-and-produce assembly systems by using an LfD method. As part of openMOS, this work aims to contribute to the growing area of research in plug-and-produce assembly systems by proposing an intuitive changeover approach. This is envisioned to be achieved by allowing operators to build a library of desired robot skills through human demonstration that can be deployed using different types of equipment that share the same atomic skills. It is expected that this will lead to efficient learning of new skills and will ultimately decrease the delay time in changeover scenarios.

II. Related Work

Within the domain of flexible manufacturing systems, the plug-and-produce paradigm facilities the introduction, replacement or removal of a manufacturing device into the system, similar to the idea of plug-and-play in computing [7]. These capabilities of plug-and-produce systems allow for the quick introduction of a new product type.

In literature, there is no clear definition of the term changeover. Generally, changeover can be described as the total of activities of making a production line or machine ready from one production run to another, which comprises the machine set-up and clean-up process [8]. The generation of a robot skill, for example, falls under the set-up phase.

In robot skill learning, the optimisation of certain task execution is enabled through learning and imitating human motions [3]. LfD has been highly studied (e.g. [5]). One field of LfD that has been studied in more detail recently is the learning of a statistical model of a trajectory [9]. Learning a trajectory allows to instinctively add new necessary manipulation skills which are essential to handle products. Previous to being able to learn a trajectory from human motion, however, means of tracking this motion are required. Tracking physical motions of humans has received great attention over the past years [10].

Before a motion can be recognised, the use of sensor technologies is required [11]. For the data collection, image- or non-image-based types of sensors can be used. The first type includes markers with an optical camera, single and stereo cameras, or depth sensors, whereas for the second one gloves,

The authors are with the Intelligent Automation Centre, Loughborough University, Loughborough, LE11 3TU, UK (+44 (0)1509 227625;
e-mail: {m.zimmer2, a.al-yacoub, p.ferreira, n.lohse}@lboro.ac.uk).

bands and even non-wearables, such as a radio frequency-based system, are considered.

As a final step, gesture classification is undertaken [5]. As this is a machine learning problem, various machine learning approaches can be found in literature. Liu and Wang [11] provide a review of the most common approaches for gesture classification, amongst others K-Nearest Neighbour, Hidden Markov Model, Support Vector Machine and Artificial Neural Networks. The authors provide a comparison of the different approaches and conclude that in order to build on their advantages, a combination of different algorithms can be deployed. Another common approach is the application of the Gaussian Mixture Model (GMM) in combination with Gaussian Mixture Regression (GMR) [3].

III. Methodology

This section describes the approach that has been taken as an initial step of providing fast skill deployment in plug-and-produce assembly systems. The central advantage of this approach is that it reduces the required time to design and program a new skill as it does not need extensive technical knowledge to programme robots. The proposed methodology follows the procedure as set out below.

Firstly, a human will demonstrate the hand movement to be learned. This movement is tracked using a motion tracker system, that allows estimating an object's position in a workspace through passive inferred markers. This tracking system has been chosen as it is non-invasive and can be attached to any object, in the case of this work, a handheld gripper. It is assumed that more than one trajectory of the same movement will be captured and it must, therefore, be ensured next that these individual trajectories are aligned for further processing. Then, using the Gaussian Mixture Model and Regression generates a new approximated trajectory. Although using these algorithms to cluster the dataset and generate a trajectory is not new, it is considered to bring advances in plug-and-produce environments such as the openMOS framework. Both, the captured trajectories and the outcome of the GMR will be displayed to the user through a Graphical User Interface (GUI). Here, the user has the possibility to make small changes to the trajectory by, for example, removing unwanted points on the line via a mouse click. Through the GUI the execution of the trajectory on the robot side can be triggered as the human will ultimately have to provide approval before deploying and testing the skill on the robot. The final coordinates of the trajectory will then be provided to the openMOS framework as an input for this new skill. An overview of these stages is depicted in **Figure 1**.

For this paper, the focus is on learning the trajectories from a dispensing task that can be used on an industrial robot. This is only the first step in the above presented methodology and is explained in more technical terms in the next subsections (see also **Figure 2**).

A. *Collected Trajectories*

The collection of the demonstrated trajectories is denoted by the set $\{T_m = (p_{m,1}, p_{m,2}, \dots, p_{m,n_m})\}_{m=1}^{M}$, where M is the number of demonstrations, m is used for indexing these demonstrations, and n_m indicates the number of points of demonstration m. Each point of a trajectory is considered as a 2-dimensional vector $p_m = ((x_1, y_1)_m, \dots, (x_{n_m}, y_{n_m}))$, for $n = 1, \dots, n_m$ as for the dispensing process a flat surface is considered. The collected data will have to be pre-processed before they can be further used for the actual problem of generating a new trajectory. This process is explained in more detail in the following sections.

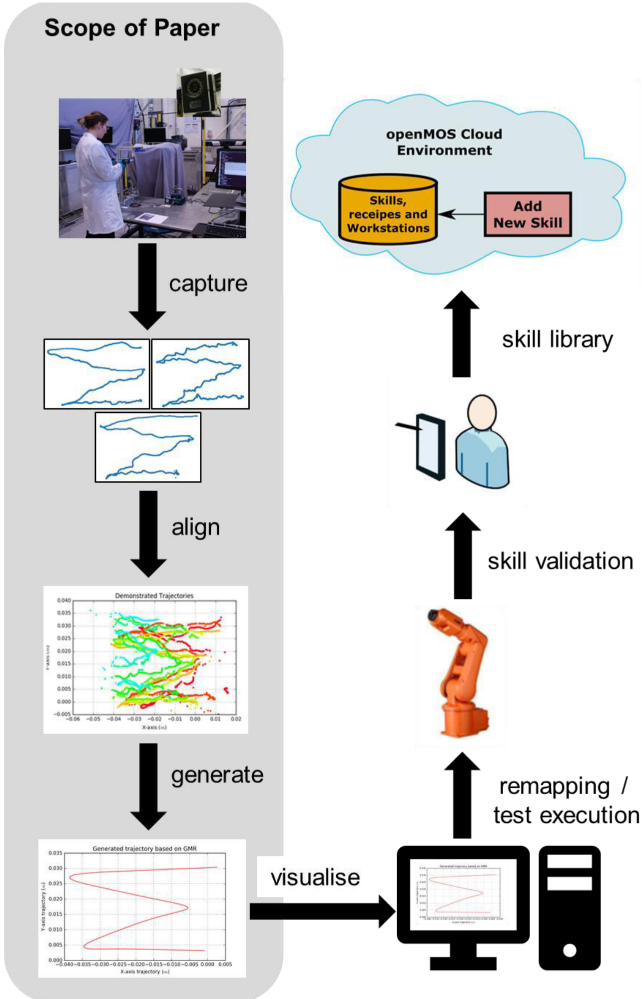

Figure 1. Overall methodology and scope of this work.

B. *Pre-processing*

Due to the nature of human demonstration, the sensory data collected during each trial are noisy and differ in length depending on the participant's speed. It is therefore essential to filter and align the collected trajectories prior to the learning process. To remove the noise, the Moving Average Filter was used, which averages subsets of the data [12]. In the next step, the individual trajectories were aligned in the time domain using the multi-dimensional Dynamic Time Warping (DTW) algorithm [13]. This algorithm is often used to determine time series similarity, classification, and to find corresponding regions between two-time series. DTW has a quadratic time and space complexity that limits its use to only small time series data sets. In this paper, FastDTW [14] was applied, which approximates DTW and has a linear time and space complexity.

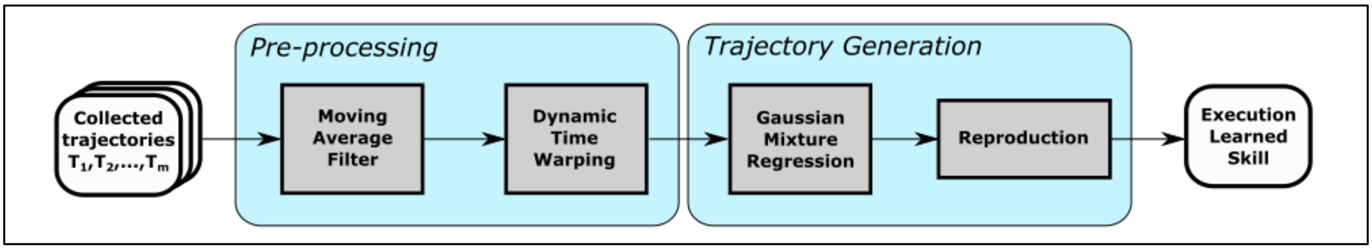

Figure 2. More detailed overview of the technical work done within the scope of this paper.

C. Gaussian Mixture Model

In general, mixture modelling is a simplified approach for density approximation of continuous or discrete data [15]. Such models allow for an appropriate flexible trade-off between model complexity and variations of the available demonstration data. From a mathematical perspective, mixture models are represented as a K component density function as shown in **Equation**

(1).

$$P(p_i) = \sum_{k=1}^{K} P(k)P(p_i \mid k) \tag{1}$$

where p_i is the i^{th} data point, $P(k)$ is the prior, and $P(p_i \mid k)$ is the conditional probability density function.

Given the demonstrated trajectories, which have been aligned previously, the dataset consists of 2D data points. These data points symbolise the operator 2D hand path during the dispensing process. This dataset is modelled by a mixture of K mixture of Gaussians. Hence, **Equation**

(1) can be re-written as seen in **Equation (2)**.

$$P(p) = \sum_{k=1}^{K} \pi_k \frac{1}{\sqrt{(2\pi)^D |\Sigma_k|}} e^{-\frac{1}{2}\left((p-\mu_k)^T \Sigma_k^{-1}(p-\mu_k)\right)} \tag{2}$$

where $\{\pi_k, \mu_k, \Sigma_k\}$ are the k^{th} Gaussian parameters, which denote the prior, mean, and covariance respectively. In this paper, we assume that the number of Gaussians is equal to the straight lines in the reference trajectory which is four.

C. Trajectory Generation

To create a general 2D trajectory form the mixture of Gaussian, GMR is applied [16]. In such a case, the sequential time steps (temporal data) are used as input data to generate the corresponding 2D trajectory values through regression. For each component in the GMM, the input (temporal data) and output parameters are separated such that the mean and covariance matrix of the k^{th} Gaussian component is defined by **Equation (3)**.

$$\mu_k = \begin{bmatrix} \mu_t^k \\ \mu_s^k \end{bmatrix} \qquad \Sigma_k = \begin{bmatrix} \Sigma_{t,k} & \Sigma_{ts,k} \\ \Sigma_{st,k} & \Sigma_{s,k} \end{bmatrix} \tag{3}$$

The conditional expectation of $p_{\{s,k\}}$, given p_k and the estimated conditional covariance of $p_{\{s,k\}}$, given p_t, are presented in **Equation (4)**.

$$\begin{aligned} \hat{p}_{\{s,k\}} &= \mu_s^k + \Sigma_{st,k}(\Sigma_{t,k})^{-1}(p_t - \mu_t^k) \\ \hat{\Sigma}_{\{s,k\}} &= \Sigma_{s,k} - \Sigma_{st,k}(\Sigma_{t,k})^{-1}\Sigma_{ts,k} \end{aligned} \tag{4}$$

According to the Gaussian distribution parameters of the k^{th} component, the estimated variable $\hat{p}_{\{s,k\}}$ and covariance $\hat{\Sigma}_{\{s,k\}}$ are mixed. Therefore, $\hat{p}_{\{s,k\}}$ can be used to estimate the mixing weighting β_k of component k as shown in **Equation (5)**.

$$\beta_k = \frac{P(k)P(p_t|k)}{\sum_{i=1}^{K} P(i)P(p_t|i)} \tag{5}$$

Successively, the conditional expectation of p_s, given p_t, and the conditional covariance of p_s, given p_t, can be estimated by using **Equations (4)** and **(5)** as given in **Equation (6)**.

$$\hat{p}_s = \sum_{k=1}^{K} \beta_k \hat{p}_{\{s,k\}} \qquad \hat{\Sigma}_s = \sum_{k=1}^{K} \beta_k^2 \hat{\Sigma}_k \tag{6}$$

Evaluating $\{\hat{p}_s, \hat{\Sigma}_s\}$ at different time steps p_t with the associated covariance matrices consequently gives an estimated trajectory $\hat{T} = \{\hat{p}_T, \hat{p}_s\}$. The time step between two consecutive points depends on the process and controller requirements of the robot and the dispensing process. It is worth mentioning that only the means and covariance matrices of the modelled Gaussians are needed to reproduce a new trajectory.

IV. Experiment

As a first step towards achieving fast skill deployment in plug-and-produce assembly systems, a manual dispensing experiment was conducted for an initial data collection. For this ethics-approved experiment (Ethics Approvals (Human Participants) Sub-Committee at Loughborough University), a total of twenty participants was recruited and each participant was asked to produce one zigzag pattern on a prepared aluminum plate (6.5x9cm). The main physical components of the setup were a time-pressure dispensing unit (Fisnar JB1113N), which was connected to a syringe and a Schunk gripper with 3D-printed handle. Vicon markers were attached to this handle to capture the trajectories the participants performed. Additionally, a push button was fixed to the handle allowing to trigger the dispensing process through a Raspberry Pi 3. A picture of a participant doing the task and exemplary outcomes can be found on the left-hand side of **Figure 1**.

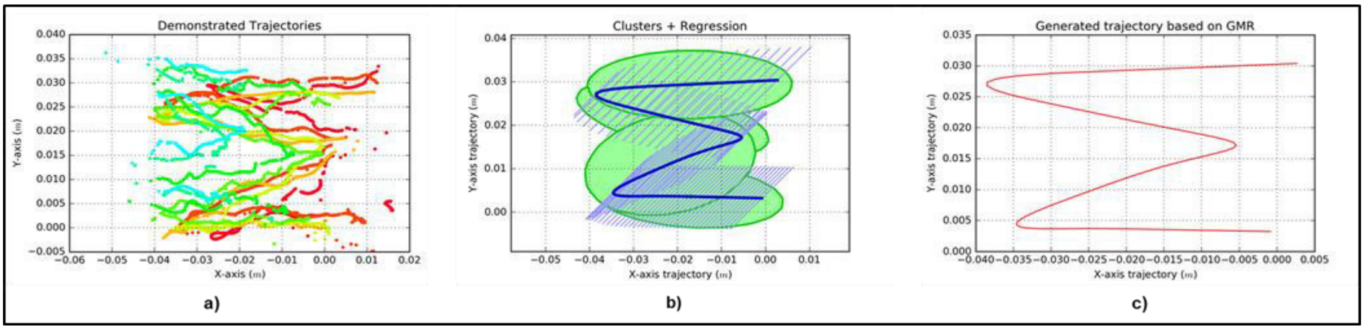

Figure 3. Results of the presented approach: a) filtered and aligned trajectories, b) four clusters found by GMM and the resulting trajectory using GMR, c) generated trajectory on its own.

V. Results and Discussion

The outcomes of applying the previously proposed methodology to the collected data are illustrated in **Figure 3**. **Figure 3a)** shows the collected trajectories after they have been aligned with the multi-dimensional DTW algorithm. As can be seen, the collected trajectories contain several outliers and noise. These are due to the measurement errors of the Vicon tracking system as well as reflective objects within the workspace that were mistakenly considered as markers. **Figure 3b)** visualises the outcome of applying GMM and GMR to the pre-processed data. The GMM was instantiated to find four clusters, each resembling an edge of the pattern. Based on this, the learned GMR was used to generate a new trajectory. The trajectory can be seen in better detail in **Figure 3c)**. Compared to the trajectories produced by humans, the generated trajectory is relatively smooth.

One limitation of the experimental setup that was noticed is that the motion was captured as long as the push button on the gripper was pressed to dispense the material. Due to the viscosity of the dispensed material, some participants released the button before the nozzle was above the last point of the pattern to let the material drop. This problem can, however, be easily solved in using a different dispensing material with higher viscosity or programming of the motion tracking.

VI. Conclusion and Future Work

In this paper, the first stage towards the transfer of a human skill into a manufacturing cloud system is presented to reduce the need for using conventional robotics programming approaches in similar context. The following has been shown: 1) Collection of trajectories while skill is demonstrated by human, 2) filtration of collected data and alignment of different trials, 3) modelling of demonstrated trials using Gaussian Mixture Regression. Future work will include the reproduction of the learned skill on the robot side ensuring to meet the semantic description of the openMOS skill. This will require to validate the reproduced trajectory and add the GMR model to the openMOS cloud system.

Acknowledgement

The research leading to these results has received funding from the European Union's Horizon 2020 research and innovation programme under grant agreement No 680735, project openMOS (Open Dynamic Manufacturing Operating System for Smart Plug-and-Produce Automation Components). Funding from the Engineering and Physical Science Research Council Centre for Doctoral Training in Embedded Intelligence (grant no. EP/L014998/1) is also acknowledged.

References

[1] B. Esmaeilian, S. Behdad, and B. Wang, "The evolution and future of manufacturing: A review," *J. Manuf. Syst.*, vol. 39, pp. 79–100, 2016.

[2] "'open Dynamic Manufacturing Operating System for Smart "Plug-and-Produce" automation components' (openMOS)." [Online]. Available: www.openmos.eu.

[3] C. Li, C. Yang, Z. Ju, and A. S. K. Annamalai, "An enhanced teaching interface for a robot using DMP and GMR," *Int. J. Intell. Robot. Appl.*, vol. 2, no. 1, pp. 110–121, 2018.

[4] A. Billard, S. Calinon, R. Dillmann, and S. Schaal, "Robot programming by demonstration," in *Handbook of Robotics*, B. Siciliano and K. Oussam, Eds. New York: Springer-Verlag, 2008.

[5] B. D. Argall, S. Chernova, M. Veloso, and B. Browning, "A survey of robot learning from demonstration," *Rob. Auton. Syst.*, vol. 57,.

[6] N. Vuković, M. Mitić, and Z. Miljković, "Trajectory learning and reproduction for differential drive mobile robots based on GMM/HMM and dynamic time warping using learning from demonstration framework," *Eng. Appl. Artif. Intell.*, vol. 45.

[7] T. Arai, Y. Aiyama, Y. Maeda', M. Sugi, and J. Ota, "Agile Assembly System by "Plug and Produce"," *Ann. CIRP*, vol. 49, 2000.

[8] K. Mustafa and K. Cheng, "Improving Production Changeovers and the Optimization: A Simulation Based Virtual Process Approach and Its Application Perspectives," *Procedia Manuf.*, 2017.

[9] M. Field, D. Stirling, Z. Pan, and F. Naghdy, "Learning Trajectories for Robot Programing by Demonstration Using a Coordinated Mixture of Factor Analyzers," *IEEE Trans. Cybern.*, vol. 46, no. 3, 2016.

[10] C. Li, H. Ma, C. Yang, and M. Fu, "Teleoperation of a virtual iCub robot under framework of parallel system via hand gesture recognition," in *2014 IEEE International Conference on Fuzzy System*.

[11] H. Liu and L. Wang, "Gesture recognition for human-robot collaboration: A review," *Int. J. Ind. Ergon.*, vol. 68, pp. 355–367.

[12] S. Hiroaki and C. Seibi, "Dynamic programming algorithm optimization for spoken word recognition," *Ieee Trans. Acoust. Speech, Signal Process.*, vol. ASSP-26, no. February, pp. 43–49, 1978.

[13] L. Biagiotti and C. Melchiorri, "Online trajectory planning and filtering for robotic applications via B-spline smoothing filters," *IEEE Int. Conf. Intell. Robot. Syst.*, vol. 9, pp. 5668–5673, 2013.

[14] S. Salvador and P. Chan, "Toward Accurate Dynamic Time Warping in Linear Time and Space."

[15] S. Calinon, *Robot programming by demonstration: a probabilistic approach*, 1st ed. Lausanne, Switzerland: EPFL Press, 2009.

[16] D. A. Cohn, Z. Ghahramani, and M. I. Jordan, "Active Learning with Statistical Models," *J. Artif. Intell. Res.*, vol. 4, 1996.

Movement and Gesture Recognition Using Deep Learning Technology

Baao Xie , Baihua Li, and Andy Harland,

Loughborough University, Loughborough, UK LE11 3TU

***Abstract*—For several decades, the pattern recognition of movement and gesture shows promise for human-machine interaction in many areas. A remarkable application in this area is gesture recognition for upper limb amputees using surface electromyography (sEMG) to capture the muscle activation as electrical signals. Another well-known application of in this field is human activity recognition (HAR). Most HAR applications are based on raw sensor inputs such as accelerometer and gyroscope signals which show its ability in learning profound knowledge about movement recognition [1]. Within the field of signal-based gesture recognition, traditional machine learning (ML) approaches have been widely used [2]. ML models give a high accuracy with large amounts of hand-crafted, structured, and under controlled data. However, traditional ML models require lengthy offline and batch training which is not incremental or interactive for real time application. In addition, ML models always cost a long period of time to extract a set of reliable features especially for high-dimensional, complex and noisy data because of the various situations in practical applications. Besides the ML methodologies, in recent years, the use of deep learning (DL) algorithms has become increasingly more prominent for their tremendous ability to extract and learn features from large amounts of data [3]. Compared to ML models, DL models make it possible for artificial intelligence to train the networks without hand-craft feature extracting. The aim of this work is to develop DL based methods for human movement and gesture recognition from time-series signals such as obtained using sEMG and IMU signals. We would like to understand the performance of DL for time-series signal analysis and accuracy, as to our knowledge, this aspect is still understudied. A series of experiments have been conducted to achieve it with different datasets and signals. The DB1 is a HAR dataset from the UCI repository. The DB2 and DB3 are sub-datasets of Ninapro database contains the recordings of 17 gestures from subjects by collecting sEMG signal. There are 4 different DL models designed for the experiments to find out the optimum solution by performance comparison: a 1-D CNN, a LSTM model, a C-RNN and 3+3 C-RNN. This is an extended abstract of a poster for the conference. The details of datasets and models are described in the methodology section, followed with the result section to present the results of different DL models on datasets.**

I. Methodology

A. Models

In the experiment, 4 DL models were used for gesture and movement recognition. The first one is a 1-D CNN which was inspired by [4]. The model processes separable convolution operation on each channel of the data rather than do the convolution on the entire input matrix. There are 2 convolutional layers in the model with max pooling and activation function applied after each convolution layer. The output of several separable convolution layers is the feature maps of inputs from different channels. And a fully-connected layer will be applied on these nodes, following by the classifier to generate the result. The second competing model is a basic LSTM with the sequence length of 128 which equals to the sliding window size. There is a dropout layer after the LSTM layer with problem rate of 0.8 to overcome the overfitting problem. And a fully-connected layer will be applied on these nodes, following by the classifier to generate the result.

The third model and fourth model is hybrid model combined with CNN and RNN. Convolutional layers are applied as a feature extractor in the structure. The output of the convolutional layers is the feature map of the input signal which contains useful information for other layers. The LSTM layers focus on the influence from previous time point and generate a probability map for each input. In the early stage of the experiment, a basic C-RNN model was developed including 1 convolutional and 1 recurrent layer. After some literature reviews and modifications, another advanced C-RNN model was built with 3 convolutional layers and 3 recurrent layers. In this section, the structure of the 3+3 C-RNN is described with more details.

As shown in Figure 1, the input of the 3+3 C-RNN model should be a signal piece fixed by a sliding window. The width of the input is in the time domain, and the size equals to the window size w. The height of the signal should always be 1. C represents the number of input channels while the signal from each channel will be fed into 1-D convolutional layers separately. For one round of training, a batch of such signal piece will be fed into the network where the batch size equals to i. As Figure 2 shows, the number of filters of the 1st Conv layer is designed as C*2, with the filter size of 2 and stride size of 1. The zero-padding approach is applied after each Conv layer to generate a feature map (FM) in the same width. The output format of 1st Conv layer should be [$B(i)$, w, $C*2$]. The 2nd and 3rd Conv layers are designed to have the same filter size and stride size but twice of the number of filters. The output of the 3rd Conv layer should be [$B(i)$, w, $C*8$]. It is worth mentioning that, the parameters in the layers are controllable for a better performance. And different from traditional CNN, there is no max pooling layer after convolution which aims to keep the integrality of data and ensure the fixed length of the sequence to feed into LSTM layers.

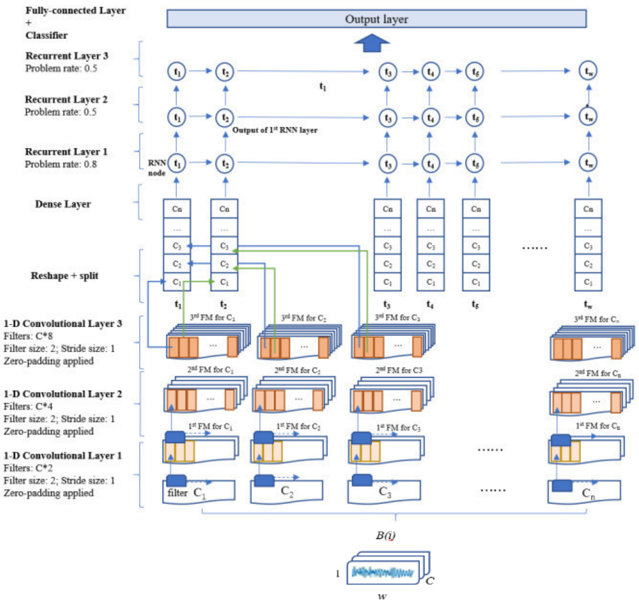

Figure 1. Structure of 3+3 C-RNN.

As shown in Figure 1, the output of convolutional layers are sequences of the feature map. These feature sequences will be reshaped into a node for recurrent layers. The width of the sequence is treated as the time period of recurrent layers which equals to *w*. Then, a dense layer will transform these nodes and feed them into the LSTM cells, each with the dimension LSTM size (*Ls*). This size parameter is designed to be 3 times larger than the number of channels, which is the similar way in the embedding layers in text applications where words are embedded as vectors from a given vocabulary. Then the sequence with the length of window size will be feed into three LSTM layers continuously. The input of each layer is the output from the previous layer. The dropout function is applied with problem rate of 0.8 for 1st and 2nd layers. And for the 3rd recurrent layer, the problem rate will be 0.5. In addition, the gradient clipping approach is added to improve training by preventing exploding gradients during back propagation. Only the last member of the sequence at the last LSTM layer is used as the final result, which will be feed into the fully-connected layers and a Softmax layer for classification.

B. Datasets

Database 1: The DB1 used in the experiment is the HAR dataset from the UCI repository. The dataset is taken from with 30 subjects within an age range of 19-48 years. Each volunteer was asked to perform six movements (walking, walking upstairs, walking downstairs, sitting, standing and laying) wearing a smartphone on the waist. The accelerometers, gyroscope, and body accelerometer signals were recorded at a sampling rate of 50 Hz. The dataset was separated into two parts randomly where 70% of the set was selected as training set and 30% as the testing set. In the pre-processing step, noise filters were applied to the signals. The signals sampled in the fixed-width sliding window of 2.56 sec with 50% overlapping [5].

Dataset 2: The DB2 and DB3 used in the experiment are sub-datasets of Ninapro database which provides a repository of sEMG data. sEMG measures the electrical activity when muscles are moving and exercising. It is an important attribute of the nervous systems aimed at collecting more muscular force or compensating for force losses. The purpose of the Ninapro project is to aid research on advanced hand myoelectric prosthetics with public datasets [6]. Currently, there are 7 databases available, each containing results from a series of movements where volunteers performed sets of hand, wrist and finger movements in controlled laboratory situations. The DB2 is the sub-dataset 5 of Ninapro database which contains data acquisitions of 10 subjects. The sEMG signals in the set were collected using two Thalmic Myo armbands with 16 electrodes, providing the upsampled sEMG signal at 200 Hz. The armbands were fixed close to the elbow according to the Ninapro standards. Each subject repeats 17 different hand movements for 6 times. Each movement lasts for 5 seconds and following by 3 seconds of rest as shown in Figure 3.

(a) Isometric, isotonic hand configurations.

(b) Basic movements of the wrist.

Figure 2. 17 gestures in Ninapro databases.

The subject 1-7 were treated as training set and subject 8,9,10 were selected as the testing set.

Dataset 3: The DB3 is the sub-dataset 2 of Ninapro database, which contains data acquisitions of 40 subjects. The sEMG signals in the set were collected using 12 electrodes from a Delsys Trigno Wireless System, providing the raw sEMG signal at 2 kHz. The type of movements of DB3 is same as DB2. The dataset was separated into two parts randomly where 70% of the set was selected as training set and 30% as the testing set. More details and attributes information of DB2 and DB3 are available at http://ninapro.hevs.ch/node/7.

II. RESULT

For each model, the learning rate is set at 0.0001 and the epoch size is set as 1000. The batch size is designed as 600. The training and testing are implemented on a computer with GPU of GTX 1080ti and CPU of Intel(R) Core(TM) i7-7700k @ 4.20Ghz. The programming platform is Tensorflow with python. Table 1 and Figure 3 show the average accuracy of different models when applied on datasets. It is obvious that 3+3 C-RNN gives the best performance on three datasets, which are 90.29%, 83.61% and 63.74%. For the Ninapro datasets (DB2 and DB3), 1-D CNN produces aresult of 53.17% when compared to other models. It is clear that for these 2 datasets, the models containing LSTM layer give a better accuracy, which means the relationships between different time points have more influence on the sEMG signal recognition.

TABLE I. PERFORMANCE OF DL MODELS

Models	DB1	DB2	DB3
1-D CNN	88%	72.49%	52.17%
LSTM	86.8%	78.13%	55.3%
C-RNN	87.62%	82.1%	59.31%
3+3 C-RNN	90.29%	83.61%	63.74%

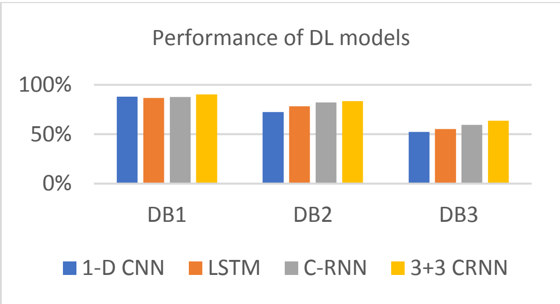

Figure 3. Experiment results of DL models on different dataset

However, for the HAR dataset, 4 models produce a high accuracy (above 85%). The one reason is the HAR database has fewer classes (6) than the Ninapro database (18) which makes it easier to classify. In addition, the class of ‘rest’ in Ninapro datasets seems to cause a decrease of the accuracy.

It is also worthy to mention that a large number of subjects (40 for DB3) with insufficient sample data cause a confusion for DL models and lead to a lower accuracy. Theoretically, this situation should be ameliorated if more sample data are fed to the networks. For the future experiments, we plan to compete the models with other existing researches using traditional ML or DL models. In addition, we will have a series of trials on different hyperparameters such as window sizes, filter sizes and batch sizes. We should also improve the structure of 3+3 C-RNN based on the experiments mentioned above to get a better performance in the future.

REFERENCES

[1] Wang, J., Chen, Y., Hao, S., Peng, X., and Hu, L. 2018. Deep Learning for Sensor-based Activity Recognition: A Survey. *Pattern Recognition Letters* 103,1 (Feb. 2018), 1-9.

[2] Lara, O.D., Labrador, M.A. 2012. A survey on human activity recognition using wearable sensors. *IEEE Communications Surveys & Tutorials* 15, 3 (Nov. 2012) 1192-1209.

[3] LeCun, Y., Bengio, Y., Hinton, G. 2015. Deep learning. *Nature* 521,1 (May. 2015), 436-444.

[4] Saeed, A., 2016. Implementing a CNN for Human Activity Recognition in Tensorflow. Retrieved from https://aqibsaeed.github.io/2016-11-04-human-activity-recognition-cnn/

[5] Anguita D, Ghio A, Oneto L, et al. 2013. A public domain dataset for human activity recognition using smartphones. In *Proceedings of European Symposium on Artificial Neural Networks, Computational Intelligence and Machine Learning*. (Bruges, Belgium).

[6] Pizzolato, S., Tagliapietra, L., Cognolato, M., Reggiani, M., Müller, H., & Atzori, M. 2017. Comparison of six electromyography acquisition setups on hand movement classification tasks. PloS one, 12, 10 (Oct. 2017), e0186132.

Visual Features as Frames of Reference in Task-Parametrised Learning from Demonstration

Shirine El Zaatari, Weidong Li

Abstract— **Task-parametrised learning from demonstration (TP-LfD) is suitable for programming collaborative robots (cobots) for collaborative industrial tasks, since the algorithm is able to encode complex mappings between observed states to the cobot's actions. TP-LfD relies heavily on perception, since detected objects and people serve as task parameters. This is a challenge since 1) industrial objects are difficult to detect due to their irregular shapes and sizes and 2) using marker stickers for detection is not desirable in manufacturing scenarios. Moreover, another challenge of using TP-LfD is that although it is an intuitive programming method, it is difficult for operators to initialise it due to their lack of underlying theoretical knowledge as opposed to the researchers that previously tested the algorithm. We aim to address these two challenges simultaneously by building an automatic task parametriser in which reinforcement learning is used to assign task parameters from a set of randomly detected visual features. In this paper, we introduce our solution and the progress done so far.**

I. Introduction

Industrial parties are growing increasingly interested in implementing human-robot collaboration (HRC) on their shop floors. Collaborative robots (cobots) bring many benefits to manufacturing including mass customisation and improved operator working conditions. For these benefits to be attained, the cobot must have a high level of intelligence and flexibility since it will be working alongside a human. It must act according to real-time operator and object states while respecting task requirements. The cobot should ideally also be easily programmable by a non-expert operator to ensure quick deployment and adjustability. One promising algorithm is learning from demonstration (LfD), in which the operator can intuitively teach the cobot an industrial task by recording a few demonstrations of it being done. Different variants of learning from demonstration are able to capture different levels of mapping complexities between states and actions. Task-parametrised learning from demonstration (TP-LfD) is thought to be able to capture the widest range of task instances, making it a generic algorithm for learning the widest range of collaborative industrial tasks [1].

However, although many algorithms exist that enable humans to intuitively teach cobots complex tasks, these algorithms are not yet popular in the industry. There are two main reasons behind this: 1) Some of these algorithms are not as intuitive to use by operators as researchers think they are. For example, in LfD, researchers record demonstrations while understanding the underlying theory behind the algorithm. These demonstrations are more likely to yield the desirable results as opposed to ones recorded by operators. Moreover, assuming perception is going to be achieved using sticker markers, the operator must decide where to paste the markers as to avoid occlusion, respect the shape and function of the work piece, avoid redundancy and not miss key objects, etc. This is often a challenge and could yield to errors if not done well. 2) These algorithms heavily rely on cobots' perception abilities, since the cobot must localise and detect relevant objects and people in a stochastic environment. Deep learning solutions aren't useful to identify industrial objects due to the lack of large training data on industrial parts. Pasting stickers is undesirable on manufacturing products and can be impossible due to part size and shape. Therefore, in this paper, we propose a solution to address the two main problems above.

In this paper, we discuss the methodology, while highlighting the contribution of this project. Moreover, the project progress is described and the future steps are outlined.

II. Methodology

The steps of our algorithm are outlined in Figure 1. Demonstrations are done by kinesthetic teaching and recorded by logging cobot joint data (angles and torques) and an RGB recording of the scene. The RGB images are used to detect and localise objects, in order to provide input to the TP-LfD algorithm. RGB images are inputted in a perception algorithm that extracts prominent visual features, further described in Section II-B. Since a large number of visual features will be detected, they are inputted into a reinforcement learning (RL) algorithm, briefly described in Section II-C, that filters and eliminates those with a high chance of irrelevance or redundancy. This RL policy updates according to a cost function calculated based on the performance of the TP-LfD. The TP-LfD outputs a Gaussian Mixture Model (GMM), as a mapping between the task parameters, which are the visual features, and the cobot joint data. The cobot will be able to reproduce the tasks recorded after performing Gaussian Mixture Regression (GMR) on the trained model.

A. *TP-LfD for Industrial Tasks*

Human-robot collaboration is identified as instances when the human and the cobot are working in close proximity without a barrier. A list of industrial human-robot collaboration tasks was identified and categorised (Figure 2) as follows:

- Independent: industrial applications done by the cobot after receiving instruction from the human, e.g.

Shirine El Zaatari is with the Institute of Advanced Manufacturing and Engineering at Coventry University, Coventry, UK (e-mail: elzaatas@uni.coventry.ac.uk).

Professor Weidong Li is with Engineering, Environment and Computing Faculty at Coventry University, Coventry, UK(e-mail: aa3719@coventry.ac.uk).

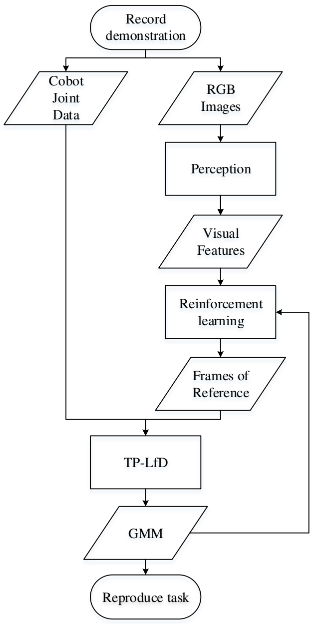

Figure 1 Flowchart showing our algorithm.

drilling, pug-in-hole, screwing, tightening bolts, surface finish, etc… The human and the cobot work in close proximity.

- Simultaneous: the cobot and the human perform similar actions towards the same goal, e.g. pick-and-place, assembly, etc... In this situation, both the cobot and the human can perform the set of actions, but distribute the actions in an optimised way according to time and space constraints.
- Sequential: the cobot performs sequential actions with the human, towards the same task goal, e.g. fetch, handover, pick-and-place, assembly, etc… The cobot should ideally understand and cater for the task needs as well as human action preference.
- Supportive: industrial applications in which the cobot is aiding the human during the task, e.g. co-manipulation, co-lifting, fixture, soldering, illumination, etc… Here, the cobot can be compliant, allowing the human to move it around. The cobot adjusts its actions according to the pace and position of the human, as well as according to task progress

In the four task categories, we identify 3 different motion types:

- Safe motion: the start and end location are known and the path is optimised/planned for collision avoidance and energy minimisation, etc.
- Compliant motion: the human is able to move the cobot manually.
- Constraint motion: the cobot follows a predefined path. This also included paths of zero length, i.e. when the cobot has to be rigid in a fixed position.

Ideally, the learning from demonstration algorithm should be able to learn the different motion types. Rozo et al. showed that TP-LfD is capable of learning the difference between compliant motion and constraint or safe motion [2]. Moreover, TP-LfD encodes variance and hence, it can differentiate between safe and constraint motion such as in [3].

TP-LfD can also capture locational and temporal constraints (motion-level actions), such as the cobot accommodating the position and the pace of the human during a supportive task [4]. This makes it suitable for supporting most of the HRC tasks in the four categories mentioned above.

Regarding task-level action decisions, e.g. subtask sequencing and scheduling, this can be modelled using Hidden Markov Model's such as in [5]. This would not interfere with the TP-LfD learnt model but rather would overlay it.

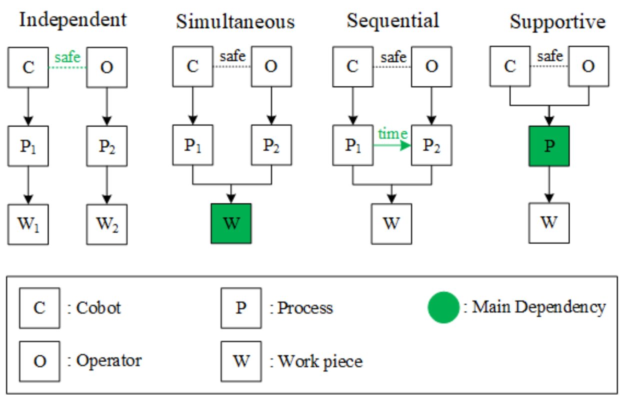

Figure 2 Categories of human-robot collaboration in industrial scenarios.

B. Reinforcement Learning on Frames of Reference

Although TP-LfD automatically calculates the relevancy of a task parameter, it will perform better if given a few task parameters of high chance of relevancy. Huang et al. were the first to tackle the problem of optimizing task parameters (frames of reference) in TP-LfD [1]. In their work, several frames of reference are initialised. Then, a reinforcement learning algorithm is used to shift the pose of these frames such that a task-specific cost function is minimised. Moreover, Huang et al. also suggest an automatic frame selection algorithm [1]. Given a number of frames, their algorithm is able to identify which frames play the biggest role in minimising the cost function. This helps eliminate frames of reference that have low influence on learning which speeds up computation and improves performance.

There are several limitations in the work of Huang et al. [1]. First, they do not tackle the question of how to visually detect frames of reference, but rather they are specified as fixed positions with respect to the cobot's end-effector. This eliminates cases in which the frames of reference are intrinsically defined on non-static objects. Second, in automatic frame selection, different subsets of frames are iteratively combined to assess different combinations of frames. This can get very computationally expensive as the number of frames increase. Third, each frame is defined as a duple $\{\mathbf{A}_t, \mathbf{b}_t\}^{(j)}$ where $\mathbf{A}_t^{(j)}$ is the rotation matrix and $\mathbf{b}_t^{(j)}$ is the translation vector of frame j at time step t. The RL algorithm updates $\mathbf{A}_t^{(j)}$ and $\mathbf{b}_t^{(j)}$, therefore, adjusting the pose of the frames of reference. This is not suitable when the frame of reference is visually detected and dynamic rather than manually specified and static.

In this project, we aim to combine a generic frame of reference detector with an automatic frame selector/optimiser. In a generic industrial task, the cost function should guarantee path optimisation and obstacle avoidance, making the cost function in [1] suitable. The update function is adjusting a relevancy score of each frame as well as a redundancy vector. The relevancy of each frame would help eliminate frames belonging to objects and locations irrelevant to the task. The redundancy vector would identify frames that belong to the same object. That way despite their relevancy, only one is incorporated in the TP-LfD. Moreover, if one frame is occluded in some portion of the demonstration, another frame from the same object/location is identified using the redundancy vector and used instead. We define our frames as a quadruple $\{\mathbf{A}_t, \mathbf{b}_t, \mathrm{r}, \mathbf{R}\}^{(j)}$ where r is the relevancy score and R is the redundancy vector, a (J-1) vector where J is the number of frames of reference. $\mathrm{R}_i^{(j)}$ is a score indicating the probability of frame i and j belonging to the same object/location.

C. *Visual Features as Task Parameters*

In TP-LfD, task parameters are usually specified as frames of reference with respect to which the cobot's motions is encoded. Task parameters can be locations in fixed space, e.g. corner of work table, or a point on an object, e.g. plate center, or action point of a tool, e.g. knife tip. These points are often marked with stickers, which are easily localised by the camera. In this project, we are looking to use visual features instead of stickers. Visual features are things like corners and edges. For a visual feature to be suitable as a frame of reference, it should satisfy certain conditions:

- Uniqueness: The feature should be relatively unique to the object/location to be localised.
- Has 6D pose: A 6D pose should be definable for the feature or through the feature.
- Easily detected and tracked: The feature should be prominent, as to be easily detected and identified from several viewpoints.

To obtain features of such characteristics, we aim to explore two main options:

1. Extracting them from feature layers of deep learning object pose estimation networks, such as Deep-6DPose [6] which takes 2D images as input.
2. Obtaining them from interest point detection deep learning networks, such as SuperPoint [7]. Figure 3 shows an example of interest points detected in a scene, extracted from [7].

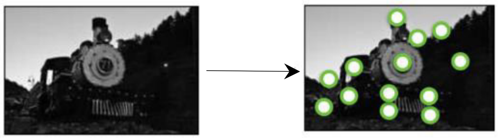

Figure 3 Example of interest point detection from SuperPoint [7].

One object can have more than one prominent feature, which if grouped together, can help solve the problem of partial occlusion.

III. Implementation (Progress and plans)

This project is divided into three main stages, reflecting the different algorithmic blocks mentioned in the methodology: 1) validating TP-LfD in industrial scenarios, 2) validating RL to automatically select frames and 3) using visual features as frames of reference.

The TP-LfD was first validated in simulation for a co-grasping task. In this task, an object was graspable from several sides. A leader agent chooses the closest side to grasp while the follower agent (the cobot), has to grasp the opposite side. This task was specifically designed to check the performance of TP-LfD on synchronised motions (the follower agent moved at a pace similar to that of the leader agent) and on conditional actions (the location of grasping of the follower agent was dependent on that of the leader agent's), which are two important attributes of HRC industrial tasks. The results, and given TP-LfD's performance on other scenarios in literature,

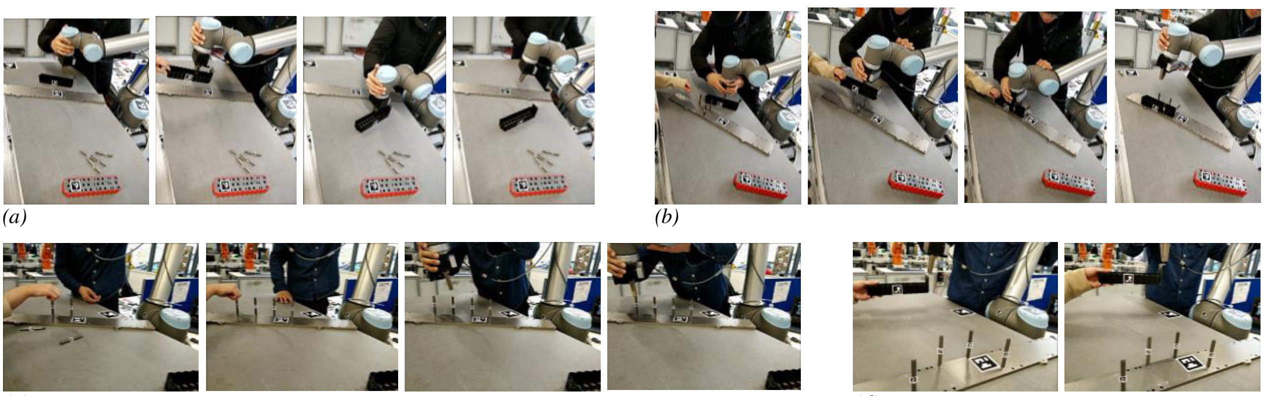

(a) *(b)* *(c)* *(d)*

Figure 4 Examples from the recorded demonstrations of industrial sub-tasks, with battery assembly parts. (a) Pick and place from variable to variable positions. (b) Pick and place from variable to fixed positions. (c) Collaborative sequenced bolt tightening. (d) Handover task.

were satisfactory to consider TP-LfD as a promising generic programming algorithm for HRC industrial tasks.

Next, real-life training data was collected from an industrial scenario of a collaborative car battery assembly. This assembly process is usually done manually. However, it involves a few tedious tasks such as stacking battery holders, screwing bolts and carrying heavy parts. Therefore, we have chosen to explore the possibility of converting it into a collaborative task. We extracted four simple subtasks from the battery assembly process and recorded them as demonstrations:

- Pick-and-place from variable to variable positions (Figure 4(a)): In this scenario, we recorded the cobot picking up a battery box from one side of a table and placing it on the other end of the table. This is analogous to scenarios in which the cobot fetches objects for the human to work on, such a heavy battery storage boxes.
- Pick-and-place from variable to fixed positions (Figure 4(b)): In this scenario, we recorded the cobot picking up a battery box from one side of the table and sliding it into a precise location on a cooling plate. Sliding onto the plate is a constraint motion to be learnt by the TP-LfD.
- Tightening bolts (Figure 4(c)): In this scenario, the human places four bolts in random locations on a cooling plate in a random sequence. The cobot follows to touch the tip of the bolt in the same sequence. This is to learn action sequences as well as to generalise over arrayed motions.
- Handover (Figure 4(d)): In this scenario, the human changes his hand position and the cobot follows the hand. This is to teach the cobot to adjust to the human's pose and pace.

The demonstrations were recorded with sticker markers as task parameters, as an initial step in the project. In the first step of the project, we aim to learn the tasks using TP-LfD with well-placed markers as task parameters. This will give us an intuition on the performance of TP-LfD on our specific tasks. This will give further guidance on the implementation of the other project stages. The recording of the demonstration and extraction of marker poses was further proof of the challenges faced when trying to use sticker markers in an industrial scenario, namely occlusion, size limitation, and task obstruction.

In the second stage of the project, we aim to validate the RL algorithm on demonstrations with an abundance of randomly-placed markers. Third, we aim to learn from marker-less demonstrations in which visual features are the task parameters.

IV. Conclusion

Task parameterised learning from demonstration (TP-LfD) is a generic algorithm suitable for intuitively programming collaborative robots (cobots) for industrial tasks. TP-LfD requires the user to specify "frames of reference" with respect to which the cobot's motion will be encoded. These frames of reference must be relevant to the task, easy detectable and not prone to occlusion. Sticker markers have been used to specify such frames. However, using sticker markers is not desirable in industrial scenarios. Therefore, we propose the use of randomly detected visual features as frames of reference. If given a large number of frames of reference, as opposed to a select few, TP-LfD will decrease in performance. Therefore, we need to add a reinforcement learning algorithm to filter through the large set of visual features, so that only a few are passed on to the TP-LfD as frames of reference. In this paper, we present this research problem and outline our methodology, progress and future works.

Acknowledgment

Our research is supported by Coventry University, Unipart Powertrain Application ltd. and High Speed Sustainable Manufacturing Institute (HSSMI).

References

[1] Y. Huang, J. Silverio, L. Rozo and D. G. Caldwell, "Generalized Task-Parameterized Skill Learning," in *2018 IEEE International Conference on Robotics and Automation (ICRA)*, 2018.

[2] L. Rozo, S. Calinon, D. G. Caldwell, P. Jimenez and C. Torras, "Learning Physical Collaborative Robot Behaviors From Human Demonstrations," *IEEE Transactions on Robotics,* vol. 32, no. 3, pp. 513-527, 2016.

[3] C. Perez-D'Arpino and J. A. Shah, "C-LEARN: Learning geometric constraints from demonstrations for multi-step manipulation in shared autonomy," in *2017 IEEE International Conference on Robotics and Automation (ICRA)*, 2017.

[4] S. Calinon, "A tutorial on task-parameterized movement learning and retrieval," *Intelligent Service Robotics,* vol. 9, no. 1, pp. 1-29, 2016.

[5] D. Vogt, S. Stepputtis, S. Grehl, B. Jung and H. B. Amor, "A system for learning continuous human-robot interactions from human-human demonstrations," in *2017 IEEE International Conference on Robotics and Automation (ICRA)*, 2017.

[6] T.-T. Do, M. Cai, T. Pham and I. Reid, "Deep-6DPose: Recovering 6D Object Pose from a Single RGB Image," *arXiv preprint arXiv:1802.10367,* 2018.

[7] D. DeTone, T. Malisiewicz and A. Rabinovich, "SuperPoint: Self-Supervised Interest Point Detection and Description," 2017.

Can underwater environment simulation contribute to vision tasks for autonomous systems?

Jiangtao Wang, Yang Zhou, Baihua Li, Qinggang Meng, Emanuele Rocco and Andrea Saiani

***Abstract* — To simulate the underwater environment and test algorithms for autonomous underwater vehicles, we developed an underwater simulation environment with the Unreal Engine 4 to generate underwater visual data such as seagrass and landscape. We then used such data from the Unreal environment to train and verify an underwater image segmentation model, which is an important technology to later achieve visual based navigation. The simulation environment shows the potentials for dataset generalization and testing robot vision algorithms.**

I. Introduction

In the robotics field, it is a common strategy to verify applications and algorithms in a simulation environment; this is especially important for autonomous underwater vehicles (AUVs), as frequently testing the algorithms on physical prototype in real underwater environment is costly and risky due to the unpredictable environment. Furthermore, it is difficult and time consuming to collect data and generate the corresponding labels for visual-based algorithms, in particular for deep learning which usually needs high numbers of data to train a model. On the other hand, developing a realistic underwater simulation environment that is close to the real world is a laborious task.

In this paper, we developed an underwater simulation environment with Unreal Engine 4 (UE4) and, since image segmentation is an important technology to achieve visual-based navigation, used the visual dataset generated from Unreal to train a segmentation model and to verify the feasibility of using synthetic images to train underwater deep learning models. The experiment results show that the Unreal simulation environment has the capability for helping robot vision research by easily generating dataset and validating deep learning algorithms.

II. Methodology

A. Unreal Engine

The UE4 is the 4th version of Unreal Engine, and it provides useful development tool sets for building a virtual environment from enterprise applications, cinematic experiences to games on PC, mobile and so on. Hence, UE4 has the required quality to produce a realistic simulation environment for robotics research. Furthermore, the camera view in the UE4 can be controlled by keyboard and commands and there are plenty of plugins to allow developers expand UE4 functionalities. In terms of testing robot vision algorithms by communicating with the unreal environment, the UnrealCV[1] provides commands to control the UE4 for testing robot vision tasks. We can easily get four different views of the camera with UnrealCV in UE4: camera view, depth view, surface normal view and mask view.

B. Underwater environment simulation

We used UE4 to simulate the underwater environment. The environment contains seagrass, seabed, stone, rock fish and a 3D scan of a real wreck. It can simulate the light and visual conditions in the underwater environment. The views are changing varying from depth of the sea and distance towards the objects. For example, the wreck looks very hazed from distance and becomes clearer when the camera approaches to it.

C. Dataset Generation

Image segmentation dataset is collected from the simulation environment. In the UE4, we can move the camera and adjust the locations and rotations to collect a great number of image data and the segmentation labels.

D. Image segmentation

For image segmentation, we proposed a network architecture based on autoencoder network which consists of encoder and decoder networks. Our encoder network uses the architecture from VGG-16 [2] that is pre-trained on the ImageNet[3] dataset. We add a batch normalization layer[4] and a ReLU layer[5] to each convolutional layer. The Vgg-16[4] network has 5 max-pooling layers to reduce the size of feature maps. The decoder network is the symmetric structure of our encoder network, having 5 un-pooling layers to expand the feature maps from de-convolutional layer.

Inspired by U-Net [6], we concatenate the feature maps from the last two encoders to the corresponding decoders. Moreover, we only keep concatenation operators for final two blocks of the encoder network, responsible for generating the dense feature maps, in order to reduce the training used memory.

Concatenation allows decoder network to learn from the dense feature maps by directly providing the feature maps from encoders to decoders

Jiangtao Wang is with Loughborough University, Loughborough, The United Kingdom, LE11 3TU (e-mail: J.Wang4-18@student.lboro.ac.uk).

Yang Zhou is with Loughborough University, Loughborough, The United Kingdom, LE11 3TU (e-mail: Y.Zhou5@lboro.ac.uk).

Baihua Li is with Loughborough University, Loughborough, The United Kingdom, LE11 3TU (e-mail: B.Li@lboro.ac.uk).

Qinggang Meng is with Loughborough University, Loughborough, The United Kingdom, LE11 3TU (e-mail: Q.Meng@lboro.ac.uk).

Emanuele Rocco is with Witted Srl, Piazza Manifattura, 1 38068 Rovereto (Tn) Italy (e-mail: emanuele@witted.it).

Andrea Saiani is with Witted Srl, Piazza Manifattura, 1 38068 Rovereto (Tn) Italy (e-mail: andrea@witted.it).

III. Preliminary Results

Figure 1 shows the screenshots of four different views in the simulation environment. The lit view is camera view that shows the underwater scenery from current position. The mask view represents different objects, which will be colored with a specific color. The objects can be extracted from the mask. The normal view shows the surface of the objects. Depth view provides the relative depth of each object in current view.

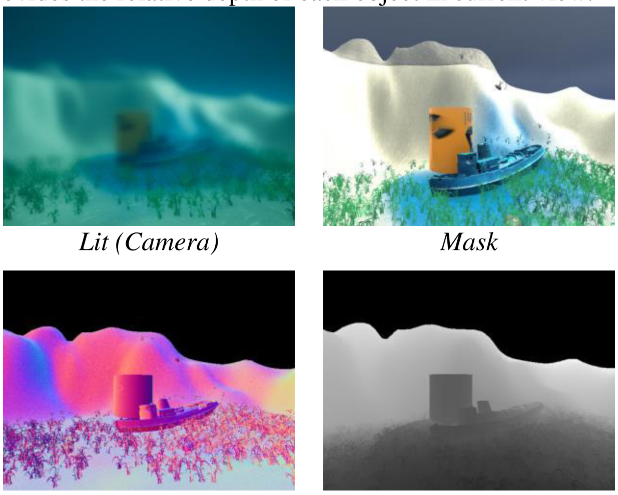

Figure 1. Screenshots of underwater simulation

We get the label with a simple calculation of two images. First one is background only, and the second contains background and object. We can get the segmentation label of the objects by subtracting these two images. Figure 2 shows a training data and their label in underwater simulation segmentation dataset.

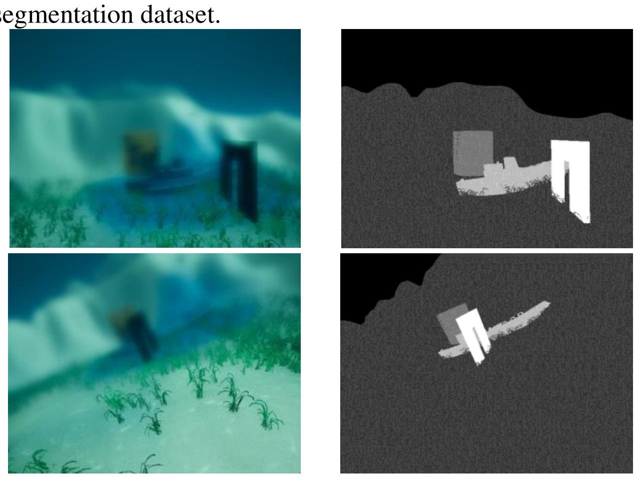

Figure 2. Sample of simulation dataset

The result of segmentation algorithm that runs on simulation environment is shown in Figure 3. The seafloor, background, ship and other objects can be accurately segmented.

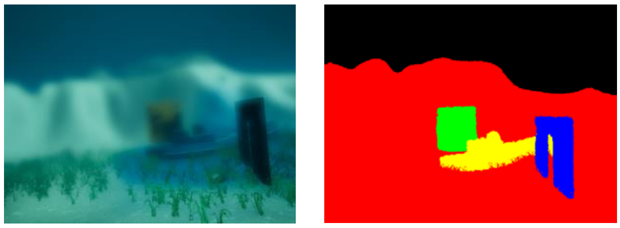

Figure 3. Result of segmentation in Simulation data

IV. Conclusion

In this paper, we used UE4 to develop an underwater simulation environment. In this simulation environment, we can easily generate visual data for robot vision tasks and test visual algorithms. We also found that we can train the segmentation model with the dataset and labels generated from our simulation environment. In the future, a more realistic simulation that can combine with underwater dynamics is useful for further testing the visual and motion algorithms. Furthermore, since with further work the simulation environment can realistically replicate the actual underwater imagery, the model trained on the UE4 simulation could be transferred to the real world too. In future research, we would like hence to pre-train a model with synthetic data and then use transfer-learning with real data to train image segmentation model for applications in real underwater environments.

V. Acknowledgement

We would like to express our thanks to Gabriele Saracco for the early development of the UE4 prototype, Ubaldo Pantaleo - ubica srl (Underwater bio-cartography) for the wreck 3D scans and Luca Fabbian for the early testing of possible ROS-UE4 integration solutions.

References

[1] Qiu, W., & Yuille, A. (2016). UnrealCV: Connecting Computer Vision to Unreal Engine BT - Computer Vision – *ECCV 2016* Workshops. In G. Hua & H. Jégou (Eds.) (pp. 909–916).

[2] K. Simonyan and A. Zisserman, "VERY DEEP CONVOLUTIONAL NETWORKS FOR LARGE-SCALE IMAGE RECOGNITION," *CORR*, 2014.

[3] D. Jia, D. Wei, S. Richard, L. Li-Jia, L. Kai, and F.-F. Li, "ImageNet: A large-scale hierarchical image database," *2009 IEEE Conference on Computer Vision and Pattern Recognition*. IEEE, Jun-2009.

[4] S. Ioffe and C. Szegedy, "Batch Normalization: Accelerating Deep Network Training by Reducing Internal Covariate Shift." *Proc. 32nd Int. Conf. Mach. Learn.*, vol. 37, 2015.

[5] X. Glorot, A. Bordes, and Y. Bengio, "Deep Sparse Rectifier Neural Networks," *Proc. 14th Int. Con- ference Artif. Intell. Stat.*, vol. 15, 2011.

[6] O. Ronneberger, P. Fischer, and T. Brox, "U-Net: Convolutional Networks for Biomedical Image Segmentation." in *Lecture Notes in Computer Science (including subseries Lecture Notes in Artificial Intelligence and Lecture Notes in Bioinformatics)*, 2015, vol. 9351, pp. 234–241.

Development of a Simulated Production Environment for Plug-And-Produce Architecture Testing

William Eaton

***Abstract*— This paper describes the development of a simulated production demonstrator, used in the development of the openMOS plug-and-produce architecture. Primarily designed to allow synthetic testing of plug-and-produce technologies, the intention is to simulate real production hardware, such that there is no perceivable difference to the production controller. Communication with the main production controller is achieved via network, using individual embedded computers to act as PLC based 'device adaptors'. Each production device is also either simulated using the same embedded computer, or externally on a more powerful computer, with simulation specific information (such as material flow) transferred using ROS. Testing has proven the concept to work well, allowing for a larger demonstration of the openMOS project but at a fraction of the cost.**

I. Introduction

The global manufacturing industry is currently moving to the next generation of automation, often termed 'Industry 4.0'. One goal of this effort is to increase efficiency, allowing more products to be created to help satisfy the increasing global demand for consumer goods. At the same time, smart-manufacturing can also be used outside of traditional mass production, offering products in smaller numbers but with other advantages; such as reduced time-to-market, increased product complexity or lower production cost.

As automation equipment becomes more prevalent, Small and Medium-sized Enterprises (SMEs) are now rapidly investing in robotics and equipment previously only available to the largest and most technology advanced of companies. Although much of the technology is the same, SMEs face different challenges to large companies, typically due to costs. Unlike large companies which can afford bespoke solutions, SMEs are often limited to using existing "Off-the-shelf" equipment, sourced from whichever supplier is most cost effective. Production systems are then created by integrating equipment from multiple suppliers, often including 'legacy' systems with very low levels of automation.

To simplify this process and make the benefits of smart manufacturing more obtainable, efforts are being made to develop unifying "smart-automation" architecture, capable of integrating varied equipment into a cohesive system. This form of architecture must combine both software and hardware elements, to communicate and control the diverse range of equipment used in manufacturing. The work described in this paper has been undertaken during the development of such a system, as part of the openMOS (**Open**-source **M**anufacturing **O**perating **S**ystem) project [1].

*Research supported by the European Commission.

W.H. Eaton is with the Intelligent Automation Centre, at Loughborough University, UK. (e-mail: w.h.eaton@lboro.ac.uk).

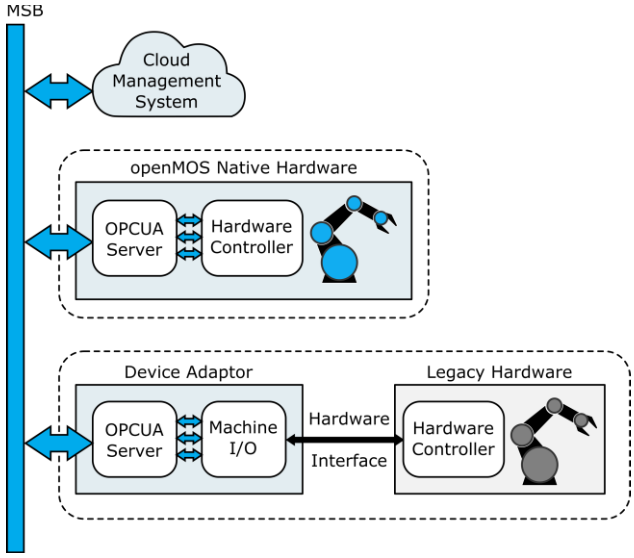

Figure 1. High-level openMOS Architecture for native and legacy equipment

A. *openMOS Architecture*

The openMOS project is an openly-accessible software-architecture, intended to provide a standardised platform for automation in manufacturing. One of the key goals of the project is to provide 'plug-and-produce' (P&P) [2] functionality, allowing any compatible equipment to be integrated into a system with minimal manual setup. Although other P&P systems have been proposed, they typically focus on low level integration, such as local-discovery, where each device announces itself upon connection [3] [4].

Although such functionality is required, these systems do not currently attempt to solve the more difficult task of conveying to the rest of the system what the new device can accomplish. For openMOS, this is achieved by abstracting the *product* from the equipment as much as possible. For a device to be compatible, its capabilities must be encapsulated as 'skills'. (These could be entirely unique or highly generic skills such as 'hole drilling'.) To provide P&P functionality, each device declares its skills and parameters to the overall system upon initial connection. Each product is then defined using a 'recipe', which is an ordered list of skills which must be applied to the input material for the final product to be created. As transportation between equipment is also considered, the most efficient flow of material through the manufacturing facility is automatically determined. These features are intended to facilitate 'Flexible automation', [5] in which either existing equipment can be rapidly reconfigured to meet changing demand, or new equipment added to increase capability.

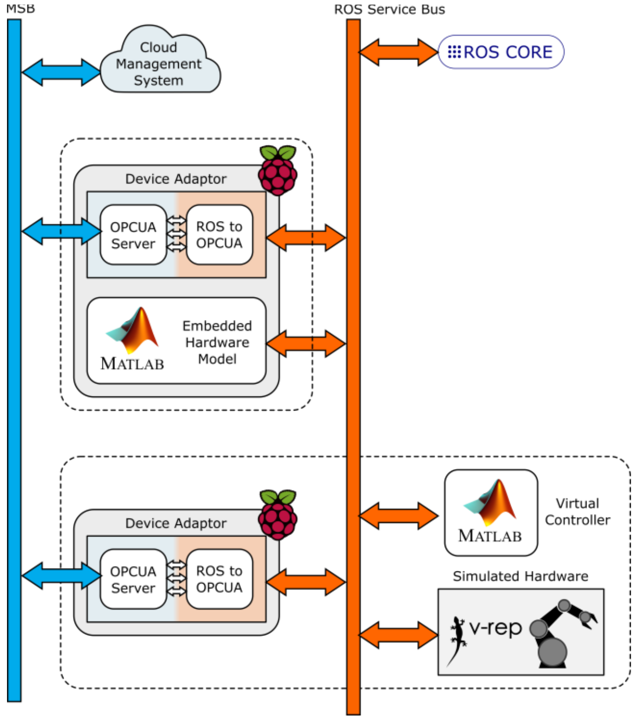

Figure 2. High-level openMOS Architecture for simulated equipment

During production, the core functionality requires all devices to be connected to a common Manufacturing Service Bus (MSB) [6] running on a local network, as shown in Figure 1. The MSB is used to transmit "skill" requests and sensor data, providing every device access to any data it requires. Overall control of the production task is achieved via an agent-based Cloud Management System (CMS). For a device to be openMOS compatible, it must fulfil both hardware and software requirements. Although new production devices featuring openMOS are natively compatible, existing devices are usually not equipped to support P&P interfaces and may lack network connectivity, making interfacing difficult. Therefore, legacy support is introduced through 'device adaptors' which interface between the device and the MSB. Each DA is essentially a small embedded computer, which converts openMOS skill commands into an equipment specific interface.

B. Simulation

For any automated manufacturing environment, the cost of equipment represents an enormous initial investment. As the openMOS architecture has been co-developed by several SME's and academic institutions, the scale of testing has been limited. Therefore, although several physical production demonstrators have been created, each has been a compact representation of a specific capability of the overall architecture. Instead, it was decided that a simulated approach could be used to demonstrate openMOS capabilities at a larger scale. Furthermore, the development of a simulation approach would be useful for any SME wishing to adopt the openMOS platform, allowing them to verify the functionality of the system without applying it to their production environment. This paper presents the development of a scalable approach to virtual system development, intended to provide multiple levels of fidelity.

II. Simulator Requirements

A. Computational Hardware

Although the term 'simulator' is used here to describe the entire system, it should be recognised that there are two distinct parts; the first being the openMOS architecture itself. For the results to be meaningful, openMOS must be deployed using hardware comparable to what would be used in a production environment. This applies to both the computers which run the software, as well as the networking equipment and interfaces for each machine.

The second part is the simulated plant operations used to produce representative data. At the most basic, this consists of responding to openMOS skill requests and replicating the sensor data that would be created by actual equipment. As a single production facility could include many hundreds of connected devices, the computational requirements could be quite large, especially for high fidelity simulation. Therefore, as the primary purpose of the simulation is to test the performance of the openMOS control system, it is essential that the simulator must be implemented in a way does not affect the performance of the MSB. This is most easily achieved through hardware separation, in which openMOS and the simulator are run on independent equipment. Moreover, as using a single computer limits the scale of the manufacturing process which can be modelled, a distributed computing approach is to be used; with multiple computers working in conjunction to produce a facility scale simulation.

B. Distributed Computing, Networking and Device Adaptors

To ensure that the demonstrator is representative, the interface between openMOS and the simulation must replicate what would be found on an actual deployment. One critical element is that the openMOS communication protocols rely on each device having a unique IP address, to ensure that each device can be separately addressed by the controller. Returning to Figure 1, there are two methods for openMOS to interact with hardware:

- Natively supporting openMOS within the hardware controller itself
- Using a dedicated openMOS device adaptor to support legacy equipment.

Native support of openMOS is the eventual goal of the project, with manufacturers producing devices already compatible with openMOS installations. However, as the devices within this work are simulated, such an approach would require including openMOS interface protocols directly within the simulation. The downside of this approach is that any latency in the simulation could introduce delays to the MSB which are actually specific to the simulator, rather than openMOS itself. Furthermore, although it is possible that both network interface and controller could be virtualized, to ensure compatibility it is far simpler to use separate physical devices. This also allows the 'Plug and Produce' functionality to be tested directly, simply by unplugging equipment to represent failure, and attaching new equipment during production to test how the system responds. As such, custom hardware device adaptors will be used to communicate between the simulation and openMOS.

III. Scenario

Although the simulation approach has been developed to allow for a large number of devices, the initial implementation is more modest, aiming to begin with twenty simulated devices and their device adaptor counterparts. The main goal of this initial setup is to demonstrate flexible process simulation, in which machines can be added or removed from the production environment.

The chosen scenario is the assembly of a generic electronic product consisting of four components: two casing parts and two electronic internals. Both the product casing and internals have variants allowing for individual products to be customised. The simulated facility consists of several different workstation types (each with several instances) through which the products flow in a non-linear order, as shown in Figure 3:

- 4 Laser cutting stations
- 3 Painting Stations
- 3 Gluing Stations
- 1 Final Marking Station
- 2 Assembly Stations
- 2 3D-Printing Stations
- 6 Assembly Stations

Variation in each individual product can require parts to revisit workstations multiple times, requiring the CMS to determine the best use of available equipment. For example although there are 3 distinct assembly tasks, the 6 assembly stations are each capable of performing every action, and can adaptively share workload. Finally, product flow through the simulated facility is achieved using a small number of Automated Ground Vehicles (AGVs). A single AGV controller is used to assign jobs to AGVs, which move products on predefined routes.

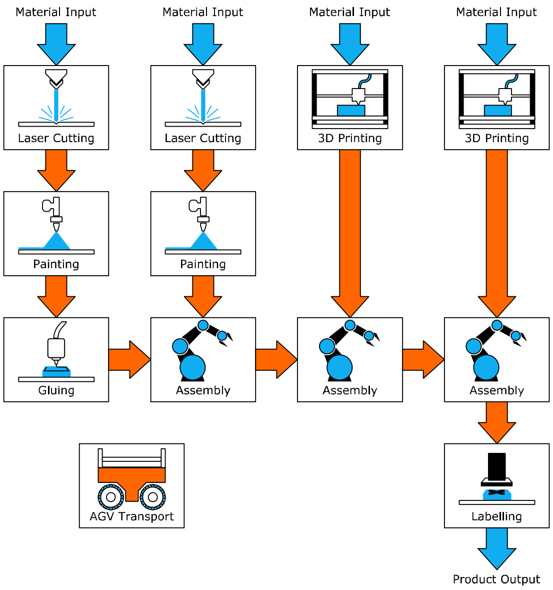

Figure 3. Material flow between stations for single product completion within simulation scenario.

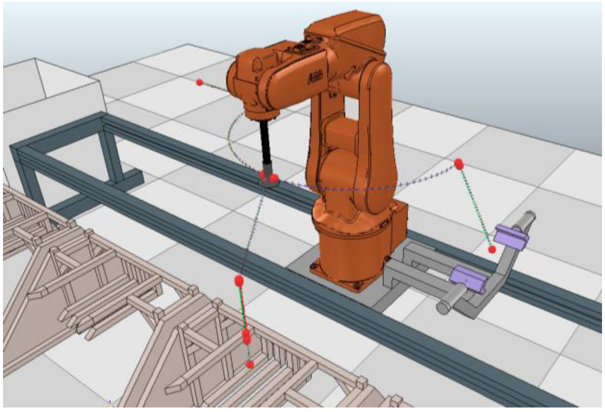

Figure 4. A virtual assembly workstation shown in VREP, along with the preplanned motion paths.

IV. Implementation

To achieve the requirements of the simulation, several different software packages were combined across a range of different hardware. Figure 1 shows a high-level depiction of the software setup for openMOS, as it would be deployed in an actual production environment. Figure 2 shows a similar depiction of the software used in the simulation. Comparing Figures 1 and 2, the most obvious difference is the inclusion of the Robotic Operating System (ROS) to act as a secondary communication protocol. As the simulation is distributed, consisting of equipment controllers and simulations, ROS was identified as the most suitable method of communication within the simulation itself, without interfering with the openMOS MSB. With its wide adoption and ease of use, ROS also allows an extensive range of existing software to be easily deployed, or additional capabilities to be added quickly using its well-defined software architecture. As previously discussed, for each simulated device within the demonstrator, an embedded computer was required to act as the device adaptor. Owing to their popularity and wide range of software available, the decision was made to use the Raspberry Pi 3 (RasPi) in this role.

In an actual openMOS installation, communication between devices is primarily achieved via an Open Platform Communications Unified Architecture (OPCUA) [7] server/client model. Each device hosts an OPCUA server (which is essentially just a database of variables which can be accessed or updated in real-time), allowing connected clients to read/write data as appropriate, via the MSB. Due to the success of OPCUA in communicating between the device adaptor and the MSB, OPCUA was also seen as an appropriate method for the device adaptor to communicate with the simulation (effectively running two OPCUA servers for each device adaptor). Therefore at minimum, each RasPi is running two OPCUA servers – one 'facing' the MSB and one 'facing' the simulation – and acts an 'adaptor', converting openMOS skill requests into ROS based simulation triggers.

For the OPCUA server which connects to the MSB, a standalone Java OPCUA implementation was used, to maintain consistency with how a typical openMOS install would function. By contrast, the simulation facing OPCUA server was implemented using the ROS_OPCUA package, which directly maps ROS topics and services into a OPCUA database. This simplifies integration to the extent that when the device adaptor identifies an openMOS skill request on the MSB-facing OPCUA server, it can simply set a variable on the simulation-facing OPCUA server to trigger the appropriate ROS service within the simulation.

As shown in Figure 2, for extremely simple simulated devices, (such as the 3D printing stations which simply output a product at a fixed rate) the required simulation was simple enough to run on the same RasPi. This was achieved using an Embedded Simulink model, which communicated with the OPCUA server onboard via an additional ROS node on the same RasPi. For all other stations, a higher fidelity simulation was used to model the physical interactions of equipment and product. This allowed the quality of the output (such as paint coverage and glue distribution) to be assessed, to confirm that the virtual station models were appropriately complex as to represent real equipment. For these stations, Matlab was used as a virtual controller, with the simulation provided using the VREP simulation environment on a dedicated desktop PC per station. An additional standard desktop PC was connected to the openMOS network to run the CMS and MSB software.

Finally, to provide high speed network connections between all devices, two commercial DLink DGS-1100-24 Gigabit Switches were used to provide network connectivity typical of a small production environment. Although only 20 devices were used in this initial scenario, 48 RasPi device adaptors were created for future simulation scenarios.

V. Assessment of Suitability

As stated in the introduction, the purpose of this simulation is not to produce the most accurate reconstruction of a production environment, but is instead intended to provide a facsimile of the interactions between openMOS and a production system, without having to invest in the hardware. The simplest method of assessing whether this solution is suitable is to compare a simulated workstation with a practical example; as the simulation is intended to replicate the data provided by equipment, the CMS should not be able to differentiate between simulated and practical equipment.

For this purpose, one of the simulated stations within the scenario was selected to exactly mimic an actual workstation already available. The virtual `gluing station' was designed to replicate the motions and actions of a physical ABB IRB120 industrial robot arm. In addition to the robot itself, a gluing nozzle and temperature sensor were also included. By creating a ROS package for the physical system, the software implementation was nearly identical to the simulated devices, requiring minimal integration. As the ROS_OPCUA adaptor automatically exposes ROS topics and services, there was no additional setup beyond allocating separate ROS namespaces to each station so as to differentiate between them. (As such, it can be also be concluded that that integrating physical equipment into the simulation is extremely easy, provided that a ROS package is available).

Having installed both virtual and physical versions of the same workstation, both systems were linked to the MSB and an empirical analysis of the data carried out. As there was no substantial difference in the data produced, the simulation was judged to be an accurate representation of the actual robot, validating that the simulated approach produced an accurate portrayal of production hardware.

Following this, repeated testing has been undertaken to validate the P&P functionality of openMOS, by removing RasPis from the simulation during operation. It has been found that the system is capable of responding to this by re-routing product to additional instances of the same workstation, where possible. When these machines are then restored, openMOS is once again able to make use, without the need to restart the entire facility. As both simulated and real-world process devices can function together, the simulation can be assessed to produce an output equivalent to that provided by actual hardware. Therefore, the simulation is capable of generating network traffic representative of an actual physical production facility, but at a greatly reduced cost.

VI. Conclusion

This paper has outlined the creation of a simulated production system, designed to replicate the data and signals from real world equipment to verify many aspects of the openMOS architecture. The developed simulation approach is highly straightforward, in addition to being easily expandable to simulate production facilities of greater size.

Following on from the initial testing covered here, the intention is for future work to include a comparison between the simulation and a hardware infrastructure with known timings; intended to allow an objective comparison to determine if openMOS is truly capable of performing on a large scale without performance loss. Finally, the simulation infrastructure developed here also has the potential for training activities, as well as potentially serving as a basis for benchmarking and certification

References

[1] Openmos website. [online] Available at: https://www.openmos.eu/ [Accessed 05 Apr. 2018].

[2] T. Arai, Y. Aiyama, Y. Maeda, M. Sugi, J. Ota, "Agile Assembly System by "Plug and Produce"," CIRP Annals, Volume 49, Issue 1,Pages 1-4,

[3] L. Durkop, J. Imtiaz,H. Trsek, L.Wisniewski, J. Jasperneite. "Using OPC-UA for the Autoconfiguration of Real-time Ethernet Systems". In Proc. 11th IEEE International Conference on Industrial Informatics (INDIN), 2013, pp. 248-253.

[4] V , Hammerstingl., G. Reinhart. "Unified Plug&Produce architecture for automatic integration of field devices in industrial environments". In Proc. IEEE International Conference on Industrial Technology (ICIT), 2015, pp. 1956-1963.

[5] P. Neves, L. Ribeiro, J. Dias-Ferreira, M. Onori and J. B. Oliveira, "Layout validation and re-configuration in Plug&Produce systems", Journal of Assembly Automation, Volume 36, 0pp. 412-428, 2016

[6] N. Lohse, P. Ferreira, I. Pereira, "Deliverable: D3.1: Open Plug and Produce Architecture Specification", [online] Available at: https://www.openmos.eu/ [Accessed 05 Apr. 2018].

[7] B. Lydon, "Non-Proprietary Controller-to-Controller Communications" February, 2014, [online] Available at: https://www.automation.com/portals/manufacturing-operationsmanagement/opc/non-proprietary-controller-to-controllercommunications [Accessed 05 Apr. 2018].

A Novel Wireless Measurement While drilling System for Geotechnical and Geophysical Applications *

M. Khater and W. Al-Nuaimy

Abstract— **This paper presents the development of a wireless measurement system based on 2.4GHz wireless technology and waveguide theory. The prototype system is installed on a rotary geotechnical drilling rig with the purpose of providing a wireless communication link between down-hole sensor(s) contained inside the drilling string and a logging computer/ receiver on the surface. In hazardous environment, this setup can be attached to an autonomous vehicle or robot while data can be remotely collected. The results are promising, the developed system significantly reduce the time and cost of a wide range of geophysical borehole investigation methods. This includes detection and clearance of deeply-buried Unexploded Bombs (UXBs). In this paper, the structure of the system and results from practical test will be introduced and discussed.**

I. Introduction

Borehole geophysics is a branch of geophysical methods usually conducted at a depth to measure different physical properties; it involves manually lowering sensors into a borehole to record continuous data. Common borehole geophysical methods include down-hole seismic, borehole magnetometry, borehole resistivity and borehole gamma ray logging. Basic applications of borehole geophysics include mapping and characterising of subsurface infrastructure, groundwater and bedrock depth and supporting civil and geotechnical engineering investigations.

Borehole geophysical methods require a borehole to be drilled and cased before the start of the survey. The borehole is usually drilled using a suitable rotary drilling method. Once the required depth is reached, the drill string is withdrawn from the borehole and a suitable casing is installed to prevent the borehole from collapsing. After that, an appropriate probe is lowered down manually and the data are collected. In some cases the drilling of the borehole is carried out in stages (typically 1m) at each stage, for example, the clearance of unexploded bomb using borehole magnetometry.

It is obvious that traditional borehole geophysical methods are very time-consuming and costly. Cone penetration Test (CPT) is a more efficient method that provides real time borehole data [1]. It works by pushing an instrumented cone into the ground under hydraulic pressure using a CPT rig. The collected data are transmitted over a cable that runs through the string to the logging device/computer located inside the CPT truck. Limitations of this method are ground conditions which prevent penetration of the cone to the required survey depths. As a result, the CPT method cannot be employed in more than 40% of greater London [2].

In this paper we present a novel wireless telemetry system that helps to conduct several borehole geophysical surveys in a more efficient way by providing real time down-hole measurements during the drilling process. The system is to be fitted on a rotary drilling rig which can penetrate most ground conditions and this overcomes the limitation of the CPT method. In particular, this system will greatly improve the efficiency and the safety of detecting deeply-buried UXBs.

The proposed solution can be attached to autonomous or tele-operated robotics systems for use in hazard and risky environments. Mobile robots fitted with rotary drilling systems are used for ground, underwater and space application [3-4]. In addition, robotics systems are widely employed for de-mining activities [5]. The suggested system can be combined with these robotics technologies to offer an efficient and safe survey method for deeply UXBs.

II. The drilling method of choice

Various drilling methods may be found in oil and gas, construction and geotechnical industries. The proposed telemetry system would suit a dry rotary drilling method such as Auger drilling [6]. Where the drilling operation is carried out without water or fluid, instead, it is removed by a mechanical mean. Thus, the electronics for the proposed system can be placed inside the drill string without disturbing the cutting removal mechanism. In addition, having a hollow drill string with no drilling fluid would ease the communication with the surface as we will see in the following section.

III. The drill string as a waveguide

The main challenge associated with the development of the proposed system is the transmission of the down-hole data from the bottom of the borehole to the surface while drilling in real time. This telemetry system needs to be wireless due to the nature of the drilling procedure and the rotation of the drill pipe, however, direct radio frequency (RF) link through the ground to the surface is not feasible as the electromagnetic (EM) signal will get highly attenuated by the ground layers.

In the oil and gas industry, measurement while drilling (MWD) systems do exist, they provide operators with real time information such as formation properties and borehole geometry while the borehole is being drilled. The main MWD method used in the oil and gas industry is the mud pulse telemetry; other less frequently used methods include EM telemetry and acoustic telemetry. Current MWD

*Research supported by the Knowledge Transfer Partnership programme UK (KTP) and Zetica Ltd.

Dr. Moutazbellah Khater, Deep Sea Electronics PLC, North Yorkshire, United Kingdom (e-mail: moutaz_k@hotmail.com).

Dr. Waleed Al-Nuaimy, Department of Electrical Engineering and Electronics, University of Liverpool, Liverpool, United Kingdom (e-mail: wax@liverpool.ac.uk).

methods used in oil and gas industry are generally complex and expensive as they have been designed to operate at very deep depths and extreme conditions. In addition, these methods provide very limited bandwidth [7].

Due to the facts that the wall of the drill string is made out of a conductive metal and that the drill string is hollow, a novel approach can be applied here that utilise the drill string itself as a communication channel. The idea is to consider the stem of the drill string as a circular waveguide and by carefully choosing the carrier frequency; electromagnetic waves can be guided along the metal pipe up to a receiver at the top of the drill string.

Waveguides are usually carefully designed to meet particular frequency requirement. The waveguide will be excited by a basic antenna that radiates inside the hollow drill string. Inside the waveguide, there are different possible field configurations or patterns, each pattern is called mode. Each mode has a specific cutoff frequency. In order for a wave to propagate through the waveguide, it has to be greater than the lowest waveguide cut-off frequency. The first mode to propagate is the mode with lowest cutoff frequency and it is called dominant mode. The cutoff frequency depends mainly on the dimensions of the waveguide, mode of propagation and the characteristic of the fill material, the cut-off frequency for circular waveguide is [8]:

$$f_{c-TM} = \frac{p_{nm}c}{2\pi a\sqrt{\epsilon}} \qquad (1)$$

$$f_{c-TE} = \frac{p'_{nm}c}{2\pi a\sqrt{\epsilon}} \qquad (2)$$

Where p_{nm} and p'_{nm} are the m^{th} root of the n^{th} order Bessel function of the first kind and its derivative respectively. Values of p_{nm} and p'_{nm} are given in mathematical tables.

The dimensions of hollow stem drill pipes are not standardised between various drill pipes manufacturers. A typical range of hollow stem pipe diameters is shown in table 1. The table also list the cutoff frequency for the TE_{11} mode which is the dominant mode for a circular waveguide.

TABLE 1. TYPICAL DRILL PIPE SIZES WITH CORRESPONDING TE11 CUTOFF FREQUENCY

Auger Internal Diameter (mm)	**Outside (Flights) Diameter (mm)**	**Weight (kg)**	**TE_{11} cutoff frequency**
57.2	136.5	20.9	3.07 GHz
82.6	187.3	37.2	2.13 GHz
100	200	40	1.76 GHz
111	215.9	50	1.58 GHz
168.3	273.1	57.2	1.04 GHz
209.5	314.3	67.1	839.2 MHz
260.3	368.3	114.8	675.4 MHz
311.2	419.1	134.7	564.9 MHz

By evaluating the lowest cutoff frequencies for typical drill pipe diameters listed in table 1, it can be noticed that the popular 2.4 GHz ISM band can propagate through most of commercially available drill pipe sizes. This fact will greatly simplify the design challenge since the 2.4GHz band requires no special license and 2.4GHz-based radio frequency modules are widely available off the shelf at low prices.

IV. SIGNAL ATTENUATION

A standard drill pipe with 100mm diameter was considered. At 2.4 GHz, two modes can propagate, TE_{11} and TM_{01} with cutoff frequencies of 1.76GHz and 2.29GHz respectively. If more than one mode is propagating, the waveguide is said to be overmoded. In waveguide applications, multimode propagation is not desirable and usually avoided as it may increase transmission loss.

The power inside a waveguide drops exponentially with the distance. Fig. 1 depicts the theoretical attenuation constant expected inside the drill pipe for TE_{11} and TM_{01} modes over the frequency range of interest. The total power will be distributed between the excited modes. The overall attenuation constant depends on power radiated in each mode, which in turn depends on the antenna radiation characteristics, antenna orientation and position inside the drill pipe, waveguide cross sectional area and operating frequency [9].

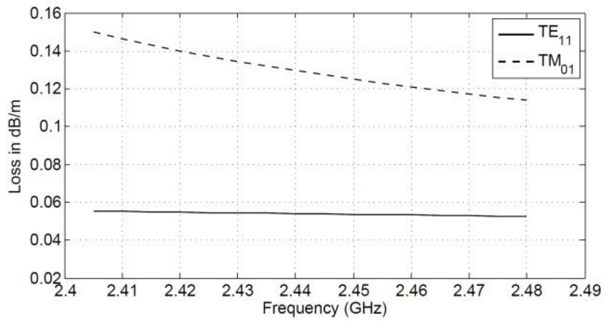

Figure 1. Attenuation constant in dB/m for TE_{11} and TM_{01} modes

It is fairly complex to accurately calculate overall signal attenuation inside a drill pipe. This is mainly due to the fact that the drill pipe is not an ideal waveguide. There are some other factors that affect signal propagation. In addition to the dielectric and metallic loss which are experienced in any waveguide, the drill pipe suffers from the following:

- Drill pipe sections are made from steel which is vulnerable to rust and corrosion, as a result, the conductivity of the material reduces and the metallic loss increases.
- The excitation of the drill pipe is not optimal. The requirement of simple integration into different drill pipe sizes and drilling rigs dictates that the radiating element (antenna) is randomly placed inside the drill pipe, thus, maximum power transfer may not be achieved and antenna coupling loss may increase.
- At both ends, the drill pipe is terminated with metallic objects, acting as reflectors. As a result, each antenna will receive multiple reflections from both ends, leading to an extra loss.
- The EM signal will get attenuated by the dust, water and mud which may penetrate into a badly-sealed drill string during drilling activities.

- Extra losses may arise by the joints between drill pipe sections and the roughness of the internal wall of the drill pipe.

Even with all the loss factors mentioned above, total channel loss is expected to be relatively low when compared to free space and indoor communications.

A general exact solution for the path loss inside the drill pipe is fairly complex. In addition, there are several random factors associated with the channel such as conductivity of the drill pipes used, modes excitation conditions and other signals disturbances mentioned above. Analysis of similar propagation conditions do exist in the literature, waveguide effect and propagation in tunnels and mine like environment has been studied in the past (10). The most relevant study was done by a group of researchers where indoor radio wave propagation using heating, ventilation and air conditioning duct (HVAC ducts) was proposed and studied in details [11-13]. Pavel Niktin and others proposed [12] a simple analytical propagation model for straight duct, the model accounts for mode excitation, reflections from terminated ends but it requires knowledge of mode-dependant antenna impendence. T. Ozan and others [14] presented an empirical model to predict path loss inside an HVAC duct operating in the 2.4 – 2.5 GHz, experimental measurements were used to determine attenuation loss and antenna coupling loss for HVAC duct of 0.3m diameter, the attenuation loss was found to be 0.16 dB/m, while the antenna coupling loss was 14.8 dB.

V. CONCEPT DEMONSTRATION

A simple test was conducted to validate the concept of using the drill pipe as a communication channel. The test was performed with a drill string of 3.2 m length (two drill pipe sections). Two IEEE 802.1.5.4 2.4GHz wireless transceivers modules have been used. Each module consists of a programmable PIC® microcontroller and MRF24J40A transceiver [15]. The used transceiver has a sensitivity of -94dBm and maximum output RF power of 0dBm.

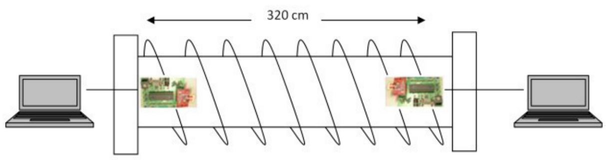

Figure 2. Test setup for measuring the frequency response of the auger/drill pipe

The transceiver has the option of adjusting the output power from a minimum of -38.75 dBm up to a maximum of 0 dBm in steps of 1.25 dB. It also provides a measure for the received signal strength with an accuracy of +/- 5dBm. Accordingly we were able to vary the output power and to measure the received signal strength in different conditions. For a reliable communications, the received signal strength needs to be higher than -80dBm.

The MRF24J40A supports the IEEE 802.1.5.4 standard, which divide the 2.4 GHz ISM band into 16 channels. Fig. 3 plot the frequency response obtained by varying the operating frequency and measure the average of the received signal strength. The centre frequencies of the 16 supported channels were tested. Fig. 3 shows two curves, the first curve represents the measurements obtained with both ends of the drill pipe are open, this condition simulate a matched load as there is no reflection from the ends. The second curve is for the measurements obtained while the ends of the drill pipe are terminated by a conductive metal sheet, this simulate a short circuit condition in which reflections from both ends are expected. It can be noticed that the loss due to reflections from the terminated ends is quite small. This agrees with the results achieved by other researchers [12, 14].

Among the frequency range of interest, the average of overall loss is 12dB. The attenuation constant of the waveguide is expected to be very low (see Fig. 1), for the HVAC duct, 0.12 dB/m was reported by stencil [13] and 0.16 dB/m reported by Ozan [14]. It is believed that, the majority of the loss mainly comes from antenna coupling. An antenna coupling loss of 14.8 dB was reported by Ozan [14] for a monopole antenna radiating inside a HVAC duct. Stencil [13] also estimated an antenna coupling loss of 20 dB. If we ignore losses due to joints and conservatively assume a 25 dB coupling loss, 0.2 dB/m waveguide loss and 10dB error margin, then, for a receiver with -80 dBm sensitivity, the communication range would be 225 meters.

In order to assess the reliability and the quality of the communication through the drill pipe, 1000 messages were transmitted from the first modem to the second modem at the other side of the drill pipe, and the number of the received messages was counted. This experiment was repeated for the 16 tested channels and there was no message loss at all.

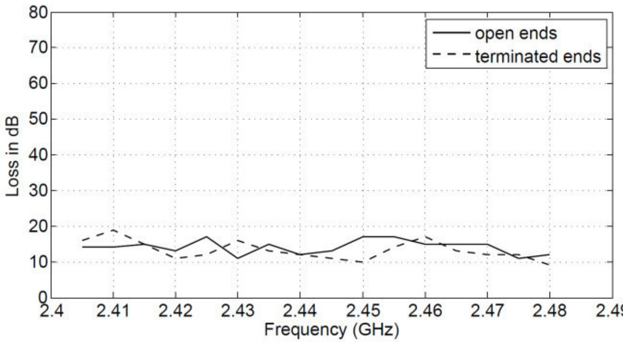

Figure 3. Frequency response measured inside a drill pipe of 3.2 meter length and 100mm diameter.

VI. PROTOTYPE AND FIELD TEST

In order to test the proposed measurement system, a prototype has been built and fitted on a rotary drill rig. Fig. 4 shows the block diagram of the implemented system. The system consists of four main units, namely: down-hole unit, relay unit, logging unit and the logging computer. The down-hole unit is located at the bottom of the drill pipe; it comprises down-hole sensors, processor, wireless transceiver and a rechargeable battery. The down-hole unit sample and process the outputs of the sensors in order to transmit them; In general, it will control the operations of the down-hole system and act as a slave unit which responds to the enquiries of the logging computer (the master unit). The relay unit is fitted at the top of the drill pipe. This unit will receive the data transmitted from the down-hole unit and retransmit them over a long-range external communication link. The external wireless link operates at 868 MHz. an extended antenna is connected to the unit to allow data to be transmitted to the free space. The logging computer runs the application software and acts as a master that controls the complete measurement system. The logging computer collects down-hole data from the sensors wirelessly through the logging unit, which provides a wireless interface for the system. In addition, the logging computer record instantaneous borehole depth which is provided by the drill rig instrumentation through a serial cable. The collected data are processed by the logging computer and then displayed against the depth in real time.

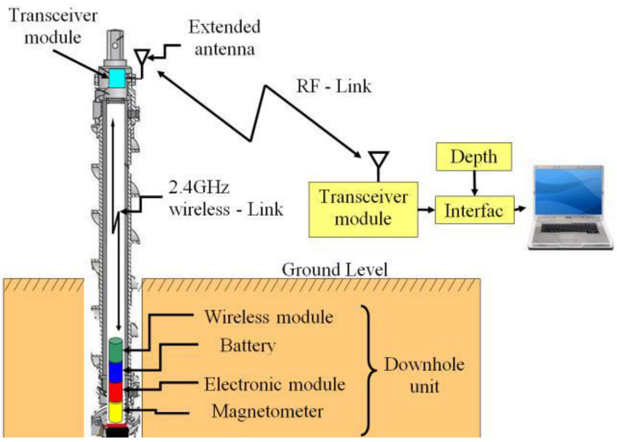

Figure 4. System block diagram

The reliability of the system was tested by drilling several boreholes under various drilling conditions. For each borehole, the signal strength inside the drill pipe was monitored and recorded. The results are shown in Fig. 5, the received signal strength was very high as expected. The received signal strength for borehole 4 has dropped to -50dBm at one stage because we have encountered water during the drilling and some water/mud has penetrated into the drill string.

VII. Conclusion

This paper introduces a novel down-hole telemetry method. The method is based on guiding the electromagnetic waves inside the drill string. The possibility of communication through a hollow drill pipe has been validated experimentally through a simple test. The proposed method has been implemented and successfully tested in the field. Results show that the loss is relatively low and long communication range can be achieved. The low cost and the reliability of the telemetry system alongside with the long communication range allow the system be utilised in several geotechnical drilling applications or in other areas of research applications. For example, down-hole vibration, sound, temperature and gamma rays can be monitored in real time and provide sensitive information about the underground layers and formation. In addition, robotics systems with drilling capabilities can utilise the presented telemetry system for the detection of deeply buried UXBs and metal objects.

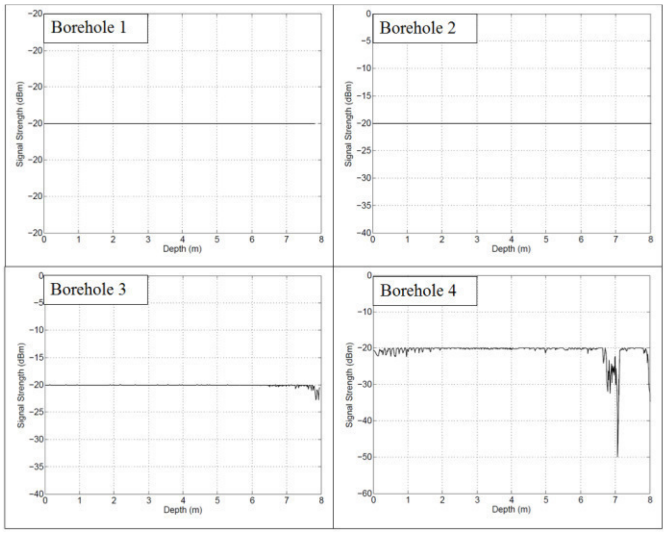

Figure 5. Signal strength measured inside drill pipe in different drilling tests.

Acknowledgment

I wish to express my sincere thanks to Zetica Ltd for supporting this work.

References

[1] J.J.M. Brouwer. In-situ Soil Testing. IHS BRE Press, 2007.

[2] Map for the geology of greater London , Zetica Ltd, www.zetica.com.

[3] Beji, L. ; Benchikh, L. (2017), 'A Method of Drilling a Ground Using a Robotic Arm', World Academy of Science, Engineering and Technology, International Science Index 131, International Journal of Mechanical, Aerospace, Industrial, Mechatronic and Manufacturing Engineering, 11(11), 1821 - 1826.

[4] Glass, Brian & Thompson, Sarah & Paulsen, Gale. (2010). Robotic planetary drill tests. Proc. 13th Int. Symp. on Artificial Intelligence, Robotics and Automation in Space. 464-470.

[5] Y. Baudoin, M.K. Habib, I. Doroftei, Mobile robotics systems for humanitarian de-mining and risky interventions, Using Robots in Hazardous Environments,Woodhead Publishing,2011, Pages 3-31.

[6] Morris R. England B. and Wakeling R. Drilling Technology. British Drilling Association, 1992.

[7] Baker Hughes INTEQ, Houston,USA. Baker Hughes INTEQ Guide to Measurement While Drilling, September 1996.

[8] D.M. Pozar. Microwave engineering. Wiley, 3rd edition; 1997.

[9] P.V. Nikitin, D.D. Stancil, A.G. Cepni, A.E. Xhafa, O.K. Tonguz, K. Areklett, and D. Brodtkorb. Antennas in a waveguide propagation environment. In Antennas and Propagation Society International Symposium, IEEE, pages 1181 – 1184 vol.2, June 2003.

[10] C.L. Holloway, D.A. Hill, R.A. Dalke, and G.A. Hufford. Radio wave propagation characteristics in lossy circular waveguides such as tunnels, mine shafts, and boreholes. Antennas and Propagation, IEEE Transactions on, 48(9):1354 –1366, Sep 2000.

[11] H. Andersson, P. Larsson, and P. Wikstrom. The use of HVAC ducts for WCDMA indoor solutions. In Vehicular Technology Conference. VTC 2004-Spring. 2004 IEEE 59th, pages 229 – 233 Vol.1, May 2004.

[12] P.V. Nikitin, D.D. Stancil, A.G. Cepni, O.K. Tonguz, A.E. Xhafa, and D. Brodtkorb. Propagation model for the HVAC duct as a communication channel. Antennas and Propagation, IEEE Transactions on, 51(5):945 – 951, May 2003.

[13] D.D. Stancil, O.K. Tonguz, A. Xhafa, A. Cepni, P. Nikitin, and D. Brodtkorb. High-speed internet access via HVAC ducts: a new approach. In Global Telecommunications Conference, 2001. GLOBECOM '01. IEEE, volume 6, pages 3604 –3607 vol.6, 2001.

[14] O.K. Tonguz, A.E. Xhafa, D.D. Stancil, A.G. Cepni, P.V. Nikitin, and D. Brodtkorb. A simple path-loss prediction model for HVAC systems. Vehicular Technology, IEEE Transactions on, 53(4):1203 – 1214, July 2004.

[15] MRF24J40MA 2.4 GHz IEEE Std. 802.15.4 RF Transceiver Module. Data sheet, Microchip Technology Inc, 2008.

Integration of Calibration and Forcing Methods for Predicting Timely Crop States by Using AquaCrop-OS Model

Tianxiang Zhang, Jinya Su, Cunjia Liu, Wen-Hua Chen, IEEE, Fellow
Department of Aeronautical and Automotive Engineering, Loughborough University
Loughborough, LE11 3TU, U.K

***Abstract*— This paper presents a framework for predicting canopy states in real time by adopting a recent MATLAB based crop model: AquaCrop-OS. The historical observations are firstly used to estimate the crop sensitive parameters in Bayesian approach. Secondly, the model states will be replaced by updating remotely sensed observations in a sequential way. The final predicted states will be in comparison with the groundtruth and the RMSE of these two are 39.4155 g/m^2 (calibration method) and 19.3679 g/m^2 (calibration with forcing method) concluding that the system is capable of predicting the crop status timely and improve the performance of calibration strategy.**

Keywords-data assimilation; Bayesian calibration; sequential forcing method; crop model; remote sensing; states prediction

I. Introduction

Timely and accurate estimation of crop status before harvest allow framers to make a decision on field management and irrigation plan, which is of importance for national food security assessment and maximining the economic impacts [1]. Therefore, crop model has been improved from qualitative research to quantitative research simulating the whole growth phase under various stress, like WOFOST, DASSAT, STICS and AquaCrop model [2-5]. Individual crop model performance may be affected due to the uncertainties of soil properties, canopy states and meteorological data resulting in a large error in crop states prediction when localized in one certain area. These uncertainties of crop growth model can be reduced by providing more information to improve model parametrization and calibration and increase the final data assimilation accuracy.

There are three approaches to employ remotely sensed data into crop model: parameter calibration, forcing method and update method. Jin et al. adopted particle swarm optimization (PSO) method to calibrate AquaCrop model by using historical remote sensing data making a prediction of biomass and final yield before harvest [6]. Moreover, Tripathy et al. directly replaced model predict leaf area index (LAI) by index-based LAI to improve the prediction performance [7]. The rapid development of remote sensing platforms provides high property data with high spectral and spatial resolutions accurately estimating the crop states than ever. The integration of crop model and remotely sensed data has been an effective tool to not only calibrate the crop model but also make a prediction in time.

The new water driven crop model, AquaCrop, with characters of simplicity, robustness, accurateness, was proposed in 2009 by Steduto indicating better results in predicting crop growth status. Compared with other crop models, the AquaCrop simulation model can model the dynamic change of crop growth status in response to water [8]. According to the principle of AquaCrop model, Foster et al. developed it into an open-access software AquaCrop-OS programmed by MATLAB enabling the code to be linked quickly with other disciplinary models to support yield estimation, water resource management and intelligent irrigation program in 2016 [9].

From previous literature, most of the researchers focus on adopting the data assimilation method individually, however, each method has their own limitation on crop states prediction. Calibration strategy always relies on the historical data and cannot make real-time prediction. Forcing method will involve in new observation error. In addition, update method is also flawed as it requires expensive calculation and new uncertainties. In our paper, a real time crop states prediction system is presented to combine calibration strategy and forcing method to reduce the parameters uncertainties and improve a timely prediction.

The summary of the contribution in this paper is organized as follows:

1. Rather than traditional optimization-based calibration, a Bayesian-based parameter estimation method is pointed.
2. It is the first time to program the AquaCrop-OS model to realize a sequential update function.
3. The integration of calibration method and forcing method is able to predict the processed states variables in real time
4. In addition to the timely sates, weather information can also be updated timely.

II. Methodology

In this section, materials related to our research will be presented, including whole framework, model formulation, data collection, calibration strategy and forcing method strategy. Due to the character that the model can simulate most

*This work was supported by Newton Fund UK-China Agri-Tech Network Plus which is managed by Rothamsted Research on behalf of Science and Technology Facilities Council (STFC). Tianxiang Zhang would also like to thank Chinese Scholarship Council (CSC) for supporting his study in the U.K.

of the crops, like spring wheat, spring wheat, maize and corns. A specific simulation time from 05/10/2014 to 30/05/2015 on winter wheat was chosen.

A. Framework

As is shown in Fig. 1, the whole framework of real-time states variables prediction is divided into two stages: crop sensitive parameters estimation and forcing method data assimilation. The calibration process is to estimate the most sensitive parameters with the historical remote sensing data by Bayesian estimation based on Markov Chain Monte Carlo (MCMC) techniques. Additionally, the timely updated data will be assimilated into the AquaCrop-OS model by employing forcing method.

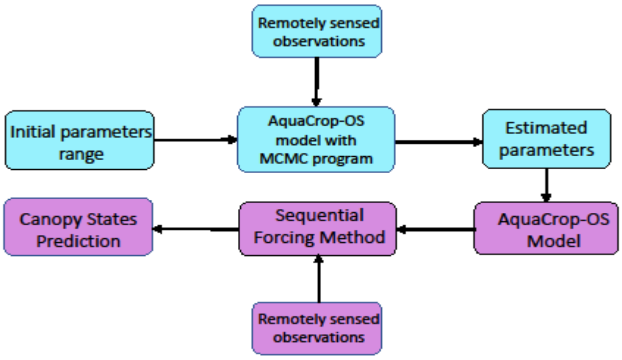

Fig. 1 The framework of real-time states prediction system

B. Model Formulation

The AquaCrop-OS model are programmed by using Markov process on the basis of AquaCrop model. A simplified formulation can be achieved according to Eq. 1 and Eq. 2.

$$X_{t+1} = f(X_t, \theta') \tag{1}$$

$$Y_{t+1} = g(X_t, \theta') + \varepsilon_t \tag{2}$$

where f represents the AquaCrop-OS function relative with all required crop parameters θ' and the states variables X. Y indicates the measurement with a proper mean and variance gaussian noise ε_t.

C. Data Preparation

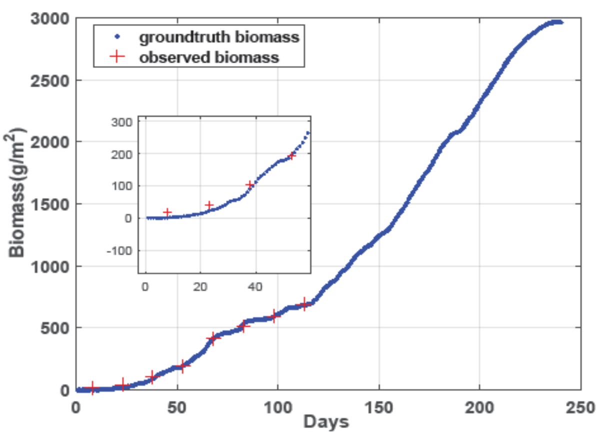

Fig. 2 Biomass groundtruth and observation data

In our study, due to the lack of real remotely sensed data, the simulated observations can be produced by groundtruth states adding a Gaussian noise. The default parameters of AquaCrop-OS model are described as the truth parameters and thus generating groundtruth states variables. Biomass and canopy cover are selected as the state variables for model calibration and sequential forcing (see Fig. 2, Fig. 3). There are eight-day observations totally, the first five-day historical observations of biomass and canopy cover are adopted for estimating the crop parameters, and the overall eight-day measurements is employed for forcing method.

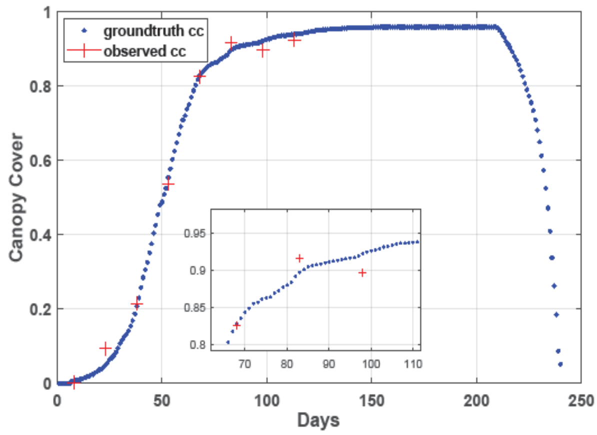

Fig. 3 Canopy cover groundtruth and observation data

D. Calibration Strategy

In our case, the sensitive parameters to be calibrated is selected as θ = [gdd, p_up3, wp, cgc, ccx, mat, eme, kcb] describing the typical characters during crop growth and treated as uniform distribution. The historical observations are selected at intervals of 15 days from day 8 to day 68 for crop model parameter calibration.

Bayesian calibration aims to derive the posterior probability distributions for parameters of interest conditional on measurements, where the uncalibrated parameter posterior distribution $p(\theta|D)$ is proportional to the prior distribution $p(\theta)$ and the measurement likelihood function $p(D|\theta)$, given by:

$$p(\theta|D) \propto p(\theta) \times p(D|\theta) \tag{4}$$

where θ means the pending parameter vectors and D represents the observed data. The likelihood function $p(D|\theta)$ evaluates each value for θ on the basis of how well the model with parameter θ is able to reproduce the data D [8].

To effectively estimate the parameters posterior distribution that direct sampling is difficult, a Markov Chain Monte Carlo (MCMC) algorithm entitled Metropolis-Hastings algorithm is employed.

E. Forcing Method

The model uncertainties have been reduced by estimating the sensitive parameters with the historical measurement. Forcing method can provide the researchers a feasible way to directly replace the crop model simulation data by timely observation data where the time step can be daily, weekly or monthly, offering the farmers a chance for real-time decision make [1]. In our case, the total of 8 observations will be conducted to do forcing method.

III. RESULTS

In this part, the model calibration results and forcing method prediction results will be presented. The estimated parameters involving biomass and canopy cover measurements will be compared with the truth; meanwhile, the forcing strategy embedded calibration results will be in comparison with calibration strategy by using the remaining days states from the whole growth period.

A. Parameters Estimation Results

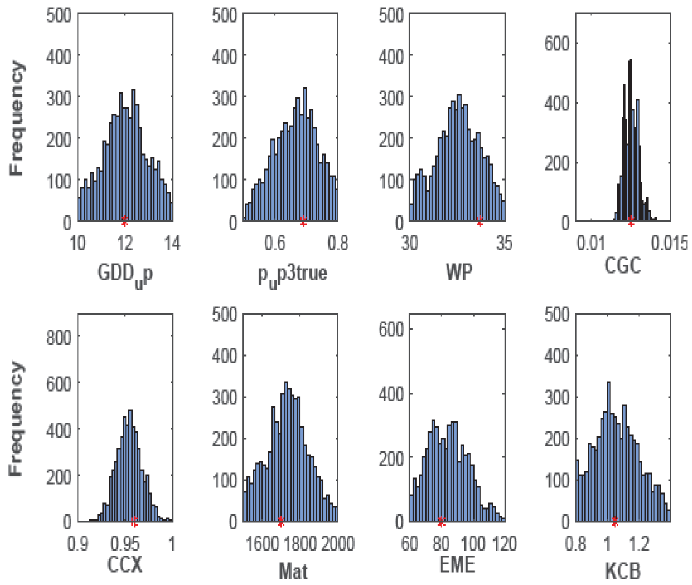

Fig. 4 Estimated parameters posterior distribution

The posterior distribution with the observations is shown in Fig. 4, where the red star represents the truth parameters. The mean value was calculated of each parameter distribution and compared with the truth parameter (see TABLE I). The error of each parameters is less than 4% with truth parameter, moreover, the overall error of eight parameters is only 2.2902% (see Eq. 3). The result is corresponding to the literature [8] decreasing the uncertainties.

TABLE I. COMPARISION BETWEEN ESTIMATED AND TRUTH PARAMETERS

Sensitive Parameters	Estimated Parameters	Truth Parameters	Error (%)
GDD_up	12.0187	12	0.1557
P_up3	0.6648	0.69	3.6494
WP	32.5386	33.7	3.4463
CGC	0.0125	0.0125	0.0220
CCX	0.9544	0.96	0.5845
MAT	1733	1700	1.9514
EME	84.0916	80	5.1145
KCB	1.0616	1.05	1.1073
Average			**2.2902**

$$\text{Error} = \frac{|\text{Estimated Parameters} - \text{Truth Parameters}|}{\text{Truth Parameters}} * 100\% \tag{3}$$

B. Forcing Method Results

Forcing method is able to provide a timely update strategy after directly replace the model data by observations. The prediction states of AquaCrop-OS applying forcing method are shown in Fig. 5-6. Compared with goundtruth, the Root Mean Squared Error (RMSE) of predicted biomass with the technique of parameter estimation and forcing method embedded parameter estimation are 39.4155 g/m^2 and 19.3679 g/m^2, respectively.

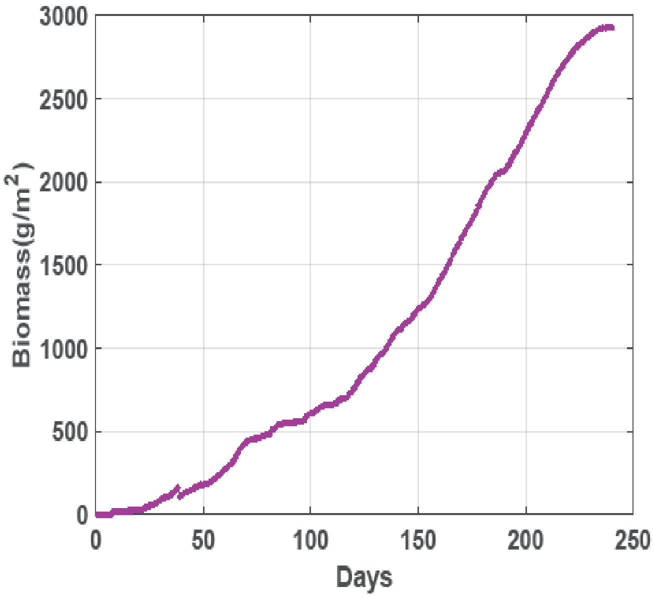

Fig. 5 Real time prediction by forcing timely biomass

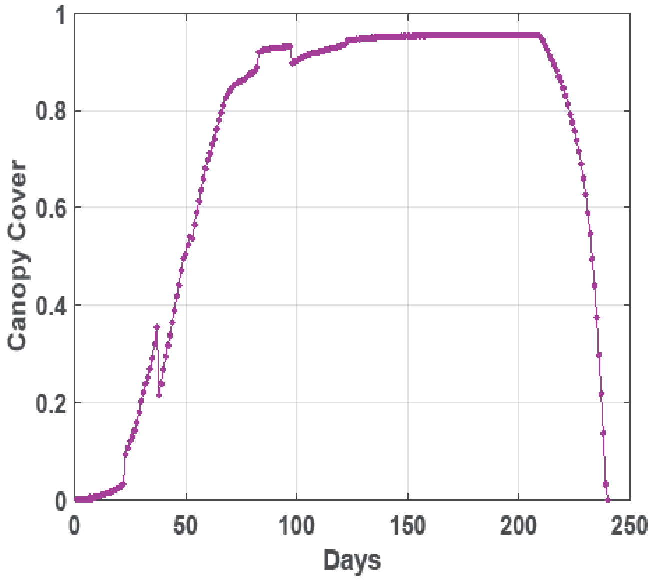

Fig. 6 Real time prediction by forcing timely canopy cover

The states prediction of various method with the observation of biomass can also be obtained from Fig. 7, which can be concluded that the real-time system prediction line is much closer to truth states. The prediction performs better especially after forcing method.

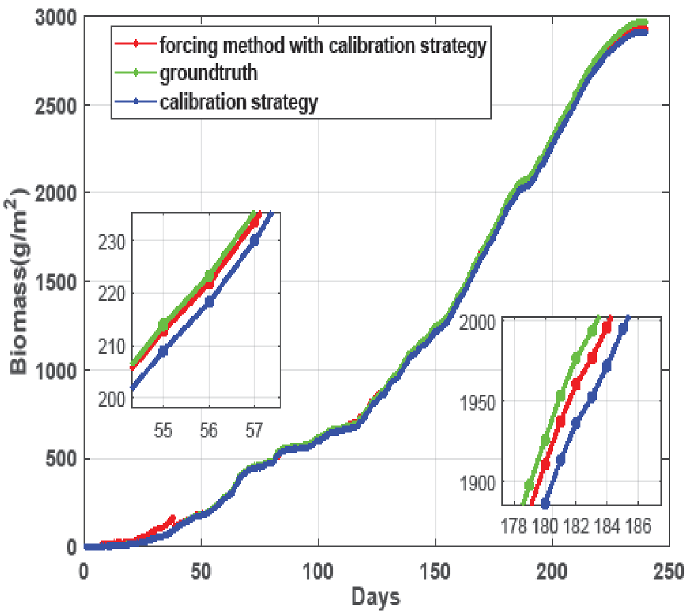

Fig. 7 Comparison of predicted biomass with different methods

IV. CONCLUSION

This work aims at exploiting the potentials of integrating calibration strategy and forcing strategy on crop states timely prediction with multiple observations. Results showed that the performance of our system outperforms individual calibration strategy, especially after new measurement updates. Therefore, it can be used on states variables prediction and irrigation decision-making or field management during the period of crop growth.

V. FUTURE WORKS

Future work on this direction is summarized in the following aspects:

(i) To reduce the uncertainties of observations in forcing method, some sequential Monte Carlo algorithm could be applied, such as Particle Filter.

(ii) Crop parameters and crop states can be estimated at the same time during particle filter process.

(iii) Remote sensing data may also be collected from UAVs at a higher spectral resolution.

REFERENCES

[1] X. Jin et al. "A review of data assimilation of remote sensing and crop models." *European Journal of Agronomy*, vol. 92, pp. 141-152, 2018.

[2] M. Todorovic, R. Albrizio, L. Zivotic, M. Saab, C. Stöckle and P. Steduto, "Assessment of AquaCrop, CropSyst, and WOFOST Models in the Simulation of Sunflower Growth under Different Water Regimes", *Agronomy Journal*, vol. 101, no. 3, p. 509, 2009.

[3] R. Sarkar, "Use of DSSAT to model cropping systems.", CAB *Reviews: Perspectives in Agriculture, Veterinary Science, Nutrition and Natural Resources*, vol. 4, no. 025, 2009.

[4] G. Jégo, E. Pattey and J. Liu, "Using Leaf Area Index, retrieved from optical imagery, in the STICS crop model for predicting yield and biomass of field crops", *Field Crops Research*, vol. 131, pp. 63-74, 2012.

[5] P. Steduto, T. Hsiao, D. Raes and E. Fereres, "AquaCrop—The FAO Crop Model to Simulate Yield Response to Water: I. Concepts and Underlying Principles", *Agronomy Journal*, vol. 101, no. 3, p. 426, 2009.

[6] X. Jin, L. Kumar, Z. Li, X. Xu, G. Yang and J. Wang, "Estimation of Winter Wheat Biomass and Yield by Combining the AquaCrop Model and Field Hyperspectral Data", *Remote Sensing*, vol. 8, no. 12, p. 972, 2016.

[7] R. Tripathy et al., "Forecasting wheat yield in Punjab state of India by combining crop simulation model WOFOST and remotely sensed inputs", *Remote Sensing Letters*, vol. 4, no. 1, pp. 19-28, 2013.

[8] T. Zhang et al. "Bayesian Calibration of AquaCrop Model." *2018 37th Chinese Control Conference (CCC)* (2018): 10334-10339.

[9] T. Foster, N. Brozović, A. Butler, C. Neale, D. Raes, P. Steduto, E. Fereres, and T. Hsiao, "AquaCrop-OS: An open source version of FAOs crop water productivity model," *Agricultural Water Management*, vol. 181, pp. 18–22, 2017.

Locust Recognition and Detection via Aggregate Channel Features

Dewei Yi, Jinya Su, and Wen-Hua Chen

Abstract— **Locust plagues are very harmful for food security, quality and quantity of agricultural products. With this consideration, precise locust detection is significant for preventing locust plagues. To achieve this task, aggregate channel feature (ACF) object detector with parameters optimization is applied to detect locusts. Experiment results show that ACF object detector with optimized parameters can achieve 0.39 for average precision and 0.86 for log-average miss rate. Moreover, ACF is a non-deep method using a simple model to detect objects. That is, the proposed method is promising to be embedded in a real-time locust detection system.**

I. Introduction

Pests have brought significant negative effects on food security, agricultural economy and quality of agricultural products [1]. Nowadays, pests are usually detected by human beings. Manual monitoring is a labor-intensive job and expensive for large farms. To tackle this problem, computer vision techniques have provided a promising solution for detecting pests.

In [2], edge features (histograms of oriented gradients) are combined with support vector machine which can efficiently identify aphids. Moreover, support vector machines incorporating with selecting suitable region and color index can achieve less than 2.5% in identifying thrips [3]. Different from conventional image processing techniques, deep learning methods become very popular for pest identification. In [4], a convolutional neural network is trained to detect moths which shows a very promising result. In [5], pest identification is achieved by using deep residual network and its accuracy is 98.67% for classifying 10 classes. The deep residual learning is also used to classifying pests from complex background [6].

However, most research of pest identification is treated as an image classification problem, which gives a class label for an image and cannot point out the locations and the number of pests in an image. Ideally, pest identification should be treated as an object detection problem. Both locations and the number of pests can be provided. In addition, different regions have planted different cash crops. This causes that main pest species are different in different regions. For example, cotton is the main cash crop in Xinjiang, China. Thus, the main pests in Xinjiang are aphids [7]. Wheat is the main cash crops in Inner Mongolia, China [8]. Thus, the main pests in Inner Mongolia. In this study, we focus on detecting locusts so as helping local farmers to prevent locust plagues. However, the proposed method could be borrowed to detect other pests (such as aphids, moths). Locust detection system should be embedded system and expected to run in real time. Therefore, deep neural network related methods are not very suitable for this application due to their model too complicated. It does not only spend a plenty of time for training model but also very slow in predicting new samples.

To this end, the aggregate channel features (ACF) object detection method is used to identify locusts which is a non-deep object detector and both of training and prediction are very fast as shown in [9]. Firstly, three types of feature representations are extracted including color features, gradient magnitude features, and edge features. Secondly, a fast feature pyramids are used to generate regions of interest. Thirdly, AdaBoost classifier [10] is utilized to identify each generated region whether there is a locust inside. Overall, the first step is to extract efficient features. The combination of second step and third step can locate the position of locust in an image.

The rest of the paper is organized as follows: Section II discusses experiment setup and image data acquisition. Then, Section III elaborates the whole framework of ACF locust detector. Next, Section IV provides the experimental results and evaluates the performance. Finally, Section V concludes the paper along with future work.

II. Materials

The two key materials related to this research are experiment setup for the locust plague risk estimate and image acquisition. In the experiment setup, the settings of each experimental zone are explained in detail such as light condition, background, and the number of locusts. In image acquisition, it does not only provide the type and parameters of the used digit but also mention the height and direction of photographing images.

A. *Experiment setup*

In the experiment, the data of four different risk levels of locust plague are collected in the outdoor environment, which are non-risk, low-risk, middle-risk and high-risk. In addition, the data is collected in different weathers (sunny day and cloudy day) to guarantee the diversity and generalization. Due to limited cover range of camera, the test field is divided into 9 zones. For Zone No. 1, there are 24 locusts inside which is identified as the high-risk of locust plagues. For Zone No. 2, 3, 6, 8 and 9, there is no locusts inside which are recognized as the non-risk of locust plagues. For Zone No. 4, there are 6 locusts put inside which is termed as low-risk of locust plagues. For Zone No. 5 and 7, there are 18 locusts inside which are named as the medium-risk of locust plagues. To stay natural scenes, there are grass, dead leaves and locusts in the test field and all the locusts are in living status which can move

This work was supported by the U.K. Science and Technology Facilities Council under Grant ST/N006852/1, ST/N006712/1, and ST/N006836/1. The authors are all with the Department of Aeronautical and Automotive Engineering, Loughborough University, Loughborough LE11 3TU, U.K. E-mail: D.Yi@lboro.ac.uk (Dewei Yi); J.Su2@lboro.ac.uk (Jinya Su); W.Chen@lboro.ac.uk (Wen-Hua Chen).

randomly. Figure 1 provides the instances of non-risk level, low-risk level, middle-risk level, and high-risk level.

B. *Image acquisition*

Images are obtained from an outdoor test field in the Loughborough University, Leicestershire, UK. The image dataset is collected by the Leica dual camera (2MP, CMOS) mounted at the right above each cell of the test field. Thanks to the outdoor environment, the images are all collected under natural light condition. This is due to the color features are varied in different weather conditions. Images from different weather conditions should be used to train a model. Images were captured at 60 cm distances right above the test field.

III. ACF DETECTION FRAMEWORK

The framework of ACF detector contains three key components including feature extraction, feature pyramids, and classifier. Given an image, several feature channels are extracted and then the pixels of each block are added up with pre-smoothing and post-smoothing. Next, an AdaBoost classifier is trained to distinguish object from the background.

A. *Feature Extraction*

Before extracting feature channels, an image is pre-smoothing by a $[1\ 2\ 1]/4$ filter. This operation can suppress noise and improve the capability of capturing features. In this work, several channels are computed and extracted. These channels are normalized gradient magnitude, histogram of oriented gradients (six channels), and LUV color channels (three channels). After obtaining 10 channels, these channels are divided into 4×4 blocks and then pixels in each block are summed. Finally, these channels are post-smoothing with a $[1\ 2\ 1]/4$ filter. The post-smoothing can help aggregate integral scale.

B. *Fast Feature Pyramids*

Feature pyramids are used to propose region of interests (ROI). They are multi-scale representations of an image, where channels are computed at every scale. Therefore, computing feature pyramids is a high time-consuming task. To reduce the cost of computation, a fast feature pyramids method is applied to generate ROI, which runs 8 scales at each octave as in [9].

C. *Classifier*

AdaBoost classifier is used to recognize objects. AdaBoost is an ensemble learning algorithm which combines a number of weak classifiers to construct a powerful classifier. With considering the time-efficiency, depth-two trees are used as weak learners in this work. The pseudocode of AdaBoost classifier is presented in *Algorithm 1*.

Non-Risk Zone

Low-Risk Zone

Middle-Risk Zone

High-Risk Zone

Figure 1. Instances of different locust plague risk level

Algorithm 1: AdaBoost classifier

Initial weights as the same for all depth-two trees

For each depth-two tree **do**

Train the current depth-two tree with the given weight.

Test the current depth-two tree on the all training data.

Reset the current tree weight based on weighted error.

Reset weights based on ensemble predictions.

End for

IV. RESULTS AND DISCUSSION

In the section, main results of this work are presented. Before discussing the performance, locust detection dataset and evaluation metrics are introduced.

A. Locust Detection Dataset

There are 857 images collected by an RGB camera with the resolution of 640×480. Each image is manually labeled. For enhancing generalization and robustness, images are shuffle before splitting into training dataset and testing dataset. In the experiment, there are 60% randomly selected as training dataset and the remaining 40% are selected as testing dataset.

B. Evaluation Metrics

To evaluate the performance of ACF object detector, several metrics are introduced. They can be mainly divided into correct detection-based metrics and miss detection-based metrics. Correct detection-based metrics includes precision, recall, and average precision. Precision (P) is the number of true positives (TP) over the number of positives. The number of positives is the sum of true positives and false positives (FP).

$$P = \frac{TP}{TP + FP} \tag{1}$$

Recall (R) is the number of true positives over the number of true positives plus the number of false negatives (FN).

$$R = \frac{TP}{TP + FN} \tag{2}$$

Average precision (AP) summarizes the weighted increase in precision with each change in recall for the thresholds in the precision-recall curve, which is given by

$$AP = \sum_{i=1}^{n} (R_i - R_{i-1}) P_i \tag{3}$$

where P_i and R_i are the precision and recall at the i-th threshold and n is the total number of thresholds. Therefore, AP is a single number for indicating the object performance with varying thresholds.

Miss detection-based metrics includes miss rate (MR), false positives per image ($FPPI$), and log-average miss rate. Miss rate is the number of false negatives over the number of true positives plus false negatives.

$$MR = \frac{FN}{TP + FN} \tag{4}$$

Log-average miss rate is computed by averaging miss rate at nine $FPPI$ rates evenly spaced in log-space in the range 10^{-2} to 10^{0} [11]. Log-average miss rate provides a single value for summaries the miss detection which is convenient for presenting performance straightforwardly.

C. Performance Evaluation

The number of stages and negative samples factor are two key parameters needed to be tuned in ACF object detector. A heuristic method is utilized to find the optimal parameters showing in Table I-IV. Because locust detection can be trained offline and then running trained model in real time, the values AP, log-average miss rate and prediction speed is more important compared to training time. The number of trees in AdaBoost classifier is another parameter to be pre-defined. Because the parameter has been tuned in [9], we follow its setting of the parameter which is 2048. When the overlapping between ground truths and prediction region more than 50%, it is recognized as a true positive. From these Tables, we can see the optimal value of negative samples factor is around 4 and the optimal value of the number of stages is around 6. We also find that increasing negative samples factor after 4 may obtain more side-effects than benefits. More precisely, ACF object detector with these parameters achieves the best performance regarding to average precision and log-average miss rate.

TABLE I. OPTIMAL ACF PARAMETERS BASED ON AP

Number of Stages	Negative Samples Factor		
	2	4	6
2	0.08	0.08	0.11
4	0.32	0.35	0.31
6	0.30	**0.39**	0.34

TABLE II. OPTIMAL ACF PARAMETERS BASED ON LOG-AVERAGE MISS RATE

Number of Stages	Negative Samples Factor		
	2	4	6
2	0.99	0.99	0.98
4	0.91	0.89	0.89
6	0.91	**0.86**	0.88

TABLE III. OPTIMAL ACF PARAMETERS BASED ON PREDICTION SPEED (FRAMES PER SECOND)

Number of Stages	Negative Samples Factor		
	2	4	6
2	2.13	2.35	2.23
4	2.11	2.37	2.08
6	2.23	**1.96**	0.79

TABLE IV. OPTIMAL ACF PARAMETERS BASED ON TRAINING TIME (SECONDS)

Number of Stages	Negative Samples Factor		
	2	4	6
2	437	670	720
4	1147	1092	1321
6	1834	**1708**	1729

After obtaining appropriate parameters of ACF object detector, we use average precision, log-average miss rate to evaluate the performance. With using the selected values of parameters, we can achieve 0.39 of average precision, 0.86 of log-average miss rate. The corresponding Precision-Recall curve and log-average miss rate curve are presented in Figure 2 and 3. Prediction speed and training time based on these parameters setting are 1.96 frames per second and 1708 seconds respectively. Moreover, Figure 4 presents an example of locust detection by ACF object detector.

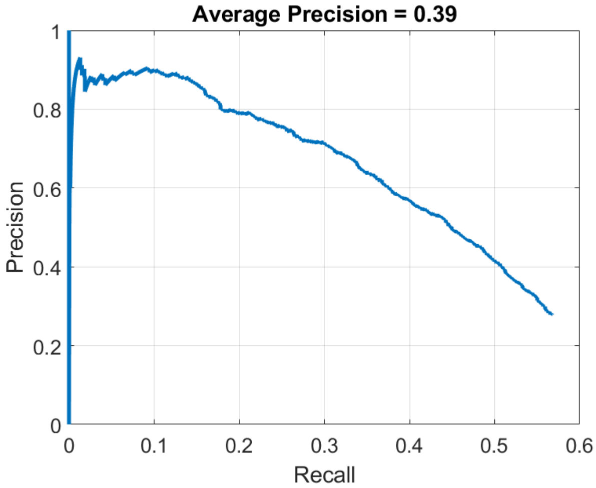

Figure 2. Precision-Recall curve of ACF object detector

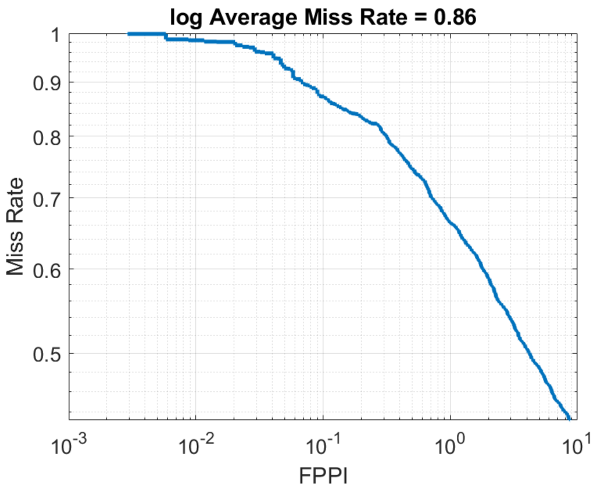

Figure 3. MR-FPPI curve of ACF object detector

V. Conclusion and Future Work

This paper focuses on locust detection problem for preventing locust plagues. This is achieved by using an ACF object detector. Different from previous work on locust identification which only gives a prediction result for a whole image, the ACF object detector can both locate the position and recognize the locusts in an image. The experimental results indicate that ACF object detector with optimized parameters can achieve 0.39 of average precision and 0.86 of log-average miss rate. Moreover, the prediction speed of ACF object detector is around 2 frames per second by using a single CPU which is a promising method to be embedded in a real-time locust detection system. Tuning the parameters of ACF object detector is a painful job. The parameters are optimized by a heuristic way. In the future, the more advanced parameter optimization methods (such as Bayesian optimization) will be combined into the framework. Moreover, other classifiers will be tested and k-fold cross validation will be used. In addition, fast modern deep learning methods (e.g. MobileNets) may be utilized to enhance the performance of object detector.

Figure 4. Example of locust detection

References

[1] L. Deng, Y. Wang, Z. Han, and R. Yu, “Research on insect pest image detection and recognition based on bio-inspired methods,” *Biosyst. Eng.*, vol. 169, no. 2000, pp. 139–148, 2018.

[2] T. Liu, W. Chen, W. Wu, C. Sun, W. Guo, and X. Zhu, “Detection of aphids in wheat fields using a computer vision technique,” *Biosyst. Eng.*, vol. 141, pp. 82–93, 2016.

[3] M. A. Ebrahimi, M. H. Khoshtaghaza, S. Minaei, and B. Jamshidi, “Vision-based pest detection based on SVM classification method,” *Comput. Electron. Agric.*, vol. 137, pp. 52–58, 2017.

[4] W. Ding and G. Taylor, “Automatic moth detection from trap images for pest management,” *Comput. Electron. Agric.*, vol. 123, pp. 17–28, 2016.

[5] C. Wen, D. Wu, H. Hu, and W. Pan, “Pose estimation-dependent identification method for field moth images using deep learning architecture,” *Biosyst. Eng.*, vol. 136, pp. 117–128, 2015.

[6] X. Cheng, Y. Zhang, Y. Chen, Y. Wu, and Y. Yue, “Pest identification via deep residual learning in complex background,” *Comput. Electron. Agric.*, vol. 141, pp. 351–356, 2017.

[7] D. Ma, K. Gorman, G. Devine, W. Luo, and I. Denholm, “The biotype and insecticide-resistance status of whiteflies, Bemisia tabaci (Hemiptera: Aleyrodidae), invading cropping systems in Xinjiang Uygur Autonomous Region, northwestern China,” *Crop Prot.*, vol. 26, no. 4, pp. 612–617, 2007.

[8] W. Dong, X. Zhang, X. Zhang, H. Wu, M. Zhang, E. Ma, and J. Zhang, “Susceptibility and potential biochemical mechanism of Oedaleus asiaticus to beta-cypermethrin and deltamethrin in the Inner Mongolia, China,” *Pestic. Biochem. Physiol.*, vol. 132, pp. 47–52, 2016.

[9] P. Dollar, R. Appel, S. Belongie, and P. Perona, “Fast feature pyramids for object detection,” *IEEE Trans. Pattern Anal. Mach. Intell.*, vol. 36, no. 8, pp. 1532–1545, 2014.

[10] Q. Yao, D. xiang Xian, Q. jie Liu, B. jun Yang, G. qiang Diao, and J. Tang, “Automated counting of rice planthoppers in paddy fields based on image processing,” *J. Integr. Agric.*, vol. 13, no. 8, pp. 1736–1745, 2014.

[11] P. Dollár, C. Wojek, B. Schiele, and P. Perona, “Pedestrian detection: An evaluation of the state of the art,” *IEEE Trans. Pattern Anal. Mach. Intell.*, vol. 34, no. 4, pp. 743–761, 2012.

An Embedded System for Real-Time 3D Human Detection

Haibin Cai, Lei Jiang, Junyi Wang, Mohamad Saada, and Qinggang Meng, Senior Member, IEEE

Abstract— **Recent years have seen great achievements in the design of deep learning network structures and the construction of large benchmark datasets for object detection. However, it still remains a great challenge to achieve real-time performance when adapting to embedded systems with low computational ability. This paper proposes an embedded system for real-time 3D human detection. The system consists of a neural computing stick for the deploy of CNN, an intel RGBD sensor for the 3D sensing and a Raspberry Pi platform. Furthermore, a novel multi-thread based human detection framework is proposed to improve the detection speed. Experimental results show that the system can effectively detection human in real-time performance.**

***Index Terms*—Embedded System, Real-time, Human Detection.**

I. INTRODUCTION

The ability of automatically detecting the 3D location of human is crucial for many embedded robot systems. For example, an intelligent robot is expected to accurately detect the localization subjects and conduct interaction with them by recognizing their actions [1], understanding their intentions or simply follow their routines for further commands. To automatically follow a target, the robot also needs to sensing the 3D information of the environment to avoid collisions and plan the routines. Although great achievements have been made in both hardware and software technologies in the recent few decades, it still remains a great challenge for a low-cost embedded system to achieve accurate and real-time human detection performance.

There has been extensive research regarding the detection of objects in the literature. For example, Ren et al. [2] proposed the Faster R-CNN model which consists of a region proposal network (RPN) and a Fast R-CNN network [3] for object detection. The RPN shares convolutional features with the Fast R-CNN network and improves the detection speed and accuracy to a large extent. However, its detection speed is still far away from real-time performance for embedded platforms. Later, Liu et al. [4] proposed a single shot multi-box detector (SSD) which uses small convolutional filters to directly predict box offsets and relative category scores. The SSD achieves real-time performance with a modern GPU. By replacing all the regular convolution with depthwise separable convolutions, the MobileNet [5] greatly improves the detection speed and reduces the model size, paving the way for the deploy on embedded platforms.

This paper proposes an embedded system for real-time 3D human detection. Although there are some embedded platforms with GPU equipped on the market such as Nivida Jetson TX2, the expensive price hinders their board applications into the industry. Thus, this paper focuses on building a low-cost system for human detection. To this end, this proposed system utilized a raspberry pi 3B+, a neural computing stick for the deploy of light weighted convolution neural networks and the Intel RealSense sensor for the sensing of 3D environments. To make the system runs in real time, this paper further proposes a novel multi-thread based human detection framework where the data sensing, analyzing and display interactions are implemented into three separate threads.

The rest of the paper is organized as follows: Section 2 describes the detail of the proposed embedded system. Section 3 demonstrates the experimental results. Finally, section 4 summarized this paper with a conclusion.

II. THE PROPOSED EMBEDDED SYSTEM

This section firstly presents the hardware configuration of the proposed embedded system and then introduce the designed software framework.

A. *Hardware Configuration*

Fig. 1 shows the functionality of the three main components of the system. Released on 2017, the Intel Neural Compute Stick is a low-power consuming device that allows deploying light-weighted deep learning network. The tiny size and fanless design make it an ideal extension for most of the embedded systems. To sense the RGB and depth information of the objects, the Intel RealSense Depth Camera D415 is employed. Unlike previous RGBD sensors such as Microsoft Kinect and Asus Xtion, D415 can be used in both indoor and outdoor environments. Its valid sensing depth distance ranges from 0.16m to 10m, which is also a big improvement over previous RGBD sensors. The Raspberry Pi is a well-known embedded platform owing to its low price and stable performance. This paper utilizes the last product of Raspberry Pi 3 Model B+ for the control of the other sensors. The ARMv8 Cortex-A53 processor and 1GB LPDDR2 SDRAM Guaranteed its outstanding performance in most cases.

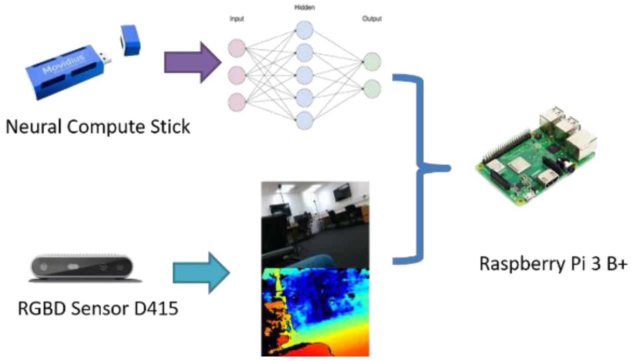

Fig. 1. The functionally of three main components of the system.

* This research is supported by YOBAN project funded by Newton Fund/Innovate UK, project number: 102871

H. Cai, L. Jiang, J. Wang, M. Saada, and Q. Meng are with the Computer Science, School of Science, Loughborough University, UK.

B. *Software Framework*

The software framework of the proposed embedded system is shown in Fig. 3. The system divides the functionalities into three groups and implement them in three different threads. The data retrieving thread continuously read RGB and Depth data from the RealSense D415 and update a shared memory space when new data arrives. The human detection thread takes the RGB data as input and conducts human detection on the intel neural computing stick. The detected bounding boxes serve as one of the inputs for the main thread, which is responsible for 3D human localization and display relative information on a screen for interaction purposes. The depth information of the human and the scene is obtained directly from the depth image in the data receiving thread. The transformation of depth data to the 3D human location in the RealSense D415's world coordinate is implemented via the following equation:

$$\frac{u-u_0}{f_x} = \frac{X}{Z}$$
$$\frac{v-v_0}{f_y} = \frac{Y}{Z} \qquad (1)$$
$$P = (X, Y, Z)$$

where P stands for a point in the world coordinate. (u,v) is its relative location in the color image whose resolution is set to be 640*480 to improve the detection speed. The intrinsic parameters of the color camera (fx, fy, u0, v0) are obtained via the classic chessboard-based calibration [6].

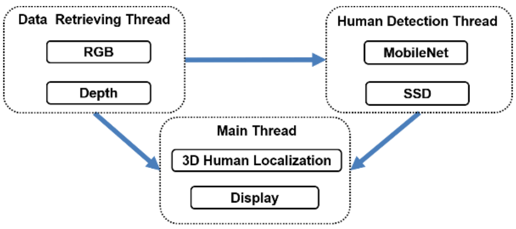

Fig. 3. The multi-thread human detection framework

To efficiently performance human detection, this paper utilized the MobileNet version of the SSD network [5]. The pre-trained model is directly used as it already includes human subjects as a target class. Trained on the coco dataset [7], this model can detect 90 classes of objects with good accuracy.

III. RESULTS

This section describes the experimental results for human detection on the embedded platform with a special focus on the speed performance.

Table 1 summarizes the time performance under different configurations. The average value of 1000 tests is used for each configuration. The first row shows the human detection speed using the Raspberry Pi 3B+ along. The 1.4 frames per second (FPS) makes it unsuitable for a robot to continuously follow a target. As shown in the second row, this system reaches around 7.3 fps when equipped with the Intel Neural Computing Stick. After further applying the proposed multi-thread framework, the system can detect human at 8.5 fps. It should also be noted that the system can still display the sensed images at 30 fps even with the low human detection speed due to the employment of the multi-thread framework. The drawback is that the detected bounding boxes will have a feeling of slow movement.

TABLE I. SPEED PERFORMANCE UNDER DIFFERENT CONFIGURATIONS

Configuration	Frames Per Second (FPS)
Pi	1.4
Pi + Stick	7.3
Pi + Stick + Multi-Thread	8.5

Fig. 4 shows an example of the human detection performance. The depth image was encoded as a color map for displaying purpose. The detected bounding box is shown directly in the RGB image. The location of the human is represented by the center point of the bounding boxes. Its 3D position is calculated via the Eq. 1.

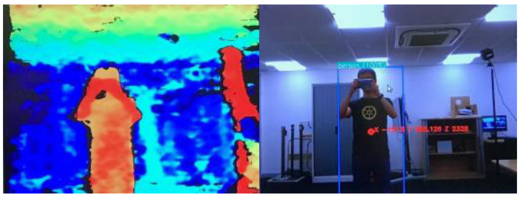

(a) (b)

Fig. 4. An example of the human detection performance. (a) Depth image;(b) Color image.

IV. CONCLUSION

This paper describes an embedded system for real-time 3D human detection. By combining a low-cost Raspberry Pi platform, a neural computing stick and an RGBD sensor together, the proposed system can detect effectively detect human subjects. Furthermore, the proposed multi-thread human detection framework enables the system to run in real-time performance. Due to the employment of light-weighted network structures, this system has difficulty in detecting small size subjects. Thus, the further direction of this research will be on improving the network structure for a better human detection performance.

REFERENCES

[1] B. Liu, Z. Ju, and H. Liu, "A structured multi-feature representation for recognizing human action and interaction," Neurocomputing, vol. 318, pp. 287–296, 2018.

[2] S. Ren, K. He, R. Girshick, and J. Sun, "Faster R-CNN: Towards Real-Time Object Detection with Region Proposal Networks," in IEEE Trans. Pattern Analysis Machine Intelligence, 2017.

[3] R. Girshick, "Fast R-CNN," Proc. IEEE Int. Conf. on Computer Vision, vol. 2015 Inter, pp. 1440–1448, 2015.

[4] W. Liu, D. Anguelov, D. Erhan, C. Szegedy, S. Reed, C. Y. Fu, and A. C. Berg, "SSD: Single shot multibox detector," European Conference on Computer Vision, pp. 21–37, 2016.

[5] M. Sandler, A. Howard, M. Zhu, A. Zhmoginov, and C. Liang-Chieh, "MobileNetV2: Inverted Residuals and Linear Bottlenecks," in Proc. IEEE Conf. Computer Vision and Pattern Recognition, 2018.

[6] Z. Zhang, "A flexible new technique for camera calibration," IEEE Trans. Pattern Analysis and Machine Intelligence, vol. 22, no. 11, pp. 1330–1334, 2000.

[7] T.-Y. Lin, M. Maire, S. Belongie, J. Hays, P. Perona, D. Ramanan, P. Dollar, and C. L. Zitnick, "Microsoft COCO: Common Objects in Context," European Conference on Computer Vision, 2014.

Walking Motion Real-time Detection Based on Walking Stick Equipped with MPU and Raspberry Pi*

Junyi Wang, Mohamad Saada, Haibin Cai, and Qinggang Meng, *Senior Member, IEEE*

***Abstract*— This paper proposes walking motion real-time detection by employing intelligent walking stick which includes MPU 6050, portable power and Raspberry pi zero w embedded with machine learning algorithms. Firstly, several types of walking motion data are collected by utilizing the walking stick. These walking motion types include fast walking, slow walking, turning left, turning right and stopping. Secondly, the machine learning classifiers can be obtained by training the collected data set. After that, the accuracy rate comparison among these classifiers are given by utilizing the testing data. Finally, the classifiers are embedded into the Raspberry pi zero w to detect walking motion in real time.**

I. Introduction

A large number of papers have investigated motion detection for the human [1, 2, 3, 4]. In [1], a method for learning the structure and parameters of a decomposable triangulated graph was described, and it was applied to learn models of biological motion. By assembling the carbon-nanotube sensors on stockings, bandages and gloves to fabricate devices, different types of human motion including movement, typing, breathing and speech can be detected in [2]. Based on [2], the highly sensitive, tunable, reproducible, and durable strain sensors were used for monitoring large-scale body and small skin in [4]. Since strain sensors can be used for measuring strains on human activities, they have recently received a great deal of attention. However, these strain sensors are covered on the body, which is not convenient for human activities.

In order to help the visually impaired people to walk safely and independently, the smart walking sticks equipped with sensors and algorithms were researched, and several kinds of smart walking sticks were designed in [5-10]. In [5], a smart walking stick based on an electronic approach was designed to assist visually disabled people. By using ultrasonic sensors and a vibrator motor scheme, the haptic walking stick was proposed, modeled and successfully tested in [6]. After that, an intelligent walking stick was represented for visually challenged people to guide them to reach their destination safely without facing any difficulties in [9]. On the other hand, in order to aid elderly people to avoid falling and connect with their family in times, the walking sticks with GPS and sensors were presented in [11-14]. Being different from these existed walking stick, a walking stick with low-cost MPU 6050 and Raspberry pi zero w possesses machine learning algorithms, which is effective to collect human motion data and realize the real-time detection based on trained machine learning classifiers.

Raspberry pi was developed in the laboratory of university of Cambridge, and the first generation was released by Raspberry pi foundation in February 2012 [15]. As a single board computer, Raspberry pi is affordable and widely available in the scientific community and practical application [16], and they are used in many products. Raspberry pi zero w with 1GHz BCM2835 single-core processor and 512MB RAM is used in the walking stick, which is about four times faster than the original Raspberry pi. The main advantages of this walking motion real-time detection system based on the walking stick can be summarized as follows. (1)The prices of Raspberry pi zero w and MPU are very low and affordable, and they are used in the walking stick. (2) Walking motion detection system is based on Scikit-Learn and python language built in Raspberry pi, which is efficient to implement the data collection, data training and real-time detection. (3) Based on this walking stick, five walking motion data are collected, and the accuracy rate comparison among several machine learning algorithms is given by using the collected data.

II. Design and Implementation

Two MPU 6050 are located on the top and in the middle of the walking stick respectively. By using jumping cables, Raspberry pi and two MPU6050 are connected to collect data, which can be seen in figure 1.

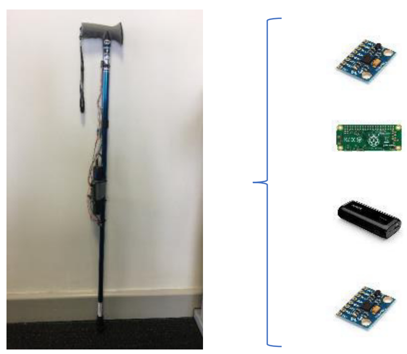

Figure 1. The composition of the walking stick

A. *Data Collection*

The portable power in the walking stick provides power for the Raspberry pi and MPU 6050. By using VNC or PuTTY, the Raspberry pi is connected with laptop. Each MPU 6050 has 3-axis accelerometers and 3-axis gyroscopes. Based on python

*Resrach supported by YOBAN project funded by Newton Fund/Innovate UK, project number: 102871.

J. Wang, M. Saada, H. Cai and Q. Meng are with Department of Computer Science, Loughborough University, Loughborough LE11 3TU, U.K. (e-mail: J.Wang2@ lboro.ac.uk; M.Saada@lboro.ac.uk; H.Cai@lboro.ac.uk; Q.Meng@lboro.ac.uk).

language codes, three thousand rows of data are collected for each walking motion by using this walking stick. Each row of data is thirteen columns vector. The first three elements represent x-axis, y-axis and z-axis accelerometer of the top MPU. The second three elements represent x-axis, y-axis and z-axis gyroscope of the top MPU. Similarly, the third and fourth three elements represent x-axis, y-axis, z-axis accelerometer and x-axis, y-axis and z-axis gyroscope of the middle MPU respectively. The last element represents the label of the walking motion.

B. Machine Learning algorithms

In order to achieve the real-time detection of walking motion, the classifiers should be obtained in advance. Based on Raspberry pi zero w, we build Scikit-Learn software machine learning library for the python programming language. For the collected data, 70% data are training set, and the rest of 30% data are testing set. Firstly, we select 100 rows data as a window, and the column elements are accelerometer and gyroscope values. The data of each window is a 100×12 dimensional matrix. Secondly, some useful statistical features such as, median, mean, variance, skewness, kurtosis, minimum, maximum, etc, are extracted for each column in the window matrix. After that, all these statistical features are connected to compose a big row vector. The calculation methods for a part of extracted features are shown in Table I.

TABLE I. CALCULATION METHODS OF THE FEATURE

Feature name	**Calculation methods**
Mean value	$\bar{x} = \frac{1}{m}\sum_{i=1}^{m} x_i$
Variance	$V = \frac{1}{m}\sum_{i=1}^{m}(x_i - \bar{x})^2$ $\bar{x}$ is mean value
Standard deviation	$Sd = \sqrt{\frac{1}{m}\sum_{i=1}^{m}(x_i - \bar{x})^2}$ $\bar{x}$ is mean value
Skewness	$S = \frac{\sum_{i=1}^{m}(x_i - \bar{x})^3}{m-1} Sd^3$ $\bar{x}$ is mean value
Kurtosis	$K = \frac{\sum_{i=1}^{m}(x_i - \bar{x})^4}{m-1} Sd^4 - 3$ $\bar{x}$ is mean value

We use machine learning algorithms, such as Support Vector Machine (SVM), Decision Tree (DT), K-Nearest Neighbours (KNN), Random Forest (RF), and Gradient Boosting Decision Tree (GBDT), to train the training set and obtain several different types of machine learning classifiers. After that, these classifiers are embedded into Raspberry pi zero w, and the classifier with the highest accuracy rate is used as walking motion detection algorithm.

III. RESULTS AND DISCUSSIONS

In this section, we used the rest of 30% data as the testing set. We can get several different accuracy rates for these obtained classifiers, which is shown in Table II. The GBDT and RF have the highest accuracy rate of 97.78%, which is 40% more than SVM with the lowest accuracy rate of 57.78%. In addition, the accelerometer and gyroscope readings for these types of walking motions based on intelligent walking stick are shown in Figs 2-6.

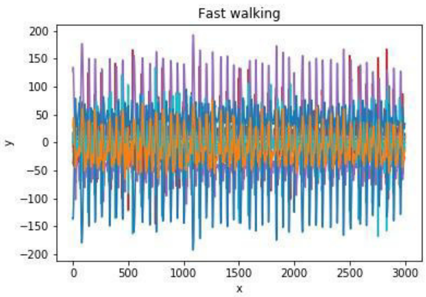

Figure 2. Accelerometer and gyroscope readings of fast walking

Figure 3. Accelerometer and gyroscope readings of slow walking

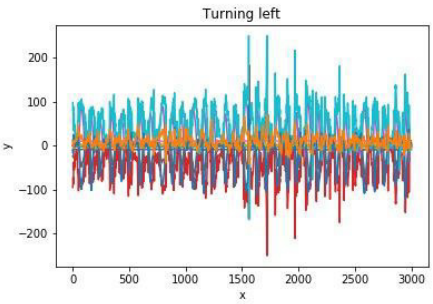

Figure 4. Accelerometer and gyroscope readings of turning left

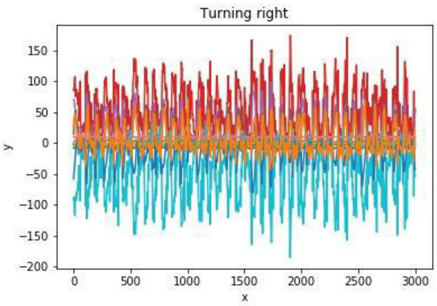

Figure 5. Accelerometer and gyroscope readings of turning right

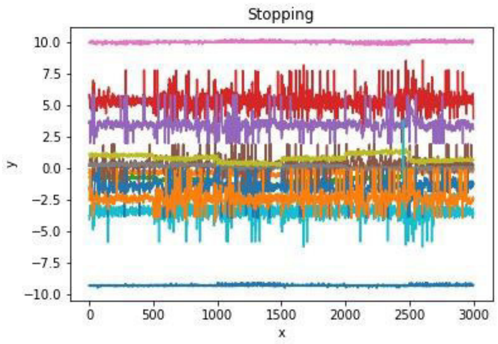

Figure 6. Accelerometer and gyroscope readings of stopping

From these Figures, we see that the 3-axis accelerometer and 3-axis gyroscope readings have pronounced difference for different type of walking motion. Hence, from extracting features of these states, we get high accuracy rates of walking motion detection by using machine learning algorithms. In this walking stick, the GBDT is embedded in the Raspberry pi. When the users apply this walking stick to do fast walking, slow walking, turning left and turning right, the motion can be detected in real time, and the detection time is about one second.

TABLE II. ACCURACY RATES OF DIFFERENT MACHINE LEARNING

Classifiers	Accuracy rates
Support Vector Machine	57.78%
Decision Tree	91.11%
k-Nearest Neighbor	95.56%
Random Forest	97.78%
Gradient Boosting Decision Tree	97.78%

The trained machine learning classifier is embedded into the Raspberry pi of the walking stick, and the real-time detection results can be recorded in the walking process. Hence, when elderly people use this walking stick, we acquire their motion situation and know their living status. In addition, we also can collect more types of walking motions to obtain more kinds of real-time detection results.

IV. CONCLUSION

In the walking stick, Raspberry pi and MPU are illustrated as affordable and effective in the data collection and real-time detection of walking motion. In this paper, based on Scikit-Learn and python language, we have collected several kinds of walking motion data including fast walking, slow walking, turning left, turning right, and stopping by using walking stick and obtained several classifiers by training these data in Raspberry pi zero w. After that, the machine learning classifier with high accuracy rate is embedded into Raspberry pi to achieve walking motion real-time detection.

REFERENCES

[1] T. Yamada, Y. Hayamizu, Y. Yamamoto, Y. Yomogida, A. Izadi-Najafabadi, D. N. Futaba, and K. Hata, "A stretchable carbon nanotube strain sensor for human-motion detection," *Nature nanotechnology*, vol. 6, no. 5, 296-301. Mar. 2011.

[2] Y. Song, L. Goncalves, and P. Perona, "Learning probabilistic structure for human motion detection," in Proceedings of the 2001 IEEE Computer Society Conference on Computer Vision and Pattern Recognition (CVPR), vol. 2, pp. 771-777.

[3] J. Lee, S. Kim, J. Lee, D. Yang, B. C. Park, S. Ryu, and I. Park, "A stretchable strain sensor based on a metal nanoparticle thin film for human motion detection," Nanoscale, vol. 6, no. 20, 11932-11939, Aug. 2014.

[4] G. H. Lim, N. E. Lee, and B. Lim, "Highly sensitive, tunable, and durable gold nanosheet strain sensors for human motion detection," *Journal of Materials Chemistry C*, vol. 4, no. 24, pp. 5642-5647, Apr. 2016.

[5] M. H. Mahmud, R. Saha, and S. Islam, "Smart walking stick-an electronic approach to assist visually disabled persons," *International Journal of Scientific & Engineering Research*, vol. 4, no. 10, pp. 111–114, Oct. 2013.

[6] M. P. Menikdiwela, K. M. I. S. Dharmasena, and AM Harsha S. Abeykoon, "Haptic based walking stick for visually impaired people," *in conf. 2013 IEEE int. conf. Circuits, Controls and Communications (CCUBE),* pp. 1-6.

[7] S. K. Chaitrali, A. D. Yogita, K. K. Snehal, D. D. Swati, and V. D. Aarti, "An intelligent walking stick for the blind," *International Journal of Engineering Research and General Science,* vol. 3, no. 1, pp, 1057-1062, Jan. 2015.

[8] S. Mohite, A. Patel, and M. Patel, "Smart Walking Stick for Visually Impaired People," *Vaishali, Smart Walking Stick for Visually Impaired People,* pp. 1-5, Oct. 2018.

[9] Y. H. Chang, N. Sahoo, and H. W. Lin, "An intelligent walking stick for the visually challenged people," *In 2018 IEEE International Conference on Applied System Invention (ICASI)*, pp. 113-116.

[10] A. Shaha, R. Shubham, and G. Sankaradithyan, "SWSVIP-smart walking stick for the visually impaired people using low latency communication," *2018 IEEE International Conference on Smart City and Emerging Technology (ICSCET)*, pp. 1-5.

[11] A. Lachtar, T. Val, and A. Kachouri, "3DCane: a monitoring system for the elderly using a connected walking stick," *International Journal of Computer Science and Information Security*, vol. 14, no. 8, pp. 1-8, 2016.

[12] A. Dabir, R. Solkar, M. Kumbhar, and G. Narayanan, "GPS and IOT equipped smart walking stick," *In 2018 International Conference on Communication and Signal Processing (ICCSP)*, pp. 0322-0326.

[13] A. Lachtar, A. Kachouri, and T. Val, "Real-time monitoring of elderly using their connected walking stick," *2017 IEEE International Conference on Smart, Monitored and Controlled Cities (SM2C 2017)*, pp. 48-52.

[14] B. Sun, Z. Li, Q. Zhang, L. Song, W. Fan, and J. Yang, "Dynamic model and control of a walking stick robot," *In 2018 IEEE* International Conference on Intelligence and Safety for Robotics (ISR), pp. 222-226.

[15] J Dean Brock, Rebecca F Bruce, and Marietta E Cameron, "Changing the world with a Raspberry Pi," *Journal of Computing Sciences in* Colleges, 29(2):151-153, 2013.

[16] M. Ambrož. Raspberry Pi as a low-cost data acquisition system for human powered vehicles. *Measurement*, vol. 100, pp. 7-18, Mar. 2017.

Subclass Discriminant Analysis based Myoelectric Hand Motion Recognition

Dalin Zhou, Yinfeng Fang, Zhaojie Ju and Honghai Liu

Abstract — **Control of prosthetic hands and other upper-limb assistive device for rehabilitation relies on the premise that users' hand motion intention is accurately recognised. Among all the feasible modalities, myoelectric hand motion recognition has been most adopted yet suffers from its intrinsic day-to-day changes. Despite the promising accuracy achieved by pattern recognition approaches in intra-day tests, the inter-day performance deteriorates in long-term use. From the users' perspective, it is desired that the hand motion recognition accuracy improves while the burden of user training is confined within 1 or 2 days. In this paper, subclass discriminant analysis is applied instead of conventional linear discriminant analysis for myoelectric hand motion recognition for long-term use. The evaluation results on 10 days' myoelectric data captured from 6 subjects show that the subclass division contributes to improved inter-day recognition accuracy with limited training data.**

I. Introduction

For prosthesis and other upper-limb assistive device users, good intuitiveness, high success rate, low latency and limited adaptation cost of the devices are the prior properties to be fulfilled [1]. In details, the premise of an ideal control is crafted by the accurate recognition of users' intention, the imperceptible delay between the execution of the mechanical extremity and the employment of users' residual limb, and their consistent feasibility for long-term use. Among various feasible approaches, electromyography (EMG) based pattern recognition for prosthetic hand control has been the most widely investigated one for its most promising performance [2]. The aim of such methodology is to distinguish users' intention of hand movement through classifying the patterns extracted from EMG signals captured during forearm muscle contractions. Increasingly high accuracy and improved robustness have been frequently published within the framework of pattern recognition in academia in terms of development of classifiers [3] and features [4]. And the superiority of pattern recognition based solutions in clinical scenarios has been stated in various recent research [5-7]. However, the intrinsic randomness of the EMG signals contributes to a degraded performance in long-term use, which has been addressed by researchers [8-10] yet not fully accommodated.

Reports have shown that long-term use will deteriorate the hand motion recognition accuracy across multiple days. Various factors that affect the consistency of long-term EMG signals have been taken into account like fatigue and electrode shift [11]. The deterioration of inter-day performance leads to the requirement of everyday training effort from the users to adjust the applied recognition algorithm. The burden of re-training and re-calibration prevents the current research prototypes from being applied in clinical settings. Less or no re-training depends on better priori knowledge of the potential invariance and inter-day relation of EMG during long-term use. The inter-day performance of EMG based hand motion recognition is improvable under the assumption that invariance and inter-day relation could be extracted from EMG, which in turn is governed by jointly improved feature selection and classifier design. Mature classification approaches like linear discriminant analysis (LDA) have been widely applied in EMG based hand motion recognition in combination with the classic Hudgins' time domain features [12] together with autoregressive coefficients (TDAR), yet not able to fully exploit the invariant part and transfer it to inter-day use. Despite the efforts in an adaptive way to accommodate the unseen data in long-term use [3,10], the improved exploitation of the seen data is rarely published. Thus it is timely and challenging to propose suitable pattern recognition approaches for long-term use which can be identified in the development of robust classifiers for inter-day scenarios. A subclass division based discriminant analysis framework is adopted in this paper to address the aforementioned challenges.

The rest of this paper is organised as follows. Myoelectric hand motion recognition is briefly introduced in Section II with an emphasis on the pattern recognition based solutions. The adopted subclass division based discriminant analysis is explained in details in Section III. And the experiment setup and evaluation results are provided in Section IV. Finally this paper is concluded in Section V with discussion.

II. Pattern Recognition based Myoelectric Hand Motion Recognition

To date, let alone the numerous manifestations that represent muscle activity, EMG remains the main equipped sensing modality for muscular activity sensing in the active control of almost every commercial upper limb prosthesis and exoskeleton for active limb motor function restoration. Pattern recognition approaches have been mostly investigated for their promising accuracy in the recognition of dexterous motion templates. A typical flowchart of pattern recognition based myoelectric hand motion recognition is shown in Fig. 1. The EMG signals are first preprocessed and segmented. Within each segment, a decision is generated through the routine of a pattern recognition approach comprising the feature extraction and classification.

Dalin Zhou is with the School of Computing, University of Portsmouth, PO1 3HE, UK (phone: +44-7835261646; e-mail: dalin.zhou@port.ac.uk).

Yinfeng Fang is with Hangzhou Dianzi University, 310018, China. (e-mail: yinfeng.fang@hdu.edu.cn).

Zhaojie Ju is with the School of Computing, University of Portsmouth, PO1 3HE, UK (e-mail: zhaojie.ju@port.ac.uk).

Honghai Liu is with the School of Computing, University of Portsmouth, PO1 3HE, UK (e-mail: honghai.liu@port.ac.uk).

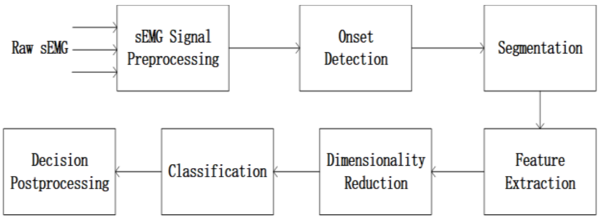

Figure 1. A typical flowchart of pattern recognition based myoelectric hand motion recognition

Classifier design plays an important role in pattern recognition based applications. Numerous classification strategies like LDA, SVM and GMM together with their modifications have been applied in myoelectric hand motion recognition. Among all the conventional recognition frameworks, LDA has been employed in the EMG based hand motion recognition for decades and remains the most important baseline for its robust performance in academic research. Liu et al. [10] addressed the reduction of user re-training while preserving acceptable inter-day recognition accuracy by using LDA with an optimised projection. Vidovic et al. [13] employed supervised adaptation to calibrate the model for inter-day use on both able-bodied subjects and amputees. The aforementioned discriminant analysis methods are mostly based on the assumption that each class is represented by a single cluster. However, separated subclasses are possibly formed because of the nonstationary and stochastic nature of sEMG signals. Overlapping subclasses among predefined classes could go against the assumptions embedded in some classification methods. For example, the distribution of pooled samples might not meet the assumption of having a common covariance matrix but different means for LDA. The potential of subclass division in the cross-day settings has not been addressed yet regardless of the widely developed modifications of LDA. Despite the intensive research interest in discriminant analysis based myoelectric hand motion recognition, the development of classifiers with a specific focus on the inter-day hand motion recognition for long-term use is rarely seen, not mentioning the emphasis on various adequateness of training samples in comparison to the testing ones. The inter-day overlapping problem is addressed in this paper by utilising the subclass division prior to discriminant analysis to exploit its advantageous capability in myoelectric hand motion recognition with inadequate training data from 1 or 2 days and the testing data from unseen days.

III. SUBCLASS DIVISION BASED DISCRIMINANT ANALYSIS

In our preliminary work [14], the effectiveness of subclass division has been proved on the force based granular modeling for grasp recognition, where the EMG signals and forces of hand grasps were captured synchronously. The grasping force was introduced by the incorporation of an additional force sensor to the EMG capturing system. And the classes of hand motions were enriched by an additional attribute describing the force levels. Let alone the accurately categorised samples, the misclassification among subclasses that belong to the same class will contribute to the improved correct classification through a mapping into the original classes at last.

Despite the improved recognition accuracy, the force driven subclass division is based on an additional attribute of force utilising extra sensory information at an ideal setting and does not reflect the real daily life scenarios, where human-object interaction is conducted without the force sensing. Thus it is essential to conduct the subclass division for hand motion recognition using solely EMG signals across multiple days with inadequate training data, whose subclasses are shaped by the inter-day changes of EMG characteristics and electrode shift caused by donning/doffing in long-term use. An intuitive approach is the implicit subclass division that utilises the subclass information without enlarging the class labels in a fining and coarsening scheme, and is realised in the discriminant analysis directly. The discriminant analysis based algorithms classify the samples with a projection of the original data into a reduced subspace with an optimised separability by simultaneously maximising the between-class distance and minimising the within-class distance. Accordingly, a general criterion of separation for most discriminant analysis algorithms is defined in (1).

$$\mathrm{S} = \frac{|\omega^T S_b \omega|}{|\omega^T S_w \omega|} \tag{1}$$

Where S_w and S_b are the scatter matrices of within-class distance and between-class distance respectively, and ω represents the direction for projection. The discriminant analysis aims to find an optimal projection direction by maximising S. Conventionally the within-class scatter matrix is defined in (2).

$$S_w = \frac{1}{N} \sum_{i=1}^{C} \sum_{j=1}^{N_i} (x_{ij} - u_i)(x_{ij} - u_i)^T \tag{2}$$

Where N is the total number of samples, C is the number of classes, N_i is the number of samples that belong to class i, x_{ij} is the j-th sample within the class i, and u_i is the mean centre of class i.

An integration of subclass division into the projection determination is utilised instead of using two independent subclass division and linear discriminant stages. The subclass discriminant analysis (SDA) algorithm proposed by Zhu et al. [15] is the first discriminant analysis considering the distance between subclasses instead of the distance between classes. The idea is adopted in combination with the nearest neighbour based division criterion in this paper to find the most convenient division of each class into multiple subclasses in an exhaustive scheme.

The between-class scatter matrix is defined in (3).

$$S_b = \sum_{i=1}^{C} \sum_{p=1}^{c_i} \sum_{j=i+1}^{C} \sum_{q=1}^{c_j} \frac{n_{ip}}{N_i} \frac{n_{jq}}{N_j} (u_{ip} - u_{jq})(u_{ip} - u_{jq})^T \tag{3}$$

where C is the number of classes, c_i is the number of subclasses within the class i, N_i and N_j are the number of samples belonging to class i and j respectively, N_{ip} is the number of samples belonging to the subclass p of class i, and u_{ip} is the mean centre of subclass p of class i. The distance between subclasses is utilised instead of the distance between classes to extract the distribution information of subclasses attributed to the overlapping classes in long-term use.

Conventionally, once the scatter matrices are acquired, the projection direction is found to linearly separate the pooled data following the generalised eigenvalue decomposition as

$$S_b \mathrm{W} = S_w W \Lambda \tag{4}$$

Where W is the projection matrix whose columns are formed by the right eigenvectors and Λ is the diagonal matrix whose diagonal elements are corresponding eigenvalues. The first k columns of W with the greatest magnitude of eigenvalues are selected to form the projection matrix W^k for a k+1-class classification problem.

Based on the definition in (3), the further calculation of projection direction requires a determined subclass division number of each class. The strategy for seeking optimal subclass divisions with the leave-one-trial-out test is adopted on the pooled dataset for both training and testing with only one trial of samples excluded to achieve the global optimum. In this paper, the selection of separate training and testing samples is adopted to address the inter-day and long-term use instead of solely considering the intra-day use. Specifically, the training samples from each class are first divided into subclasses according to their inter-sample distances. The nearest neighbour method is adopted in the distance sorting, which measures the Euclidean distance between the two samples x_{ip} and x_{iq} within the class i to determine their subclass category. Then SDA classifiers using different subclass division choices are compared with the recognition accuracy on the testing data. The one with the highest accuracy is finally selected for further validation on the subclass division number. And the subclass division driven discriminant analysis is then conducted by solving (4).

IV. EXPERIMENTS

A. Data Acquisition

In the absence of a well acknowledged benchmark for long-term inter-day myoelectric hand motion recognition, the evaluation in this paper is conducted on a locally captured dataset. A customised 16-channel EMG capturing system developed by [16] is adopted for the EMG signal capturing. The 16 bi-polar electrodes are formed by sharing each electrode with two neighbouring channels, and embedded in a stretchable sleeve to cover both the anterior and posterior compartments of forearm muscles with an optimised zig layout. The acquisition system is equipped with a sampling frequency of 1000 Hz, a gain of 3000 and an ADC resolution of 12 bits. The captured EMG signals are bandpass filtered between 20 Hz and 500 Hz by a Butterworth filter and separated from the power line noise with a notch filter. Another empty sleeve is used to cover the electrode sleeve to ensure a firm contact between the electrodes and the skin surface to alleviate movement artefacts. The digitalised EMG signals are transmitted to a personal computer via USB connection for data recording and processing. A graphical user interface is designed to display the motion hints and corresponding 16-channel filtered EMG signals.

A total of 13 hand motion candidates shown in Fig. 2 are included in this database, comprising 3 basic palm movements of hand rest (HR), hand open (HO) and hand close (HC), 4 wrist movements of wrist flexion (WF), wrist extension (WE), ulnar flexion (UF) and radial flexion (RF), 2 forearm movements of pronation (PR) and supination (SU), and 4 basic grasp types of fine pinch (FP), key pinch (KP), spherical grasp (SG) and cylindrical grasp (CG). A total of 6 able-bodied subjects (2 females and 4 males) are recruited in the experiment. The subjects are all with intact limb motor function and do no suffer from any neurological or muscular disorders. The subjects are all unfamiliar with the prosthetic control and EMG based hand motion recognition. This experiment is approved by the ethics committee of University of Portsmouth with written informed consent obtained from all subjects.

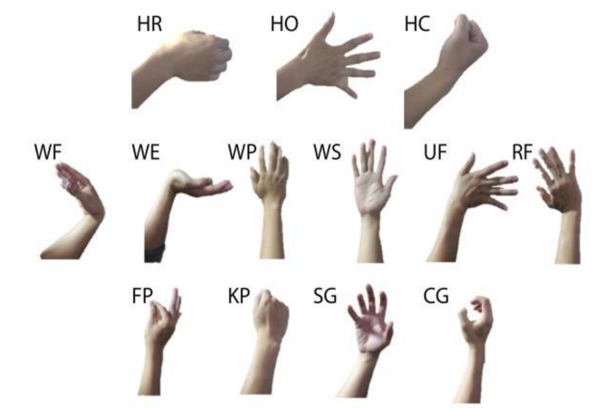

Figure 2. Hand motion candidates for recognition

The user training protocol proposed in our previous work [17] is adopted to improve the consistency of EMG patterns from users' voluntary hand motions prior to their participation in the on-site database building. It has been proved that the clustering-feedback user contributes to a consistent online performance, which leads to a more reliable evaluation result. The user training protocol encourages the subjects to adjust their muscle contraction and force control in each intra-day trial, which removes the adverse artefacts of voluntary contraction and confines the variation of EMG signals to inter-day physiological changes.

B. Experiment Results

The comparison of SDA and LDA based solutions on inter-day use is depicted in Fig. 3 and Fig. 4. The data of 6 subjects performing 13 hand motions in consecutive 10 days are adopted. The classifiers are trained by 1 day's and 2 day's data respectively and tested on the rest days' data using the same group of the 128-dimensional TDAR features, which means the recognition is totally conducted on the unseen data captured in novel days. The number of subclasses is set equal among all classes as a constraint. The average recognition accuracy increases with slight improvement utilising SDA instead of LDA. In details, an improvement of recognition accuracy across the subjects can be seen for the situation with inadequate training of 1 day, and 9 days' totally unseen data for testing, which supports the implicit incorporation of subclass division among multiple trials when inadequate training data are provided.

A detailed numerical comparison of the recognition accuracy and corresponding numbers of testing samples is shown in Table I. It is seen that the recognition accuracy increases by a large extent of around 10% when a new day's data is included for the training which aligns with the intuition. Regardless of the enriched training of 2 days' data, the total samples are still inadequate when compared to the 8 days' unseen data for prediction.

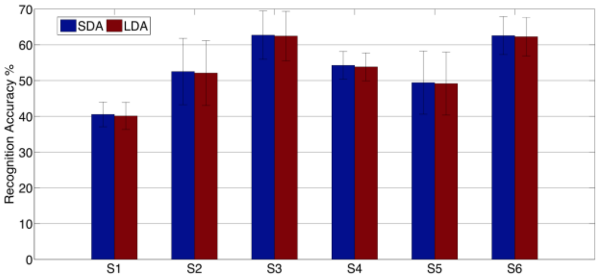

Figure 3. Recognition accuracy with training on 1 day's data

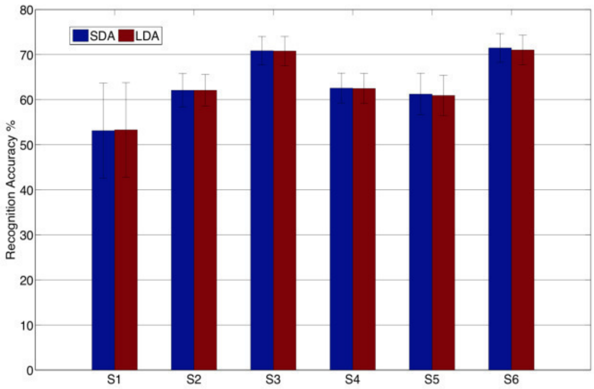

Figure 4. Recognition accuracy with training on 2 days' data

TABLE I. COMPARISON OF SDA AND LDA BASED INTER-DAY MYOELECTRIC HAND MOTION RECOGNITION ACCURACY

Subjects	**Training on 1 day**		**Training on 2 days**	
	LDA (%)	***SDA(%)***	***LDA (%)***	***SDA(%)***
1	40.11±3.79	40.54±3.46	53.29±10.50	53.12±10.51
2	52.11±9.06	52.53±9.28	62.08±3.50	62.08±3.70
3	62.46±6.91	62.72±6.76	70.78±3.25	70.85±3.18
4	53.83±3.89	54.26±3.88	62.48±3.32	62.56±3.31
5	49.17±8.82	49.43±8.83	60.93±4.45	61.24±4.62
6	62.27±5.37	62.58±5.29	71.03±3.28	71.47±3.18
Mean	**53.32**	**53.67**	**63.43**	**63.55**

V. CONCLUSION

In this paper, the subclass division based discriminant analysis is applied in the long-term and inter-day myoelectric hand motion recognition. And the results gained from the experiments on 6 able-bodied subjects in consecutive 10 days comply with the intuitive idea that the extraction of subclasses among multiple trials and multiple days will lead to a better distinguishability of the EMG signals without increasing the burden of user training.

It is worth noting that the experiments are only conducted on healthy subjects in this paper. A potential discrepancy may reside in the different motor function conditions between amputated users and able-bodied subjects. Further validation on targeted prosthesis and assistive device users is required. And the feasibility of the subclass division methods on inter-subject scenarios is also worth investigating in the future.

REFERENCES

[1] K. Englehart and B. Hudgins. "A robust, real-time control scheme for multifunction myoelectric control," *IEEE Transactions on Biomedical Engineering,* 2003 Jul;50(7):848-54.

[2] Y. Fang, N. Hettiarachchi, D. Zhou and H. Liu. "Multi-modal sensing techniques for interfacing hand prostheses: a review," *IEEE Sensors Journal*, 2015 Nov;15(11):6065-76.

[3] J. Liu, X. Sheng, D. Zhang, J. He and X. Zhu. "Reduced daily recalibration of myoelectric prosthesis classifiers based on domain adaptation," *IEEE Journal of Biomedical and Health Informatics*, 2016 Jan;20(1):166-76.

[4] A. Phinyomark, F. Quaine, S. Charbonnier, C. Serviere, F. Tarpin-Bernard and Y. Laurillau. "EMG feature evaluation for improving myoelectric pattern recognition robustness," *Expert Systems with applications*, 2013 Sep 15;40(12):4832-40.

[5] T. A. Kuiken, L. A. Miller, K. Turner and L. J. Hargrove. "A comparison of pattern recognition control and direct control of a multiple degree-of-freedom transradial prosthesis," *IEEE Journal of Translational Engineering in Health and Medicine*, 2016;4:1-8.

[6] M. M. Whiete, W. Zhang, A. T. Winslow, M. Zahabi, F. Zhang, H. Huang and D. B. Kaber. "Usability comparison of conventional direct control versus pattern recognition control of transradial prostheses," *IEEE Transactions on Human-Machine Systems,* 2017 Dec;47(6):1146-57.

[7] L. J. Hargrove, L. A. Miller, K. Turner and T. A. Kuiken. "Myoelectric pattern recognition outperforms direct control for Transhumeral amputees with targeted muscle Reinnervation: a randomized clinical trial," *Scientific reports*, 2017 Oct 23;7(1):13840.

[8] J. W. Sensinger, B. A. Lock and T. A. Kuiken. "Adaptive pattern recognition of myoelectric signals: exploration of conceptual framework and practical algorithms," *IEEE Transactions on Neural Systems and Rehabilitation Engineering*, 2009 Jun;17(3):270-8.

[9] E. N. Kamavuako, K. B. Englehart, W. Jensen and D. Farina. "Simultaneous and proportional force estimation in multiple degrees of freedom from intramuscular EMG," *IEEE Transactions on Biomedical Engineering*, 2012 Jul;59(7):1804-7.

[10] J. Liu, X. Sheng, D. Zhang, N. Jiang and X. Zhu. "Towards zero retraining for myoelectric control based on common model component analysis," *IEEE Transactions on Neural Systems and Rehabilitation Engineering*, 2016 Apr;24(4):444-54.

[11] N. Jiang, S. Dosen, K. R. Muller and D. Farina. "Myoelectric control of artificial limbs—is there a need to change focus?," *IEEE Signal Processing Magazine*, 2012 Sep;29(5):152-0.

[12] B. Hudgins, P. Parker and R. N. Scott. "A new strategy for multifunction myoelectric control," *IEEE Transactions on Biomedical Engineering*, 1993 Jan;40(1):82-94.

[13] M. M. Vidovic, H. J. Hwang, S. Amsüss, J. M. Hahne, D. Farina and K. R. Müller. "Improving the robustness of myoelectric pattern recognition for upper limb prostheses by covariate shift adaptation," *IEEE Transactions on Neural Systems and Rehabilitation Engineering*, 2016 Sep;24(9):961-70.

[14] Y. Fang, D. Zhou, K. Li, Z. Ju and H. Liu. "A force-driven granular model for EMG based grasp recognition," *In Systems, Man, and Cybernetics (SMC), 2017 IEEE International Conference*, 2017 Oct 5 (pp. 2939-2944). IEEE.

[15] M. Zhu and A. M. Martinez. "Subclass discriminant analysis," *IEEE Transactions on Pattern Analysis and Machine Intelligence*, 2006 Aug;28(8):1274-86.

[16] Y. Fang, H. Liu, G. Li and X. Zhu. "A multichannel surface EMG system for hand motion recognition," *International Journal of Humanoid Robotics*, 2015 Jun;12(02):1550011.

[17] Y. Fang, D. Zhou, K. Li and H. Liu. "Interface prostheses with classifier-feedback-based user training," *IEEE Transactions on Biomedical Engineering*, 2017 Nov;64(11):2575-83.

The Intelligent Control Strategy and Verification for Precise Water-fertilizer Irrigation System

Z. Yubin, W. Zhengying, Z. Lei, and J Weibing
School of Mechanical Engineering Xi'an Jiaotong University, Xi'an, China

***Abstract*—Aim at the precision control problems of water and fertilizer concentration during agricultural fertilization and irrigation periods, designing a control technology that based on PID control technology, the application of conductivity value and pH value to develop precise water and fertilizer irrigation control system. The thesis also performed theoretical analysis and experiment of digital PID control of EC value, the results indicated that the PID control system has the advantages of high control precision, but the control performance is degradation when the fertilizer density changes greatly. The intelligent PID controller with EC value was designed by using open-loop step response, PID control technology and inaccurate-control technology. The test results show that it has PID parameter self-controlling ability, good control performance, the stable time within 3 minutes, precision degree is within ±0.15mS/cm, overshoot less than 15%. The improved intelligent PID controller control the pH value, through using open-loop step control and PID control, the test shows that the stability time within 3 minutes, the accuracy is within ± 0.15pH, overshoot less than 15%. Combine fuzzy PID with grey prediction, the grey prediction - Fuzzy PID control of water and fertilizer concentration was developed, which has a fastest corresponding speed and better control stability. It owns a good control effective and have a better control quality**

Keywords—water-fertilizer irrigation, grey-fuzzy PID control, intelligent control strategy, precise irrigation, concentration detection

I. Introduction

The irrigation and fertilization, it also be called water and fertilizer irrigation, with the process of the water irrigation, refers the fertilizer through the irrigation system with the water for the crop and provide nutrients, it is, according to the needs of nutrients and climatic conditions of the crop growth at all stages such as fertilizer put on and even applied in the vicinity of the root system, it would be directly absorbed and applied of the roots system [1]. It means turning the soluble fertilizer into the preparation of the solution according to a certain proportion, and through the fertilizer device to the fertilizer solution into the drip irrigation system with irrigation water transported to all the drip emitter, an advanced fertilization method during the process of crop fertilization. It is a combine production between the fertilization techniques and irrigation techniques [2-3]. The irrigation and fertilization is an effective method for quantitative supply of crop water and nutrients and maintaining soil suitable water and nutrient density. In the advanced country with the agricultural technology, for instance Israel, 75% to 80% of the irrigated land was applied in irrigated and fertilized. This method was not only applied in the field of fertilization, but also for the greenhouse substrate soil-less cultivation of crop fertilization. The fertilizer utilization is full due to accurate and uniform fertilization around the root and according to the characteristics of crop fertilizer need. It could be saved the amount of fertilizer and control the depth of fertilizer infiltration to reduce the pollution of fertilization on the environment by the water-fertilizer irrigation; it also adjust the water-infiltration speed rate, well-distributed irrigation, it would not produce the ground light flow and reduce soil compaction, reduce soil surface evaporation and leakage loss ,made the utilization rate of irrigation water reach more than 90%[4-5], it has been saved 21% of irrigation water and 34% of the production fertilizer.

It has many researches of the water and fertilizer integration technology in China, but the technical promotion stayed at the initial stage and simple, it has not popularized the water and fertilizer integration equipment application, it still in the complex water-soluble fertilizer with the original stage of the application of fertilizer, lack the theoretical guidance of water and fertilizer coupling [6]. The equipment key technology subject in the controller control strategy, on one hand, it needs to control the amount of water which crops need, on the other hand, to obtain the maximum net income with the least amount of water. However, the control object is a big inertia, nonlinear and pure delay system, a precise and unified mathematical model could not be established, the traditional control method has been faced a serious challenge, the inaccurate control couldn't need to establish the mathematical model of the controlled object, to improve its nonlinear and time-varying problems effectively [7]. Combined the control effect of PID controller with inaccurate-control to improve its nonlinear control effect in the paper, it can overcome the above difficulties. The effect of water-fertilizer irrigation control strategy by simulation analysis and tests was verified in the paper.

II. The Design of Control System for Precision Water and Fertilizer Irrigation

For integrating with the control of water and fertilizer, the extensive and in-depth research has been conducted around the domestic and foreign scholars. Currently, the nutrient solution regulation could be divided into three categories: the nutrient solution in view of the EC value and pH value, the nutrient solution model that based on the nutrient control methods and the nutrient solution based on crop model [8-16], first control mode based on EC value and pH mode was researched in the paper. In order to meet of growth crops in a timely manner the different stages to adjust the proportion of water and fertilizer, supply amount and supply time, the system can realize real-time detection according to the user set fertilizer value EC value and pH value to conduct the automatic constant irrigation and fertilization, to achieve the purpose of high quality and high yield. The specific control system of water-fertilizer irrigation was composed of electrical control part, main water pipeline system, and sensor and injection pipe system, the system frame diagram shown as Fig.1.

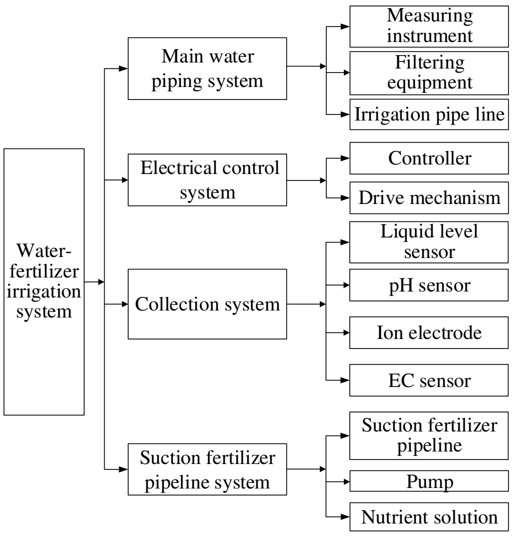

Fig. 1. Diagram of water-fertilizer irrigation control system

The main water pipeline system of water-fertilizer irrigation system is mainly composed of filter, pressure gauge, flow meter, exhaust valve, check valve, pressure regulator and other components, mainly applicate to obtain the required pressure and flow system to protect the drip water and emitter. The fertilizer pipe just has the selected-machinery diaphragm pump for the system fertilizer injection equipment, furthermore, the configuration of the pressure gauge and flow meter. Electric Conductivity (EC) sensor and pH sensor (pH) the measuring tube of the sensor is drawn from the main water pipe with the thin tube and the lead-out point was set in front of the filter, formed the real-time detection circuits. The electrical control is composed of PLC controller and transmission mechanism. The controller was embedded algorithm and model by MBD technology, which mainly used for operation and display, and executed the user's commands. The transmission mechanism adopts the AC variable frequency drive mode, to complete the water-fertilizer irrigation system goals by the steeples speed control is conducted by the AC motor.

III. THE SYSTEM FUZZY PID CONTROL TECHNOLOGY

A. *The fuzzy PID control principle of fertilizer density*

The fertilizer density control is the core control block of this system. It is mainly completed the control parameters of the conductivity parameters and pH value. The control frame diagram is shown as Fig.2.

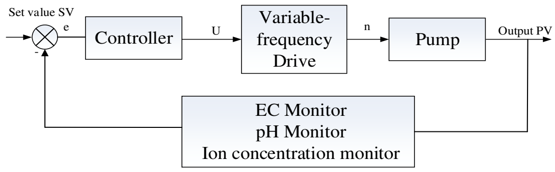

Fig. 2. Principle diagram for fertilizer concentration of PID control

The mixed fertilizer was measured by EC sensor and pH sensor from Fig.2,then the current signal was amplified and 4~20mA output , transmitter to the AD circuit into a digital signal, the control unit compare with the set value SV, after the processing of the deviation value e, the controller converts the control signal to the 4~20mA signal by the DA module, and transmits the control signal to the frequency converter, to achieve the EC value and pH constant control by the rotational speed n controls of the AC motor through the inverter.

B. *Control strategy of EC value*

The static gain K of the fertilizer solution was test by the open-loop step response application, and K is used as an adaptive factor of the intelligent PID controller, the control frame diagram shown in Fig.3.

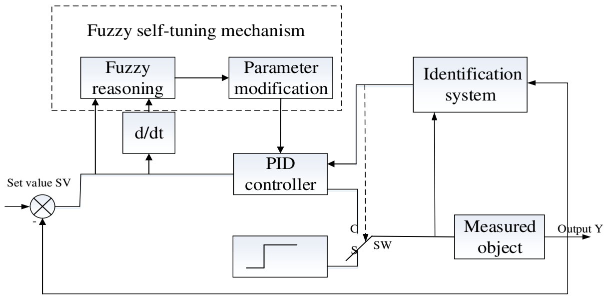

Fig. 3. Block diagram of fuzzy self-tuning PID control

Two kinds of working modes existed in the controller, identification mode and control mode. When system was started the work in every time, firstly, the identification mode was entered, the switch SW and S was connected, the input u0 of object by the step ran into the open loop state, identify the link test open loop response data automatically and identify the object by type 5 of the parameter K, and it as a PID control of an adaptive factor processing, and as to achieve automatic control PID control. After the identification is finished, the switch SW was switched from S to C, and the system switches from the identification mode into the control mode. The PID parameters in the regulation are judged by the fuzzy rules, which are advantageous to implement different control intensity for different error ranges and make up for the shortcomings of the pure PID control algorithm itself in static and dynamic performance, tracking set value and the suppress distribution [17].

The advantage of this method is lie in the identification mode, as the control is could not be conducted, it avoid the affection during the pipeline exhaust air lag time on the control performance when the pump open, the pure control is often processed is not well at this point would bring the large fluctuations, resulting in control failure, especially for the PID control algorithm; in addition, this method to test the object parameters, will not cause adverse effects on the system, the test process is an open-loop control process, a full step response process of the system would finished the parameters of the test, a good expression ideal of the open loop test, and the closed loop control. At the same time this method as long as the object to know the approximate time scale can be carried out, it could be identified according to the object parameters to decide the control mode sampling frequency.

While the input signal r (t) is a step-stage signal, the input signal would be used as the test excitation signal u0 (t) = r (t) directly, which means provide corresponds to an initial control to the system, then the system switches from the identification phase to In the control phase, there is no large distribution, especially when the static gain of the object is close to 1, it almost switching can be achieved without disturbance. So, the controller belong to the range of intelligent controller for a self-adjusting function, refers to the control strategy for the intelligent PID controller in this paper.

C. The control strategy for pH value

As for maintain the constant state of acid density in pH control, the PID controller with open-loop step control is designed in this paper , which is referred to as improved PID controller, and the diagram 4 is shown in Fig4. The self-identification structure is the same as the EC intelligent PID controller's self-identification structure basically. The difference is that the self-identifying structure in this controller is only used to determine whether the acid injection pipe is filled with piping, match with the open-loop control time. The switch SW was controlled through PV and the initial value PV(0) , and can complete the switch between the PID control and step-stage control.

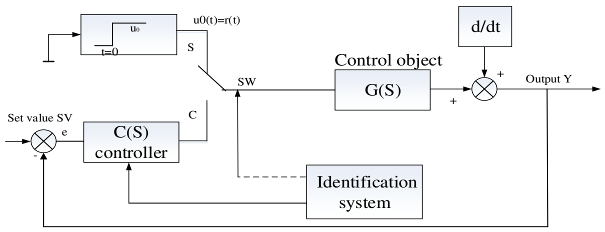

Fig. 4. Block diagram of improved PID controller

The solid line is the object step-stage response curve of the EC value in Fig.5, compared with the dotted line from Figure (a), and it is similar to the pure delay of industrial objects, therefore, the system is nonlinear, inertia. The Fig 2 showed the general estimate of T, τ, and K.

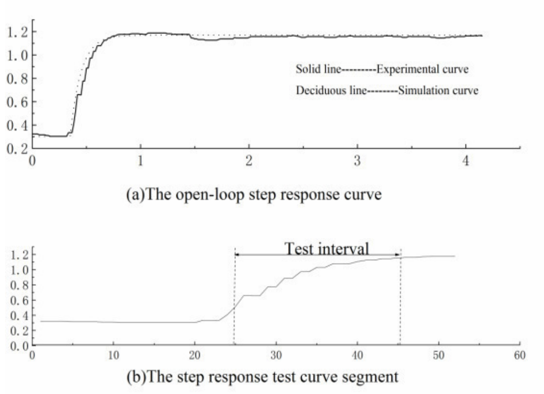

Fig. 5. EC value open-loop step response curve

IV. THE OPEN-LOOP STEP-STAGE RESPONSE OF PH VALUE

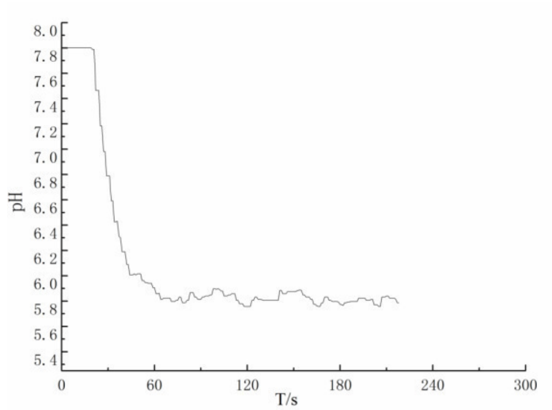

Fig. 6. pH value open-loop step response curve

The Fig.6 is the open-loop step-stage response curve for pH value. It show that the pH adjustment is a negative mode and a single self-balancing system, meanwhile, it can achieve stability for the object open-loop step response of the pH value about 60s, because of the acid pump and fertilizer pump is diaphragm pumps, and injection pipe and filling the same length of the pipeline. It can be known that the time length of open-loop control in the control strategy of pH single factor should be less than 60s, and the time should be relaxed when EC /pH value is adjusted, and it should be within 100s. Otherwise, it would be alarmed, checked the valve and pipe.

A. The PID Control Test

a) The sampling cycle test of EC controller: It can be seen that the sampling cycle is approximately in the range of (7s, 15s) from the open-loop step-stage response, and it show that the impacted curve of the PID controller control performance in different sampling cycles in the Fig.7.

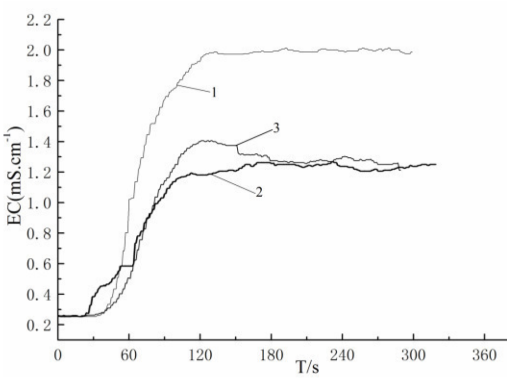

Fig. 7. Response curves of different sampling period EC value (1-5s；2-10s；3-15s)

Firstly, the scene PID parameter tuning was completed, the same fertilizer density (keep the static gain K consistent), set different sampling cycle for the experiment. As it could be seen from Fig.8 that the control cycle within 5s, 10s and 15s, and had control effect roughly the same, furthermore, cycle 5s seems better. So, the EC controller sampling cycle to select 5s.

b) The PID controller adaptability test： The comparison curve of the PID controller adaptability test result showed in Fig.8. It can seen that the PID controller parameter setting is low in the fertilizer density(fertilizer density 1) under the circumstances. Fertilizer density 1 has a better control performance as shown in Fig.8 left the curve 1, the overshoot is less than 10%, no oscillation. From the right side of Fig.9, it could be seen that the response curve 1 is also relatively gentle. However, the relatively high concentration of fertilizer was controlled by this controller, the control performance is greatly deteriorated, the left curve 2 of Fig.8 showed that the overshoot reached about 70%, the amplitude is about 0.8mS/cm, the oscillation cycle is long about 5 minutes before the basic stability. As it could be seen from curve 2 in Fig.8, the change in EC value lag control is about 30 seconds, so, it is a big inertia in the system.

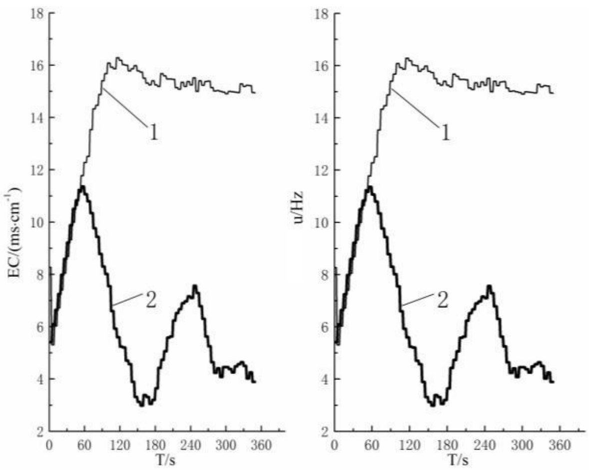

Fig. 8. Adaptive test of PID controller

B. 3.2 The control performance test of the EC value and pH value

The nutrient solution control performance is the control quality of the EC/pH value from the drip effluent, therefore it could not look at the control of control quality only, and it needs to test the droplet fertilizer density to verify the system controller control quality in the different time. The experimental method is the normal operation of the system controller at the beginning of the drip interval 30s with a measuring cylinder for 10s after the instrument measurement. It can be seen that EC value and pH value control performance curve for the system nutrient solution and the test amount curve during the changing in the Fig.9.

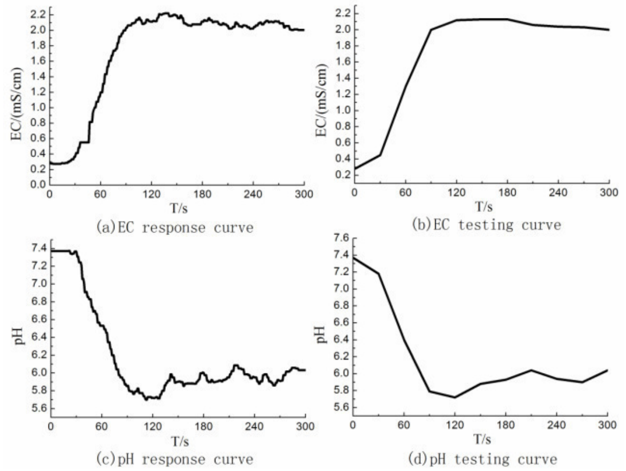

Fig. 9. System control performance test

It could be seen that the EC and pH value change curve are little difference at the drip place from the control curve of the EC value and pH value of the system controller, and the changed curve of the drip is slow and gentle, due of the average value of the measured value. Therefore it could be considered the control quality of the controller could be applied as the quality of nutrient control performance basically.

C. Application of precision water and fertilizer irrigation equipment

The research on the control strategy of water and fertilizer irrigation system is the core of the development of intelligent controller, and it is the requirement of further water and fertilizer irrigation. The precision water-fertilizer irrigation equipment can detect fertilizer concentrations, it also has the functions of irrigation control and environmental control. Its structure consists of touch screen, main control module, wireless transmission module, EC and pH measurement module and drive control module, the wireless transmission module including 433MHz wireless transmission, 4G wireless transmission, WIFI wireless transmission, SMS alarm. The driving control module was divided into three parts, fertilizer-liquid ratio drive, environmental control drive and irrigation control drive. It has equipment man-machine interface, mobile phone APP and PC irrigation control system for the operating platform. The equipment was applied for the glass greenhouse "Yong sweet 5" melon in Ningbo Agricultural Science and Technology Demonstration Garden, and the experiments of water-fertilizer irrigation were conducted about 96 days of autumn planting.

V. FUZZY PID FOR WATER AND FERTILIZER CONTROL TECHNOLOGY BASED ON GREY PREDICTION

Furthermore, in order to improve the control accuracy of water and fertilizer concentration during agricultural fertilization and irrigation periods. Grey prediction technique is used in Fuzzy PID and got a better control effect.

A. Water and fertilizer irrigation control algorithm model for grey prediction Fuzzy PID

For Fuzzy Control, which can improve the control effect of nonlinear and large inertia systems in Water and fertilizer irrigation.

And Grey prediction, it can solve the phenomenon of large time lag and can get the control beforehand for fertilizer concentration.

Control schematic of Fuzzy PID for water and fertilizer control technology based on Grey Prediction is following:

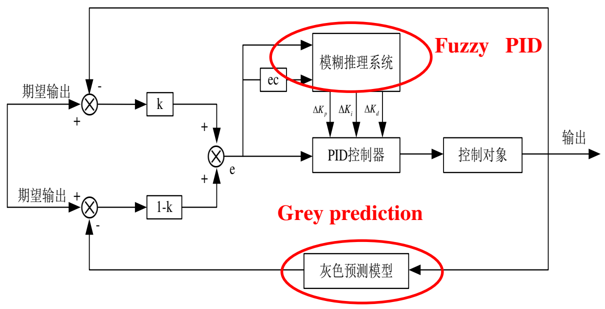

Fig. 10. Control schematic of grey prediction - Fuzzy PID

Grey Prediction - Fuzzy PID Model for water and fertilizer control technology is as follows:

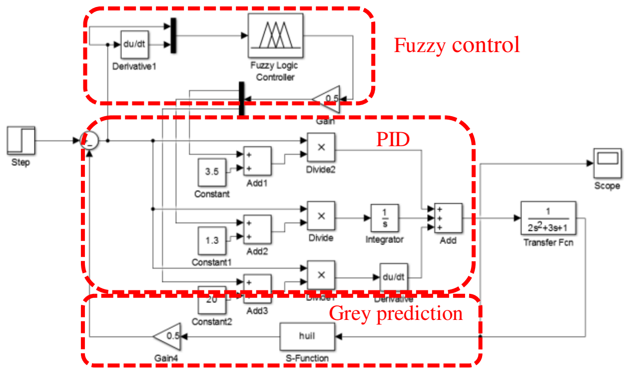

Fig. 11. The model of grey prediction - Fuzzy PID

Based on above model of Grey Prediction - Fuzzy PID for water and fertilizer control. Through SIMULINK Simulation of Grey Theory and Fuzzy Control for water and fertilizer control. The results are shown in Fig.12.

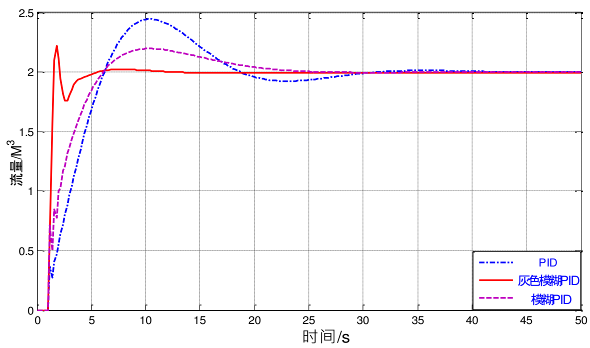

Fig. 12. SIMULINK Simulation of grey prediction - Fuzzy PID controy

It can be found that grey prediction - Fuzzy PID control system has a smooth response curve, small overshoot and good stability compared with PID and fuzzy PID.

B. Research on experiment for the grey prediction - Fuzzy PID control of water and fertilizer control technology

Using above experimental test device, the experiment for the grey prediction - Fuzzy PID control of water and fertilizer concentration was conducted. The control curves are shown in fig.13.

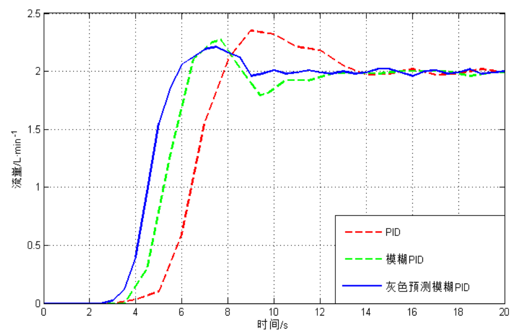

Fig. 13. Experiment results of grey prediction - Fuzzy PID controy

In which, grey prediction - Fuzzy PID control of water and fertilizer concentration has a fastest corresponding speed and better control stability.

Table 1 Experimental performance index

	Delay t_d (S)	Rise t_r (S)	Peak t_p (S)	Overshoot σ %	Adjustment t_s (S)	Steady-state error e_{ss}
PID	3.493	5.302	12.5	25.59	33.5	0.0004
Fuzzy PID	2.0142	3.698	10.4	9.82	20.1	0
Grey-Fuzzy PID	1.2787	0.424	1.8	10.91	4.48	0.0002

From above Experimental performance index, it can be seen that the flow value of water-fertilizer in 0-3 s is zero, and the flow sensor range is 1-30 L/min. The reliability of data below 1 L/min is not high. Under Grey Prediction -

Fuzzy PID, the control basically reaches a steady state at 8.5 s. Compared with that the fuzzy PID and PID are basically stable to 12.5 s and 13.5 s, respectively.

VI. Conclusions

The system control strategy has been further discussed in the paper, the intelligent irrigation control technology has been researched based on the fuzzy PID control, The research shows that the system had a stronger adaptability, a good control performance and robustness.

Firstly, it is an effective solution to solve the problem of water-saving irrigation uncertainty model according to the PID control, and it can solve the problem of large inertia and nonlinearity of the system by the fuzzy PID successfully.

Secondly, the intelligent PID controller integrated applied the open-loop step-stage response and the PID integrated style parameter setting method, the one-dimensional fuzzy control technology, it has been introduced to speed up the response and suppress the overshoot. The control performance of the different liquid concentration is reaching the PID control for good performance of the work basically; it shows that it has been the ability for PID parameters self-tuning.

Thirdly, combine fuzzy PID with grey prediction, the grey prediction - Fuzzy PID control of water and fertilizer concentration was developed, which has a fastest corresponding speed and better control stability. It owns a good control effective and have a better control quality.

Acknowledgment

The work is supported by National Key R&D Program of Plan under Grant Nos. 2017YFD0201504.

References

[1] Jian-Dong Y U, Wu-Zhong N I, Yang X E. A New Technique for the Management of Fertilizers and Water- Fertigation. Chinese Journal of Soil Science, vol. 34,pp. 148-153,2003.

[2] Patricia Imas. Recent Techniques in Fertigation of Horticultural Crolps in Israel.Recent Trends in Nutrition Management in Horticultural crops. Dapoli, Maharashtra, INDIA: 1999.

[3] Fusheng L I, Shennian L U. Study on the fertigation and its application. Plant Natrition & Fertilizenence, vol. 6,pp. 233-242, 2000.

[4] Margaret A C, Jackie B L, Peter M A T, et al. Effects of nutrient solution electrical conductivity on the compositional and sensory characteristics of greenhouse tomato fruit. PostharvestBiology and Technology, vol. 74,pp. 132-140,2003.

[5] Alberto P, Fernando M, Incrocci L, et al. A comparison between two methods to control nutrient delivery to greenhouse melons grown in recirculating nutrient solution culture. Scientia Horticulturae, vol. 95,pp. 89-925,2002.

[6] H Yuan, L Li, J Wang, H Wang, NA Sigrimis.Design and test of regulation and control equipment for nutrient solution of water and fertilizer integration in greenhouse. Transactions of the Chinese Society of Agricultural Engineering , vol. 32,pp. 27-32,2016.

[7] Zhang Yubin, Wei Zhengying, Ma Shengli, et al. Grey Prediction Fuzzy-PID Control Technology for Irrigation. China Rural Water and Hydropower, vol. 2,pp. 5-8,2016.

[8] Mao, Hanping, et al. Regression Model of the Mother Liquid Dosage and the Value of EC/pH in Facility Cultivation.Journal of Agricultural Mechanization Research, vol. 34,pp. 2012.

[9] WEI Zhengying,GE Lingxing. Development of Automatic Control System of Fertigation Technique.Journal of xi'an jiaotong university. Mar. vol. 42,pp. 347-349,2008.

[10] Daniele M, Mattson N S, Lieth H. An empirical model to simulate sodium absorption in roses growing in a hydroponic system. Scientia Horticulturae, vol. 118,pp. 228-235,2008.

[11] Daniele M, Incrocci L, Maggini R. Strategies to decrease water drainage and nitrate emission from soilless cultures of greenhouse tomato[J]. Agricultural Water Management, vol. 97,pp. 971-980,2010.

[12] Marcelis L, Dieleman J, Boulard T, et al. CLOSYS: Closed system for water and nutrient management in horticulture. Acta Horticulturae, vol. 718,pp. 375-382,2006.

[13] Carmassi G, Incrocci L, Maggini R, et al. An aggregated model for water requirements of greenhouse tomato grown in closed rock wool culture with saline water. Agricultural Water Management, vol. 88,pp. 73-82,2007.

[14] Gallardo M, Thomopson T B, Rodriguez J S, et al. Simulation of transpiration, drainage, N uptake, nitrate leaching, and N uptake concentration in tomato grown in open substrate. Agricultural Water Management, vol. 96,pp. 1773-1784,2009.

[15] Savvas D, Mantzos N, Barouchas P E. Modelling salt accumulation by a bean crop grown in a closed hydroponic System in relation to water uptake. Scientia Horticulturae, vol. 111,pp. 311-318,2007.

[16] Varlagas H, Savvas D, Mouzakis G, et al. Modelling uptake of Na+ and Cl− by tomato in closed-cycle cultivation systems as influenced by irrigation water salinity. Agricultural Water Management, vol. 97,pp. 1242-1250,2010.

[17] Shinn-Horng Chen, Jyh-Horng Chou,Jin-Jeng Li. Optimal grey-fuzzy controller design for a constant turning force system. International Journal of Machine Tools & Manufacture, vol.42,pp.343-355,2001.

A Framework for Anomaly Detection in Activities of Daily Living using an Assistive Robot

Salisu Wada Yahaya, Ahmad Lotfi, *Senior Member, IEEE*, Mufti Mahmud, *Senior Member, IEEE*

***Abstract*— This paper presents an overview of an ongoing research to incorporate an assistive robotic platform towards improved detection of anomalies in daily living activities of older adults. This involves learning human daily behavioural routine and detecting deviation from the known routine which can constitute an abnormality. Current approaches suffer from high rate of false alarms, therefore, lead to dissatisfaction by clients and carers. This may be connected to behavioural changes of human activities due to seasonal or other physical factors. To address this, a framework for anomaly detection is proposed which incorporates an assistive robotic platform as an intermediary. Instances classified as anomalous will first be confirmed from the monitored individual through the intermediary. The proposed framework has the potential of mitigating the false alarm rate generated by current approaches.**

I. Introduction

The world population of older adults (i.e. people between the age of 65 and above) is increasing and it is estimated to be over 1.92 billion in 2050 [1]. This leads to increase in cost of care for the senior citizens. Moreover, study has shown that these senior citizens prefer to live in their own homes rather than being looked after in a care homes [2] [3]. Given the health-related challenges associated with older people, systems are set in place to monitor the Activities of Daily Living (ADL) in order to promote the independent living and improve the quality of life for older adults. ADL are those activities an individual must be able to perform in order to be able to live independently such as eating, maintaining personal hygiene and continence, mobility etc. Abnormalities in these activities can be an indication of health decline or challenges related to Mild Cognitive Impairment (MCI) such as Dementia, which are detrimental to wellbeing.

The current approaches to anomaly detection in ADL suffer from high rate of false alarms making the system unreliable, and therefore, leads to dissatisfaction by carers and clients [4]. This may be connected to the dynamic nature of human activity which is subject to changes based on seasonal or other physical factors. To build a reliable anomaly detection system and reduce the rate of false alarm, the user's behaviour must be modelled accurately by taking into account the changes in the individual behavioural routine.

This can be achieved by building a computational model that can adapt to changes in human behaviour. Using a robotic platform as an intermediary in the anomaly detection system is proposed in this paper. Activities classified as anomalous will be queried through the robotic platform for confirmation from the user. This will enable the model to obtain the user's feedback in real time before making its final prediction.

II. Anomaly Detection in Activities of Daily Living

In the context of ADL, anomaly is any significant deviation from individual's usual behavioural routine. Research has been conducted to detect abnormality in ADL using different computational methodologies. Hoque et. al. [5] developed an ADL anomaly detecting system termed "Holmes" using DBSCAN clustering. Similarly, the duration of performed activities, time and number of sensor events are extracted and clustered using DBSCAN in [6]. Instance with unusual duration or irregular sensor events are classified as anomalous. A method based on detecting temporal relation between activities is used for detecting anomaly in [7]. Since human behavioural routine varies from one individual to another, the most common approach is to model the behaviour of an individual to serve as a baseline. Subsequent behavioural routines are compared to the baseline and deviations are classified as anomalies. The same approach is applied in [8] with One-Class Support Vector Machine (OC-SVM) to detect abnormality in sleeping pattern. While these approaches are able to detect anomalous instance of activities, they are not flexible to accommodate changes in user's behavioural routine that are not anomalous. This may be due to the lack of a feedback mechanism.

III. Robots for Social Interactions

Robots for social interactions also known as Socially Assistive Robots (SAR) are robots that provides assistance via social means (i.e. through interactions) rather than through physical means [9]. In recent years, researchers have been applying SAR for various purposes ranging from health care monitoring, social engagement and as motivational agent. For example, in [10] an exercise trainer robot is built to coach and motivate older adults to perform physical activities. The robot uses Kinect sensor to analyse human pose and gives feedback in form of facial expression and speech. Similarly, a companion robot for people living with MCI is proposed in [11]. This robot assists with keeping track of reminders (e.g. taking medication), administering cognitive exercises and establishing communication with relatives and carers. A research is conducted in [12] using an SAR to help children

S. W. Yahaya is PhD student at the Dept. of Computing & Technology, School of Science & Technology, Nottingham Trent University, Clifton, Nottingham, NG11 8NS, UK (e-mail: salisu.yahaya2015@my.ntu.ac.uk).

A. Lotfi is a Professor of Computational Intelligence at the School of Science & Technology, Nottingham Trent University, Clifton, Nottingham, NG11 8NS, UK (phone: +44 (0)115 848 8390; e-mail: ahmad.lotfi@ntu.ac.uk).

M. Mahmud is a (Senior) Lecturer of Computing & Technology, School of Science & Technology, Nottingham Trent University, Clifton, Nottingham, NG11 8NS, UK (e-mail: mufti.mahmud@{ntu.ac.uk,gmail.com}).

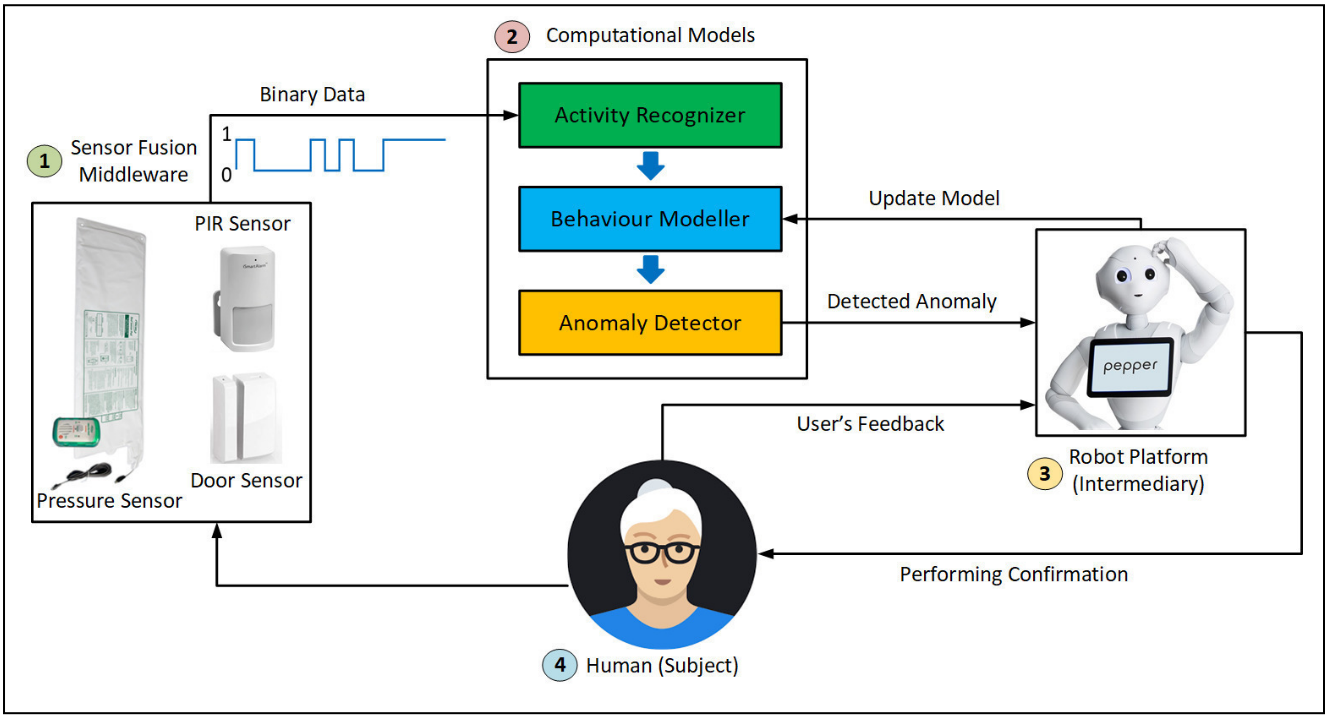

Figure 1. Proposed architecture for anomaly detection in ADL.

with diabetes learn how to manage the condition while in [13], a robot is used to teach children living with Autism Spectrum Condition (ASC) how to see things from a different person's perspective which is also known as Visual Perspective Taking (VPT).

Taking advantage of the potential of these devices in home settings, as well as robot's support for multi-modal interaction through gesture, touch and speech, they can serve as a good intermediary for an anomaly detection system. Moreover, studies have shown that the physical embodiment of robots facilitates Human-Robot Interaction (HRI) [14] [15].

IV. Proposed Architecture for Anomaly Detection

A schematic diagram is shown in Figure 1 of the proposed framework for anomaly detection consisting of four interconnected layers, namely; Sensor Fusion, Computational Models, Intermediary and Human layer. The Computational Models layer has three components; Activity Recogniser, Behaviour Modeller and Anomaly Detector.

The Sensor Fusion layer consists of a network of interconnected low-level sensors for data collection. These sensors include Passive Infrared (PIR) Motion Sensors in the various location of the house, Pressure sensor on bed and on chair, Door sensor on the door etc. This is the most widely acceptable sensing modality due to its non-invasive nature compared to vision based approached which raises privacy concerns [2]. The data generated by these sensors are binary in nature with 0 and 1 signifying inactive and active states respectively. The data is then sent to the Computational Model layer for processing.

The Activity Recognizer component interprets the binary data into readable human activities. Rule-based approaches are used for the recognition. The recognized activities involve eating, preparing meal, toileting, sleeping etc. Each activity is accompanied by its start time, end time, and location as shown in Table 1.

TABLE I. SAMPLE DATA FOR ACTIVITIES OF DAILY LIVING.

Start Time	End Time	Activity	Location
2018-05-01 17:19:31	2018-05-01 17:28:45	Eating	Dining Room
2018-05-01 17:28:59	2018-05-01 20:34:31	Toileting	Toilet
2018-05-01 22:49:43	2018-05-02 07:46:07	Sleeping	Bedroom

The Behavioural Modeller component builds a model of the person's behavioural routine. Apart from our recent work in [8], other computational models such as those capable of learning temporal and sequence data such as Hidden Markov Model (HMM) and Recurrent Neural Network (RNN) will be explored.

The Anomaly Detector component compares the subsequent user's behaviour against the model build by the Behaviour Modeller. Deviation from the built model that can be an indication of abnormality will be sent to the Intermediary layer (robot) for confirmation.

The Intermediary layer serves as a bridge between the Computational Models layer and the Human. The robot platform will have a bi-direction communication capability to enable it to interact with humans. It will confirm activities that are classified as abnormal by the Anomaly Detector component. The user's response will be fed back to the Behaviour Modeller. In a situation where the user's response goes contrary to the prediction of the Anomaly Detector over a

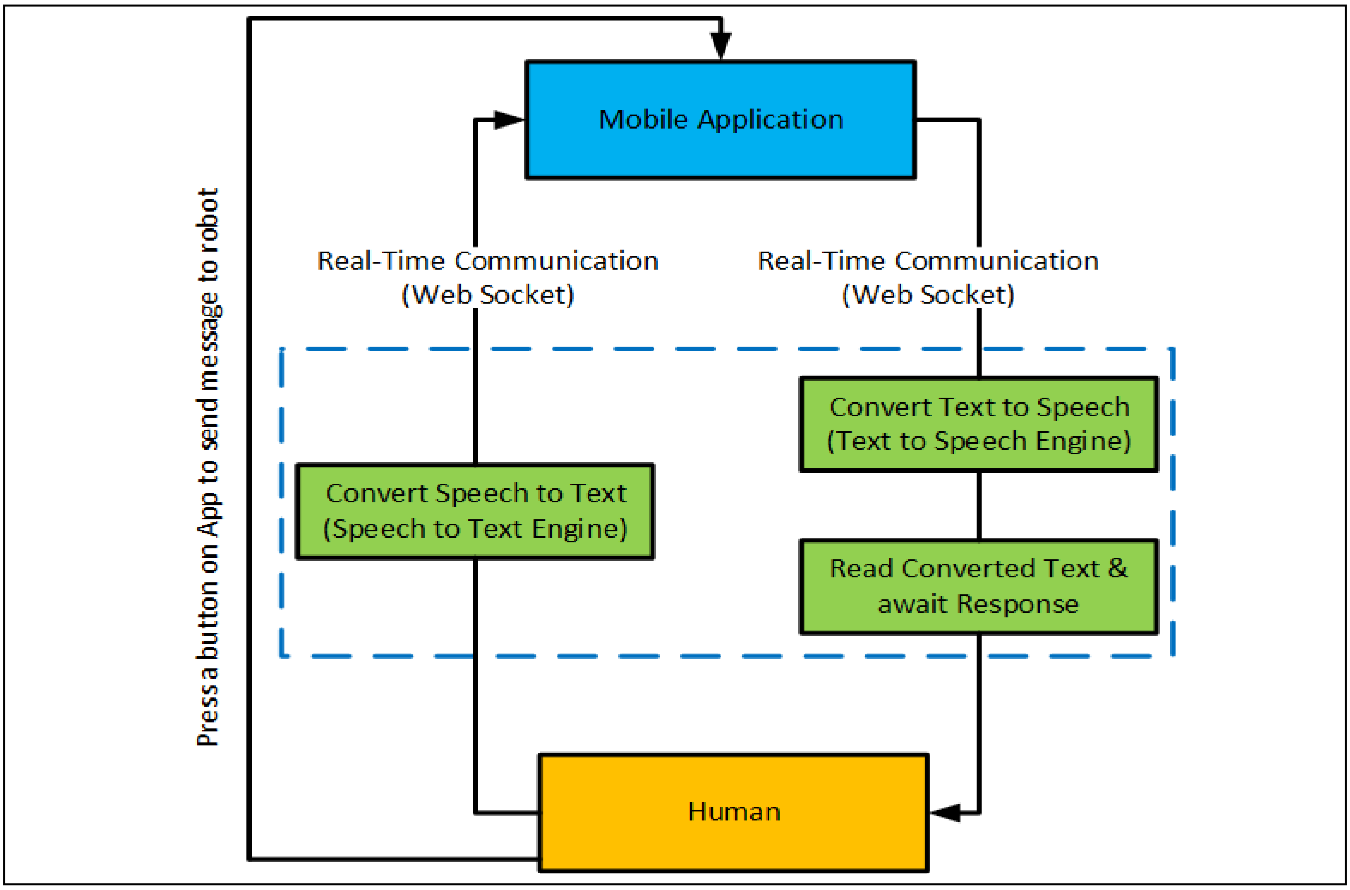

Figure 2. Implementation diagram for real-time human-robot communication.

certain threshold, the user's response along with the model's prediction will be forwarded for an expert evaluation. The expert, in this case, can be the carer or medical personnel. The expert's opinion is given more weight and serves as the final prediction. Important design guidelines for HRI such as error prevention and correction, consistency, user control and freedom [16] [17] will be taken into consideration as well as the concept of persuasive psychology in order to increase the acceptability of the platform and make it less invasive. To make the proposed framework more robust, computational models based on the concept of active learning will also be explored. This will enable the Behaviour Modeller to learn in a progressive manner based on the feedback received from the Human.

V. Evaluation Strategy

The different layers of the proposed anomaly detection framework will be evaluated. The ability of the Sensor Fusion middleware to aggregate the heterogenous sensors for data collection will be evaluated. At the Computational Model layer, the evaluation will focus primarily on the system's ability to model the individual's behavioural routine and detects abnormalities in it. Publicly available ADL datasets as well as experimental data collected specifically for this research will be utilized. Different anomalous instance will be simulated to test the robustness of the computational models.

Evaluation of the Intermediary layer will focus on HRI to assess the acceptability of the platform for behaviour monitoring. Devices capable of serving as an intermediary such as mobile phones and screen-only based interface will be tested. While assistive robots provide the advantage of physical embodiment and support for multi-modal interaction, factors such as the cost of the platform, trust-related issues and technical difficulties might make other intermediaries more suitable. The monitored individuals, carers and experts will be incorporated in the evaluation of the proposed architecture.

To test for the feasibility of using a robot platform as an intermediary, an application is implemented with a bi-directional communication capability using Pepper robot. Pepper is a humanoid robot from SoftBank Robotics equipped with a touch screen display and wheels for mobility. It is capable of interacting with humans, recognizing faces and basic human emotions [18].

The implementation diagram for real-time human-robot communication is illustrated in Figure 2. A mobile application is built to simulate the Anomaly Detector component. A user presses a button on the app to send a message to the robot similar to how the Anomaly Detector will broadcast an anomalous activity to the intermediary. The generated message is transmitted via web socket in real-time to the robotic platform. The Robot uses a Text to Speech engine to convert the message to an audio format, reads it out and waits for the user's feedback. The user's response in form of speech is converted to text using Speech to Text engine. The converted text is then retransmitted via web socket to the mobile application in real-time. This is a simulation of the intermediary component without the Computational Models and Sensor Fusion layers.

VI. Conclusion

In this paper, a framework for anomaly detection in ADL incorporating a SAR platform is presented. The platform serves as an intermediary between the anomaly detection model and the human for performing confirmation of detected anomalies in order to reduce the rate of false alarm affecting the current approaches. Using computational models based on active learning, an anomaly detection system can be built that can adapt to changes in individual's behaviour routine with less false alarm. Future work will include testing and deployment of the complete system in a real home environment.

References

[1] S. Chernbumroong, S. Cang, A. Atkins and H. Yu, "Elderly Activities Recognition and Classification for Applications in Assisted Living," *Expert Systems with Applications,* vol. 40, pp. 1662 - 1674, 2013.

[2] P. Rashidi and A. Mihailidis, "A Survey on Ambient-Assisted Living Tools for Older Adults," *IEEE Journal of Biomedical and Health Informatics,* vol. 17, pp. 579-590, 2013.

[3] A. Lotfi, C. Langensiepen, S. Mahmoud and M. J. Akhlaghinia, "Smart homes for the elderly dementia sufferers: identification and prediction of abnormal behaviour," *Journal of Ambient Intelligence and Humanized Computing,* vol. 3, pp. 205-218, 2012.

[4] K. Z. Haigh, L. M. Kiff and G. Ho, "The Independent LifeStyle Assistant: Lessons Learned," *Assistive Technology,* vol. 18, pp. 87-106, 2006.

[5] E. Hoque, R. F. Dickerson, S. M. Preum, M. Hanson, A. Barth and J. A. Stankovic, "Holmes: A Comprehensive Anomaly Detection System for Daily In-home Activities," in *2015 International Conference on Distributed Computing in Sensor Systems*, 2018.

[6] L. G. Fahad and R. M., "Anomalies Detection in Smart-Home Activities," in *2015 IEEE 14th International Conference on Machine Learning and Applications (ICMLA)*, 2015.

[7] V. Jakkula, D. J. Cook and A. S. Crandall, "Temporal pattern discovery for anomaly detection in a smart home," in *2007 3rd IET International Conference on Intelligent Environments*, 2007.

[8] S. W. Yahaya, C. Langensiepen and A. Lotfi, "Anomaly Detection in Activities of Daily Living Using One-Class Support Vector Machine," in *18th UK Workshop on Computational Intelligence*, 2018.

[9] D. Feil-Seifer and M. J. Mataric, "Defining socially assistive robotics," in *9th International Conference on Rehabilitation Robotics*, 2005.

[10] A. Lotfi, C. Langensiepen and S. W. Yahaya, "Socially Assistive Robotics: Robot Exercise Trainer for Older Adults," *Technologies,* vol. 6, 2018.

[11] H. -M. Gross, C. Schroeter, S. Mueller, M. Volkhardt, E. Einhorn, A. Bley, T. Langner, C. Martin and M. Merten, "I'll keep an eye on you: Home robot companion for elderly people with cognitive impairment," in *2011 IEEE International Conference on Systems, Man, and Cybernetics*, 2011.

[12] L. Cañamero and M. Lewis, "Making New "New AI" Friends: Designing a Social Robot for Diabetic Children from an Embodied AI Perspective," *International Journal of Social Robotics,* vol. 8, pp. 523--537, 2016.

[13] L. Wood, B. Robins, G. Lakatos, D. S. Syrdal, Z. Abolfazl and D. Kerstin, "Utilising humanoid robots to assist children with autism learn about Visual Perspective Taking," in *UK Robotics and Autonomous Systems Conference*, 2017.

[14] J.-J. Cabibihan, H. Javed, M. J. Ang and S. M. Aljunied, "Why Robots? A Survey on the Roles and Benefits of Social Robots in the Therapy of Children with Autism," *International Journal of Social Robotics,* vol. 5, pp. 593-618, 2013.

[15] J. Wainer, D. J. Feil-seifer, D. A. Shell and M. J. Mataric, "The role of physical embodiment in human-robot interaction," in *15th IEEE International Symposium on Robot and Human Interactive Communication*, Hatfield, 2006.

[16] C. Breazeal, "Social interactions in HRI: the robot view," *IEEE Transactions on Systems, Man, and Cybernetics, Part C (Applications and Reviews),* vol. 34, no. 2, pp. 181-186, 2004.

[17] O. M. -.. E. Sucar, S. H. Aviles and C. Miranda-Palma, "From HCI to HRI - usability inspection in multimodal human - robot interactions," in *12th IEEE International Workshop on Robot and Human Interactive Communication*, 2003.

[18] SoftBank, "Pepper the humaoid robot," SoftBank Robotics, [Online]. Available: https://www.softbankrobotics.com/emea/en/pepper. [Accessed 03 01 2019].